EPFL

Thèse n° 9889

Disorder-induced electronic, magnetic, and optoelectronic properties of two-dimensional materials

Présentée le 23 septembre 2022

Faculté des sciences et techniques de l'ingénieur
Laboratoire d'électronique et structures à l'échelle nanométrique
Programme doctoral en science et génie des matériaux

pour l'obtention du grade de Docteur ès Sciences

par

Cheol Yeon CHEON

Acceptée sur proposition du jury

Dr A. Hessler-Wyser, présidente du jury
Prof. A. Kis, directeur de thèse
Prof. M. Guimarães, rapporteur
Prof. J. Ye, rapporteur
Prof. M. Luisier, rapporteur

École polytechnique fédérale de Lausanne

2022

Acknowledgements

Living and studying abroad for 4 years in a foreign country was long enough for me to encounter something unfamiliar. I happened to come across how people manifest their beliefs differently than I do. I learned how to appreciate the difference, which soon allowed me to better evaluate myself objectively. For the first time in my life, I started to genuinely question the beliefs which I was holding onto. It was like tearing down an old structure and building a new one again with my own strength, and it was not easy. As I became more aware of how I perceived the data measured in the lab and how I reacted to the things encountered in daily life, I could make my own belief that my living will be better when I see things as they are, without their perception being defined from the outside. After all, my PhD experience has been mostly an intellectual journey to discover a better way of living. The entire journey would not have been possible without the profound influence I have received from the people I have worked with. So, I would like to take this small opportunity to express my gratitude to those who have shared their honest thoughts which have helped me find my own way.

First of all, I give my gratitude to my PhD supervisor, Prof. Andras Kis. Without the opportunity he gave me to be in Switzerland, I wouldn't be able to experience something new and be the person I am right now. I learned from my supervisor that the balanced perspective between ideal and reality is a crucial thing in solving almost anything, even useful to be considered in scientific endeavors. Reflecting on myself, I was often dealing with problems with an ideal mindset for no clear reason, and I have been avoiding pragmatic approaches that I could possibly take. The necessity of the balanced viewpoint later resonated in many fields of my understanding. I now value a complementary approach, which will be important for me to better understand the world and solve challenges ahead.

I thank my friend Dr. Juan Francisco G. Marin for his friendly support in and outside of the lab. Whenever I had doubts, he was the first person to talk to. Thank you for your kindness and honest words.

I give my thanks to Dr. Zhe Sun, who made me strongly value intellectual reasoning in making a decision. He showed me how he understands scientific problems while I tried to follow the logic behind his reason. I learned a lot from his scientific mind.

I cannot thank enough Yanfei Zhao, Utku Karaca, Dr. Mukesh K. Tripathi, Dr. Martina Lihter, and Dr. Wayne Yang, who have shown me their unbiased opinions. They are the people who have broadened my view. I hope they did it too from me. To Dr. Wayne, I especially thank him for the valuable discussion on science and philosophy.

I thank Fedele Tagarelli for his help in making my life easier with data acquisition in experiments. I have admired his instrumental knowledge in both hardware and software and, from his approach, I have been able to build an attitude toward solving technical problems.

I want to also thank Prof. Ahmet Avsar, Dr. Alberto Ciarrocchi, and Dr. Dmitrii Unuchek. They were the seniors when I joined the lab and helped me familiarise myself with the lab environment. They helped me whenever and whatever I needed and taught me their know-how on device fabrication and measurements. My knowledge and hands-on skills stem from theirs.

I would like to thank Souad Di Meo, who has provided me with administrative support in the lab. If it weren't for her, I wouldn't be able to focus solely on my studies. For the same reason, I give my gratitude to Anne Kolly and Chrystelle Demierre from the EDMX department. For 4 years, they gave me friendly support when I had trouble with school administration and helped me with the course-taking.

I would like to give my thanks to the CMI staff in EPFL, Rémy Juttin, Guy-François Clerc, Patrick A. Madliger, and Zdenek Benes, who have always been supportive. They were helpful whenever I had trouble running equipment in the clean room. They are responsible and knowledgeable, and I will always try my best to be like that.

I also thank Prof. Jianting Ye, Prof. Mathieu Luisier, and Prof. Marcos H. D. Guimarães. They were my PhD Jury committee who had revised my manuscript and gave valuable scientific feedback. I appreciate their scientific comments during my doctoral examination as well.

To my dear Ei Thazin Lin, who I love the most. You provide me with the safest place where I can express my thoughts and feeling in difficult times. Thank you for being by my side, always willing to listen to me and helping me organize my thoughts. Just knowing your presence has given me the courage to overcome my weakness.

Lastly, to my parents, I send my infinite love and respect. Whenever there was a difficulty, I made an effort to look at the most fundamental value I believed in. Thank you for believing in me. Thank you for your endless support.

Abstract

Technological advancement has been in cadence with material development by improving the purity of single crystals and, at the same time, controlling their imperfections. These capabilities have been especially vital for developing new technologies based on two-dimensional (2D) van der Waals (vdW) materials for future electronic and optoelectronic applications. This is because the inherent properties of 2D vdW materials is highly susceptible to the presence of intrinsic structural defects and extrinsic disorders due to large surface-area-to-volume ratio. The successful reduction of these disorders has significantly improved material properties and led to the discovery of novel physical phenomena in vdW materials. On the other hand, structural defects – for instance, 0-dimensional point defects – can induce completely new properties that are otherwise absent in the prefect lattice. To harness the full potential of vdW materials, it is thus essential to produce high-quality crystals and understand how the disorder affects their material properties, which is the central idea of this dissertation.

In this dissertation, we first present the work of high-quality epitaxial growth of NbS_2. Based on atmospheric-pressure chemical vapor deposition, we have successfully synthesized the two polymorphs (2H and 3R) of NbS_2 with the largest lateral size grown to date. Their distinct superconducting and metallic properties were examined under low-temperature charge transport, respectively. Our finding demonstrates the practical synthesis method for phase-controllable growth of 2D transition metal dichalcogenides and can benefit future studies in mesoscopic devices and large-area applications of 2D superconductors.

Secondly, we present the work of discovering defect-induced novel properties in ultrathin layers of $PtSe_2$. Although bulk $PtSe_2$ is non-magnetic, we observe the appearance of magnetism in monolayer and bilayer $PtSe_2$. We were able to measure the magnetoresistance (MR) of mono- and bilayer $PtSe_2$ under perpendicular magnetic fields using proximitized graphene, and found antiferromagnetic and ferromagnetic MR responses for mono- and bilayer, respectively. The appearance of such different magnetic states is theoretically explained by the first-principle density functional theory calculation, suggesting the origin of induced-magnetic moments from intrinsic Pt vacancies for both layers. Moreover, we also found that structural disorder in $PtSe_2$ can induce bulk photovoltaic effect (BPVE). The second-order optical nonlinear effects, such as BPVE, require broken structural inversion symmetry and crystal symmetry can be reduced by the presence of structural defects. The broken local inversion symmetry from structural disorder in centrosymmetric $PtSe_2$ is manifested by the generation of zero-biased photocurrent under homogenous illumination. We observe linear and circular polarization-dependent photocurrents in defective $PtSe_2$, which is largely absent in the pristine crystal. Our findings in $PtSe_2$ emphasize the importance of the structural disorder for generating completely new properties and stress the need for defect-engineering for realizing the practical use of $PtSe_2$ in spintronic and photovoltaic applications.

Keywords

two-dimensional materials, niobium disulfide(NbS_2), platinum diselenide($PtSe_2$), disorder, defect, superconductivity, magnetism, magnetic materials, optoelectronic, photovoltaic effect, non-linear optics.

Résumé

Les progrès technologiques ont été en cadence avec le développement des matériaux en améliorant la pureté des cristaux, et en même temps, en contrôlant leurs imperfections. Ces capacités ont été vitales pour la réalisation de dispositifs basées sur des matériaux vdW 2D, où les défauts structurels intrinsèques et les troubles extrinsèques ont souvent obscurci les propriétés inhérentes en raison du rapport surface/volume extrêmement élevé. La réduction réussie des deux facteurs a considérablement amélioré les propriétés des matériaux et conduit à la découverte de nouveaux phénomènes physiques dans les matériaux vdW, ce qui en fait un candidat attractif pour les futures applications électroniques et optoélectroniques. D'autre part, les défauts dans ces matériaux- par exemple, les défauts ponctuels 0D - peuvent induire des propriétés complètement nouvelles qui seraient autrement absentes dans leur forme primitive. Afin d'exploiter tout le potentiel des matériaux vdW, il est donc essentiel de comprendre le rôle des défauts et de pouvoir contrôler le niveau de désordre dans les cristaux de haute qualité.

Afin d'exploiter tout le potentiel des matériaux vdW, il est donc essentiel de comprendre le rôle des défauts et de pouvoir contrôler le niveau de désordre dans les cristaux de haute qualité. La première étape nécessaire pour atteindre cet objectif est de produire un matériau hautement cristallin. Nous présentons d'abord les travaux de croissance épitaxiale de haute qualité de NbS_2 par dépôt chimique en phase vapeur à pression atmosphérique. Nous avons réussi à synthétiser deux polymorphes, 2H- et 3R-NbS_2, avec la plus grande surface latérale à jour, et leurs propriétés supraconductrices et métalliques, respectivement, ont été examinées sous transport de charge à basse température. Cette méthode de synthèse pratique pour la croissance contrôlable en phase des supraconducteurs peut bénéficier à de futures études dans les dispositifs mésoscopiques et aux applications à grande surface des supraconducteurs 2D.

Ensuite, nous présentons la découverte que des défauts peuvent introduire du magnétisme dans le semiconducteur $PtSe_2$, autrement non magnétique. Dans le cadre de mesures de magnéto-transport, nous avons comparé les propriétés de magnétorésistance (MR) entre $PtSe_2$ monocouche et bicouche à l'aide d'une sonde de graphène à proximité. Alors que le MR de la monocouche montre une réponse à deux plateaux, le MR de la bicouche montre une réponse ferromagnétique avec une hystérésis claire, et l'apparition d'états magnétiques aussi différents est théoriquement expliquée par le calcul de la théorie fonctionnelle de la densité de premier principe, suggérant l'origine de l'induction par des moments magnétiques provenant de défauts intrinsèques de Pt. De plus, nous montrons dans le même matériau que le désordre intrinsèque peut fournir la source d'un effet photovoltaïque non linéaire. Alors que le $PtSe_2$ vierge est centrosymétrique, la symétrie d'inversion locale brisée due au désordre structurel local dans le cristal - défauts en forme d'amas et défauts ponctuels - se manifeste par la génération d'un photocourant sous un éclairage homogène où nous observons des courants linéaires et circulaires dépendant de la polarisation à zéro -condition de biais. Ces découvertes révèlent l'importance du désordre structurel dans $PtSe_2$ pour créer de nouvelles propriétés et soulignent la nécessité d'une ingénierie des défauts afin d'avancer vers des applications spintroniques et photovoltaïques pratiques.

Mots-clés

matériaux bidimensionnels, disulfure de niobium (NbS_2), diséléniure de platine ($PtSe_2$), désordre, défaut, supraconductivité, magnétisme, matériaux magnétique, optoélectronique, effet photovoltaïque, optique non linéaire.

Contents

Acknowledgements ..... **i**

Abstract ..... **ii**

Keywords ..... **ii**

Résumé ..... **iii**

Mots-clés ..... **iii**

Contents ..... **v**

List of figures ..... **viii**

Chapter 1 Introduction **10**

1.1 Dissertation introduction 10

1.2 Content outline 11

Chapter 2 Two-dimensional van der Waals materials **12**

2.1 2D vdW materials 12

2.1.1 Graphene 12

2.1.2 Transition metal dichalcogenides 13

2.2 Intrinsic disorder in TMDCs 15

2.3 Improving the crystal quality of TMDCs 16

2.4 Benefit of defects in TMDCs 18

2.5 Property of platinum diselenides 20

Chapter 3 Experimental methods **23**

3.1 vdW sample fabrication 23

3.1.1 Top-down synthesis : mechanical exfoliation 23

3.1.2 Bottom-up synthesis : CVD 24

3.2 Thickness characterization 25

3.2.1 Optical microscopy 25

3.2.2 Atomic force microscopy 27

3.3 Optical characterization 28

3.3.1 Micro-Raman optical spectroscopy 28

3.3.2 Micro-PL spectroscopy 29

3.4 Deterministic transfer methods of vdW materials 29

3.4.1 PMMA carrying layer method 29

3.4.2 PDMS transfer method 30

3.4.3 vdW pickup method 30
3.5 Device fabrication in cleanroom 32
3.5.1 E-beam lithography 32
3.5.2 Vacuum metallization 33
3.6 Electronic and optoelectronic measurements 33
3.6.1 Charge transport measurements 33
3.6.2 Photocurrent measurement 35
3.6.3 Applying vertical displacement fields 36
Chapter 4 Phase-correlated electronic properties of 2D NbS_2 38
4.1 Introduction 38
4.1.1 2D superconductivity in vdW materials 38
4.2 2D NbS_2 grown by chemical vapor deposition 39
4.2.1 CVD growth method 39
4.2.2 Epitaxial growth of 2D NbS_2 41
4.3 Thickness-dependent structrual phase transition 42
4.3.1 Controlled growth of NbS_2 with different thicknesses 42
4.3.2 TEM and Raman analysis : two polymorphs in CVD-grown NbS_2 43
4.4 Device fabrication and electrical transport measurement 45
4.5 Charge transport in 2H, 3R, and their mixed phase NbS_2 46
4.6 Superconductivity in 2H-NbS_2 48
4.7 Discussion 50
4.7.1 Possible origin of structural transition 50
4.7.2 Large area bottom-up growth of NbS_2 50
4.8 Conclusion 51
Chapter 5 Defect-induced magnetic properties of ultrathin $PtSe_2$ 52
5.1 Introduction 52
5.1.1 Two-dimensional magnetism 52
5.1.2 2D magnetism in vdW materials 53
5.1.3 Disorder-induced magnetism in vdW materials 54
5.2 Sample fabrication 56
5.2.1 Identifying atomically thin $PtSe_2$ 56
5.2.2 Transferring ultrathin $PtSe_2$ 57
5.2.3 Ultrathin $PtSe_2$/graphene electronic device 58
5.3 Charge transport in monolayer $PtSe_2$ 59
5.4 Visualizing atomic defects in $PtSe_2$ 60
5.5 Magnetic properties of monolayer and bilayer $PtSe_2$ 60
5.5.1 Magneto-transport in monolayer and bilayer $PtSe_2$ 60
5.5.2 The first principle calculation – defect-induced magnetic moments 63

5.6 Summary and future perspectives 64
5.6.1 Achieved results 64
5.6.2 Further development 64
5.6.3 Future perspective 64
Chapter 6 Disorder-induced photovoltaic effect in centrosymmetric semiconducting $PtSe_2$ 66
6.1 Introduction 66
6.2 Sample fabrication 68
6.3 Sample characterization 69
6.3.1 Signature of structural defects by Raman spectroscopy 69
6.4 Optoelectronic measurement result 1 73
6.4.1 Spatial photovoltage reponse in pristine and defective $PtSe_2$ 73
6.4.2 Linear- and circular photocurrent in defective $PtSe_2$ 74
6.5 h-BN encapsulated sample fabrication 77
6.6 Optoelectronic measurement result 2 79
6.6.1 Optoelectronic response reproducing earlier result 1 79
6.6.2 Consistency between photocurrent and photovoltage 80
6.6.3 Spatial dependence of BPVE 81
6.6.4 Power dependence of BPVE 82
6.7 Discussion 82
6.7.1 Possible origin of LPGE, CPGE and offset 82
6.7.2 TEM analysis on defective $PtSe_2$ 85
6.7.3 Charge transport in pristine and defective $PtSe_2$ 86
6.7.4 Macroscopic mechanism of LPGE 87
6.7.5 Determination of crystallographic axis based on point-defect induced LPGE 88
6.8 Summary 95
6.8.1 Acheived results 95
6.8.2 Future perspective 95
Chapter 7 Conclusion and outlook 97
7.1 Epitaxial growth of 2D superconducting NbS_2 97
7.2 Disorder-induced novel properties in semiconducting $PtSe_2$ 98
List of abbreviations and symbols 100
Bibliography 103
Curriculum Vitae 108

List of figures

Figure 2-1. **Monolayer transition metal dichalcogenides.** 13
Figure 2-2. **Disorder during material growth and metal deposition.** 15
Figure 2-3. **Reducing intrinsic defect density.** 16
Figure 2-4. **Application of defects in TMDCs.** 18
Figure 2-5. **Defect-enhanced superconductivity and induced magnetism.** 19
Figure 2-6. **$PtSe_2$ crystal structure and its growth.** 20
Figure 2-7. **Electronic properties of bulk and few-layer $PtSe_2$.** 21
Figure 3-1. **Mechanical exfoliation.** 23
Figure 3-2. **Optical contrast and photoluminescence of WSe_2 on SiO_2/Si substrate.** 25
Figure 3-3. **Optical contrast of ultrathin $PtSe_2$ on SiO_2/Si substrate.** 26
Figure 3-4. **Atomic force microscopy for vdW materials** 27
Figure 3-5. **Experimental design for Raman optical spectroscopy**. 28
Figure 3-6. **E-beam lithography and metal evaporation for vdW device.** 32
Figure 3-7. **Charge transport measurement scheme**. 34
Figure 3-8. **Experimental setup for photocurrent microscopy.** 35
Figure 4-1**. CVD growth of NbS_2 crystals.** 40
Figure 4-2. **Selected area electron diffraction of NbS_2.** 41
Figure 4-3. **AFM on as-grown NbS_2** 42
Figure 4-4. **Histogram of NbS_2 thickness at different $NbCl_5$ precursor concentrations.** 42
Figure 4-5. **Atomic crystal structure of NbS_2.** 43
Figure 4-6. **Raman spectra of as-grown NbS_2 on sapphire substrate.** 44
Figure 4-7. **Multi-terminal NbS_2 device.** 45
Figure 4-8. **Schematic of differential resistance measurement.** 45
Figure 4-9. **Temperature-dependent resistance of different polytype NbS_2.** 46
Figure 4-10. **Superconductivity in 2H phase NbS_2.** 48
Figure 4-11. **BKT type superconducting transition in 2H-NbS_2.** 49
Figure 4-12. **Comparison of CVD grown NbS_2 from other literature.** 50
Figure 5-1. **2D magnetism in vdW materials and its tunability**. 53
Figure 5-2. **Inducing magnetism in 2D vdW materials**. 54
Figure 5-3. **Magnetism in multilayer vdW $PtSe_2$.** 55
Figure 5-4. **Identifying atomically thin $PtSe_2$.** 56

Figure 5-5. **Transferring exfoliated $PtSe_2$.** 57
Figure 5-6. **Ultrathin $PtSe_2$ electronic device** 58
Figure 5-7. **Semiconducting monolayer $PtSe_2$.** 59
Figure 5-8. **Imaging atomic structure of $PtSe_2$.** 60
Figure 5-9. **Magneto-transport in monolayer $PtSe_2$** 60
Figure 5-10. **MR of graphene with and without proximitized $PtSe_2$.** 62
Figure 5-11. **Magneto-transport of graphene channel with bilayer $PtSe_2$.** 62
Figure 5-12. **Localized magnetic moments induced by Pt vacancy in $PtSe_2$.** 63
Figure 6-1. **Symmetry engineering for enhanced BPVE.** 66
Figure 6-2. **Schematics describing the process of Au-assisted $PtSe_2$ exfoliation.** 68
Figure 6-3. **Ultrathin $PtSe_2$ fabricated by regular and Au-assisted tape exfoliation.** 69
Figure 6-4. **Raman spectra of $PtSe_2$ produced by two different exfoliation techniques.** 70
Figure 6-5. **Raman signatures of defective $PtSe_2$** 71
Figure 6-6. **Raman spectra of pristine $PtSe_2$ after mild Ar plasma treatment.** 72
Figure 6-7. **Raman spectra across the area of mono-, bi- and trilayer $PtSe_2$.** 72
Figure 6-8. **Scanning photovoltage microscopy of defective and pristine 2L $PtSe_2$.** 73
Figure 6-9. **Polarization-resolved photovoltage from defective and pristine 2L $PtSe_2$.** 74
Figure 6-10. **Fabrication of dual-gate h-BN encapsulated $PtSe_2$ device.** 77
Figure 6-11. **Dual-gate h-BN encapsulated 2L $PtSe_2$ device.** 78
Figure 6-12. **Scanning photocurrent microscopy of h-BN encapsulated 2L $PtSe_2$.** 79
Figure 6-13. **Consistency between photocurrent and photovoltage.** 80
Figure 6-14. **Position-dependent zero-biased photocurrents.** 81
Figure 6-15. **Laser power dependence.** 82
Figure 6-16. **Photovoltage from six diagonal pairs.** 83
Figure 6-17. **Displacement field dependence of LPGE and CPGE.** 84
Figure 6-18. **Imaging of atomic defects in 2L $PtSe_2$ through high-resolution TEM.** 85
Figure 6-19. **Charge transport showing possible defect-induced midgap states in $PtSe_2$.** 86
Figure 6-20. **Asymmetric scattering mechanism of LPGE.** 87
Figure 6-21. **Single Se vacancy in $PtSe_2$, a source of asymmetric scattering potential.** 88
Figure 6-22. **Modeling Se point defect (V_{se})-induced LPGE.** 89
Figure 6-23. **LPGE with experimentally accessible coordinates.** 90
Figure 6-24. **Contact electrode angles in x, and y coordinate axes.** 92
Figure 6-25. **Fitting the measured photovoltage with a model equation.** 92
Figure 6-26. **Extracting electrode angles and the angle of one zig-zag edge of PSe_2** 93
Figure 6-27. **Determining crystallographic axis of $PtSe_2$.** 94
Figure 6-28. **BPVE efficiency of defective $PtSe_2$.** 95

Chapter 1 Introduction

1.1 Dissertation introduction

Crystals tend to have small defects, and this imperfection often governs the overall material properties. Grain boundaries, considered as planar defects, separate the inner regions of different crystal orientations of polycrystalline materials. The presence of grain boundaries is particularly important for steel, as it dominantly determines the mechanical yield strength and hardness of the bulk. As for smaller-sized defects, there are 0-dimensional(0D) point defects, such as missing atoms or impurities. They are responsible for the colors of gemstones, for instance, ruby and sapphire, the crystal of aluminum oxides. They are otherwise transparent unless a small number of foreign atoms - chromium or titanium ion – are added.

Realizing desired properties of any material requires understanding and precise control over the disorder. For instance, the single crystalline growth of silicon wafer was a critical factor in developing modern electronics, as the defects mentioned earlier – grain boundaries and 0D defects – inevitably lower the charge carrier mobility and hinder the device performance. At the same time, to achieve the best of its electrical properties, one had to precisely add impurities by substitutional doping either boron or phosphorous atoms to make it perform as desired. Without these capabilities, it was impossible to build integrated circuit devices made of billions-of-transistors with all functioning in a single chip. The importance of understanding the role of defects in material further extends to next-generation technologies. This is evident in the case of optically active defects in diamonds. The optical color center of diamond negatively charged nitrogen-vacancy (NV) offers a well-isolated two quantum system, the state of which can be controlled at room temperature with resonant microwave pulses. Defects in diamonds are considered one of the promising platforms for realizing solid-state quantum computers[1].

Technological advancement has been in cadence with material development by improving the purity of single crystals and, at the same time, controlling their imperfections. This has been particularly relevent for developing low-dimensional materials such as 2D van der Waals (vdW) materials. Initiated with the discovery of semi-metallic graphene, the number of vdW materials has grown rapidly. Many can stably exist in atomically thin layers, including transition metal dichalcogenides (TDMCs) and hexagonal boron nitride (h-BN). The range of properties includes metals, semimetals, semiconductors, insulators, and much more[2], and are considered as attractive candidates for next-generation electronic, optical, and optoelectronic applications. However, as the material is entirely surface itself, it is prone to disorder due to the large surface-area-to-volume ratio. Their intrinsic properties were often uncertain due to inherent crystal defects and extrinsic disorders – strain, surface absorbate and oxidation[3].

Protecting 2D vdW materials from the disorder has been vital for successful material research. For semi-metallic graphene, the dominant disorder came from the outside source. The surface absorbate or the charged traps in SiO_2/Si substrate introduced charge density puddles[4], the cause of enhanced charge scattering when electric current flows. These sources have significantly affected the charge carrier mobility and the minimal conductivity of early graphene devices on SiO_2/Si substrate[5–7]. The dramatic enhancement of electronic properties was achieved by minimizing such charged disorder, and the most successful method, to date, has been encapsulation with h-BN[8] or by suspending it in vaccum[9]. In the effort to further reduce the disorder, improved fabrication techniques were developed[10], and as a result, the state-of-art low-disorder graphene device allowed the observation of strong electronic correlation[11] and highly non-equilibrium transports phenomena[12].

As for TMDCs, structural defects are more abundant than graphene as the defect formation energy of TMDCs is much lower than that of graphene. For example, chalcogen vacancy formation energy is 2-3eV for MX_2 (M= Mo and W; X= S, Se and Te)[13], and carbon vacancy formation energy is 7-8eV for graphene[14]. The large concentration of intrinsic defects in TMDCs (typically $10^{13}cm^{-2}$) not only degraded the electronic mobility of TMDCs but also negatively affected the optical properties. To overcome this issue, there have been many strategies developed particularly for TMDCs to produce defect-free crystals. For

example, the best tungsten diselenides (WSe_2) crystal so far is produced from the liquid self-flux growth technique and contains a defect density of $10^{11}cm^2$[15]. Alternatively, post-treatments with thiol chemistry could repair the chalcogen vacancies, which enhanced the low quantum efficiency (0.01-6%) of TMDCs[16] to almost near-unit value[17]. Further improvement in the optical properties of TMDCs has been realized by the encapsulation minimizing the external source of disorder, from which the linewidth of photoluminescence in TMDCs greatly improved[18,19]. The cleaner devices have led to the discovery of novel phenomena in TMDCs such as exciton condensate[20], and room temperature exciton transport[21].

However, the atomic disorder in low-dimensional materials can sometimes induce completely different new physical properties in TMDCs. It has been reported that magnetic moments can be introduced locally by metal point vacancies in multilayer metallic platinum diselenide ($PtSe_2$)[22] and by antisite defects in semiconducting molybdenum telluride ($MoTe_2$)[23]. Furthermore, point vacancies can break the symmetry and induce large spin-splitting in centrosymmetric media with high spin-orbit coupling strength[24], and strain gradient can generate symmetry-forbidden properties such as flexo-photovoltaic effect[25]. Last but not least, it has been demonstrated in insulating h-BN of a large bandgap (5-6eV) that local boron vacancies can act as a single-photon emitter with lower transition energy (1.4-2eV)[26] and can provide the system for optical spin-resonance[27].

Therefore, on the one hand, it is crucial to improve the existing synthesis of 2D vdW materials and produce finer crystalline crystals free from structural defects. However, it is also important to study how intrinsic structural defects alter the electronic and optoelectronic properties or even induce new functionalities in such materials. With this interest, this dissertation is centered around intrinsic structural defects in TMDCs, particularly focusing on two different vdW materials, $PtSe_2$ and niobium disulfide (NbS_2). We first introduce the work of 2D NbS_2 crystal synthesis. Next, we present our findings of defect-induced novel properties in ultrathin layers of $PtSe_2$. These works are based on two published and one unpublished work.

1.2 Content outline

Below is the outline and short explanation of the chapters in the dissertation.

Chapter 2 presents a general overview of the physical properties of 2D vdW material and provides a brief literature review on the structural defects in transition metal dichalcogenides and their relevant physical properties. The purpose of this chapter is to provide background information to help understand the content of the dissertation.

Chapter 3 describes the experimental methods of fabricating and characterizing the vdW devices which are used for the studies presented in the following chapters 4, 5, and 6.

Chapter 4 contains the work related to the epitaxial growth of 2D NbS_2 and the study of its electronic properties. We have investigated the electronic properties of two-grown polymorphs of NbS_2, 2H- and 3R-NbS_2 via low-temperature charge transport.

Chapter 5 discusses the experimental work on two-dimensional magnetism in semiconducting $PtSe_2$ and provides the theoretical background based on the first principle density functional theory calculation.

Chapter 6 reports disorder-induced photovoltaic generation in $PtSe_2$. We explain the importance of disorder-induced symmetry breaking in generating linear and circular polarization-dependent photocurrents in $PtSe_2$.

Lastly, **chapter 7** provides the conclusion of this dissertation and provides the future perspectives of defect-induced properties in $PtSe_2$.

Chapter 2 Two-dimensional van der Waals materials

This chapter provides background knowledge on two-dimensional (2D) van der Waals (vdW) materials, focusing on transition metal dichalcogenides (TMDCs) and their structural defects. We provide a literature overview on how the defects affect the physical properties of various TMDCs. At the end of this chapter, we explain the basic properties of platinum diselenide ($PtSe_2$), the main material studied in this dissertation.

2.1 2D vdW materials

2.1.1 Graphene

Since the successful production from graphite using the famous tape exfoliation method[28], graphene, made of a single sheet of carbon atoms, quickly gained tremendous attention in academic research and industrial applications due to its extraordinary properties. Just to name a few, it is only 0.3nm-thick, the thinnest material, but physically and chemically stable. It is flexible, but its mechanical strength is about 100-300 times stronger than stainless steel. It has high thermal conductivity (10^3W/m·K)[29] and can withstand several-orders higher current density ($\sim 1.6\times10^9$ A·cm^{-2}) than copper[30]. The fascinating electronic properties of graphene stem from the fact that quasi-particles obey the linear dispersion of energy and momenta near the Dirac points at the K and K' edges of the Brillouin zone[31]. Unlike the ordinary semiconductors having parabolic band structure, the linear relation dictates the vanishing effective mass of the quasi-particles, which leads to the Fermi velocity as high as 10^6m/s. This feature of massless quasi-particle underpins the description of later discovered various novel quantum transport phenomena in graphene. Despite its rich physics and ultra-high carrier mobility, the gapless electronic band structure made graphene semi-metallic and seriously limited its use in modern electronic devices. Basically, the field-effect transistor made of graphene cannot be switched off with the external gate voltage. Chemical modification and ribbon-shaped fabrication are suggested as viable methods to transform this sheet of metal into a semiconductor but have not been successful so far. Bilayer graphene, however, can have a small bandgap (Eg) of 250meV on the condition of an applied electrical field[32]. But the current on/off ratio (I_{on}/I_{off}) in bilayer graphene field-effect transistor (FET) is only ~100 at room temperature[33].

2.1.2 Transition metal dichalcogenides

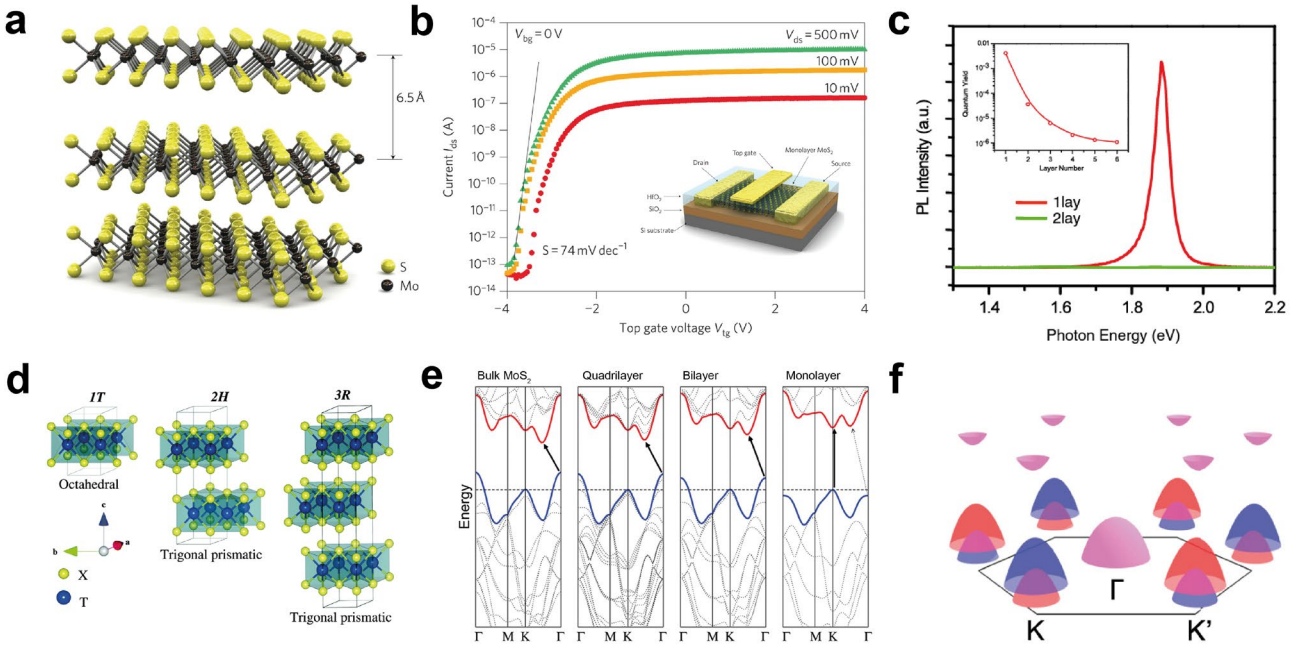

Figure 2-1. **Monolayer transition metal dichalcogenides.** a) 3D atomic structure of molybdenum disulfide. A single-layer is 6.5Å thick. b) High-performance field-effect transistor made of 1L MoS_2 with hfO_2 as the gate dielectric. c) Photoluminescence from monolayer and bilayer MoS_2. Inset is the quantum yield with different layer numbers. Monolayer shows the highest value. d) Structural representation of polytypes (1T, 2H and 3R) with their metal coordinations. e) Calculated MoS_2 bandstructure from bulk to monolayer thickness. Monolayer has a direct bandgap located at the *K* point of reciprocal space. f) Schematic of monolayer band structure with spin-split bands at K and K' points of hexagonal Brillouin zone. Red (blue) color indicates spin-up(spin-down) band. Panels are adapted with permission. Panel a-b) are from ref[34], Springer Nature Ltd. Panel c) is from ref[35], American Physical Society. Panel d) is from ref[36], Royal Society of Chemistry. Panel e) is from ref[37], American Chemical Society. Panel f) is from ref[38], American Physical Society.

The discovery and the methodological success of isolating graphene from bulk graphite have stimulated the search for another wonder material from the other 2D van der Waals(vdW) materials. The difficulty of turning graphene into a semiconductor turned the focus to bulk vdW semiconductor in a hope of achieving a single-layer semiconductor. This was actually the original idea intended by Radisavljevic et al. [34], who have successfully demonstrated, for the first time, the high-performance FET device made of a single layer molybdenum disulfide (MoS_2). A few-layer MoS_2-based transistor was already realized at that time; however, with the poor mobility in the range of 0.1-10 $cm^2 \cdot V^{-1} \cdot s^{-1}$. Radisavljevic et al. instead made MoS_2 FET with a high-k hafnium oxide (HfO_2) as the gate dielectric, which could effectively screen the charge impurities that limit the device performance. This gating scheme greatly improved the field-effect mobility (μ_{FE}) higher than 200 $cm^2 \cdot V^{-1} \cdot s^{-1}$ at room temperature. The device could be completely turned off by the gate voltage in the range of 2V, and the I_{on}/I_{off} is higher than 10^8 with sub-threshold swing S = 74 mV/dec. Around the same time, Mak et al. have extended the potential in the material by discovering the direct bandgap feature of monolayer MoS_2[35]. Although bulk MoS_2 has an indirect bandgap (E_g=1.29eV), it is found that in the thin limit, the electronic properties of MoS_2 are dependent on the number of layers. Inferred from the photoluminescence (PL) spectroscopy, its bandgap increases more than 0.6eV with the decreasing number of layers from six-layer to monolayer, and indirect bandgap in bulk changes to direct bandgap in monolayer. The nature of direct bandgap was manifested by a strong enhancement of PL quantum efficiency in monolayer compared to bulk.

MoS_2, a prototypical semiconducting vdW material, belongs to a bigger material category known as transition metal dichalcogenides (TMDCs), which is the relevant class of material in this dissertation. TMDCs has the stoichiometry of MX_2, where M is a transition metal in group 4, 5 and 6 of the periodic table and X is a chalcogen and the group has more than 60 different compounds. The unit layer is structured as three atomic planes(chalcogen-metal-chalcogen), where one transition metal layer is sandwiched by two chalcogen layers, and thicker material is essentially formed with vertically-stacked layers under van der Waals force. Different crystal structures can form depending on the stacking order and the metal coordination. In MoS_2, there are three different polytopes: 1T, 2H and 3R. 1T-phase has octahedral coordination of metal and has a tetragonal(T) unit cell consisting of one layer with AA stacking where inversion symmetry is preserved in the monolayer. Both 2H-

and 3R-phase have trigonal prismatic coordination of metal, but 2H-phase has a hexagonal(H) unit cell consisting of two-layer with AB stacking, whereas 3R has a rhombohedral(R) unit cell consisting of three-layer with ABC stacking. The inversion symmetry of the 2H phase is broken for the odd number of stacking and preserved for the even number of stacking. Inversion symmetry of the 3R phase, however, is broken regardless of any number of layers.

Various compounds in TMDCs can be either semiconducting or metallic. They can be distinguished by the different transition metal atoms and the layer stacking order. For example, Mo and W compounds are generally semiconducting, whereas those made of Ta and Nb are metallic[39]. Among them, the most studied materials are 2H-phase semiconducting compounds of Mo and We with Se and S. They are indirect semiconductors in bulk where a valence band maximum is at the center (Γ point), and a conduction band minimum is positioned in the middle of $\Gamma - K$ direction of the hexagonal Brillouin zone. In the monolayer form, they undergo a transition from indirect to direct bandgap[37]. The local minimum of the bands, which are also called valleys, is located at the six corners of the hexagonal Brillouin zone ($\pm K$ points), and the monolayer TMDCs compounds have the band-to-band transitions within the range of 1.5-2.0eV. The bandgaps in the visible spectrum indeed offer a broader material choice not only for digital electronics but also for numerous photonic and optoelectronic applications such as light emitters and photodetectors. Furthermore, the use of TMDCs can be extended as monolayer TMDCs hold rich spin and valley-related properties. Because of the broken inversion symmetry in the monolayer, strong spin-orbit interaction lifts the degeneracy and splits the conduction and valence bands. The splitting is largest at the valence band due to the heavy elements of transition metal; $\Delta \sim 0.46$eV in WSe_2 and $\Delta \sim 0.15$eV in MoS_2[40]. Uniquely, the band edges of K and K' points are lifted in opposite directions due to the time-reversal symmetry, so spin and valley degrees of freedom are inherently coupled. This is called as spin-valley locking. Due to this intriguing property, the law of conservation of angular momentum permits the selective population of a particular valley using circularly-polarized optical pumping, producing valley polarization. Consequently, a number of intriguing valley-contrasting phenomena have been demonstrated, including valley-polarized exciton[41,42], valley coherence[43], and valley Hall effect[44]. In addition, circularly-polarized light can generate spin and valley-polarized photocurrent in TMDCs, where the current polarization is determined by the light helicity[45,46]. This feature makes TMDCs a promising platform for building spintronic and valleytronic devices, harnessing the full potential of its inherent spin-valley physics.

2.2 Intrinsic disorder in TMDCs

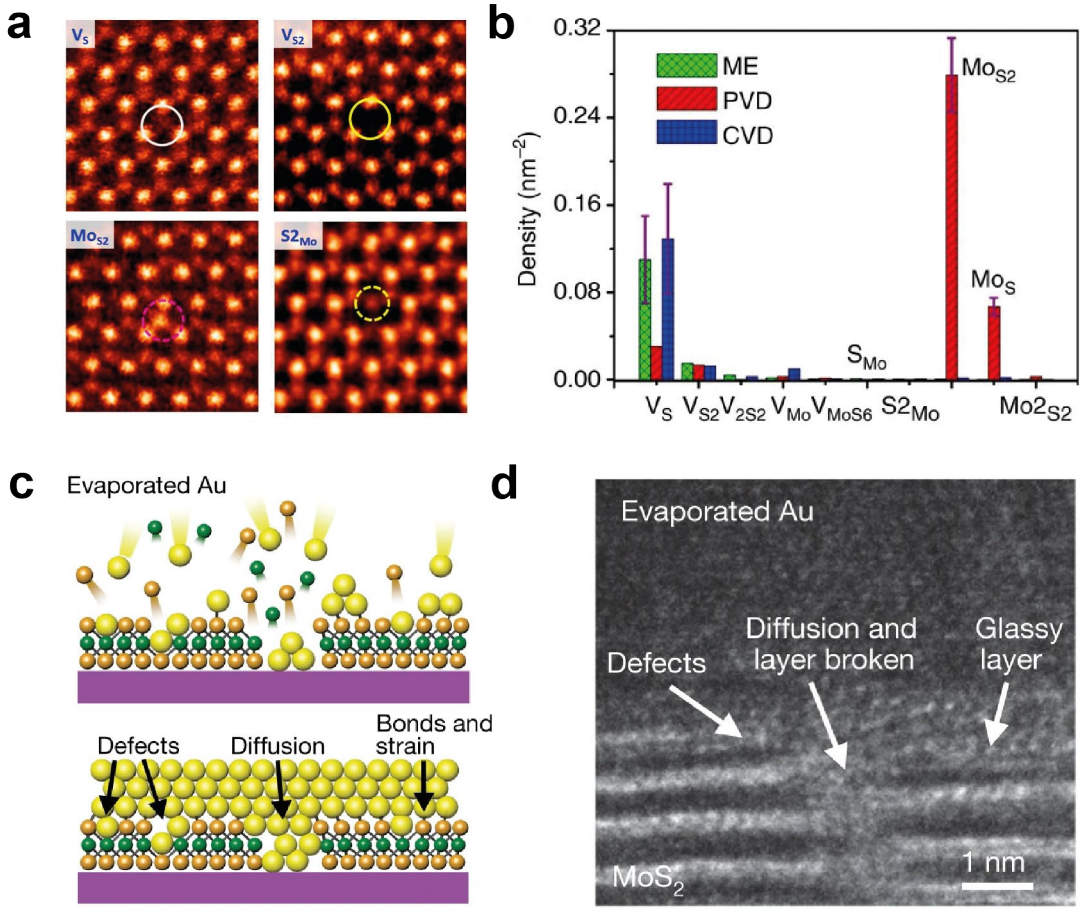

Figure 2-2. **Disorder during material growth and metal deposition.** a) ADF STEM images revealing major 0D point defects in MoS_2 (V_S: monosulfur vacancy, V_{S2}: disulfur vacancy, Mo_{S2}: a Mo atom substituting a S_2 column, $S2_{Mo}$: a S_2 column substituting a Mo atom). b) Density of various point defects compared with different syntheses (ME: mechanical exfoliation, PVD: physical vapor deposition, CVD: chemical vapor deposition). c) Schematic of e-beam deposited Au electrodes on top of MoS_2 damaging the surface of MoS_2 by the Au atom bombardment. d) Cross-sectional TEM image of MoS_2 with top Au electrodes. Panels are adapted with permission. Panel a) is from ref[47], American Chemical Society. Panel b) is from ref[48], Springer Nature Ltd. Panel c-d) are from ref[49], Springer Nature Ltd.

Nevertheless, these rich properties of TMDCs are often overshadowed. One of the main reasons is that the structure of real TMDCs materials always deviates from the perfect arrangement of atoms. The direct imaging of TMDs has been performed by experimental instruments such as scanning tunneling microscope (STM) and annular dark-field scanning tunneling electron microscope (ADF STEM), finding various intrinsic defects in the crystals. **Figure 2-2(a)** shows the STEM image of the point defects in MoS_2, which shows single sulfur vacancy and metal and chalcogen anti-sites[47]. **Figure 2-2(b)** compares the concentrations of major point defects found in MoS_2 obtained by various synthesis methods, which are mechanical exfoliation, chemical vapor deposition (CVD) and physical vapor deposition (PVD)[48]. For these production methods, chalcogen vacancy is the dominating defect type, with a very high concentration of around $10^{13}/cm^2$. Yet, among them, mechanical exfoliation gives the best crystal quality with the lowest defect density. This overall high defect concentration can be understood by its low defect formation energy during the synthesis. For both metal and chalcogen-rich growth conditions, the formation energy of the most common chalcogen vacancy in MoS_2 is around 2-3eV[13]. This energy scale is similar for all other TMDCs, and the formation energy of chalcogen vacancies is significantly lower than that of carbon vacancies. (~8eV) in graphene[14]. The intrinsic defect density in mechanically exfoliated graphene is around $\sim 10^{10}/cm^2$[50], which is extremely lower than TMDCs.

Given the ultra-thin nature of 2D TMDCs, these structural defects have significantly affected their intrinsic physical properties. Many monolayer TMDCs suffer from the poor internal quantum yield of PL, which means that the number of the

radiated photons is significantly lower than the number of excited electron-hole pairs. Typically, exfoliated tungsten disulphide (WS_2) and MoS_2 show an internal quantum yield of ~6%[51] and ~0.1%[52], respectively, which is primarily due to the defect-mediated non-radiative recombination process. This low yield makes the current quality of TMDCs not adaptable for display applications. Indeed, the same defects have dominantly influenced their electrical properties and the FET device performance. Although intrinsic conduction band mobility of MoS_2 is expected to be large as 400$cm^2 \cdot V^{-1} \cdot s^{-1}$[48], the measured mobility is proportionally lowered with an increasing defect density. Therefore, the mobility strongly depends on how the material is synthesized, and the reported room-temperature field-effect electron mobilities are 44-81$cm^2V^{-1}s^{-1}$ for mechanical exfoliation[53,54], 6-22$cm^2V^{-1}s^{-1}$ for chemical vapour deposition[55–57], and below 0.5 $cm^2 \cdot V^{-1} \cdot s^{-1}$ for physical vapour deposition[48,58]. It is theoretically studied that MoS_2 is particularly sensitive to the presence of anti-site defects where hole mobility of MoS_2 can be 3-4 times lower than that of intrinsic MoS_2[48]. In addition, defects can provide trapped charged states acting as a scattering center[59–61]. Also, hopping transport caused by strongly localized disorder can be part of the overall transport along with band transport[62,63]. All of these inevitably affect the device mobility and lead to a large underestimation of the true band mobility of TMDCs.

Moreover, its atomically thin nature and low sputtering energy make their crystal prone to be damaged during the conventional device fabrication process, such as e-beam lithography and physical vapour deposition. **Figure 2-2(c-d)** shows the schematic and cross-sectional TEM image of the damaged MoS_2 during this process[49]. Metal electrodes contacting TMDC are considered crucial for any electronic and optoelectronic devices as they govern the charge injection from metal to 2D materials or vice versa. However, the metal/TMDCs interface constructed by metal deposition such as e-beam evaporation can introduce considerable defects, strain and metal diffusion. This has resulted in high contact resistance due to significant Schottky barrier or interfacial states at 2D/metal contacts which pins the Fermi level, deteriorating the overall electronic performance, such as current on/off ratio and field-effect mobility.

In summary, ultra-high-quality TMDCs with enhanced synthesis are essential for producing high-performance devices. However, maintaining the quality during device manufacturing is equally important.

2.3 Improving the crystal quality of TMDCs

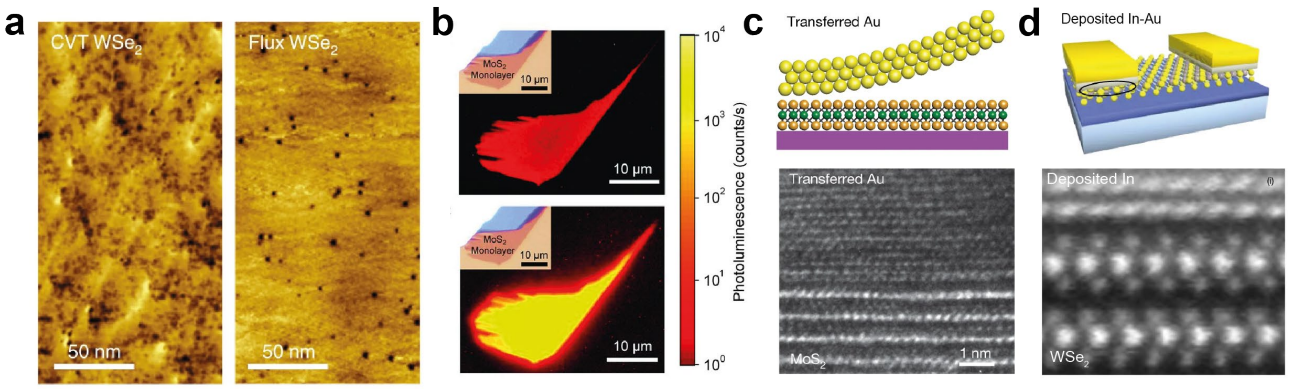

Figure 2-3. **Reducing intrinsic defect density.** a) STM image of CVT-grown WSe_2(left) and flux-grown WSe_2(right) comparing the level of defects. b) PL images of monolayer MoS_2 before (top) and after (bottom) superacid treatment. c) Schematic and cross-sectional TEM image of MoS_2 with Au electrode mechanically transferred by PMDS stamp. d) Schematic and cross-sectional ADF STEM image showing the WSe_2-In/Au electrode interface. Panels are adapted with permission. Panel a) is from ref[15], American Chemical Society. Panel b) is from ref[17], AAAS. Panel c) is from ref[49], Springer Nature Ltd. Panel d) is from ref[64], Springer Nature Ltd.

The formation of defects during the synthesis of TMDCs is the natural result of thermodynamics, which energetically favors imperfect structure. However, for the field to advance, it must continue to reduce the number of defects. To date, the best TMDCs crystal is obtained by the self-flux method[49]. This state-of-art growth showed a considerable reduction of the defect density in WSe_2 below $10^{11}/cm^2$, approaching the intrinsic limit of defect formation. PL measurements were performed

to measure the radiative response versus its crystal quality. Due to low defect concentration in the flux-grown sample, the PL efficiency of WSe_2 is measured to be significantly larger (a hundred-fold) than that of CVT-grown WSe_2.

However, if we convert the defect density of the best-grown WSe_2 to its bulk concentration, it is around $\sim 10^{18}/cm^3$. This is still significantly higher, at least 3-4 orders, than those obtained in the III-V semiconductor films[65]. In practice, there is still room for improving the crystallinity. Apart from the production of high-quality crystals, we can also focus on repairing defects after the growth. First, repairing chalcogen vacancy can be done by annealing with a supplement of appropriate chalcogen source. In the case of monolayer MoS_2 with sulfur vacancies, oxygen substitutes the vacancies when left in the air by the oxidation process. At this point, it is found that the oxidized area can recover its pure MoS_2 phase when annealed with H_2S at 200°C[66]. Similarly, line defects composed of Se vacancies in vanadium diselenide (VSe_2) can restore to its pristine form by depositing Se on the sample, followed by annealing to 240°C[67]. Apart from this dry method by annealing, wet solution treatment based on nonoxidizing organic superacid can repair the chalcogen defects. Amani et al. have used bis(trifluoromethane) sulfonimide (TFSI) to repair the sulfur vacancies of as-exfoliated 1L MoS_2[17]. As evidence of restoration, MoS_2 achieves a dramatic PL enhancement (190 times increase) before and after the treatment. The treatment strongly eliminates the defect-mediated non-radiative process without changing the overall shape of the PL spectrum.

Also, there has been continued effort to maintain defect-free TMDCs during the fabrication of contact electrodes. Two successful strategies realized ideal metal-2D semiconductor junctions by low-energy material integration processes: physically transferring pre-fabricated metal electrodes[49] and soft metal deposition[64]. Both monolayer and few-layer MoS_2 received the benefits from these highly efficient and damage-free fabrications, which resulted in high room temperature electron/hole mobilities. Here, we briefly introduce their methods. The former was introduced by Yuan Liu et al., who demonstrated transferring metal electrodes onto few-layer MoS_2 using polydimethylsiloxane (PDMS) stamps[49]. This method allowed to transfer of various metals under the same transfer protocol; thus, it was possible to transfer a metal with the work function matching the energy level of conduction or valence band edge. Those metal electrodes are prepared on a silicon substrate by conventional clean-room fabrication methods and functionalized with a hexamethyldisilazane (HMDS) layer, followed by spin-coating polymethyl methacrylate (PMMA) film. With the pre-functionalization, PMMA weakly adheres to the substrate, allowing it to be peeled off by the PDMS stamp, carrying the underneath metal electrodes. A gently transferred metallic layer forms a van der Waals metal-semiconductor junction with few-layer MoS_2 without chemical bonding and contamination such as adsorbed water and hydrocarbon. The atomically clean interface with a silver metal film made it possible to achieve high electron mobility ($260 cm^2 \cdot V^{-1} \cdot s^{-1}$) at room temperature. The second approach is introduced by Yan Wang et al., where monolayer MoS_2 is deposited with 10nm indium metal capped with 100nm gold electrodes[64]. The key factor that allowed to form a clean interface is the soft deposition nature of indium, where cross-sectional ADF STEM and X-ray photoelectron spectroscopy (XPS) show no sign of damage to the MoS_2 and chemical bondings between In and MoS_2. This method achieved high electron mobility (e.g. $167 cm^2 \cdot V^{-1} \cdot s^{-1}$) and the lowest contact resistance (e.g. 3000ohm-um) up-to-date.

2.4 Benefit of defects in TMDCs

On the other hand, the presence of crystal defects in 2D TMDCs has provided us with novel routes to tailor existing properties or even introduce new functionalities. Here, we briefly introduce some of the prominent findings of defect-induced properties and the attractive uses of defects in 2D materials.

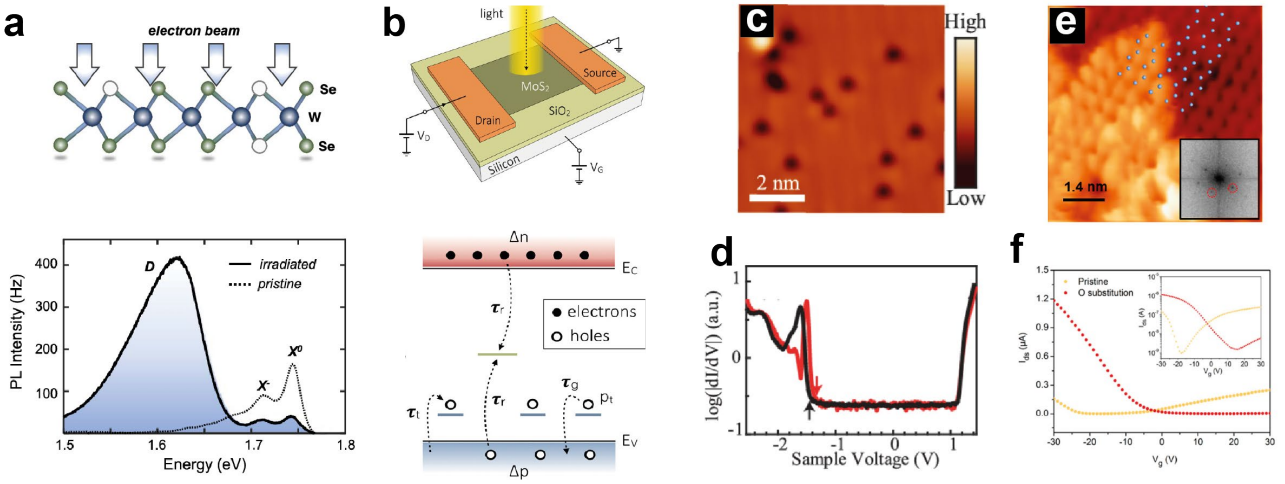

Figure 2-4. **Application of defects in TMDCs.** a) Schematic illustration (top) of electron-beam irradiation on WSe_2, intentionally creating selenium vacancies in the crystal. PL spectra (bottom) at 5K acquired from as-exfoliated WSe_2 and after e-beam irradiation. A broad emission appears in the lower energy range due to defect-assisted recombination. b) Schematic (top) of 1L MoS_2 photodetector operation scheme. Simple energy diagram (bottom) showing charge trapping at the valence band tail of 1L MoS_2. c-d) Topographic STM image of 1L WSe_2 c), showing individual metal vacancies (black area) and *dI/dV* spectrum d), acquired from a defect-free region (black line) and on the defect (red line). The arrow marks the onset of the valence band, and a shift of the valence band edge is observed on the defect site. e-f) Topographic STM image of $PdSe_2$, e) showing bright region (oxidized) and dark region (pristine). The position of Se atoms (cyan dots) is the same for oxidized and pristine, meaning that the overall structure is intact. Device characteristic of $PdSe_2$ FET f), before and after the oxidation. Panels are adapted with permission. Panel a) is from ref[68], American Physical Society. Panel b) is from ref[69], American Chemical Society. Panel c-d) are from ref[70], American Physical Society. Panel e-f) are from ref[71], American Chemical Society.

The 0D defects - for instance, chalcogen vacancies - can strongly impact optoelectronic and optical properties in TMDCs. The defect states in TMDCs are commonly present within the bandgap. Acting as deep recombination centers, defect states provide a non-radiative recombination path for direct semiconductors, negatively affecting the efficiency of PL emission. However, defect-induced band-tail states also exist, below the edge of the conduction and above the edge of the valance band. This provides shallow traps of excited carriers, which can enhance the photoconductivity, and eventually the gain of photoresponse in optoelectronic devices. The experimentally measured photoconductivity (more precisely responsivity) in monolayer MoS_2 is found to be two-order higher than that of trap-free MoS_2, which is attributed to hole-trapping in MoS_2 band-tail states[69]. Also, semiconducting few-layer platinum diselenide ($PtSe_2$) also shows higher photoresponse with the increase of defect concentration (from 3% to 7.9%)[72], under the similar mechanism of enhanced photoconductivity found in MoS_2. In addition, the presence of defect can create a new path of optical excitation and emission in monolayer TMDCs. Moody et al. demonstrate that chalcogen defects in WSe_2 can be created simply by electron-beam irradiation[68]. In the defective WSe_2, a band of new PL emission appears at lower energy than the energy of pristine PL, which is associated with broadened resonance via multiple defect bands formed by chalcogen vacancies. Through time-resolved PL spectroscopy, the recombination lifetime of a defect-bound exciton is found to be ~200ns. The defect transitions exhibit large circular dichroism where time-resolved circular polarized emission reveals the valley lifetime of >1 μs, indicting stable valley pseudospin of defect-bound exciton inherited from the spin-valley coupling of the host material.

Engineering atomic defects can also provide wealth control over the charge trasport properties of TMDCs. The atomic vacancies are suggested to be the crucial element causing the uni-polar transport in TMDCs. Chalcogen vacancies, prevailing in

many TMDCs, typically bring electron(n-type) doping. Therefore, most 2D TMDCs exhibit n-type conduction. However, in the rare case of metal vacancies, it can give rise to hole(p-type) doping[70]. Substitutional doping can also effectively alter the dominant carrier-type conduction. Nb-doped MoS_2 where Nb atom replacing Mo atom can make p-type conduction of MoS_2[73]. The partial oxygen substitution of the chalcogen vacancies is also an alternative route to modulate the carrier type. It is found that oxidation of the top layer of 2D $PdSe_2$ (thickness=3.7nm) by low temperature (60°C) ozone treatment can also progressively convert its ambipolar transport to p-type conduction[71]. The larger modulation of electronic properties is observed in few-layer defective $PtSe_2$ through defects. Few layer $PtSe_2$ is intrinsically semiconducting. However, when a large amount of Se point-defects are introduced in the pristine layers by Ar-plasma treatment, the electronic properties undergo semiconductor to metal transition witnessed by significantly suppressed Vg dependency with increased electrical conductance[74]. This is attributed to the large amount of mid-gap states induced by the defects, which is commonly observed in many other TMDCs.

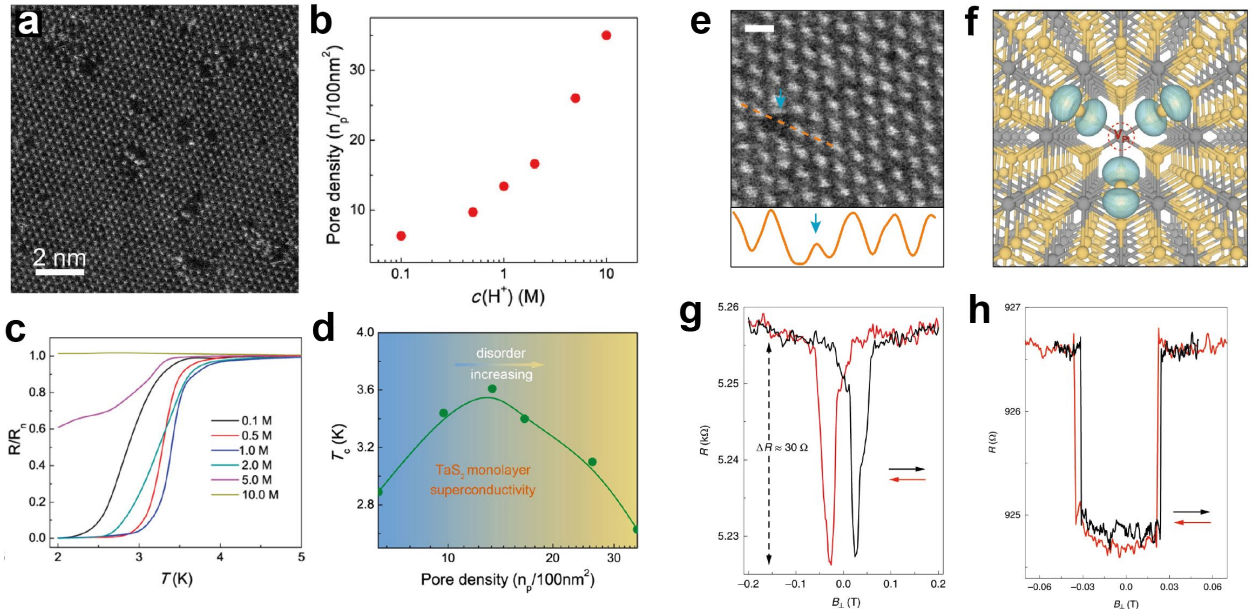

Figure 2-5. **Defect-enhanced superconductivity and induced magnetism.** a-d) Monolayer TaS_2 superconductivity in relation to its structural defect. Atomic structure of monolayer TaS_2 with the apparent disorder from chemical exfoliation a) and the relation of pore density with acid concentration during the chemical exfoliation b). Temperature-dependent resistance of 1L TaS_2 with different acid concentrations c) and the relation of critical temperature versus pore density d). e-f) Defect-induced magnetism in $PtSe_2$. Atomic structure of bilayer $PtSe_2$ with the position of a Pt vacancy indicated by blue arrow e), where the bottom panel shows the contrast profile along the dashed orange line. 3D illustration of the magnetic moments around a single Pt vacancy f). Magnetoresistance of 9nm-thick $PtSe_2$ g) and 5.2nm-thick $PtSe_2$ h), showing ferromagnetic and antiferromagnetic response. Panels are adapted with permission. Panel a-d) are from ref[75], American Chemical Society. Panel f-h) are from ref[22], Springer Nature Ltd.

Defective samples sometimes surprise us with unexpected properties. Abnormal enhancement of superconductivity has been observed in defective monolayer 2H-tantalum disulfide (TaS_2), which was prepared by acid-assisted chemical exfoliation[75]. This finding is peculiar because, in order to achieve better superconducting properties, the disorder is the first thing to be removed since it is the source of electron/Cooper pair localization. STEM identified in the chemically exfoliated monolayer the presence of arbitrary distributed pore-like defects in the lattice, the density of which can be controlled by the H+ concentration during the fabrication. Temperature-dependent 4-probe resistance measurement shows the superconducting critical temperature transition is enhanced from 2.89K (pristine) to 3.61 K (with 1.0 M H+ concentration). The enhancement maximizes at the optimal defect concentration showing the dome-shaped correlation between superconductivity and disorder. This improvement is explained by the increment of hole carrier density induced by Ta atomic defects.

In order to make TMDCs magnetized, doping with 3d transition metal atoms such as Fe, Co, and Ni has been the main strategy to induce magnetic ordering into the host materials. However, intrinsic structural defects have also been consistently suggested by theoretical studies that particular single point defects, such as metal vacancy in monolayer $PtSe_2$[76], and chalcogen vacancy in monolayer rhenium disulfide (ReS_2)[77], can trigger local magnetic moments (1-3μ_B for 1L ReS2 and 6μ_B for

1L PtSe2) in otherwise non-magnetic TMDC materials. Other structural defects, such as chalcogen-deficient line defect, can induce magnetism. This has been highlighted for the line defects in VSe_2[67], which may play a key role in the conflicting reports on the room temperature ferromagnetism of VSe_2. Recent experimental work, however, uncovered the induced magnetism from structural defects. It has been demonstrated in multilayer $PtSe_2$ that the surface Pt vacancies can induce long-range magnetism[22], the effect of which is probed by magneto-transport measurement. Interestingly, the magnetic ground states of ferromagnetic and antiferromagnetic ordering can be controlled by the number of layers, similar to the layer-dependent magnetism observed in intrinsic CrI_3. Defect-induced long-range magnetism is also experimentally discovered in bulk semiconducting Mo-based TMDCs by means of muon spin rotation (mSR)[23]. This work was supported by the density functional theory(DFT) calculations showing that the anti-site point defect in Mo-based TMDCs (e.g. 2H-$MoTe_2$ and 2H-$MoSe_2$), which is Mo at the chalcogen site, can induce magnetism.

2.5 Property of platinum diselenides

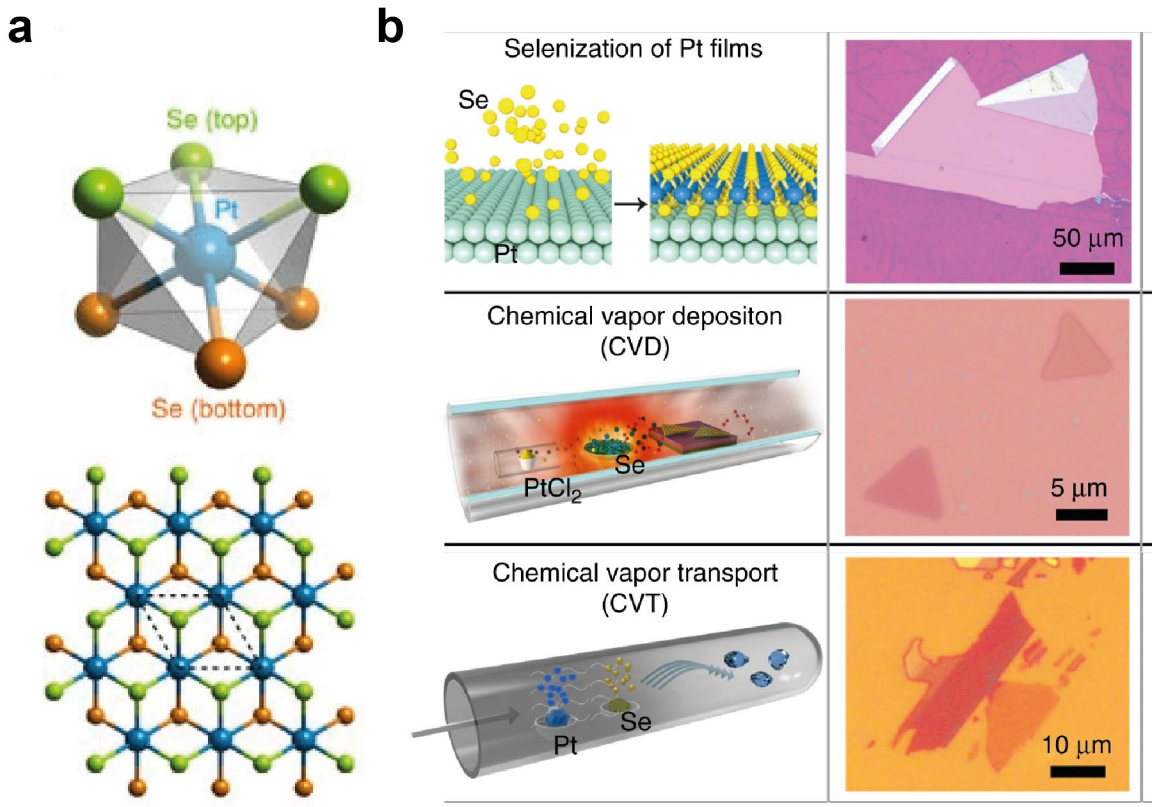

Figure 2-6. **$PtSe_2$ crystal structure and its growth.**a) A trigonal unit cell of $PtSe_2$ (top) and top view of its structure (bottom). b) Schematic of experimental growth setups (left) and the optical microscope image of fabricated samples (right). The image of the CVT-grown sample is shown after mechanical exfoliation. Panels are adapted with permission. Panel a) is from ref[78], Springer Nature Ltd. Panel b) is from ref[72], Springer Nature Ltd.

$PtSe_2$ is part of a recently investigated material family called noble-metal dichalcogenides, which includes PtS_2, PdS_2, and $PdSe_2$. This vdW crystal possesses a typical 1T-type hexagonal crystal structure. In the monolayer form, one Pt layer is sandwiched between the two Se layers, where one Pt atom is covalently bonded in octahedral prismatic coordination with 6 Se atoms. Regardless of the layer numbers, the crystal is centrosymmetric, having the space group P-3m1 for global structure. Pt and Se atomic sites belong to polar point groups of C_{3v} and D_{3d}.

Unlike MoS_2, $PtSe_2$ is a synthetic crystal and cannot be obtained as a natural mineral. Thus diverse synthesis method has been developed to obtain high crystalline $PtSe_2$. The first experimental production of monolayer $PtSe_2$ was done by the

direct selenization of Pt substrate[79]. About this method, first, Se is physically deposited on the Pt substrate at room temperature under an ultra-high vacuum condition. This is then followed by annealing at 270°C to form a large area(mm-size) monolayer $PtSe_2$. Although the selenization produced high-quality epitaxial $PtSe_2$, it was limited by self-terminating growth, and the thicker $PtSe_2$ could not be grown reliably. Later, molecular beam epitaxy enabled the precise thickness-controlled growth of $PtSe_2$ from monolayer to multilayers (22layers) on the bilayer graphene substrate[80]. Although both methods produced a large-area epitaxial growth of high-quality $PtSe_2$, the growth relied on the presence of metallic substrates, which can hinder electronic applications. Thus, synthesizing $PtSe_2$ on an insulating substrate was preferred. CVD has been an effective method to grow $PtSe_2$ on the insulating substrate, such as SiO_2/Si. One approach was suggested using $PtCl_2$ and Se powder precursors[72]. They were evaporated first at high temperature and carried to the reaction area, followed by the deposition of $PtSe_2$ on the SiO_2/Si substrate. CVT method improved the quality of material compared to the CVD method. As it produces bulk crystals, mechanical exfoliation was followed to produce thin 2D crystals on a substrate. The reported CVT growth involves reactions with temperature 900°C for 40 hours, followed by 700°C for 5 days[72]; thus CVT method has the disadvantage of high thermal budget and long growth time. Still, compared to CVD and other growth means, it produces the best crystal quality with a smaller number of structural defects.

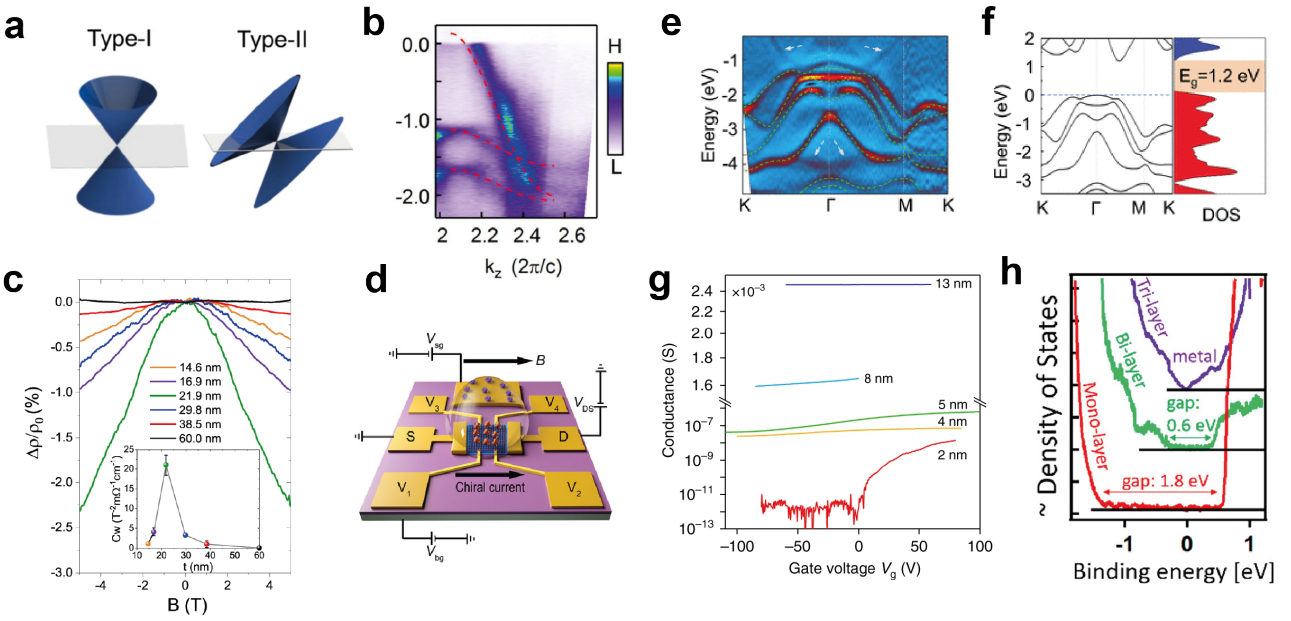

Figure 2-7. **Electronic properties of bulk and few-layer $PtSe_2$.** a-d) bulk $PtSe_2$. a) Schematic drawing of type-1 and type-2 Dirac band structures. b) k_z dispersions of CVT-grown bulk $PtSe_2$ measured by ARPES, which shows tilted Dirac cone crossing at 1.48eV below the Fermi level. c) Negative magnetoresistance in metallic $PtSe_2$ with various thicknesses. d) Illustration of chiral-based FET device made of $PtSe_2$. e-f) ARPES data e), and calculated bandstructure and density of states f) of monolayer $PtSe_2$. g-h) Few-layer $PtSe_2$. g) Conduction modulation from FET device made of different thicknesses of $PtSe_2$. At 2nm thickness, I_{on}/I_{off} significantly increases. h) Bandgap of mono-, bi- and trilayer $PtSe_2$ by scanning tunneling microscopy. Panels are adapted with permission. Panel a-b) are from ref[81], American Physical Society. Panel c) is from ref[82], Springer Nature Ltd. Panel d) is from ref[83], John Wiley and Sons. Panel e-f) are from ref[79], American Chemical Society. Panel g) is from ref[84], Springer Nature Ltd. Panel h) is from ref[85], American Chemical Society.

Experimental research in bulk and few-layer $PtSe_2$ crystals has been carried out after the successful development of high crystalline CVT synthesis. $PtSe_2$ is iso-structural compound to $PtTe_2$, which has been reported to have with a tilted 3D Dirac cone in the bandstructure[86]. Therefore, the bulk $PtSe_2$ was expected to have the same bandstructure and to be type-II Dirac semimetal. The direct experimental evidence for type-II Dirac fermions was confirmed recently by angle-resolved photoemission spectroscopy (ARPES) from the cleaved sample from CVT-grown $PtSe_2$[81]. The measured band structure shows that the tilted Dirac node is 1.3 eV below the Fermi level. Owing to this large energy difference, the observation of topological effects in this material is expected to be difficult by experiments. However, the chiral anomaly of Dirac fermions has been consistently observed in relatively thick samples (d=17nm to 60nm) with an appearance of negative magnetoresistance[82,87].

Progressively, the tuning of the Fermi level to the Dirac point was demonstrated lately from the advanced gating scheme by ionic liquid gating. This made it possible to build a chiral-based FET transistor made of bulk $PtSe_2$[83].

While the bulk is known to be metallic, early calculation of the band structure and density of state of the few-layer $PtSe_2$ pointed to a semiconductor with a bandgap energy of 2.0eV (G_0W_0 approximation)[88]. Later, DFT calculation suggested the lower bandgap of 1.2eV, which was in good agreement with the ARPES experiments from the monolayer $PtSe_2$ on Pt substrate obtained by the selenization method[79]. The DFT calculation further suggested that the bandgap opens below three layers of $PtSe_2$, and monolayer, and bilayer exhibit bandgaps of around 1.2eV and 0.2eV[89]. This particular thickness-dependent evolution of bandgap is due to a strong interlayer interaction and quantum confinement effect. The field-effect transistors made of CVT-$PtSe_2$ have been used to investigate the nature of the metallic-to-semiconducting transition[84]. Another direct experimental data was obtained by scanning tunneling microscope on MBE grown $PtSe_2$, which suggested that the band gap of mono- and bilayer $PtSe_2$ are 1.8 and 0.6 eV, respectively[85]. Yet, the exact bandgap of monolayer $PtSe_2$ has not been resolved, looking at the bandgap mismatch values so far obtained experimentally by ARPES and STM.

Nevertheless, the wide range of bandgap tunability from 0 to 1.2 eV achievable with a single material is particularly attractive. Theory also predicts intrinsic monolayer to have highly mobile charge carriers at room temperature with the mobility reaching up to 4000 $cm^2V^{-1}s^{-1}$. The bandgap covers the near-infrared (IR) range, unlike other semiconducting TMDCs, which can only cover 1.5eV-2.0eV in the visible spectral range. Indeed, black phosphorus (BP) is similar to $PtSe_2$, as it has high carrier mobility and the near-IR range bandgap, but $PtSe_2$ has the advantage of high environmental stability compared to air-degradable BP. Therefore, it is a promising candidate, beyond BP and graphene, for electronic devices, mid-infrared photonics and optoelectronic devices.

Last but not least, few-layer $PtSe_2$ exhibits rich spin-related phenomena as well. Firstly, pristine monolayer $PtSe_2$ holds hidden spin polarization of the spin-degenerate state near the Fermi level of monolayer $PtSe_2$, which is experimentally probed by ARPES measurement[78]. For monolayer $PtSe_2$, all the bands are expected to be spin-degenerate without any polarization because of structural inversion and time-reversal symmetries. Therefore, the spin-polarized ARPES data was rather unexpected. This intriguing observation is explained by two opposite local dipole fields within the single layer breaking the local-inversion symmetry (local Rashba effect). ARPES further spatially resolved opposite helical spin textures at the top and bottom Se layers induced by the two local fields. On the other hand, it is theoretically suggested that native point defects can also create spin polarization. It is found that a Se vacancy, which locally breaks the inversion symmetry of monolayer $PtSe_2$, can induce spin-split mid-gap states[24]. The largest spin-orbit splitting (Δ=152meV) is located at the K points of the hexagonal Brillouin zone. Another interesting phenomenon is defect-induced magnetism experimentally observed in multilayer metallic flakes[22]. The magnetic ground states can be switched between ferro- to antiferromagnetic states by controlling the number of layers. The first-principle calculation explains that the magnetism is due to native Pt vacancies on the surface of $PtSe_2$. Large spin-orbit coupling, presence of sizable bandgap, and high carrier mobility make few-layer $PtSe_2$ a strong candidate for building various spintronic devices, such as spin-transistor and spin-orbit-torque devices.

Chapter 3 Experimental methods

This chapter introduces the experimental characterization methods employed in this dissertation to study ultrathin vdW materials. We aim to deliver basic information on device fabrication and electrical/optoelectrical measurements, presented in more detail later in chapters 4, 5 and 6.

The subchapters are organized according to how we proceeded with our experiments: first with vdW sample fabrication, then the clean-room fabrication process, and progressively toward electrical/optoelectrical measurements. Each subchapter begins with relevant background information, proceeds to experimental details or instructions, and ends with its relevance to the content of later chapters.

3.1 vdW sample fabrication

3.1.1 Top-down synthesis : mechanical exfoliation

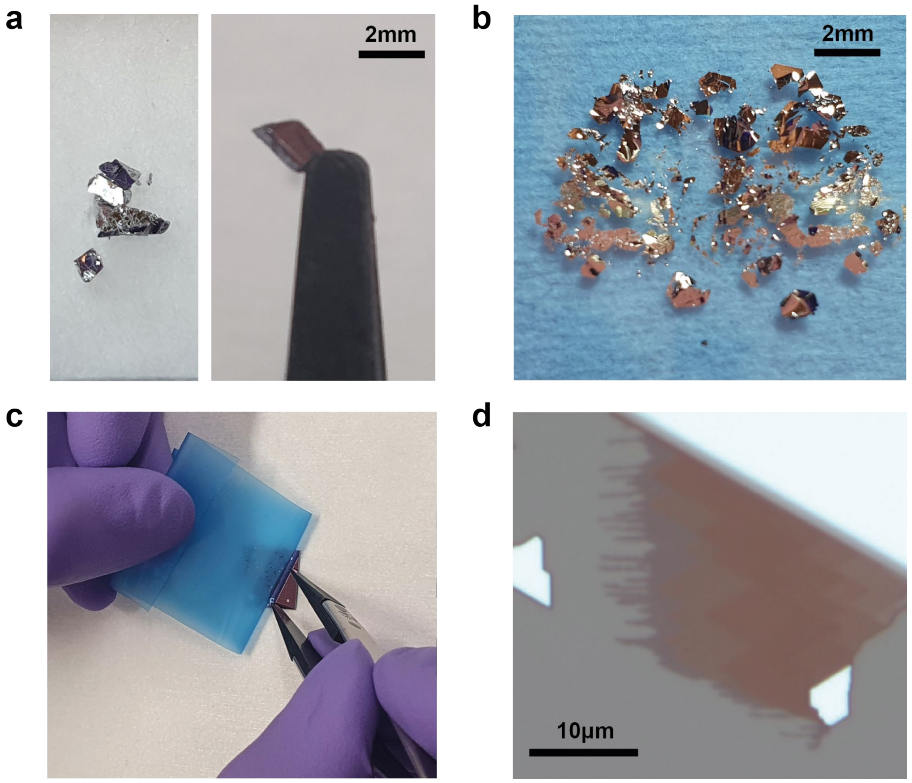

Figure 3-1. **Mechanical exfoliation.** a) Bulk $PtSe_2$ crystal source. b) $PtSe_2$ flakes exfoliated on a tape. c) Transferring flakes to silicon oxide substrate. d) Optical microscopy image of $PtSe_2$ flakes on the substrate.

A mechanical exfoliation technique was performed in order to fabricate a few layer-thick vdW materials. After its successful production of monolayer graphene from graphite using this technique, this has been the major experimental tool for producing various high-quality vdW materials in condensed matter experiments. Owing to the weak vdW interaction between layers, and strong in-plane covalent bonding, vdW materials can be peeled off layer by layer using ordinary scotch tapes. It is economic and at the same time reliable method to achieve various high-crystalline vdW materials. Throughout the work presented in this dissertation, we've worked with various vdW materials produced by such technique, including $PtSe_2$, graphene, h-BN and so forth. The source of bulk $PtSe_2$ is purchased from a company, HQ graphene, which has provided us high-quality CVT-grown crystals. We received Graphite from NGS Naturgraphit, and a collaborating group (T. Taniguchi and K. Watanabe) in Japan provided us h-BN.

Figure 3-1(a) shows the optical image of the bulk $PtSe_2$ source. For the exfoliating tape, we've mainly used single-sided Nitto tapes (purchased from a company, Nitto), as shown in **Figure 3-1(b)**. Compared to other kinds of tape, e.g. scotch tape, it leaves little tape-related polymer residues on the sample after exfoliation, which chemicals, e.g. Acetone, can easily clean. **Figure 3-1(c)** shows the process of transferring vdW flakes onto a silicon oxide wafer (270nm SiO_2/doped Si), which we have mainly used as the substrate for exfoliating vdW materials. It is a conductive substrate compatible with various clean-room-related fabrication processes involving high-density electron beam, such as e-beam lithography. One can benefit from using it to fabricate easily field-effect transistor made of exfoliated vdW materials using already-present doped Si as a back gate electrode and SiO_2 as dielectric layer, without the need to fabricate additional structures. **Figure 3-1(d)** shows the optical microscopy image of $PtSe_2$ on the substrate.

As for other substrates, viscoelastic materials such as PMMA/Si or Polydimethylsiloxane (PDMS) (purchased from Gel-Pak) are used for their advantage of producing a larger area of monolayer flakes than silicon oxide wafer from the exfoliation. The lateral size can be produced up to a few-tenth of micrometers. These substrates can also serve as carrying substrates of exfoliated materials. Therefore, they are particularly useful when producing materials that need to be transferred to another material to build a hetero-interface/structure.

Below is the instruction for mechanical exfoliation on the silicon oxide substrate. This instruction is optimized for silicon oxide substrate based on the best statistical results (not shown) of finding monolayers of various TMDCs, including $PtSe_2$.

1. For a better yield of producing monolayers, silicon oxide substrate is treated with O_2 plasma to remove any remaining polymer from previous wafer fabrications. Alternatively, it can be soaked in KOH solution to partially etch away the surface oxide layer. These treatments are to produce a clean surface of oxide before exfoliation.
2. Exfoliate a material on a Nitto tape. Separate tweezers were assigned to handle different vdW materials, to prevent any source contamination.
3. Once the total exfoliated area on the tape can cover the area of target substrates, the tape with exfoliated materials is gently pressed onto the substrate for a few minutes.
4. The substrate, together with the tape, is baked on the hotplate at an elevated temperature (e.g. 70°C for Nitto) for 30-60minutes. This is to have more flakes be transferred onto the substrate. However, the polymer residue also increases with temperature. Therefore, the optimum temperature can be determined by compensating between the density of flake and the amount of polymer residues. It depends on what kind of tape product is being used.
5. The tape is detached as slowly as possible at an angle of 45° from the substrate.

There is no best exfoliation method yet known. However, during the 2nd step of instruction, it is worth exfoliating materials on the tape with a few mechanical folding and unfolding. This improved the chance of finding ultrathin materials on all substrates, including the viscoelastic substrates. Also, the size of starting material of exfoliation matters; a small bulk source tends to give thin flakes with small area. We've kept all the source materials inside an inert Ar-filled glovebox before and after their use to prevent contamination.

This mechanical exfoliation technique produced all the vdW materials studied in chapters 5 and 6. Those materials are specifically, $PtSe_2$, graphene, and h-BN.

3.1.2 Bottom-up synthesis : CVD

Bottom-up synthesis methods such as metal selenization, MBE and CVD can also provide high-quality ultrathin vdW materials. Among those methods, CVD has successfully produced a larger area of vdW materials with better crystal quality. The size of synthesized material can be as large as 2 to 4-inch, covering the whole wafer, and the synthesis parameters can well control the number of grown layers. Chapter 6 presents work related to CVD-grown niobium disulfide (NbS_2).

3.2 Thickness characterization

3.2.1 Optical microscopy

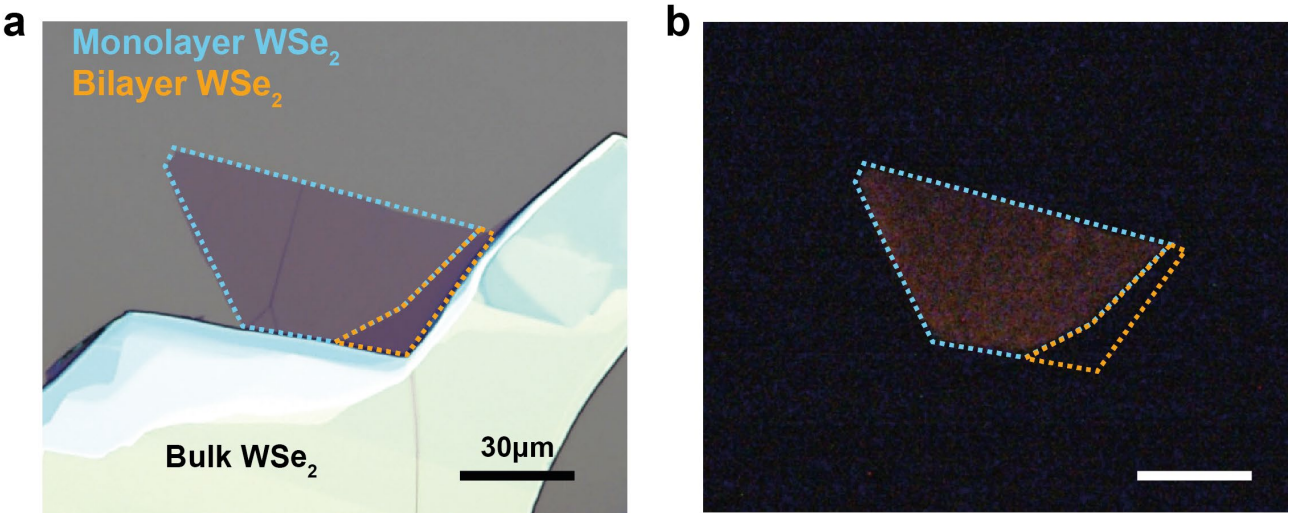

Figure 3-2. **Optical contrast and photoluminescence of WSe_2 on SiO_2/Si substrate.** a) Optical image of monolayer, bilayer and bulk WSe_2 exfoliated on a Si substrate with 270nm SiO_2. b) Dark-field photoluminescence of WSe_2. White light filtered with 650nm low-pass filter is used for the optical excitation.

Layer number of various vdW materials can be determined from different optical contrast, which, under the reflected light, can be related to differential reflectivity, that is $(R - R_0)/R$ where R and R_0 are reflectivity with and without the flake on the exfoliated substrate, respectively. A conventional microscope can demonstrate this optical scheme of finding the desired thickness of vdW materials. The reflected optical images of exfoliated samples are taken from a white light source, and the averaged contrast from the reflected light is calculated by weighting the light intensities from different channels (red, green, and blue) of a color camera.

As for the sample substrate, silicon oxide substrate can provide high visibility of finding few-layer TMDCs and graphene and few-layer h-BN. The oxide thickness of 270nm has been determined, giving the highest optical contrast for monolayer TMDCs with the white light source. This is satisfied by the optimum optical interference between the flake and the substrate, combined with the large absorption of monolayer TMDCs in the visible range of the light spectrum. **Figure 3-2(a)** shows the optical image of monolayer and bilayer on WSe_2 on a silicon oxide substrate, which are distinguishable by their optical contrast. Under the same optical source, the visibility of monolayer TMDCs in other substrates, such as PDMS and PMMA film on Si substrate, are also high, enough to determine directly under the naked eye through the eyepiece of the microscope.

Alternatively, the photoluminescence intensity and wavelength can be used to determine the number of layers in semiconducting vdW materials. This can be performed using the same microscope but with additional use of optical filters in the excitation and detection light path. The spectral filters must be appropriately chosen according to the photoluminescence energies, which are given by the type of material under study. PL spectroscopy is especially effective when searching for monolayer TMDCs, as they have a strong photoluminescence emission originating from the direct bandgap in reciprocal space. **Figure 3-2(b)** shows the dark-field photoluminescence image of a monolayer WSe_2. Bilayer WSe_2, known to have an indirect bandgap, shows negligible emission intensity compared to monolayer WSe_2.

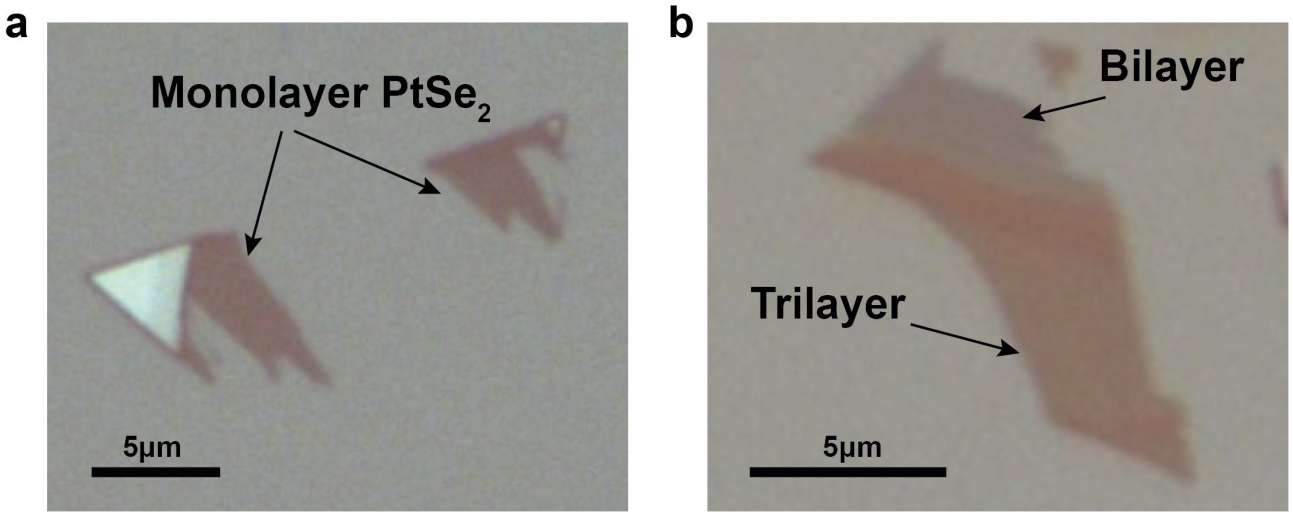

Figure 3-3. **Optical contrast of ultrathin $PtSe_2$ on SiO_2/Si substrate.** a-b) Optical image of monolayer $PtSe_2$ a), and bilayer and trilayer of $PtSe_2$ b).

For the work presented in chapters 4 and 5 of this dissertation, there has been a major effort to produce and search for ultrathin $PtSe_2$. However, the aforementioned optical spectroscopies (optical contrast and PL) were ineffective in determining the number of layers precisely for few-layer $PtSe_2$. Particularly, there is little difference in optical contrast between 1, 2 and 3 layer $PtSe_2$, as shown in **Figure 3-3**, even with the averaged contrast measured from the optical camera. The nature of the indirect bandgap of these few-layer $PtSe_2$ makes photoluminescence measurement not an applicable method for thickness identification. Therefore, we mainly relied on atomic force microscopy to characterize its thickness.

3.2.2 Atomic force microscopy

Thickness of vdW materials can be determined more accurately by atomic force microscopy(AFM). AFM is a simple, and non-destructive technique to determine the vertical and lateral dimensions of a material, and thus can provide its 3D structural image.

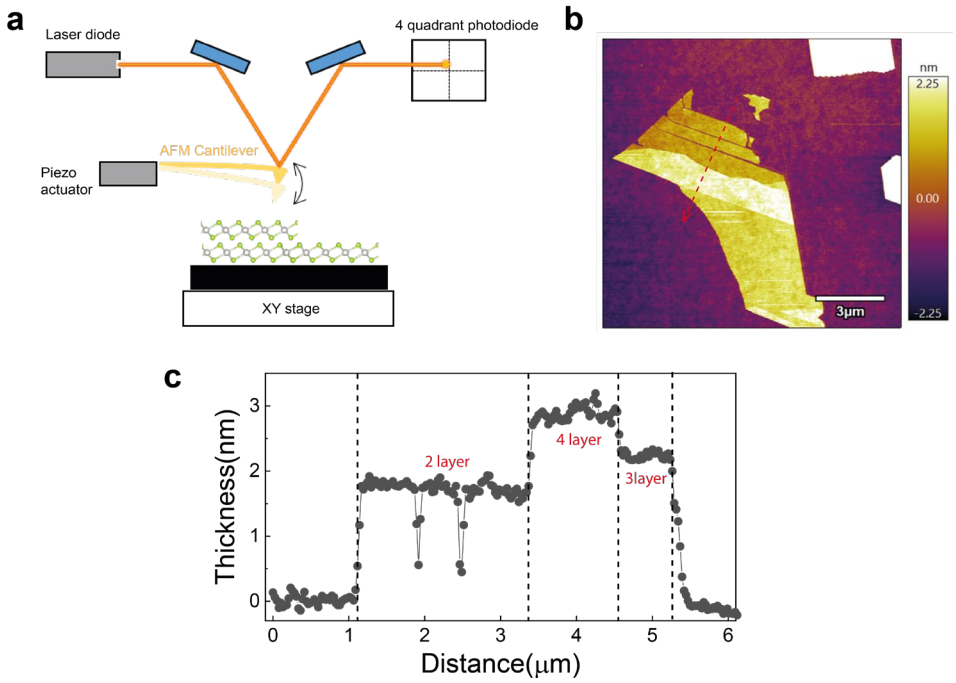

Figure 3-4. **Atomic force microscopy for vdW materials**. a) Schematic of AC contact mode, applied to measure the thickness of exfoliated vdW materials. b) 2D height scan of flake in **Figure 3-3(b)** measured by AC mode**.** c) 1D thickness profile along the direction of red dotted line in b).

AFM comes with two representative imaging modes, contact mode and AC mode (also called tapping mode), using a cantilever, a mechanical probe which scans the sample surface. In contact mode, the cantilever touches the sample surface, and the mode images the surface morphology by maintaining constant deflection of the cantilever. In AC mode, the cantilever vibrates near its resonance frequency by an attached piezo actuator, with the oscillation amplitude of a few tenths of nanometers. As the cantilever is being brought close to the surface, AC mode senses a small change in the vibrational properties of the cantilever due to interaction between the tip and the surface, and images the surface morphology by maintaining the constant amplitude of the cantilever oscillation.

Figure 3-4(a) shows the schematic of AFM running in AC mode. We have used AC mode to characterize the thickness of vdW materials as it renders less physical damage on the sample surface than contact mode. This is because the tip of the cantilever under AC mode touches intermittently with the probing sample surface, and thus lateral frictional force applied to the sample becomes negligible due to low interaction force.

In AC mode, the vibration amplitude decreases as the cantilever approaches the sample surface. This information is carried by the oscillating laser light reflected from the top surface of the cantilever. This optical signal is detected by a four-quadrant photodiode and converted into a digitalized electrical voltage signal, from which mechanical information (e.g. amplitude, phase, frequency) of the cantilever motion is extracted. The feedback loop sets a constant amplitude of cantilever oscillation by adjusting appropriately the z-height position of the piezo actuator, which provides information on sample thickness. **Figure 3-4(b)** shows the 2D thickness scan of the ultrathin sample of $PtSe_2$, shown in **Figure 3-3(b)**. The line thickness profile along the red dotted line in **Figure 3-3(b)** is shown in **Figure 3-3(c)**. Layer number can be identified considering the multiples of the unit thickness of monolayer $PtSe_2$, which is around 0.7-0.8nm.

3.3 Optical characterization

3.3.1 Micro-Raman optical spectroscopy

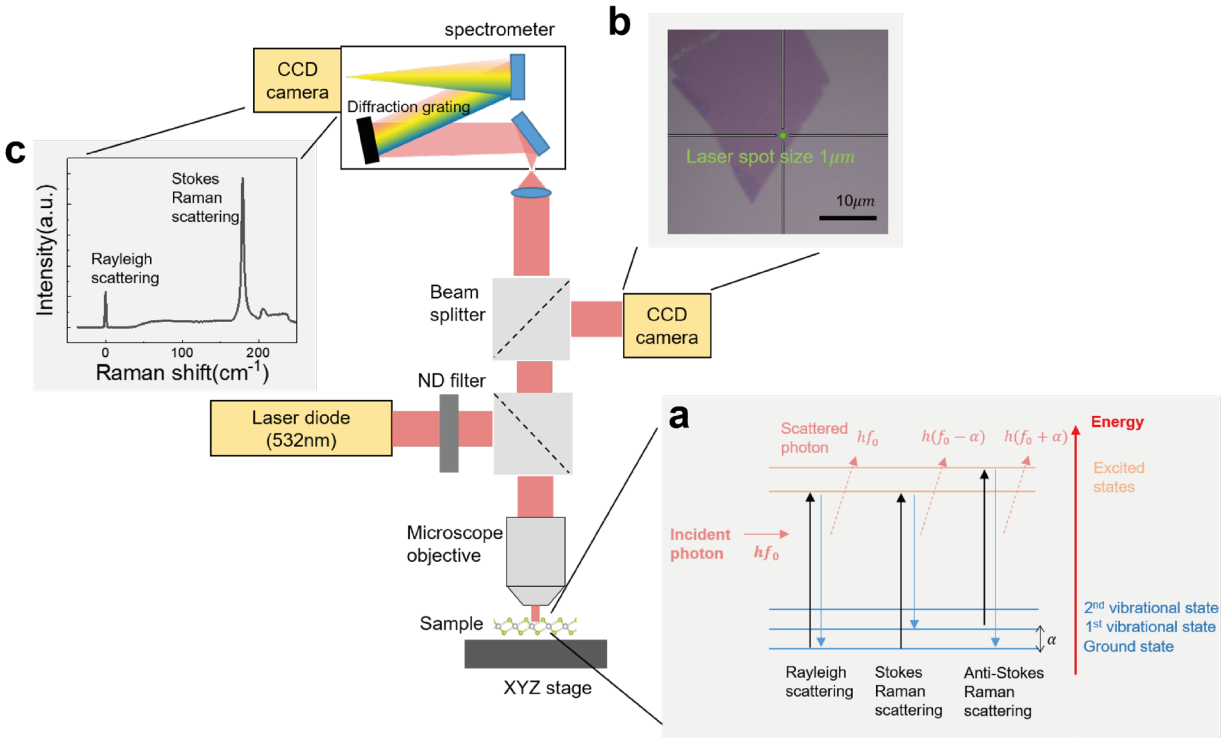

Figure 3-5. **Experimental design for Raman optical spectroscopy**. a) Scattering process of an incident photon with phonon modes. b) Optical image taken by CCD camera to guide the experiment. c) Raman spectra of monolayer $PtSe_2$. Rayleigh and anti-Stokes Raman scattering modes are identified from the selected range of wavelengths in the CCD camera of spectrometer.

Raman spectroscopy is a non-destructive technique to gain the structural information of a target material. It is based on so-called Raman scattering, which refers to the inelastic scattering of an incident photon with another quasiparticle, such as phonon (lattice vibration), or magnon (spin wave), excited within the material. **Figure 3-5** shows the experimental optical design of Raman spectroscopy, and typically, the sample is illuminated with a monochromatic laser beam. The energy of scattered photons can be lower (Stokes Raman scattering) or higher (anti-Stokes Raman scattering) than the incident photon frequency, as illustrated in **Figure 3-5(a)**.

We have used Raman spectroscopy as an additional tool to examine the structural phase and the number of layers of vdW materials. Characteristic Raman active modes appear owing to distinct vibrational modes given by the structure, and therefore, structural polymorphs of 2D materials, such as 2H, and 3R-stack, can be identified readily from their distinguished Raman active modes. The intensity and energy of Raman modes are also sensitive to the thickness of vdW materials down to the monolayer limit, due to the influence of interlayer coupling on their vibration modes.

Raman spectroscopy was performed using a confocal Raman spectroscope(Renishaw) installed in Crystal Growth Facility at the Institute of physics, EPFL. Two detectors were involved in optical experiments. One is a charge-coupled device(CCD) camera used for imaging a sample (**Figure 3-5(b)**), and the other is a spectrometer (grating coupled to CCD) to resolve light intensity at different wavelengths. A laser beam of 532nm wavelength was used as an excitation source for various vdW materials, including $PtSe_2$, and WSe_2, while the scattered photon was collected and analyzed using 3000 lines/mm grating. The measurement is performed at room temperature, and the sample is kept at atmospheric condition all the time. **Figure 3-5(c)** shows an example of Raman spectra of monolayer $PtSe_2$, where the characteristic Stokes Raman mode of 1T $PtSe_2$ is visible. The details of this Raman mode are explained in chapter 6.

Using Raman spectroscopy, we investigated the structural disorder in ultrathin $PtSe_2$ in chapter 6 and examined the polymorphs of CVD-grown NbS_2 in chapter 4.

3.3.2 Micro-PL spectroscopy

Photoluminescence refers to light generation due to the recombination of photo-excited electrons and holes within a material. Strong PL appears for monolayer TMDCs such as WSe_2 and MoS_2 as it becomes a direct semiconductor. Thus, monolayer TMDCs can be easily identified by PL measurements, with an experimental setup analogous to that of Raman spectroscopy.

PL measurement was performed in LANES laboratory with a customized optical setup. To measure PL from monolayer $PtSe_2$, a continuous wave (CW) 647nm laser diode was used to excite charge carriers above the bandgap energy (1.25eV from DFT calculation). The light emitted from the sample is collected by the same objective and sent to a spectrometer (Andor Shamrock). The diffraction grating in the spectrometer separates light at different wavelengths, and the resulting spectral intensity is measured by a calibrated CCD camera (Andor Newton). Elastically scattered radiation corresponding to the wavelength of the laser is filtered out by a long pass 650nm filter.

3.4 Deterministic transfer methods of vdW materials

This section presents deterministic transfer methods of vdW materials that we have used to build our electronic and optoelectronic devices. We have used three different methods: PMMA (polymethyl methacrylate) carrying layer method, PDMS (polydimethylsiloxane) transfer method, and van der Waals pickup method. Each has its distinct advantage, and below, we explain it one by one with detailed instructions.

All the methods have been demonstrated in the customized transferring setup with a microscope. The setup is equipped with two manual actuated micro-positioners. One is used to move the surface of accepter material, and the other is used to move the transferring flakes. Transferring flake can be moved in all x, y and z directions, and independently, accepter material can be moved in x and y directions and rotated at any arbitrary angle in the xy-plane. A long working distance objective is used to focus on both materials to monitor their relative position while bringing them close to each other. The setup is also equipped with a resistive heater that can elevate the temperature of accepter material during the transfer if needed. The transfer is done at atmospheric conditions, outside of the glovebox.

3.4.1 PMMA carrying layer method

PMMA carrying layer method involves detaching already-exfoliated material to transfer it to another location. Using this method, vdW monolayer, initially exfoliated on SiO_2/Si substrate, can be detached by PMMA and transferred onto a desirable surface of other material. This method is particularly useful for detaching as-grown material from the grown substrate. It was first introduced in the pioneering work of high-quality graphene electronic devices, where they fabricated mono- and bilayer graphene devices on a single-crystal h-BN substrate[8].

The detailed steps of the process are the followings:

[1] Prepare a glass slide. Stick one side with double-sided tape. Puncture a hole through the glass slide.

[2] Spin-coated PMMA on the substrate with a material.

[3] PMMA can be delaminated from the substrate, if SiO_2/Si substrate, by partial etching of SiO2 using KOH solution and, if Al_2O_3 substrate, by intercalation of DI water between hydrophilic Al_2O_3, and hydrophobic PMMA film. Ideally, the flake is attached to the PMMA, and delaminated PMMA film carries the flakes. Once it is completely detached, the film should be floating on the solution.

[4] Prepare DI water in a beaker, and have the PMMA film floated on the surface of DI water by dipping the substrate into DI water.

[5] A washer is used to pick up PMMA film from the surface and then placed on top of the hole of the prepared glass slide. The size of the washer should be larger than the size of the punctured hole.

[6] Using laboratory paper towels, dry out the remaining DI water around the washer and on the PMMA film. Clamp the glass slide to one of the micro-positioner in the setup. Load a target material at the other micro-positioner.

[7] Using both microscope and micro-positioner from the setup, align the position of transferring material to the target material while making both materials in contact. Once the heterostructure is formed, the temperature can be elevated up to 80deg for better adhesion.

[8] The glass slide is slowly lifted up while leaving PMMA film on the target material. Remove the washer from the glass slide.

[9] Clean the PMMA film with Acetone, and IPA.

We have used this method to transfer a few-layer NbS_2 from its grown sapphire substrate to SiO_2/Si substrate. It is also used for transferring mono- and bilayer $PtSe_2$, initially exfoliated on SiO_2/Si substrate, to another substrate.

3.4.2 PDMS transfer method

The second is the PDMS transfer method, where vdW material is exfoliated on a viscoelastic stamp[90]. Relying on the stamps as a carrying material, it is considered a complete dry-transfer method. Compared to the previous method with PMMA, it has the advantage of transfer speed as wet chemistry at the lab bench is not involved during the entire process.

The detailed steps of this method are shown below:

[1] Commercially available PDMS film (Gelfilm by Gelpak) comes in two-sided. Attach one of its sides to a glass slide.

[2] On the other exposed side of PDMS, mechanically exfoliate vdW material using Nitto tape. Under the microscope, search for the desired thickness of material to be transferred.

[3] Clamp the glass slide on the micro-positioner with the exposed side facing toward the surface of the target material. Align the position of transferring material to the target material while making both materials in contact.

[4] Once both materials are in contact, lift up the glass slide slowly. This will gently detach the transferring material from the PDMS onto the target material. The target substrate should be attached firmly to the micro-positioner at this step. Otherwise, the substrate will be picked up by PDMS and lead to failed transfer.

[5] Since the transferred sample has been in contact with PDMS, the top surface of the heterostructure can be further cleaned with Acetone and IPA to remove any polymer residue.

We have used this method to transfer thick h-BN onto metal films to fabricate a bottom gate capacitor for a h-BN encapsulated dual-gated device. The method is used to fabricate optoelectronic devices of $PtSe_2$ shown in chapter 6.

3.4.3 vdW pickup method

The last method is the van der Waals pickup method, which utilizes van der Waals force to lift up a vdW material using another vdW material[10]. This method can efficiently build a heterostructure of multiple different vdW materials with continuous dry transfers and pickups. Once the repeated dry-transfer procedures are optimized, it can be the fastest fabrication method to stack multiple vdW materials.

Except for the first and last vdW layer, the stack of inner material layers is free from any impurities trapping at all the interfaces. They are well protected by the external environment, such as air, water molecules or carbon contaminants, which tend to degrade the material properties. This method can realize high-quality 2D conducting channels. Thus, the method is considered one of the cleanest transferring techniques for building high-quality heterostructures and devices.

Insulating h-BN is the typical starting vdW material used to pick up other vdW materials. The other materials to be transferred are exfoliated on the SiO_2/Si substrate. This method relies on a PDMS stamp covered with polycarbonate(PC) film.

The principle of this methods are the following:

[1] Prepare PDMS stamps on a glass slide with PC film being coated. On top of the film, h-BN is exfoliated, and during the exfoliation the film mustn't wrinkle. Search for the right size and thickness of starting h-BN under the microscope.

[2] Place the glass slide at one of the micro-positioner and place a substrate with vdW flake to be transferred to the other positioner.

[3] Approach the glass slide to the substrate while monitoring the relative alignment of h-BN and the flake.

[4] Once they are in contact, in order to pick up the vdW flake with h-BN, wait for 5min while the substrate is heated up to 60°C for better adhesion between the two vdW materials.

[5] Gently lift up the glass slide, and remove the substrate. Check under the microscope that the target flake is picked up by h-BN. Repeat the previous steps [2] to [5] to pick up other vdW flakes.

[6] In order to release the stack, heat up the substrate once in contact, upto 170°C, which is higher than the glass transition temperature(150°C) of PC. Wait until all the PC film becomes viscous.

[7] Gently lift up the glass slide. PC films carrying the stack will be released from the PDMS stamp.

[8] Clean the PC films with Chloroform and then with IPA.

We have used this method to fabricate h-BN encapsulated optoelectronic device made of $PtSe_2$. To be specific, we transferred ultrathin $PtSe_2$ picked up by h-BN onto the bottom gate capacitor, which is made by the PDMS transfer method.

Typically, for all the methods, randomly distributed bubbles form at the interfaces of vdW materials, which are the aggregation of contaminants, that includes water molecules or carbon contaminants. For the purpose of removing the bubble density, the heterostructure is post-annealed under a high vacuum ($P<10^{-7}$mbar) at 340°C for 6hrs. After chemically cleaning the transfer-related polymers, this post-treatment further improves the heterostructure quality by having a cleaner interface.

3.5 Device fabrication in cleanroom

3.5.1 E-beam lithography

We have used e-beam lithography to design a pattern for fabricating metal electrodes in our electronic and optoelectronic vdW devices. It utilizes the focused beam of electrons to create the pattern on the electron sensitive polymer resist. Although the patterning speed is slower than photo-lithography due to the time required for scanning of focused beam within the area of interest, it has advantage in high-resolution, and flexibility. This feature makes it the most adequate lithography technique for fabricating devices made of 2D materials. However, some care needs to be taken for the materials that are sensitive to e-beam irradiation, such as indium selenide (InSe).

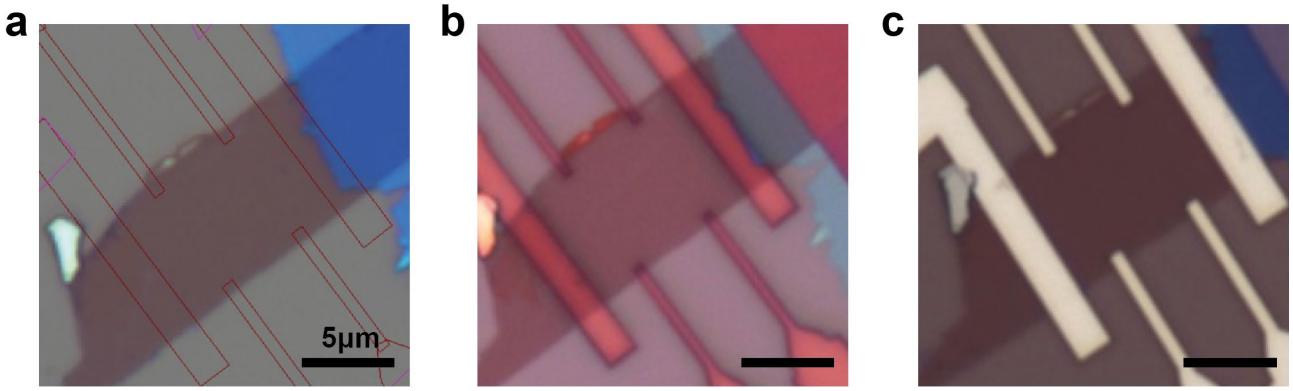

Figure 3-6. **E-beam lithography and metal evaporation for vdW device.** a) E-beam mask design for electrodes. b-c) Optical microscopy image of e-beam patterned polymer after developing b), and e-beam evaporated Pd electrodes after lift-off.

We have used the e-beam lithography equipment, Raith EBPG5000, that is housed in the custom cleanroom of Center of Micro Nano Technology(CMI), EPFL. With the lithography performed at 100keV, well-grounded conductive substrates are required, and SiO_2/Si substrate, where we exfoliate vdW materials and build vdW heterostructures, meets this requirement. As we target on patterning metal structures, we have used double-layer e-beam resist with higher(lower) molecular weight on the top(bottom) layer, which can create a desirable undercut resist profile in the bottom layer for better lift-off. We have used double-layer positive-tone e-beam resists of MMA (8.5) (methyl methacrylate) EL6 (6% MMA in Ethyl Lactate) as the bottom layer and 950 PMMA (poly methyl methacrylate) A2 (4% PMMA in Anisole) as top layer both of which are positive-tone e-beam resists. These layers are spin-coated sequentially on the SiO_2/Si substrate at 4000 RPM and 1500 RPM, giving a spin-coated thickness of around 150nm and 100nm for MMA and PMMA, respectively.

Optical microscopy images with the pre-defined markers allow us to locally design software masks for e-beam by precisely locating the target 2D material or heterostructure. Both high and low magnified optical images were taken using different objectives (5x, 20x, 50x and 100x) as the reference, on which we have drawn the customized e-beam mask patterns using Design CAD software. **Figure 3-6(a)** shows one example of a software-drawn e-beam mask, the design of which is for making metal contact electrodes on $PtSe_2$.

In one e-beam mask design, two different e-beam lithography conditions were used for different electrode sizes. With a fixed e-beam dose of 950uC/cm^2, 50nm-resolution e-beam spot size was used to pattern large electrodes, whereas 5nm-resolution spot size was used for small electrodes. The former is mainly applied when fabricating metal electrodes with lateral dimensions required to be around micrometer, and the latter is applied to less critical contact pads, the area of which is large for the wire bonding. This scheme minimizes the e-beam drawing time as a smaller spot size takes significant time to scan the large area.

Once the e-beam lithography is done, we have developed the lithography pattern using a cold solution mixture of IPA and DI water (H_2O: IPA=1:3) followed by warm IPA (99.99%) and blowing the solvent with an N_2 gun. **Figure 3-6(b)** shows the e-beam pattern on polymer after the developing.

3.5.2 Vacuum metallization

In this section, we explain the procedure of depositing metal coatings on the e-beam developed area. This work is done by e-beam evaporation, a physical vapor deposition method, using the processing machine Leybold Optics LAB 600H, which is installed inside the clean room of CMI, EPFL. The machine allows to deposit of metals, such as Au, Pd, and Ti, using an e-beam thermalizing gun, with the thickness in the range of a few nm to a few hundred nm, precisely.

The machine is equipped with wafer-size(100mm) substrate holders, capable of large area metallization. The holders can be set to rotate continuously while deposition, thereby enhancing thickness homogeneity. In preparation for loading the patterned samples, chips were taped on a single Si wafer with vacuum compatible Kapton tape. When fabricating multiple samples as a batch, they were closely positioned at the center of the wafer to reduce, if any, thickness variation of deposition within the wafer area. After manual loading of the wafer, the whole process runs automatically under a recipe whose deposition parameters (e.g. thickness, deposition rate) can be user-defined prior to the process. Equipped with additional cryogenic pump, all the deposition carried out once vacuum is better than 10^{-6} mbar.

All the samples were immediately processed to evaporation after developing the e-beam pattern in order to reduce the contamination on the exposed region that may affect the quality of metallization. After the deposition, samples were kept inside Acetone for 3-6 hours for the lift-off process of masked polymer, followed by cleaning with IPA and then blowing with N_2 gas. **Figure 3-6(c)** shows the electrodes fabricated on $PtSe_2$ from e-beam evaporation after lift-off.

In the entire work presented in this dissertation, we have used only e-beam evaporation as the deposition method to prepare all the contact electrodes. This is the case for all the devices shown in chapters 4,5, and 6. Here is the summary of materials and their thickness used for various metal electrodes shown in this dissertation. For the bottom and top gate metals, 1nm Cr/ 4nm Pt and 5nm Pt were deposited, respectively, with a low deposition rate of Pt, 0.1A/s. For the pre-made contacts on h-BN presented in chapter 3, 1nm Cr/ 9nm Pt was deposited on h-BN. Metal contact electrodes on vdW materials were made either with Pd 80nm or 1nm Ti/ 80nm Au.

3.6 Electronic and optoelectronic measurements

3.6.1 Charge transport measurements

Electronic properties of vdW 2D materials, such as carrier mobility, and sheet resistance, were characterized by charge transport measurement. We fabricated field-effect-transistor(FET) devices to modulate the carrier density of the semi-conducting channel, with multiple metal electrodes to perform two- and four-terminal measurements. A heavily doped silicon substrate is used as a back gate to modulate the carrier density, with 270nm SiO_2 as an oxide dielectric layer.

Alternatively, h-BN layer can be chosen as the dielectric layer to have better electronic transport performances. This is because of its lower scattering source for charge carrier, provided by its atomically sharp surface and fewer interfacial traps than the SiO_2 layer. To use h-BN as the dielectric media for FET device, h-BN is transferred on to thin metallic film of 5nm Pt, which acts as a local gate. The channel material is later transferred on h-BN.

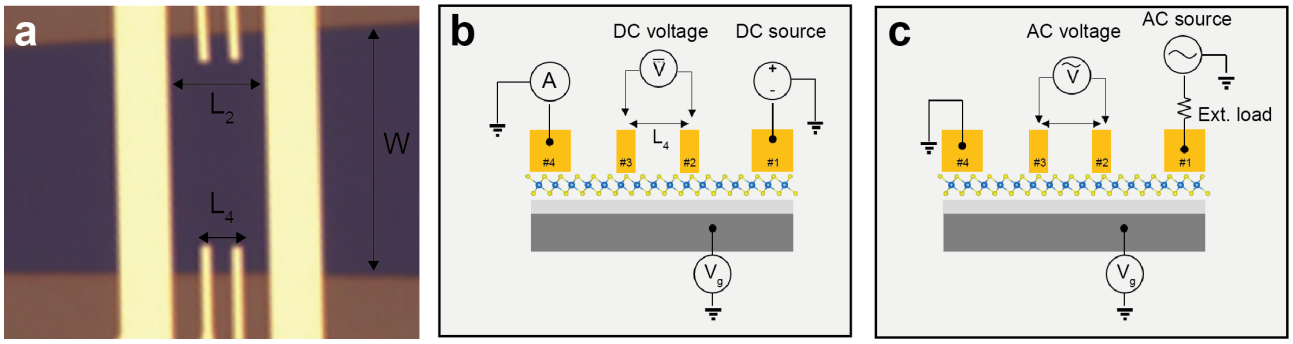

Figure 3-7. **Charge transport measurement scheme**. a) Optical image of multi-terminal Hall bar device where the channel material is a few-layer NbS_2. L_2, and L_4 refer length of conducting channel between the outer two electrodes and between the inner two electrodes, respectively. W is the width of conducting channel. b-c) Schematic of DC b) and AC c) measurements.

Figure 3-7(a) shows an example of a multi-terminal device on SiO_2/Si substrate, and **Figure 3-7(b)** displays the schematics of DC measurement principles. A bias voltage(V_{14}) is applied between the source (#4) and drain (#1) using the outer two electrodes and the current(I_{14}), which flows through the 2D vdW channel, is simultaneously measured. The voltage drop (V_{23}) between the inner two electrodes (#2 and #3) was also measured at the same time. The 2 terminal sheet conductance ($G_{2,sh}$) and 4 terminal sheet conductance ($G_{4,sh}$) can then be computed as,

$$G_{2,sh} = \frac{I_{14}}{V_{14}}\frac{L_2}{W} \tag{1}$$

$$G_{4,sh} = \frac{I_{14}}{V_{23}}\frac{L_4}{W} \tag{2}$$

both of which corresponds to charge conductivity normalized to geometric dimensions, L_2, L_4 and W, shown in **Figure 3-7(a)**.

The 2D field effect mobility can be calculated using the following expressions.

$$\mu_{2,FE} = \frac{dG_{2,sh}}{dV_g}\frac{1}{C_{ox}} = \frac{dI_{14}}{dV_g}\frac{L_2}{V_{14}WC_{ox}} \tag{3}$$

$$\mu_{4,FE} = \frac{dG_{4,sh}}{dV_g}\frac{1}{C_{ox}} = \frac{dI_{14}}{dV_g}\frac{L_4}{V_{23}WC_{ox}} \tag{4}$$

where V_g and C_{ox} refer to gate voltage and oxide capacitance, respectively.

The 2 terminal mobility ($\mu_{2,FE}$) calculated from Eq. (3) is generally lower than the 4 terminal mobility ($\mu_{4,FE}$) calculated from Eq. (4). This is due to large contact resistance between the metal electrode and vdW material, which leads to a sizable voltage drop when the current passes through this interface. This voltage drop is not considered in Eq. (3) and the applied bias(V_{14}) in Eq. (3) is therefore somewhat larger than the actual voltage difference in the channel, which results in underestimated field-effect mobility from the calculation. Under the same argument, the calculated sheet conductance in 2 terminal geometry is typically lower than the actual value. Thus, 2 terminal measurements can only give a qualitative comparison among similarly fabricated devices and, to obtain precise values of field-effect mobility and sheet resistance, 4 terminal measurement is desirable. To increase the measurement accuracy in 4 terminal geometry, the voltage probe electrodes can be placed on the very edge of channel material during fabrication, as shown in **Figure 3-7(a)**, to avoid/minimize current shunting.

As for instruments used for the DC electrical measurement, source-drain bias is applied, and the current is measured using Keithley 2636b sourcemeter. The voltage drop is measured using Keithley 2000 or nanovoltmeter. With Keithley 2636b sourcemeter or 2000, the back gate voltage is applied while measuring leakage current at the same time.

Figure 3-7(c) displays the schematics of AC measurement principles. AC measurement is performed by lock-in detection of AC voltage (between #2 and #3) with AC probe current (through #1 and #4). It can measure the sample resistance with an increased signal-to-noise ratio (SNR) by eliminating the background electrical noise, which cannot be avoided in DC transport measurement. This technique is adequate for probing low resistance samples (e.g. metals) and it is especially useful

to capture the electrical signature of material phase transition. For example, differential resistance peaks from charge density wave (CDW), and zero-resistance from superconducting transition can be measured with the AC lock-in detection scheme.

As for instruments used for the AC electrical measurement, the outer electrodes are connected 6221 Keithley AC source meter to provide the AC probe current. Alternatively, lock-in amplifier SR860, which can apply alternative voltage bias, is used with fixed input impedance to provide a constant amplitude of AC current. AC voltage is measured by connecting the inner voltage probe to the input of the lock-in amplifier. The reference frequency of lock-in is set to the same modulating frequency as the AC current. The differential resistance is computed as the measured AC voltage divided by the applied AC current. To further reduce the background noise of the voltage signal, SR560 low-noise voltage preamplifier is used before the lock-in amplifier.

The influence of the magnetic field on the material's electronic properties was investigated via magneto-transport measurement. Electrical transport, either with DC or AC bias source, is performed while the magnetic field is applied at a fixed direction, varying its field strength. The transport measurement is performed in ICE Oxford liquid helium continuous flow system, and the magnetic field is applied using a superconducting magnet. This measurement is done to characterize the superconductivity of 2H-NbS_2 in chapter 4 and the magnetism of $PtSe_2$ in chapter 5 with the magnetic field applied perpendicular to their 2D device plane. Charge transport measurements were performed to examine the semiconducting properties of $PtSe_2$ in chapters 5 and 6.

3.6.2 Photocurrent measurement

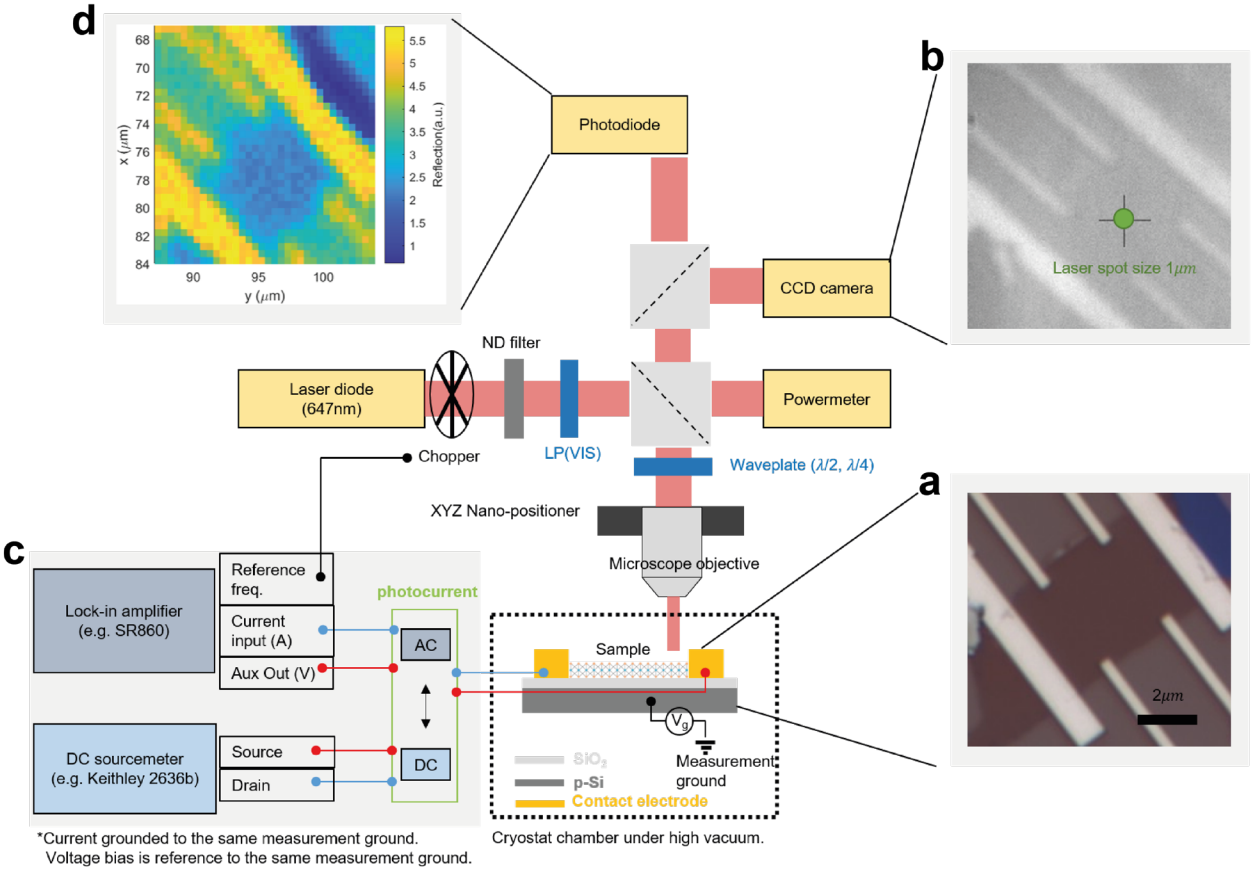

Figure 3-8. **Experimental setup for photocurrent microscopy.** a) Optical image of a sample. b) CCD camera image of the sample to guide the experiment. c) Electrical connections to instruments for measuring DC and AC photocurrent response. d) 2D reflection sample mapping from a photodiode.

Scanning photocurrent microscopy with focused light excitation was carried out to measure the optoelectronic properties of vdW materials. **Figure 3-8** shows the experimental setup with optical components and instruments. **Figure 3-8(a)**

show the optical image of a sample from a color camera, and **Figure 3-8(b)** shows the image from a charge-coupled device(CCD) camera in the setup used for guiding the experiment. The setup is combined with a microscope using a 50x objective to focus the light with a Gaussian spot size of 0.7um^2 on the sample, which is placed inside a vacuum chamber under high-vacuum value of 10^{-5}mbar. The objective is mounted on XY nano-positioner, which can precisely move under sub-micrometer distance. This allows high-resolution laser mapping of the sample and can locate the specific area of interest, for example, at the interface between metal electrodes and 2D materials.

Photocurrent measurement can be done by short-circuiting the examined materials under light illumination and measuring the current flowing in the circuit. When light is illuminated on a semiconductor, a photo-excited electron or hole can contribute to charge current when the material is voltage-biased. This contribution is called photocurrent and can be distinguished easily by comparing the charge conductance with and without light illumination. The material can possess positive(negative) photoconductivity, which is higher(lower) conductance with(without) light illumination.

The electrical connections from the device to instruments for DC and AC photocurrent measurement are illustrated in **Figure 3-8(c)**. While laser intensity is being controlled using a neutral-density (ND) filter, we've measured the 2 terminal DC charge current by connecting two electrodes from the device to the source and drain of Keithley sourcemeter K2450 or K2636. To improve the SNR of photocurrent signal, we have used, in parallel, AC lock-in detection measurement by using a mechanical chopper near the laser source. The chopper produces a square-wave optical source modulating in time with a frequency given by the frequency of its rotation. The amplitude of oscillating photocurrent signals was extracted by lock-in amplifier SR860 with the frequency being locked to the same external frequency of the chopper. This lock-in detection scheme dramatically improves the SNR than DC measurement and allows us to detect small optoelectrical signals. Unlike DC measurement, which measures the dark and photocurrent altogether, the signal measured from lock-in can be directly related to the photocurrent.

Additionally, we also measured photocurrent while controlling the incident light polarization. To control the linear polarization of illuminated light, $\lambda/2$ waveplate is used with a linear polarizer. For circular polarization, the waveplate is replaced with $\lambda/4$ waveplate. The transmission through a beam splitter is found to be slightly different between vertical and horizontal linear polarizations. To avoid the unwanted influence of transmitted polarization states, we placed the waveplates after the beam splitter.

Suppose the light is illuminated on the heterostructure or at the interface between two different materials. In that case, photo-induced current can be present by other origins, such as photo-induced thermoelectric or photovoltaic effect. As these effects can independently contribute to the total photocurrent, the information of laser position regarding device structure becomes vital to identifying the origin of photocurrent. Therefore, the reflected laser light was collected while at the same time, photocurrent signals were measured. **Figure 3-8(d)** shows the 2D mapping of reflected laser light from the device, where a photodiode measures the intensity.

Scanning optical microscopy was carried out to measure optoelectronic properties in ultrathin $PtSe_2$ in chapter 6. The experiments were focused on measuring spatially-resolved photocurrent and photovoltage responses that are sensitive to linear and circular polarization.

3.6.3 Applying vertical displacement fields

A dual-gate field-effect transistor with parallel plate capacitors can independently modulate the carrier concentration and the electrical field applied perpendicular to the sample. The capability to isolate the effect from charge carrier modulation clears the effect of symmetry breaking in electronic and optical properties of various vdW materials. The key observations with this e-field are are the bandgap opening of bilayer graphene[32], and induced inversion asymmetric properties, such as valley Hall effect[91], in centrosymmetric materials.

Top and bottom electrical displacement fields, D_t and D_b, can be defined as,

$$D_t = -\varepsilon_t \frac{V_t}{d_t} \tag{5}$$

$$D_b = \varepsilon_b \frac{V_b}{d_b} \tag{6}$$

where $\varepsilon_{t(b)}, V_{t(b)}$, and $d_{t(b)}$ corresponds to permittivity, applied voltage, and thickness of the top(bottom) dielectric layer, respectively. The sign of the displacement field depends on the sign of the coordinate. Under this definition, the difference of the two, $D_t - D_b$, leads to additional carrier concentration, and the averaged sum of the two, $(D_t + D_b)/2$, breaks the inversion symmetry. The condition of introducing zero carrier concentration in a dual gate h-BN encapsulated device is therefore,

$$\varepsilon_{h-BN}\frac{V_t}{d_t} + \varepsilon_{h-BN}\frac{V_b}{d_b} = 0 \tag{7}$$

$$\frac{V_t}{V_b} = -\frac{d_t}{d_b} \tag{8}$$

V_t and V_b are controlled by two channels of Keithley 2636b connected to the top and bottom gate, while the source and drain electrodes on the sample is connected to Keithley 2450 with the source being grounded.

In chapter 6, we have studied spontaneous photocurrent generation in $PtSe_2$, and investigated the effect of the external electric field on photocurrent generation. We fabricated dual gate h-BN encapsulated device and applied gate voltages at the condition without introducing charge carriers to the sample.

Chapter 4 Phase-correlated electronic properties of 2D NbS_2

This chapter presents our work on the epitaxially grown niobium disulfide (NbS_2) using chemical vapour deposition. We achieved the controlled growth of two different polymorphs of NbS_2, 2H-NbS_2 and 3R-NbS_2, with large lateral size (>500um) and we observed thickness-dependent structural phase transition in the grown samples. Our work was supported by complementary data from the different experimental analyses of the material properties, which are based on electrical charge transport, Raman spectroscopy and scanning transmission electron microscopy. Low-temperature charge transport measurement distinguished the different electronic properties among those polymorphs; only 2H-NbS_2 shows 2D superconducting transition around 3K while 3R-NbS_2 remains metallic.

This work was achieved by working closely together with my colleague, Zhenyu Wang, who synthesised the NbS_2 samples and performed Raman spectroscopy while I focused on characterizing low-temperature electrical transport properties. We also collaborated closely with Dr. Mukesh K. Tripathi, who performed TEM analysis on the grown samples. This work has been published: *Wang, Z., Cheon, C. Y., Tripathi, M., Marega, G. M., Zhao, Y., Ji, H. G., ... & Kis, A. (2021). Superconducting 2D NbS2 Grown Epitaxially by Chemical Vapor Deposition. ACS Nano, 15(11), 18403-18410.*

4.1 Introduction

4.1.1 2D superconductivity in vdW materials

Intriguing collective quantum phenomena often appears in low dimensional limit. One good example is 2D superconductivity, characterized by vortices and anti-vortices. Their associated thermodynamics are well explained by Berezinskii-Kosterlitz-Thouless (BKT) transition[92], the experimental demonstration of which has become the main criteria for 2D superconductivity. The materials for its early studies were thin films made of Al or Bi[93], with a thickness range from 0.3nm to few nm. Those materials are, however, amorphous and granular, presented with disorder. Being sensitive to disorder, superconductivity in such disordered systems is often suppressed due to electrons/Cooper pair localization[94].

In recent years, there has been a pursuit of finding a high crystalline system hosting 2D superconductivity and exploring the unknown properties in the clean limit[95,96]. Among these systems, vdW materials have become the central material platform as mechanical exfoliation can directly provide 2D superconductors with high crystallinity. From the bulk crystal already known for its superconductivity, single crystal thin flakes are cleaved, and 2D superconductivity has been observed in ultrathin metallic TMDCs, including NbS_2[97], $NbSe_2$[98], and TaS_2[99]. Among them, the prototypical 2D superconductor is monolayer $NbSe_2$. Thickness-dependence of T_c in ultrathin $NbSe_2$ has been determined, with monolayer $NbSe_2$ found to be superconducting with the critical transition temperature T_c of ~3.1K[100].

The advancement in exfoliation and characterization techniques of vdW materials has given us new insights into understanding 2D superconducting phenomena. Compared to their bulk form, monolayer TMDCs significantly differ in material properties due to reduced dimensionality, strong intrinsic spin-orbit coupling, and structural inversion asymmetry. Influenced by this intrinsic property of TMDCs, an exotic form of 2D superconductivity more resilient to the external magnetic field has been demonstrated in monolayer MoS_2[101,102], and $NbSe_2$[103]; Ising-type Cooper pairing with the enhanced upper critical

field. Additionally, strong electrostatic tunability in vdW materials made the electrostatic control of its superconducting transition possible. This further led to the observation of gate-induced insulator to superconductor transition in a few-layer 1T-$SnSe_2$[104], 2H-MoS_2[105] and 2H-WS_2[106] by ionic liquid gating, providing a new route to achieve superconductivity in 2D vdW system[107].

Among vdW materials, the material of interest for this chapter is niobium disulfide (NbS_2). Being one of its polymorphs, 2H-NbS_2 has shown bulk superconducting transition below T_c of 5.7K[108]. Ultrathin flakes show typically lower transition temperature than bulk (T_c of 3.5K for 7nm thickness). They have shown thickness dependence of superconducting transition temperature, where transition temperature is found to decrease with reducing thickness[97].

Unlike other intrinsic 2D superconductor, 2H-NbS_2 stands out as a superconductor without coexisting charge density waves(CDW). This is a peculiar case since this feature is opposite to what is found in other isostructural and isoelectronic compounds such as 2H-$NbSe_2$ and 2H-TaS_2, where both collective quantum phenomena, CDW and superconductivity, can emerge simultaneously. However, the theoretical work claims 2H-NbS_2 is on the verge of charge density wave transition, and the likelihood of occurrence can be enhanced in its monolayer form[109]. Furthermore, monolayer 2H-NbS_2 is also suggested with spin-wave instabilities[110,111] if magnetic impurities are present. These possibilities make ultrathin 2H-NbS_2 a potent system for studying quantum phase transitions in low dimensions.

As for the superconductivity studies in TMDCs mentioned earlier, material fabrication has mainly focused on the mechanical exfoliation technique, a top-down method to achieve high-crystalline 2D flakes from a single bulk crystal reliably. Despite its methodical success in contributing to making high-quality 2D mesoscopic devices, however, there is a critical disadvantage of this method. This is because the lateral size of an obtained flake by mechanical exfoliation is random and generally small, below a few tenths of micrometers at most, without controllability of its thickness [112]. Bottom-up synthesis of NbS_2 based on MBE was not successful in resolving such issues, as it has given low production yield with only a small grain size[113,114]. Moreover, MBE growth has been limited by the requirement of specific substrates, such as graphene or h-BN[113,114].

Our motivation is to improve the bottom-up synthesis to provide large NbS_2 with higher quality for future studies and applications. This chapter demonstrates high-quality epitaxial growth of NbS_2 based on chemical vapor deposition. The growth size of 2H-NbS_2 is the largest reported up-to-date, and its superconductivity is studied through electronic transport measurement. We observed the temperature-dependent transition of linear to non-linear I-V characteristics, a signature of BKT-type transition in a 2D superconductor. Additionally, we were able to control the growth thickness of NbS_2 by changing the spin-coated precursor concentration on the substrate prior to the growth. From this control, we found thickness-dependent structural phase transition in our CVD-grown samples. As thickness decreases, 2H-NbS_2 structurally transforms into another polytype, 3R-NbS_2, at the intermediate thickness of 4nm. This structural transformation was also confirmed independently by Raman spectroscopy and transmission microscopy.

4.2 2D NbS_2 grown by chemical vapor deposition

4.2.1 CVD growth method

2D NbS_2 was grown at atmospheric pressure using a home-built hot-wall chemical vapor deposition system by my colleague, Zhenyu Wang. Previous reports on CVD growth of NbS_2 used powder precursors, such as sulphur, niobium pentoxide(Nb_2O_5), and niobium chloride($NbCl_5$). They relied on their thermal evaporation, making it difficult to achieve a stable growth rate and uniform source distribution. Consequently, NbS_2 growth thickness could not be controlled well. Instead, we have chosen a gas precursor, hydrogen sulfide (H_2S) for sulphur and precisely controlled the gas flow rate by using a mass flow controller. For Nb precursor, niobium chloride ($NbCl_5$) precursors were spin-coated on a substrate before the growth to have a relatively uniform concentration distribution.

Substrate material has a strong impact on the quality of as-grown NbS_2. The difference in surface diffusion rate of Nb atoms resulted in different gain size of grown NbS_2 in various substrates[115]. In previous attempts, Si/SiO_2 substrates were mostly utilized to grow NbS_2, which have yielded limited the grain size and poor crystal quality[115,116]. We selected c-plane sapphire as a growth substrate because of its atomically smooth surface, which foster a large-area and high-quality growth.

With $NbCl_5$ and NaCl pre-coated on sapphire substrate, CVD growth was carried out at atmospheric pressure. The temperature of the tube and gas flow ratio of Ar and H_2S were independently varied to find the optimal growth condition. This procedure is illustrated in **Figure 4-1(a)** schematic. At the optimum condition (T=950°C, flow ratio(H_2S :Ar)=1 :3.5), as-grown NbS_2 has a rectangular morphology with long axis from all the flakes aligned along the same direction, as depicted in the optical image of **Figure 4-1(b)**. Using atomic force microscopy on this rectangular shaped flake, we can see in **Figure 4-1(c)** that this dominant alignment is due to the step edges of the sapphire substrate terrace, giving the energy barrier diffusion during growth.

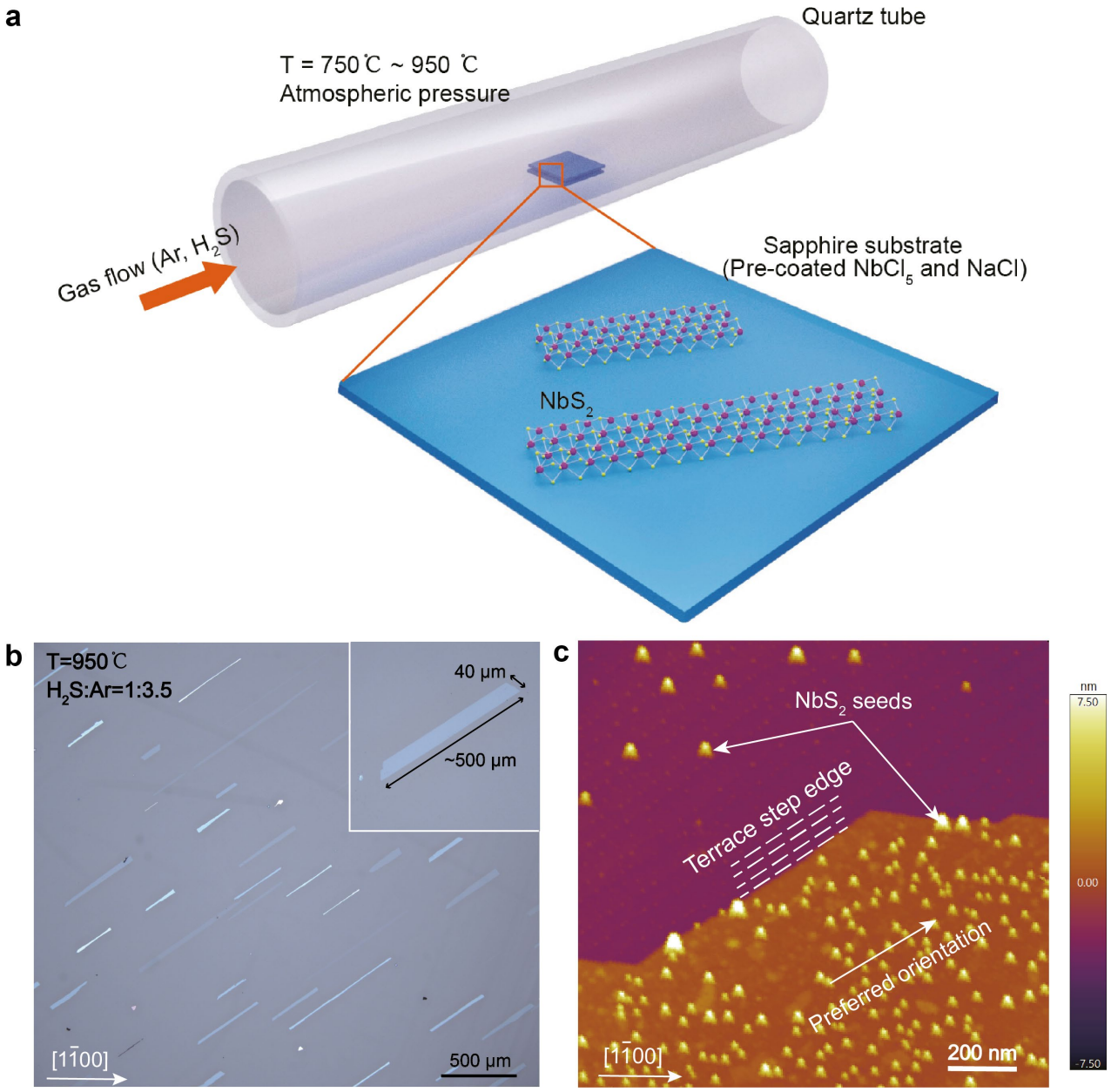

Figure 4-1**. CVD growth of NbS_2 crystals.**a) Schematic of a home-built hot-wall CVD system for NbS_2 growth. Inside the chamber, two sapphire substrates were sandwiched together with one of them spin-coated with $NbCl_5$ and NaCl precursors. b) Optical image of CVD-grown rectangular NbS_2 with its lateral size of around 500μm. c) AFM image of the sample from b), which shows the alignment of the edge of the growth sample to the terrace step edges of the sapphire substrate. Panels a-c) are reprinted with permission from ref [117], American Chemical Society.

4.2.2 Epitaxial growth of 2D NbS_2

From van der Waals interaction with the underlying sapphire substrate, our NbS_2 is grown epitaxially on sapphire substrate, meaning that we have achieved high-quality growth of NbS_2 absent of grain boundaries. We verify the single-crystal growth of our NbS_2 by conducting selected area electron diffraction (SAED) on the several consecutive holes of the TEM grid, which are covered by a grown NbS_2 flake. Five areas were examined, and each probed area is marked with numbers shown in **Figure 4-2(a). Figure 4-2(b-f)** shows the corresponding SAED patterns. All the SAED patterns show a single crystalline structure with the same lattice orientation, meaning that the lattice of all the TEM-probed areas is part of one single crystal lattice of NbS_2.

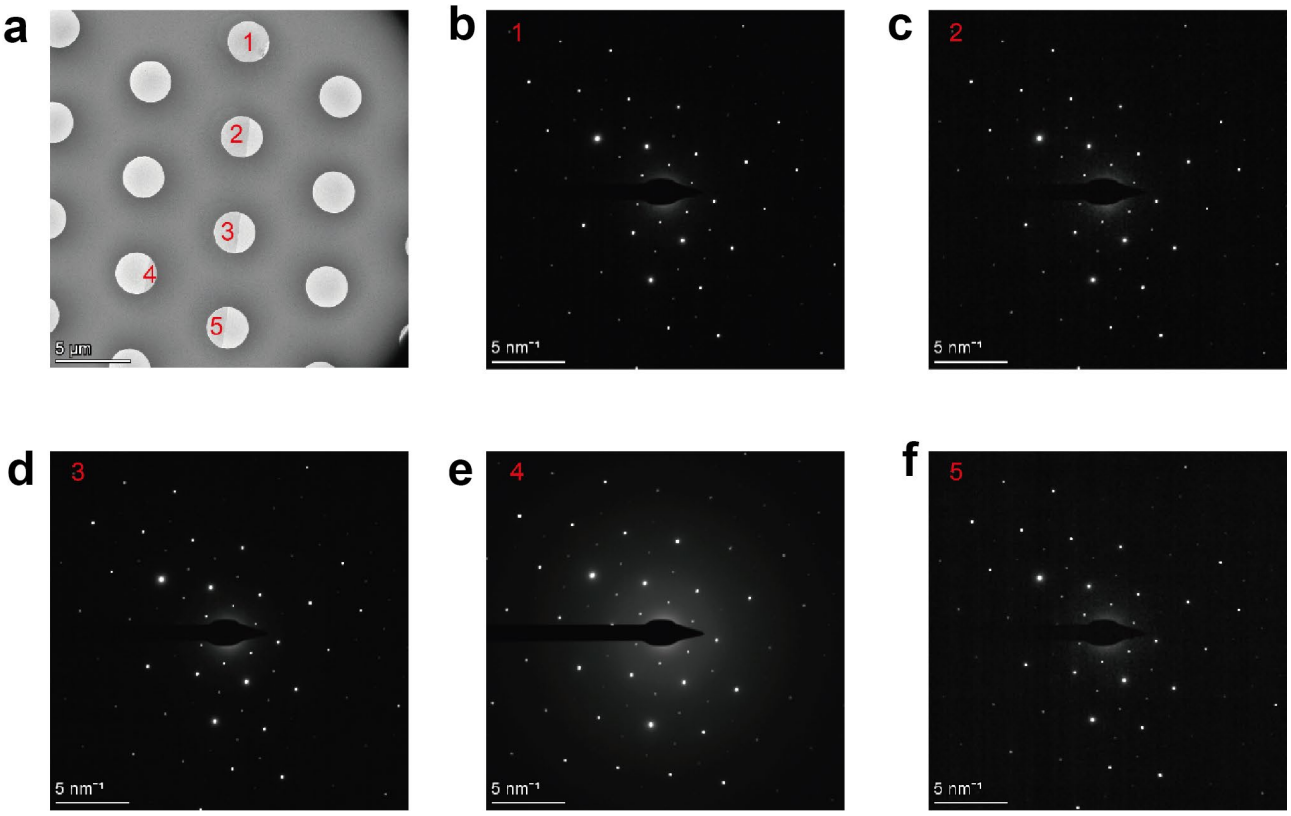

Figure 4-2. **Selected area electron diffraction of NbS_2**.a) Low-magnification TEM image of a transferred NbS_2 flake on a TEM grid. b-f) Selected area electron diffraction patterns conducted from 5 holes of TEM grid as shown in a). Panels a-f) are reprinted with permission from ref [46], American Chemical Society.

We found another supporting evidence of epitaxial growth from AFM. **Figure 4-3** displays AFM images of as-grown NbS_2 on a sapphire substrate. These images are taken from different areas of the single sapphire substrate. In **Figure 4-3(a)**, we observe that the edges of all the tiny seeds are epitaxially aligned to the same direction of the sapphire crystal axis $[1\bar{1}00]$. This implies that when the crystal grows larger, the domain formed from such seeds will merge into a single crystal without any grain boundaries, meaning that our large NbS_2 crystals should be absent of grain boundaries. AFM images from other parts of the substrate shown in **Figure 4-3(b-c)** indicate that the seeds from other areas are also aligned in the same direction. This suggests that our NbS_2 crystals are epitaxially grown on the entire sapphire substrate, and it implies the possibility of achieving large-area growth of NbS_2 with our CVD method.

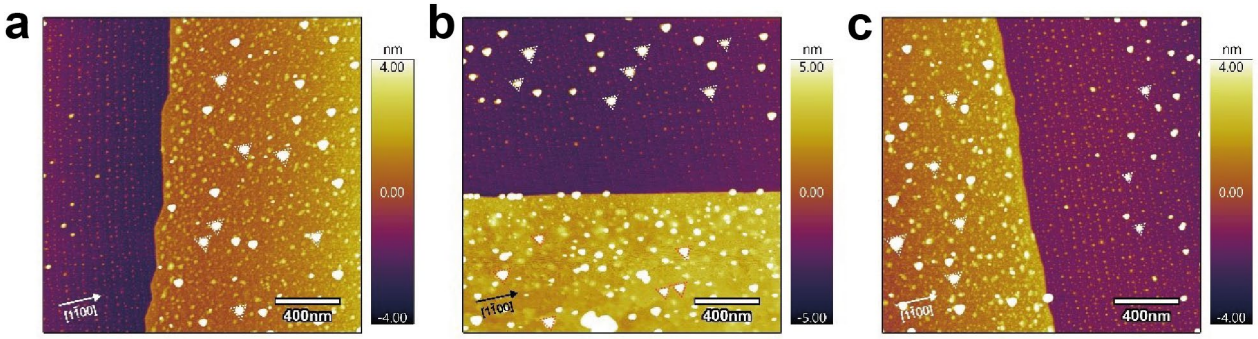

Figure 4-3. **AFM on as-grown NbS_2.** AFM images of as-grown NbS_2 flakes were taken sequentially from the different parts of a single sapphire substrate. Dotted lines indicate the edges of the small seeds, which are all aligned to the sapphire crystal axis [$1\bar{1}00$]. Panels a-c) are reprinted with permission from ref [117], American Chemical Society.

4.3 Thickness-dependent structrual phase transition

4.3.1 Controlled growth of NbS_2 with different thicknesses

Changing spin-coated $NbCl_5$ precursor concentration on the sapphire substrate allowed us to control the overall growth thickness of NbS_2 in the range of 1.5nm to 10nm. **Figure 4-4** shows the histograms of the thickness distribution of NbS_2 achieved from different precusor concentrations, where sample thickness was determined by AFM. While other growth parameters are being fixed, e.g. H_2S ratio, we see the general trend that higher NbS_2 precusor concentration yields a higher thickness sample. This is somewhat expected as a large Nb supplement would lead to a thicker NbS_2 crystal, if a sufficient sulfur level is provided for its stoichiometry.

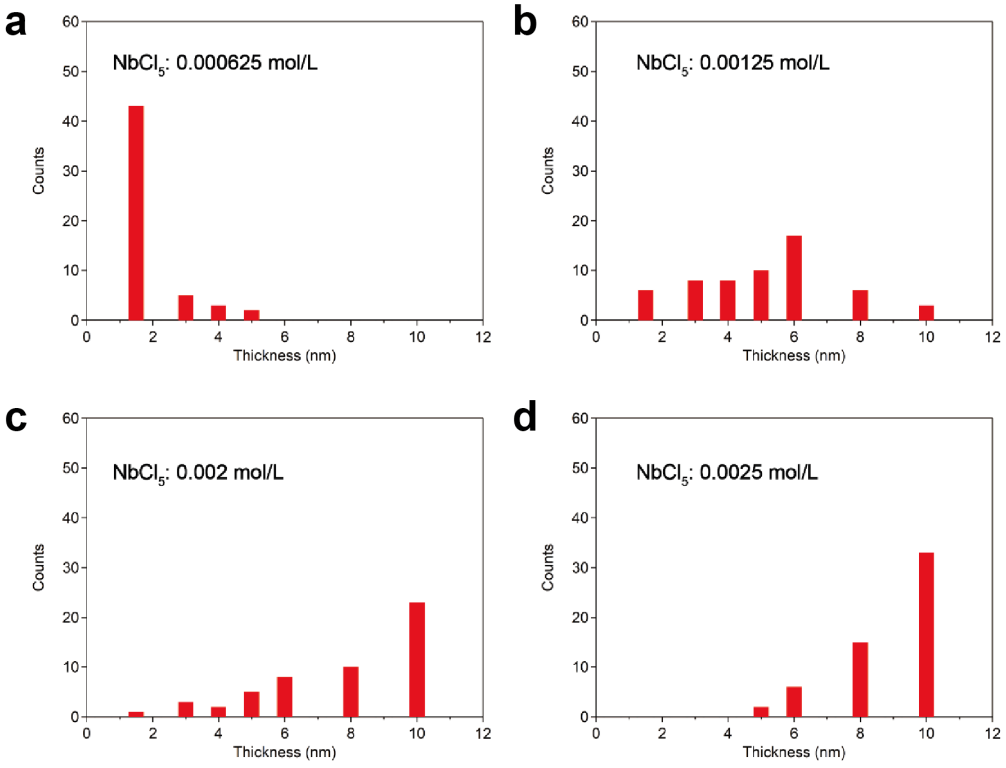

Figure 4-4. **Histogram of NbS_2 thickness at different $NbCl_5$ precursor concentrations.** Panels a-d) are reprinted with permission from ref [117], American Chemical Society.

4.3.2 TEM and Raman analysis : two polymorphs in CVD-grown NbS_2

Figure 4-5(a) shows two polymorphs of NbS_2 crystal: rhombohedral (left) and hexagonal (right), where each polytype unit cell consist of 3 and 2 layers of NbS_2, respectively. Thus, in short, they are called 3R and 2H. As constituting layers in each unit cell has distinct rotation (0deg or 180deg) and sliding with respect to one another, 3R and 2H polytype give unique atomic patterns if seen from the top surface. Interestingly, we observe this two polytypes in our CVD-grown NbS_2 at different thicknesses. The grown sample with thickness above 5nm showed 2H-polytype, wheras the thinner sample showed 3R-polytype.

From the indication that the crystal is grown epitaxially, we performed high-angle annular darkfield (HAADF) scanning transmission electron microscopy (STEM) on the grown samples to confirm and further characterize its crystallinity, e.g. structural phase. **Figure 4-5(b-d)** shows STEM images visualizing the atomic pattern of the top surfaces obtained from different thicknesses of NbS_2. To prepare the STEM sample, as grown NbS_2 was detached from the sapphire substrate and transferred onto TEM grid (transferred image is shown in the inset of **Figure 4-5(b**). As HAADF intensity is proportional to the square of atomic number ($\sim Z^2$), the position of Nb and S atoms can be distinguished by higher and lower intensity spots, respectively. In the STEM images, we marked their position as blue(Nb) and yellow(S) circles. In **Figure 4-5(b)**, six Nb atoms form a hexagonal ring with one S atom in the centor, corresponding to 3R polytype. In **Figure 4-5(c)**, three Nb atoms or three S atoms can be found around a single atom of the other, suggesting a 2H polytype. Interesting, a mixture of two polytypes is observed as shown in **Figure 4-5(d)** at the intermediate sample thickness between the thickness of 3R- and 2H-polytype samples.

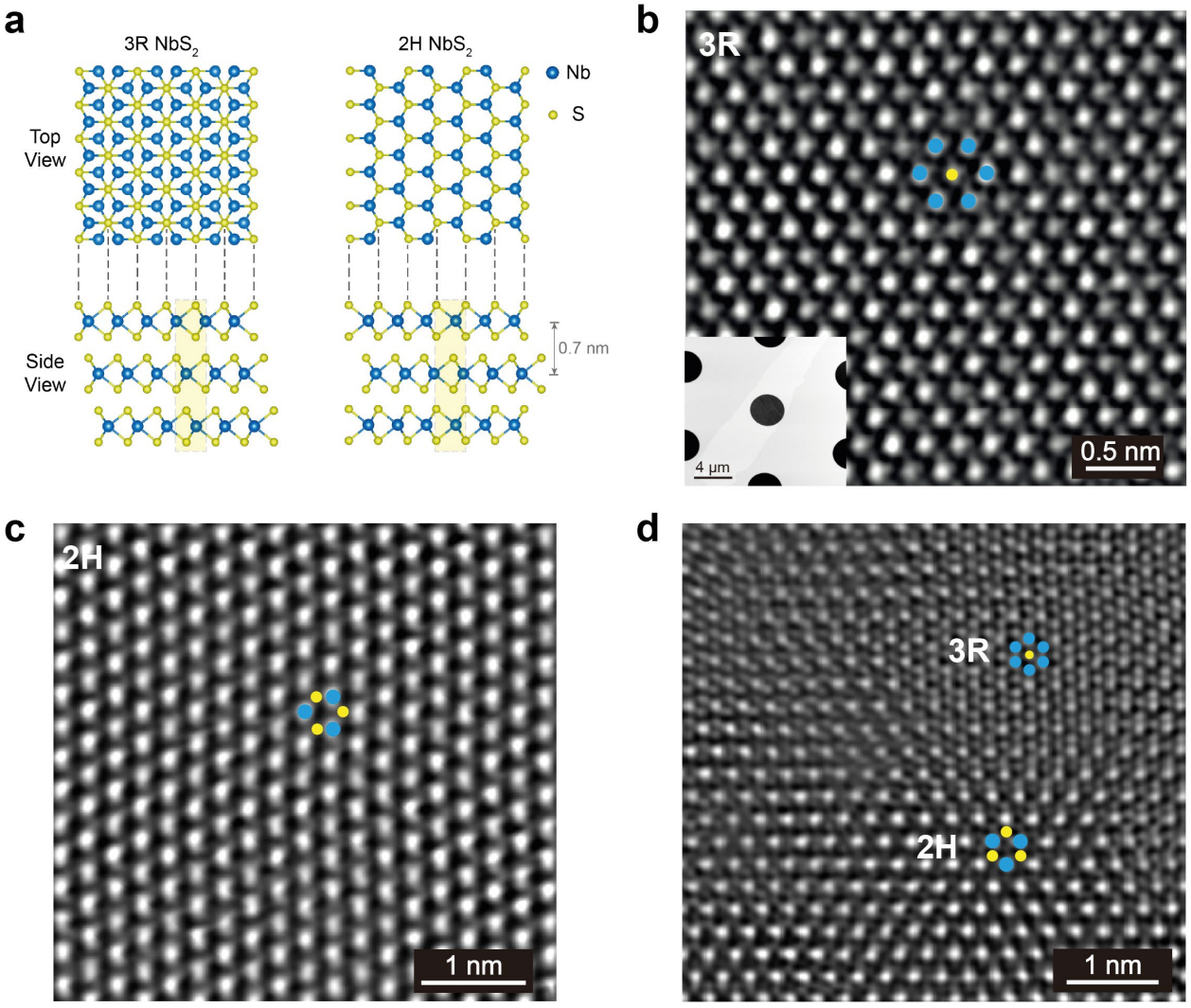

Figure 4-5. **Atomic crystal structure of NbS_2**. a) 3R and 2H polytype stacking of NbS_2. b-c) STEM images of NbS_2 with 3R b), 2H c), and the mixture of 2H and 3R polytype stacking d). Inset of b) is a low-magnification STEM image showing transferred

NbS_2 on a TEM grid. Nb and S atoms are marked with blue and yellow circles, respectively. Panels a-d) are reprinted with permission from ref [117], American Chemical Society.

Independently, Raman spectroscopy was also employed to examine the crystal structure of grown NbS_2 samples. **Figure 4-6** shows the room temperature Raman spectra of three different sample thicknesses(3nm, 4nm and 10nm) on a sapphire substrate using 532nm laser excitation (Power=1mW with 1μm spot size) with a grating of 3000g/mm. The blue curve represents the Raman spectra of the 3nm-thick sample showing the characteristic Raman modes, 348cm^{-1}(E_2) and 389cm^{-1}(A_1), which suggest the 3R polytype phase of NbS_2. The orange curve obtained from the 10nm-thick sample gives 340cm^{-1}(E_{2g}) and 379cm^{-1}(A_{1g}) modes. This is in agreement with the characteristic Raman modes of the 2H polytype phase. The purple Raman spectra measured from the intermediate thickness of 4nm shows a broad Raman mode around 384cm^{-1}, which can be decomposed into A_1 and A_{1g} from the two polytype phase, implying the possible coexistence of two phases at this thickness. Being the intermediate thickness, the structural phase transition from 3R to 2H polytype might start around this thickness.

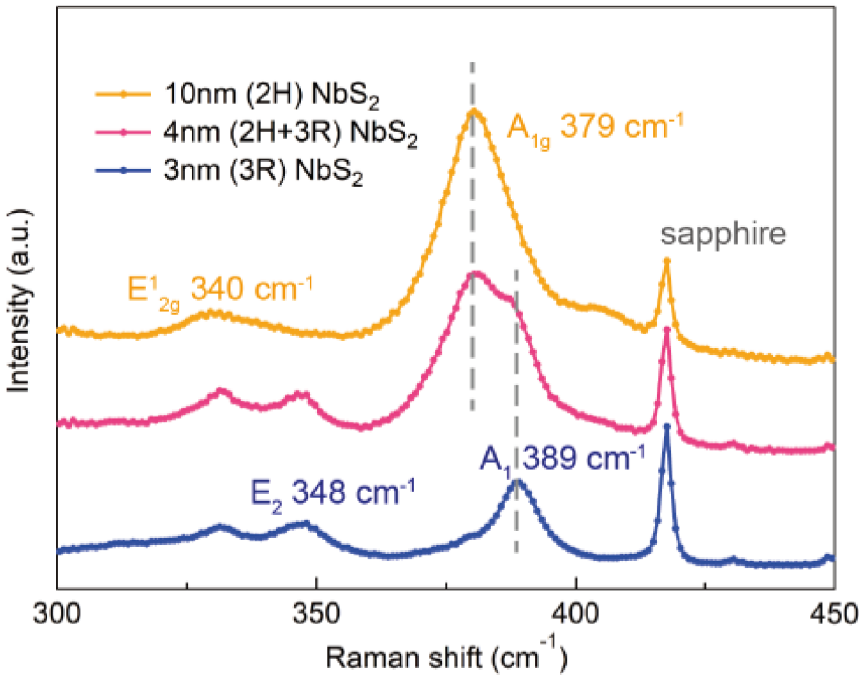

Figure 4-6. **Raman spectra of as-grown NbS_2 on sapphire substrate.** three NbS_2 samples of different thickness were measured: 3nm(blue), 4nm(purple), and 10nm(yellow). Measurements were done at room temperature. Panel is reprinted with permission from ref [117], American Chemical Society.

4.4 Device fabrication and electrical transport measurement

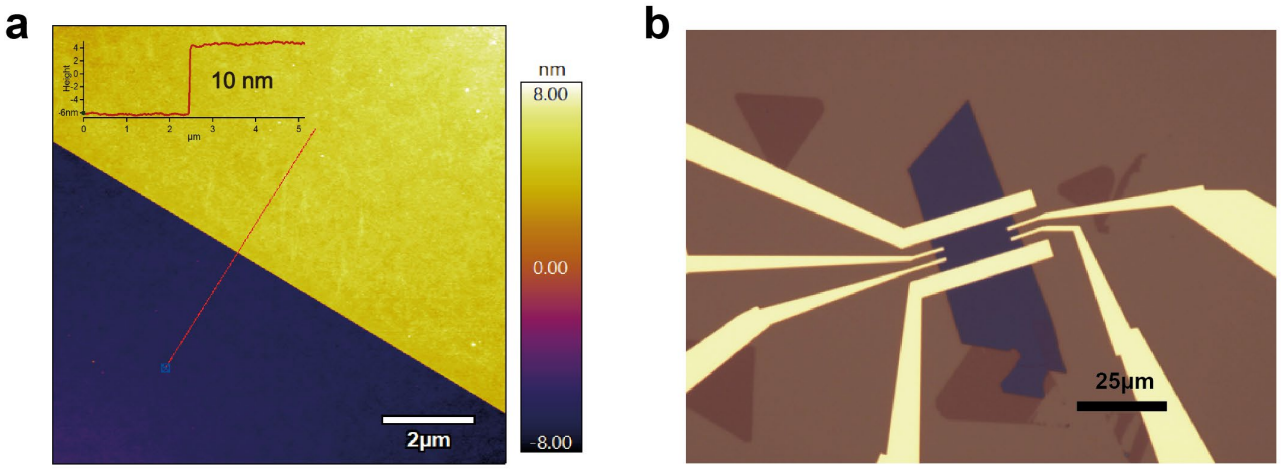

Figure 4-7. **Multi-terminal NbS_2 device.**2D AFM mapping. b) The optical micrograph of the 10nm-thick NbS_2 device for charge transport. Scale bar in b) is 25μm. Panels a-b) are reprinted with permission from ref [117], American Chemical Society.

We then moved on to characterize the electronic properties of different polytypes by performing charge transport measurements. To fabricate electronic device for such purpose, various thicknesses of flakes were selected, detached from insulating sapphire substrate, and transferred onto conductive SiO_2/Si substrate to be able to perform clean-room fabrication processes, e.g. e-beam lithography. **Figure 4-7** shows one representative device made of a 10nm-thick NbS_2. **Figure 4-7(a)** shows the AFM image of the transferred sample on SiO_2/Si, and **Figure 4-7(b)** shows the optical micrograph image of its multi-terminal Hall bar device fabricated with 2nm/80nm thick Ti/Au electrodes. Between the device fabrication steps (transfer, e-beam lithography and evaporation), samples were kept inside the glovebox to prevent the sample degradation from air.

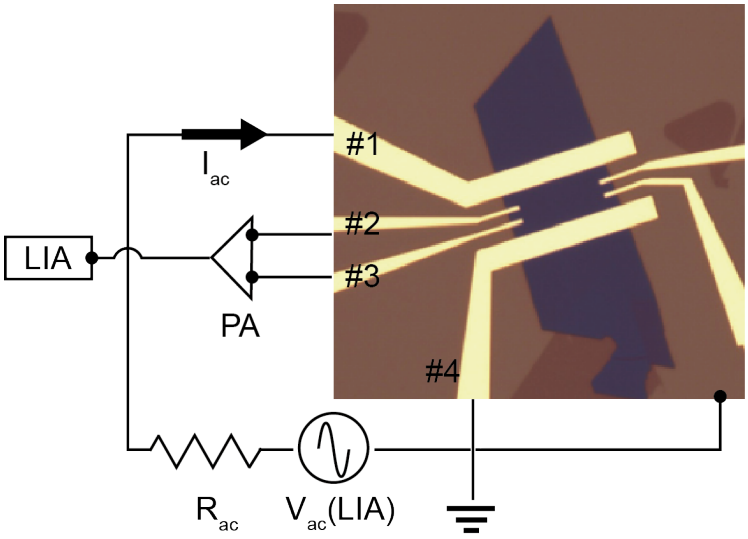

Figure 4-8. **Schematic of differential resistance measurement.** In four-point geometry, an ac current was sent through a NbS_2 sample on SiO_2/Si using contact #1 and #4. Sinusoidal voltage source (V_{pp}=0.2V with 13.3Hz, and V_{DC}=0V) provided by a lock-in amplifier (LIA) was connected to contact #1, with an external load of 1MΩ, while contact #4 and gate were grounded. The longitudinal voltage between contact #2 and contact #3 was first amplified by a low noise voltage preamplifier (PA) in differential mode and fed to the same lock-in amplifier. Unused contacts are floated during the measurement. The differential resistance was calculated based on the ratio of ac voltage to ac current.

We performed low-temperature charge transport measurements on samples with different thicknesses (3nm, 4nm and 10nm), which gave us complementary information with previous STEM and Raman spectroscopy results. As shown in **Figure 4-8**, we have used a lock-in amplifer (SR860) and a voltage preamplifier (SR560) to measure four-probe longitudinal resistance (R_{xx}). This is to increase the signal-to-noise ratio of resistance and minimize the effect of Joule heating. An ac probe current (I_{ac}=100nA at 13.3Hz) was sent through NbS_2 using contact #1, and its resistance was obtained as differential resistance (ratio of ac voltage, measured between #2 and #3, to the ac voltage). The resistance was measured continuously while the temperature was cooled down from 200K to the system base temperature of 1.4K at the rate of -0.3K/min. The temperature-dependent resistance with different thicknessess are presented in **Figure 4-9**.

4.5 Charge transport in 2H, 3R, and their mixed phase NbS_2

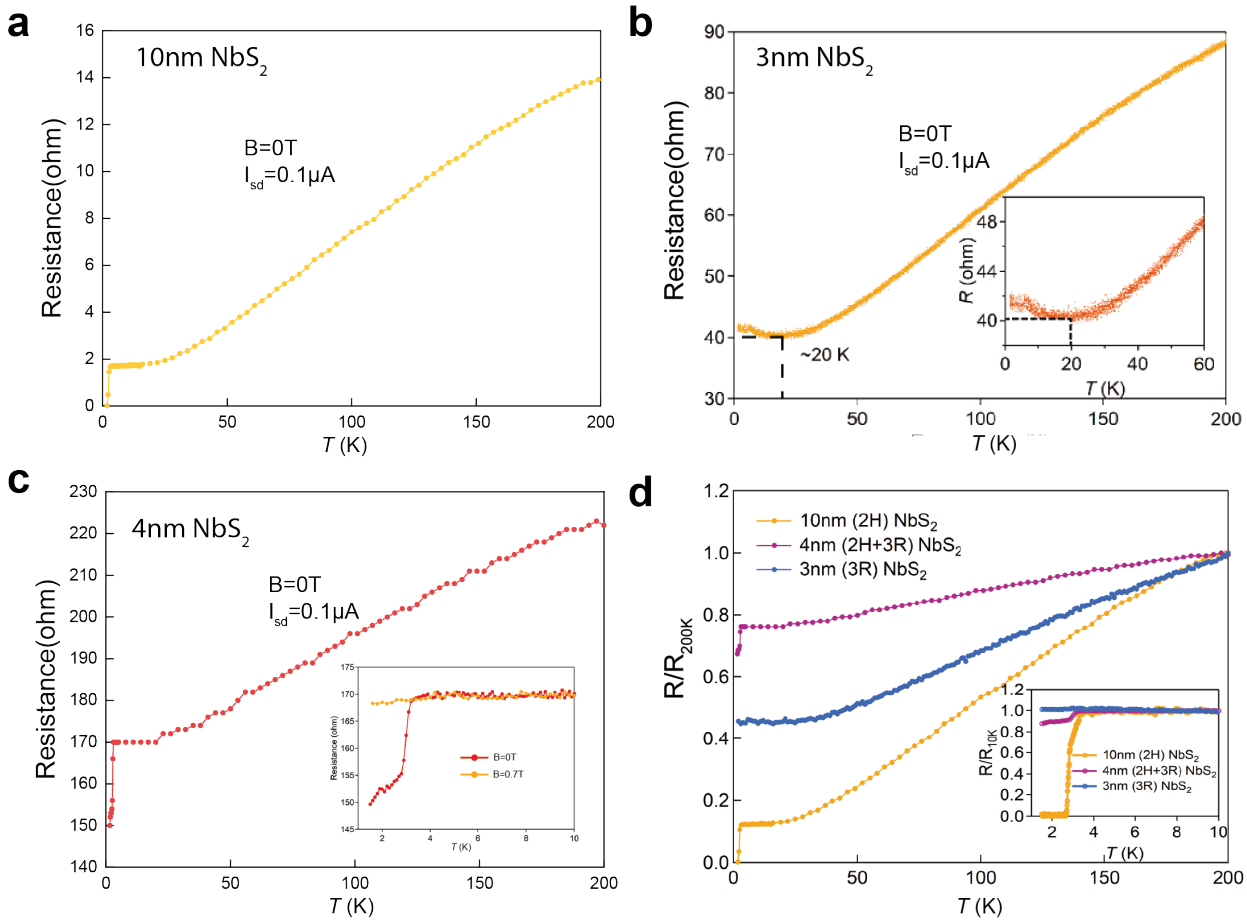

Figure 4-9. **Temperature-dependent resistance of different polytype NbS_2.** a-c) Four-probe longitudinal resistance (R_{xx}) of 10nm a), 3nm b), and 4nm c) of NbS_2 was measured while the temperature was cooled down from 200K to 1.4K without an external magnetic field. The superconducting transition occurs around 3K for 10nm-NbS_2 and 4nm-NbS_2, while resistance up-turn happens around 20K for 3nm-NbS_2. The inset of b) shows the magnified data from 4nm-NbS_2 in the temperature range from 60K to 1.4K. The inset of c) shows the resistance of 3nm-NbS_2 with and without the external magnetic fields at temperatures ranging from 10K to 1.4K. d) Normalized R_{xx} of 3nm(blue), 4nm(purple) and 10nm(yellow) NbS_2. R_{xx} was normalized to the resistance at 200K for each device. The 3nm, 4nm and 10nm-thick samples correspond to 3R, 2H, and mixed polytype, respectively, from the previous analysis of Raman spectra and TEM images. Inset shows the magnified data in the lower temperature range. Panels b), d) and the inset of panael c) are reprinted with permission from ref [117], American Chemical Society.

We see distinctly different low-temperature charge transport properties below 20K for different thickness samples. For the device with 10nm thickness shown in **Figure 4-9(a)**, the resistance drops sharply to zero around 3K, indicating metal to superconducting transition. We found the transition critical temperature T_c at 2.6K, the temperature at which $R(T_c)=0.5R_N$, with R_N being normal state metal resistance above the transition temperature. On the contrary, as shown in **Figure 4-9(b),** for

the device with 3nm thickness, we observe an upturn of resistance around 20K. A similar upturn of resistance was previously observed from other CVD-grown 3R-NbS_2. It has been attributed to electron scattering at defect or excess Nb sites[118,119] or to the possible CDW fluctuations in the presence of disorder[120,121]. Therefore, we can relate the metal-to-superconducting and metal-to-insulating transition of 2H-NbS_2 and 3R-NbS_2, respectively, to the 10nm and 3nm-thick NbS_2 samples, supporting the previous observations from STEM and Raman that there is a thickness-correlated structural phase transition in CVD-grown NbS_2.

Interestingly, as shown in **Figure 4-9(c)** for the device of intermediate 4nm thickness, its resistance drops sharply around 3K but remains at a relatively high resistance value of ~150Ω, and any other transition was not observed up to our system base temperature of 1.4K. With the application of an external out-of-plane magnetic field, this sharp transition at 3K gets suppressed, meaning that this transition can be the type of superconducting transition. This coexistence of metallic property (finite resistance) and superconducting property (zero resistance) at the base temperature can be understood again by considering the presence of mixed phases of 2H and 3R at this thickness.

Figure 4-9(d) compares the temperature-dependent R_{xx} from three different thicknesses (3nm,4nm and 10nm). Resistances were normalized with respect to their resistance at 200K for each device. The inset shows the magnified view of the normalized resistance value measured in the low-temperature range from 1.4K to 10K. Commonly from all the thicknesses of NbS_2 measured in the high-temperature range, we see that the resistance linearly decreases with decreasing temperature ($dR/dT>0$), indicating the property of metallicity. Notably, the 4nm-thick device shows slower resistance change than the other 10nm(2H-phase) and 3nm(3R-phase) devices. The relevant parameter for this feature is residual resistance ratio(RRR), which is defined as the ratio between resistance at T=300K and the normal state resistance at a lower temperature value, a standard indicator that reflects the crystal quality of metal or superconductor[122,123]. Considering the normal-state resistance at 10K, above the superconducting transition temperature of the 2H-phase, we define RRR of the 4nm-thick device to be ~1.5, which is lower than that of the 10nm-thick 2H device (11) and the 3nm-thick 3R device (3.3). Thus, we suspect this low RRR of the 4nm-thick device comes from the structural disorder, possibly due to the sulfur point and line defects between two domains of different structures, as seen from STEM image in **Figure 4-5(d)**.

4.6 Superconductivity in 2H-NbS_2

To further study the superconducting property of 2H-NbS_2, we measured magneto-transport with out-of-plane external magnetic fields. **Figure 4-10(a)** shows the superconducting transition of 6nm-thick NbS_2 with a perpendicular magnetic field (B) applied normal to its 2D crystal plane. As the amplitude of the field increases, the transition becomes gradual and moves to lower temperature values with the magnetic field, and eventually vanishes above 0.6T. In the presence of an external magnetic field, we redefine the critical transition temperature T_c as the temperature when the resistance becomes 80% of the normal state resistance.

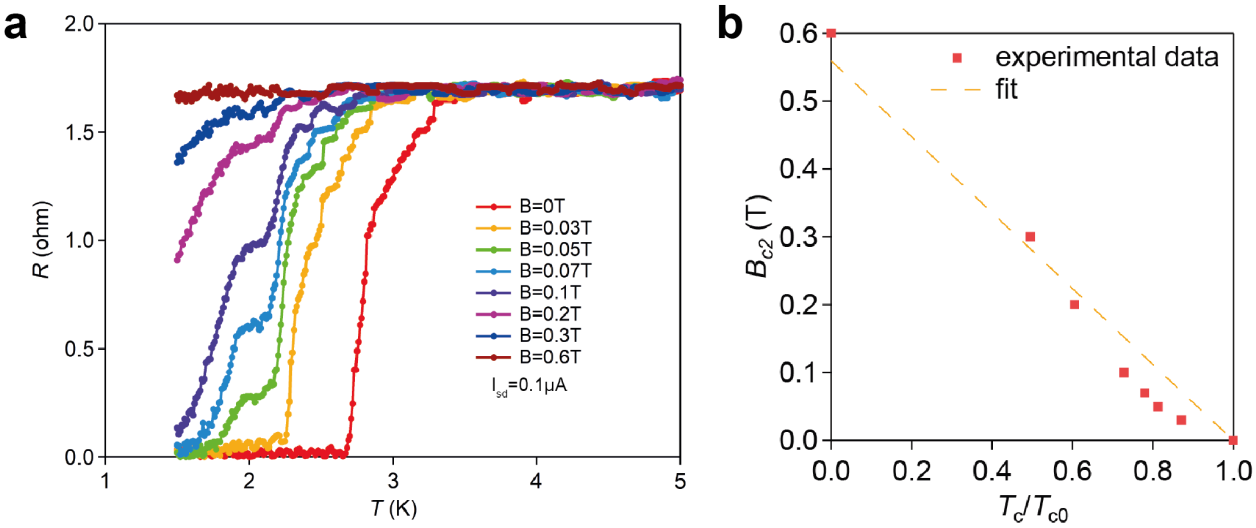

Figure 4-10. **Superconductivity in 2H phase NbS_2**.a) Field-cooled longitudinal resistance at different perpendicular magnetic field strengths. b) B_{c2} vs T_c/T_0 phase diagram extracted from the data of figure a) with its linear fit. Panels a-b) are reprinted with permission from ref [117], American Chemical Society.

Figure 4-10(b) shows the corresponding B_{c2} vs T_c/T_0 phase diagram with the reduced temperature where B_{c2} is upper critical out-of-plane magnetic field strength, and T_c is redefined critical transition temperature. Here T_0 is the critical transition temperature at zero magnetic fields. We find a linear relation between B_{c2} and T_c, which is typically observed in a 2D superconductor from perpendicular magnetic field configuration. This relation can be fitted with a formula based on linearized Ginzburg-Landau (GL) theory,

$$B_{c2}(T) = \frac{\phi_0}{2\pi\xi_{GL}(0)^2}\left(1 - \frac{T_c}{T_0}\right) \tag{9}$$

where $\xi_{GL}(0)$ is zero temperature coherence length, and ϕ_0 is magnetic flux quantum. From the fitted result, we get the coherence length of 25nm. This value is larger than the sample thickness (10nm), consistent with the 2D superconductivity behaviour. This indicates that the superconducting transition should follow the BKT type phase transition.

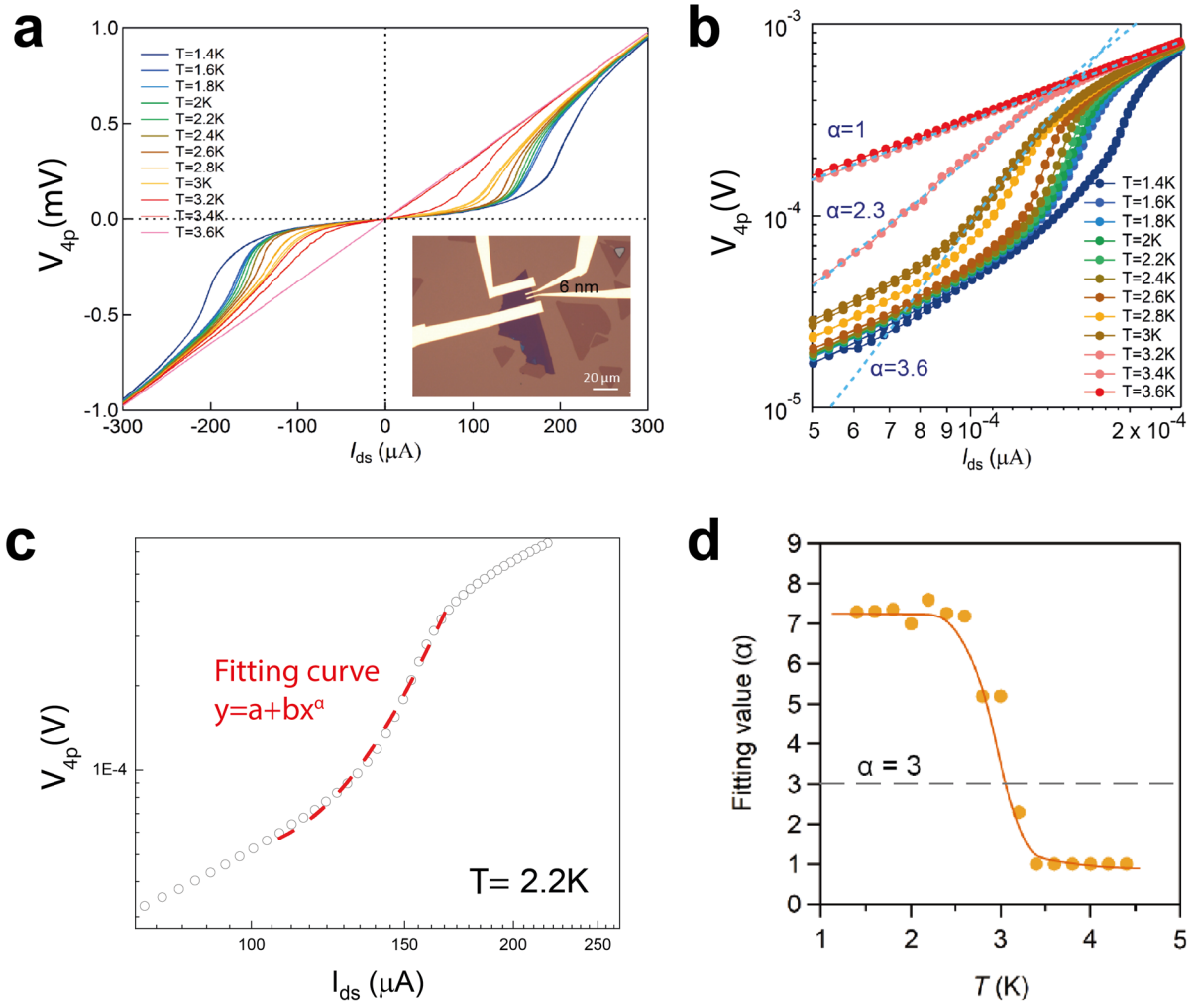

Figure 4-11. **BKT type superconducting transition in 2H-NbS_2**.a) 4-terminal V-I characterization of 6nm-thick NbS_2 measured from base temperature 1.4K to 3.6K. Inset is the optical image of the device. b) V-I curve in figure a) replotted in logarithmic scale showing $V \propto I^{\alpha}$ behaviour. The blue dashed lines with different α are from $V = bI^{\alpha}$ with arbitrary b values, fitted to the non-linear transition regions at 3.4K, 3.2K and 3K. c) An example of fitting procedure to extract parameter α. The non-linear V-I region at 2.2K is fitted with $V = a + bI^{\alpha}$. Here, a and b are offset and a proportional coefficient, respectively. d) Parameter α as a function of temperature. The red curved line in the figure is drawn to guide the eye, and the horizontal dashed grey line refers to $\alpha = 3$. Panels a, b and d are reprinted with permission from ref [117], American Chemical Society.

The BKT transition describes many unconventional 2D phase transitions including the 2D superconductivity, which involves the transition from unpaired vortices and antivortices to bound vortex-antivortex pairs below the critical temperature called T_{BKT}. The direct experimental evidence of this kind of transition can be addressed if there is a jump in the power-law exponent (α in V- I^{α}) near the supercurrent of voltage-current(V-I) characteristic from α=1 to α=3 at T=T_{BKT} as the temperature is reduced. We observe the signature of BKT type superconducting phase transition from 6nm-thick 2H NbS_2 as shown in **Figure 4-11(a)**. The inset of **Figure 4-11(a)** shows the optical image of the 4 terminal device, where DC voltage from the inner two probes was measured while varying DC current from the outer two electrodes. At 3.6K, we observe the ohmic metallic transport from the constant V-I slope. This slope gradually becomes more nonlinear as temperature decreases, and the supercurrent gap, at which the probed voltage decreases toward zero, also gradually expands. The V-I curves replotted in logarithmic scale, shown in **Figure 4-11(b)**, show this transition more clearly from linear V-I to nonlinear V- I^{α}, displaying the BKT type transition. **Figure 4-11(d)** shows the parameter α as a function of temperature from the curve fitting to the non-linear V-I region as described in **Figure 4-11(c)**. Following the standard of α=3 for determining BKT transition temperature (T_{BKT}), We estimate the temperature to be around 3K for 6nm-thick 2H NbS_2.

4.7 Discussion

4.7.1 Possible origin of structural transition

From independent analyses of STEM, Raman spectroscopy and low-temperature transport measurement, we found that NbS_2 undergoes structural phase transition as growth thickness increases. Although the detailed mechanism of the transition cannot be fully understood at this stage, we propose some possible explanations which could give some perspectives in future studies. If we consider that the phase transition from 3R to 2H comes from the thickness-dependent band structure effect of 3R NbS_2, we expect this transition to be also present in other reported 3R NbS_2 growth. However, several reports which have grown 3R-NbS_2 around the same thickness range do not show any sign of structural phase transition[118,119]. Therefore, we speculate that the thickness-dependent band structure effect is less likely to explain the phase transition we observe in our grown samples.

As we control the thickness of NbS_2 by the growth parameter (e.g., $NbCl_5$ concentration), we speculate the relation of growth condition to the phase transition. Firstly, the phase transition can be related to the localized partial pressure of the Nb and S precursor. Since the concentration of spin-coated $NbCl_5$ controls the growth thickness, it can be possible that various ratios of Nb and S coming from different $NbCl_5$ concentrations lead to different phase structures. In this case, the ratio of Nb and S is more relevant to the transition. Although it's difficult to extract the precise value, the ratio for growing 4-nm NbS_2 could be the critical condition for phase transition.

Similarly, a phase transition between bulk 3R- and 2H-NbS_2 was demonstrated depending on the pressure of excess sulfur during the growth[124]. Secondly, the phase transition could have a thermodynamic origin, considering the interaction between the sapphire substrate and NbS_2 crystals. Due to a large lattice mismatch (30.4%), strong interaction exists between NbS_2 and sapphire. As the thickness increases, the interfacial effect from bottom sapphire becomes weaker to preserve the 3R phase of NbS_2, and it could be that 4 nm is the critical thickness at which the total free energy of the 2H-phase becomes lower than that of the 3R-phase.

4.7.2 Large area bottom-up growth of NbS_2

The added value to the previous work related to NbS2 bottom-up synthesis is the large-area fabrication of NbS_2 achieved by our CVD method. We summarized below the essential information of all the other CVD-grown 2D NbS2 from the literature. Comparing the crystal size, our grown-NbS_2 is the largest up-to-date, with the lateral size exceeding 500um. Since the growth of sulfides, selenides and tellurides shares the same basic principle of growth mechanism[125], we believe our work can also provide prospects to improve the current CVD growth recipes for epitaxial growth of other Nb-based dichalcogenides as well.

Reference	Crystal shape	Crystal lateral size	Epitaxial	Phase	Electrical behaviour
W. Ge *et al.*, *Nanoscale*, 2013, **5**, 5773–5778	Triangle	2 um	No	3R	/
S. Zhao *et al.*, *2D Mater.*, 2016, **3**, 025027	Hexagon	2 um	No	3R	Metal
X. Wang *et al.*, *Nanoscale*, 2017, **9**, 16607	Hexagon	5 um	No	3R	Metal
A. Kozhakhmetov *et al.*, *Journal of Crystal Growth*, 2018, **486**, 137–141	Triangle	1 um	No	3R	Metal
Q. Lv *et al.*, *Front. Mater.*, 2019, **6**, 279	Triangle	15 um	No	3R	Metal
R.M. Stan *et al.*, *Physical Review Materials*, 2019, **3**, 044003	Hexagon	< 1 um	Yes	1H	/
Our work	Rectangle	> 500 um	Yes	3R & 2H	Metal & superconductor

Figure 4-12. **Comparison of CVD grown NbS_2 from other literature.**

4.8 Conclusion

We have demonstrated CVD synthesis of large-area and high-quality 2D NbS_2. Using sapphire as a growth substrate, NbS_2 was grown with epitaxial orientation along the crystallographic direction of the underlying sapphire. The growth thickness can be controlled in the range of 1.5nm to 10nm by changing the Nb precursor concentration. Interestingly, we observe thickness-dependent structural phase transition from 3R-polytype to 2H-polytype as thickness increases. One possible reason for such phase transition, we suspect, can be due to the interfacial effect of the sapphire substrate during the growth, but this remains the topic of further studies. Our findings were supported by Raman spectroscopy, transmission electron microscopy, and low-temperature charge transport measurement.

From the low-temperature charge transport measurements, only 2H-polytype showed the superconducting transition around T=2.6K while 3R-polytype maintained its metallicity down to the base temperature of the measurement system (T=1.3K). The temperature-dependent I-V characteristics of 2H-polytype shows a transition from linear to nonlinear one, V-$I^{\alpha}(\alpha > 1)$, below the critical temperature of T=3K, which signifies the BKT transition of a 2D superconductor.

In short, we have demonstrated the practical synthesis method for phase-controllable growth of 2D TMDC superconductors, which can benefit future studies in mesoscopic devices, and the large-area applications of 2D superconductors.

Chapter 5 Defect-induced magnetic properties of ultrathin $PtSe_2$

This chapter presents a work of discovering unexpected magnetism in ultra-thin semiconducting platinum diselenide ($PtSe_2$). We observed the magnetic properties of monolayer and bilayer $PtSe_2$ from low-temperature magneto-transport measurements using graphene as a probing material. The appearance of magnetic ground states is theoretically explained from the first-principle density functional theory calculation, which suggests that magnetism is induced from an intrinsic atomic defect, Pt vacancy.

These findings were achieved by close collaborations with Prof. Ahmet Avsar, who worked together with me on the transport measurement and device fabrication, Dr. Michele Pizzochero, who performed the first-principle calculation on the magnetic properties of atomic defects, and Dr. Mukesh K. Tripathi, who provided the atomic images of ultra-thin $PtSe_2$ through TEM. This work has been published: *Avsar, A., Cheon, C. Y., Pizzochero, M., Tripathi, M., Ciarrocchi, A., Yazyev, O. V., & Kis, A. (2020). Probing magnetism in atomically thin semiconducting $PtSe_2$. Nature communications, 11(1), 1-7.*

5.1 Introduction

5.1.1 Two-dimensional magnetism

In 2007, Albert Fert and Peter Grünberg won the Nobel Prize in physics for the discovery of giant magnetoresistance(GMR)[126,127]. In the structure of the alternating Fe and Cr magnetic thin films, they observed a giant (several tenths percentages) change of resistance with the magnetic field when the out-of-plane current flowed through the heterostructure. This variability of magnetoresistance found in heterostructure was much larger than the other types of magnetoresistance, such as anisotropic magnetoresistance (few percentages or lower) in single magnetic materials[128]. This finding, combined with spin-valve structure[129], quickly transformed into the technical realization of an ultra-sensitive magnetic sensor, thereby boosting the data storage capacity of hardware disks in modern times[130].

The key contributor to observing such physical phenomena was molecular beam epitaxy(MBE), a material deposition technique introduced in the late 1960s. This technique enabled the production of high-quality thin films with the capability of precise thickness control by selecting the number of layers being deposited. This method contributed to the study of the transition of material properties from bulk to low dimension and made it especially possible to explore magnetism in a 2D system by successful fabrication of ultrathin magnetic films[131]. Considering interaction among magnetic moments, magnetic phase transition can always occur at any finite temperature for a 3D system. In contrast, the long-range ordering can appear only at T=0K for a 1D system[132], so it is impossible to occur for a 1D system. However, in a 2D system, the transition becomes complex yet particularly interesting in that magnetism can be present or absent depending on the type of spin-spin interaction in the system.

Mermin, Wagner and Hohenberg gave the early theoretical explanation of a 2D magnetic system. Their explanation, the so-called Mermin-Wagner-Hohenberg(MWH) theorem[133,134], states that in a 2D lattice, thermal fluctuation would destroy the long-range magnetic ordering above any finite temperature for isotropic systems where spin can arbitrarily align in any direction within 2D (XY model) or 3D (isotropic Heisenberg model). However, from Onsager, magnetic phase transition

can possibly occur at finite temperature for the case of a 2D Ising system in which spins are constrained to be pointed in one direction[135]. These arguments can be summarized in the following Hamiltonian considering the interaction between the nearest neighbours i and j,

$$H = -J_{xy} \sum_{i,j} (S_i^x \cdot S_j^x + S_i^y \cdot S_j^y) - J_z \sum_{i,j} S_i^z \cdot S_j^z \tag{10}$$

where J_{xy} and J_z corresponds to exchange integral within the xy-plane and along the z-axis, respectively; S_i^a(a = x, y, z) corresponds to the spin-component along a-direction at the site i. The condition of $J_{xy} = J_z, J_z = 0, J_{xy} = 0$ can be associated with the Heisenberg model, XY model and Ising model, respectively.

In the real world, the experimental situation is not the same as the ideal assumption set by the MWH theorem. As material gets thinner, the local structural disorder becomes more prominent, and the property of a material is more prone to be influenced by the substrate on which the material lies. Both substrate and local disorder (e.g. defects and strain), in fact, can impose magnetic anisotropy on the system[97,136–138], and this anisotropy is not considered in the original Hamiltonian of the MWH model. Moreover, anisotropy induced from macroscopic dipole-dipole interaction, such as shape anisotropy, is also neglected. Consequently, contrary to the theorem, what has been generally observed in magnetic thin films is that spins tend to be preferentially aligned either along out-of-plane direction[139] or in the 2D plane with magnetic easy axis[140].

5.1.2 2D magnetism in vdW materials

In 2017, ferromagnetism was discovered in the monolayer of insulating van der Waals(vdW) material, 0.7nm-thick chromium iodide (CrI_3)[141,142]. This discovery attracted a great deal of attention as it showed the potential of vdW materials as a new system for exploring 2D magnetism[143]. Although the ferromagnetic property of bulk CrI_3 was already known for a long time, identifying its 2D magnetism in the atomically thin limit had been difficult. It has been resolved after the experimental sensitivity of the magnetic characterization techniques, such as MOKE, was improved enough to detect its small magnetic response. One of the most peculiar magnetic properties found in CrI_3 is the layer-dependent exchange interaction, which favors alternative magnetic ground states, out-of-plane ferromagnetic and antiferromagnetic orderings, depending on the number of layers (**Figure 5-1(a)**).

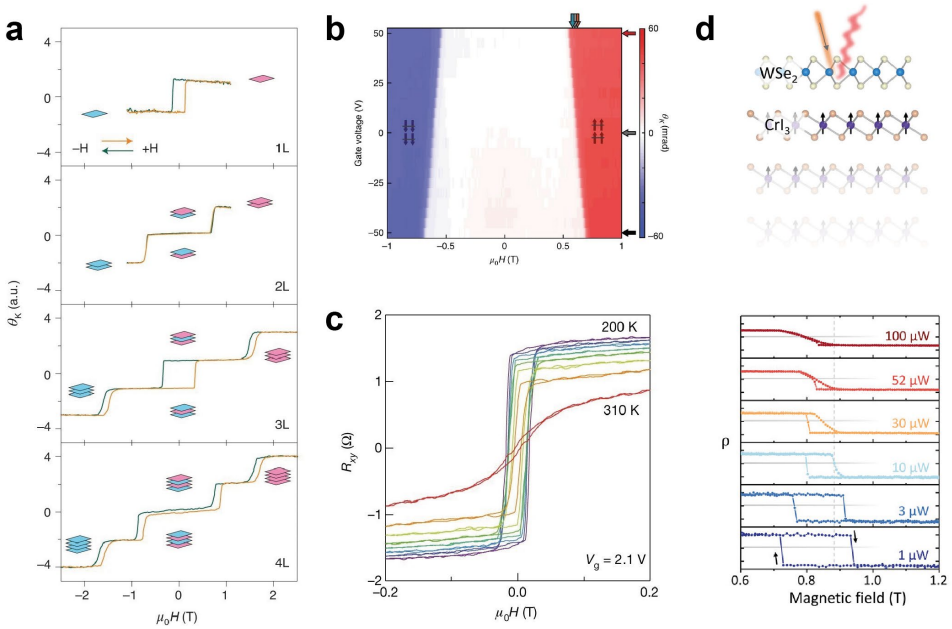

Figure 5-1. **2D magnetism in vdW materials and its tunability**.a) 2D magnetism in CrI_3 with alternating magnetic ground state, probed by polar MOKE. b) Intensity of polar MOKE in bilayer CrI_3 versus magnetic field and applied gate voltage. The critical switching field from AFM to FM states changes continuously with the gate voltage. c)Anomalous Hall voltage measured in ionic-gated Fe_3GeTe_2 where Hall resistance (R_{xy}) preserves up to room temperature. d) Magnetic proximity effect in

WSe_2/CrI_3 heterostructure. Valley polarization versus magnetic field (in bottom panel) can further be tuned by applied laser power. Panels are adapted with permission. Panel a) is from ref[143], Springer Nature Ltd. Panel b) is from ref[144], Springer Nature Ltd. Panel c) is from ref[145], Springer Nature Ltd. Panel d) is from ref[146], American Chemical Society.

Many more magnetic vdW materials were later identified and demonstrated the similar feature of layer dependence with complex yet exotic ground state spin configuration[147]. With strong in-plane covalent bonding, vdW materials can be exfoliated layer by layer, and their thickness can be precisely controlled due to the weak vdW nature of the force acting between the adjacent layers. In contrast to magnetic thin films, thin flake from layered vdW materials couples weakly to the substrate. These advantages have placed vdW material in front of other systems as a promising material platform to study dimensional crossover in magnetism from 3D to 2D and explore magnetism in two-dimensional limits[148].

As for applications, magnetic vdW materials have enabled new functionalities in already existing electronic devices. Due to its large surface-area-to-volume ratio, the material properties are sensitive to external stimuli like doping and strain. This made it possible to build the electronic device capable of controlling magnetic states electrostatically (**Figure 5-2(b)**)[149] and the Curie temperature of tri-layer metallic ferromagnet Fe_3GeTe_2 by ionic liquid gating(**Figure 5-2(c)**)[145], higher than its bulk value(~200K). Alternatively, the atomically smooth surface of a cleaved vdW magnet can serve as a substrate for magnetic coupling to the vdW films or deposited materials. This can be seen in the heterostructure of multilayer CrI_3 with monolayer WSe_2, where the valley polarized photoluminescence from WSe_2 becomes strongly tunable with external magnetic field and laser power(**Figure 5-2(d)**)[146].

5.1.3 Disorder-induced magnetism in vdW materials

In the pursuit of finding 2D magnetism in a new vdW material, most of the experimental attempts have been focused on exfoliating a thin layer from the bulk materials which are already known to be magnetic. In parallel to this effort, there has been an alternative approach, that induces magnetism in an otherwise non-magnetic material. The most studied material with this aim is graphene. Not only because it is the first-ever vdW material to be exfoliated[28], but it is also the thinnest material of all vdW materials, which can be taken as a true 2D system. In both theoretical and experimental studies, foreign adatoms and intrinsic structural disorders such as point defects or line defects can give rise to induced magnetism in graphene[150–154]. The same strategies of inducing magnetism also worked with transition metal dichalcogenides(TMDC)[23,76,155].

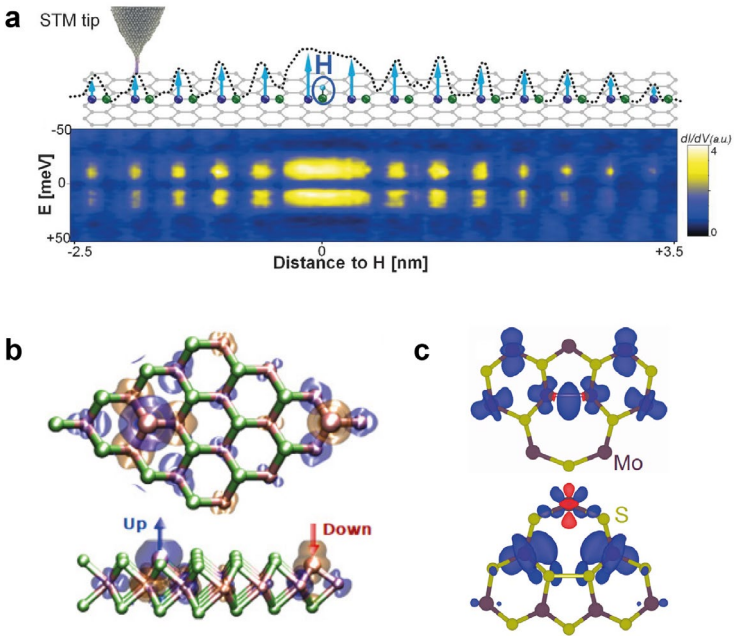

Figure 5-2. **Inducing magnetism in 2D vdW materials**.Magnetic moment in graphene induced by singe hydrogen adatom. The top panel shows the magnetic moments localized at carbon sublattices and its long-range spin texture around the adatom. The bottom panel shows the corresponding line profile of differential conductance spectra characterized by ~20mV energy

splitting in the energy-resolved local density of state due to magnetic moment. b-c) Magnetic moment induced by structural imperfections. b) Substitutional Mo atom at Te sites (Mo_{sub}) in 2H-$MoTe_2$ induces a magnetic moment that couples antiferromagnetically with the moment of the nearest Mo atom.c) Ground state magnetization in Mo-rich and S-rich grain boundaries of MoS_2. Blue and red colors denote the positive and negative magnetization direction. Panels are adapted with permission. Panel a) is from ref[150], AAAS. Panel b) is from ref[23], AAAS. Panel c) is from ref[155], American Chemical Society.

Recently, defect-induced magnetism has been experimentally observed in metallic TMDCs, platinum diselenide ($PtSe_2$)[22]. It was discovered that the surface Pt vacancy creates localized magnetic moments, and their long-range ordering in $PtSe_2$ was indirectly confirmed by magneto-transport measurement at LHe temperature. As the charge scattering is dependent on the alignment of magnetic moments, the particular shape of magnetoresistance(MR) found in $PtSe_2$ and the presence/absence of MR hysteresis could explain its magnetic ground state. Ferromagnetic (**Figure 5-3(a)**) and antiferromagnetic MR responses (**Figure 5-3(b)**) were observed at the different layer thicknesses of multilayer $PtSe_2$ from 4nm to 13nm. Interestingly, $PtSe_2$ loses its magnetism above 13nm.

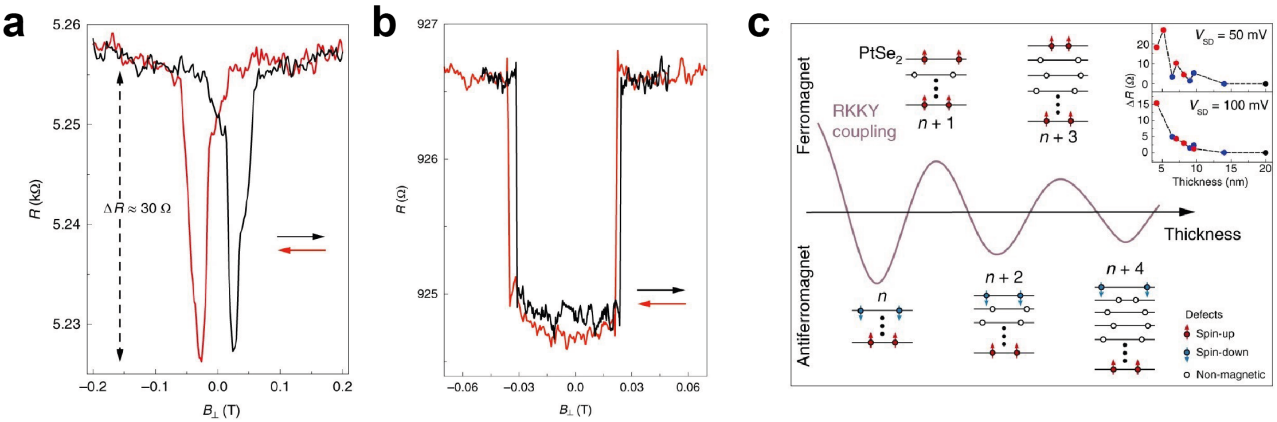

Figure 5-3. **Magnetism in multilayer vdW $PtSe_2$**.a-b) Resistance of 2-terminal $PtSe_2$ device shows ferromagnetic a) and antiferromagnetic b) response under magnetic field. c) Layer-dependent alternating magnetic ground states due to RKKY coupling between surface magnetic moments. Panels are adapted with permission. Panel a-c) are from ref[22], Springer Nature Ltd.

This system is particularly interesting because defect-induced magnetism shows layer-dependent alternative ground states, as **Figure 5-3(c)** shows. This property is similar to layer-dependent ground states observed by intrinsic 2D magnetism in CrI_3. However, the magnetic property of $PtSe_2$ disappears at the thickness of 13nm, whereas CrI_3 does not. Furthermore, alternating magnetic ground states are observed at different thicknesses. This hints at the origin of magnetic interaction in $PtSe_2$, which can be explained by Ruderman–Kittel–Kasuya–Yosida (RKKY) exchange coupling. This interaction is based on the indirect exchange interaction of magnetic ions mediated by conduction electrons. In the case of $PtSe_2$, magnetic ions induced from Pt vacancies are located at the two surfaces of $PtSe_2$, the top and bottom surfaces. The strength of RKKY interaction depends on the distance, and the experimental data of $PtSe_2$ from magneto-transport suggested that the critical thickness when the coupling vanishes is, therefore, around 13nm.

However, the previous study failed to explore the magnetism of $PtSe_2$ in the thin limit. The main reason was the poor charge conductance found in monolayer and bilayer thickness, which is more semiconducting than metallic. Unlike multilayer metallic samples, this low conductance contributed to large background current noise when performing the magneto-transport measurement, obscuring the MR signature of possible magnetism in the thin layers.

In this chapter, in an attempt to resolve magnetic properties up to the thinnest limit, we explain how we overcome this low conductance issue of thin $PtSe_2$ in transport measurement with graphene electrodes. We show our experimental observation of the antiferromagnetic(ferromagnetic) ground states in monolayer(bilayer) $PtSe_2$. This finding is further supported by the first-principle DFT calculation explaining the magnetic properties of atomic defects in ultrathin layers and by the visualization of such defects in $PtSe_2$ crystals using high-resolution TEM.

5.2 Sample fabrication

5.2.1 Identifying atomically thin $PtSe_2$

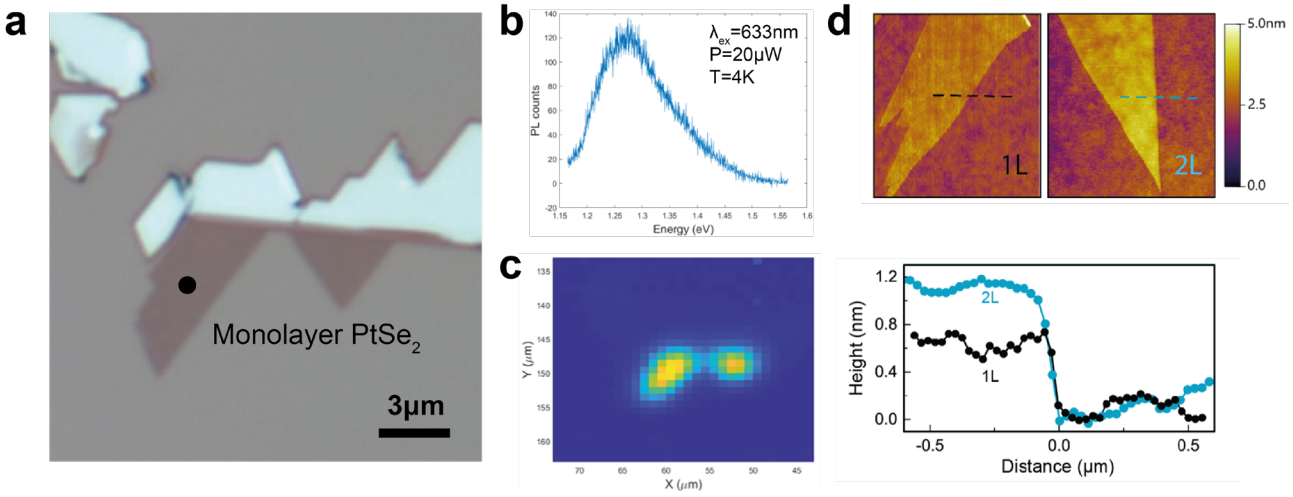

Figure 5-4. **Identifying atomically thin $PtSe_2$**.a) Optical image of monolayer $PtSe_2$. b) Photoluminescence(PL) spectrum of monolayer $PtSe_2$ at 4K with HeNe 633nm laser excitation (P= 20uW with 1μm spot size). The excitation spot is shown as a black dot in a). c) PL mapping around the $PtSe_2$. PL intensity is integrated from 1.26eV to 1.48eV, covering the broad tail in a higher energy range. The area of PL corresponds to the monolayer region of $PtSe_2$ in a). d) Atomic force microscopy mapping(up) and line profile(down) of monolayer and bilayer $PtSe_2$. The thickness of monolayer and bilayer is around 0.7nm and 1.2nm, respectively. Panel d) are are adapted with permission from ref[156], Springer Nature Ltd.

For the $PtSe_2$ source, we used the same bulk material (CVT-grown bulk $PtSe_2$ from HQ graphene) as in the prior study[22], and we relied on the mechanical exfoliation technique to obtain ultrathin $PtSe_2$.

There were several experimental difficulties in the sample fabrication of ultrathin $PtSe_2$, which is worth to mentioning here. Unlike other vdW materials like MoS_2 or WSe_2, the exfoliation of $PtSe_2$ on PDMS or PMMA polymer generally yielded a multilayer thicker than 5nm and never produced ultrathin samples of $PtSe_2$. Exfoliating on a rigid surface, such as SiO_2/Si substrate, however, was the most effective way, and we were able to obtain the mono- and bilayer samples for this study. We note that O_2 plasma treatment on the SiO_2 surface before the exfoliation improved the yield of ultrathin flakes, significantly. Figure 5-4a shows the optical image of monolayer $PtSe_2$. Still, the size of the obtained flake, in general, was a relatively smaller (below the lateral size of 5μm) than that of the other TMDCs (see **Figure 3-2**).

To identify monolayer thickness, photoluminescence(PL) spectroscopy was not useful for monolayer $PtSe_2$, contrary to its effectiveness in finding monolayer of other TMDC such as WSe_2. This is because monolayer $PtSe_2$ is an indirect semiconductor with a bandgap of 1.2-1.8eV (e.g. 1.25eV from DFT calculation[79] and 1.8eV from scanning tunneling microscopy[85]) and the expected weak PL could be only measured at low temperature. **Figure 5-4(a)** shows the optical image of exfoliated monolayer $PtSe_2$ on a SiO_2/Si substrate. **Figure 5-4(b)** shows the PL spectra of monolayer $PtSe_2$ with 633nm laser excitation taken at a temperature of 4K. The intensity peaks around 1.28eV with the full width at half maximum (FWHM) of 160meV. **Figure 5-4(c)** shows the PL mapping around the area of this exfoliated sample, where the PL intensity is integrated from 1.26eV to 1.48eV, covering the broad tail in a higher energy range. The are and shape of the PL map reflect the monolayer region in **Figure 5-4(a)**. We found this PL vanishes completely at room temperature.

Thus we mainly focused on atomic force microscopy to identify its thickness. **Figure 5-4(d)** shows AFM map images of monolayer(left) and bilayer(right) samples with the corresponding line-height profiles displayed below. The thickness of the monolayer (bilayer) is found to be around 0.7nm (1.2nm).

5.2.2 Transferring ultrathin $PtSe_2$

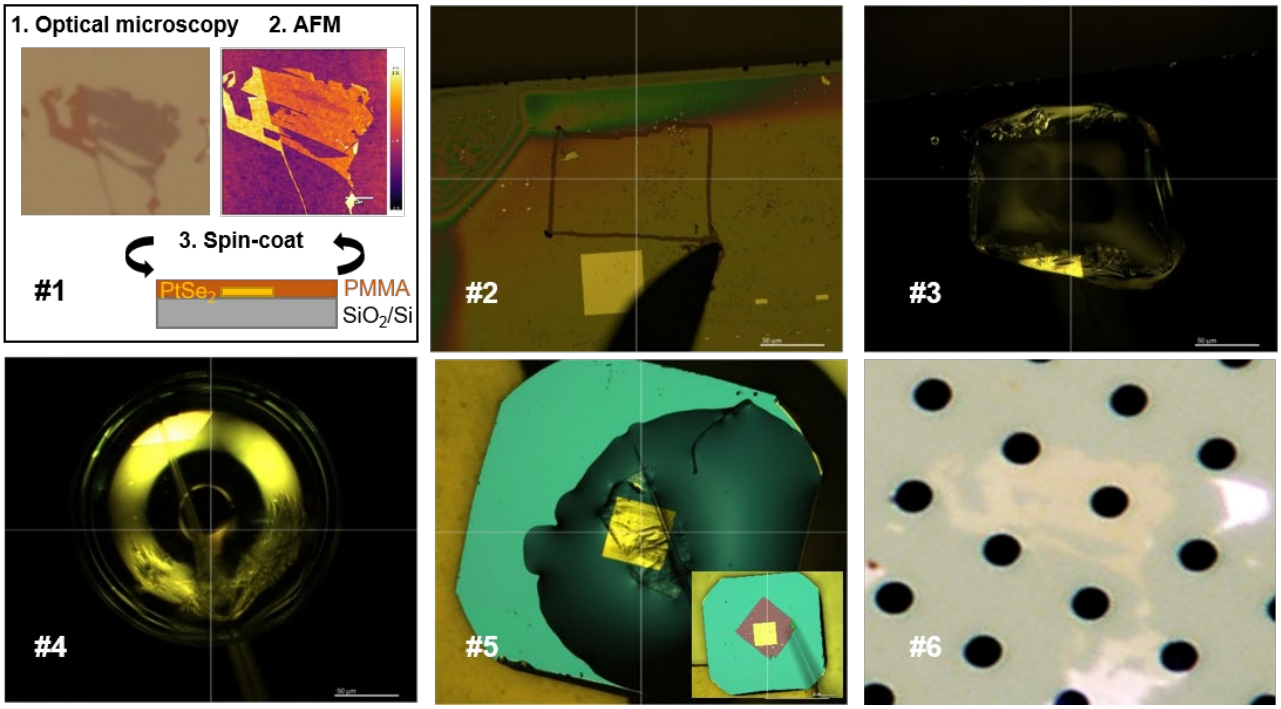

Figure 5-5. **Transferring exfoliated $PtSe_2$.** The procedure of transferring $PtSe_2$ is divided into six steps. The transfer takes from initially exfoliated SiO_2/Si to the target substrate. Following these steps, ultrathin $PtSe_2$ was transferred to build a 2D heterostructure, and make a TEM sample. Images #3 and #4 are taken with dark field for the clear contour images of the membrane floating on the surface of the KOH solution.

With monolayer $PtSe_2$, we fabricated heterostructure devices (see next subchapter) and made TEM samples. For this purpose, we had to pick up the sample from the substrate SiO_2/Si and transfer it. As a general strategy, we have used PMMA carrying layer method. We have used mild potassium hydroxide(KOH) solution to etch away SiO_2 during this method, and PMMA works as a transporting membrane. We note that a very diluted KOH concentration (0.7%) is used to minimize the unintentional creation of defects. Figure 5-5 illustrates the process of transferring ultrathin $PtSe_2$. Below is the description of the procedure. Each step is illustrated by the figure labelled with the same number in **Figure 5-5**.

1. Thin $PtSe_2$ was searched through optical microscopy, and the thickness of monolayer or bilayer was confirmed by AFM. Then PMMA polymer was spin-coated on top and baked at 60deg for 5 minutes to promote better adhesion between the flake and the polymer.

2. Scratch the PMMA polymer with a sharp metal tip around the target flake area. Flake lies within the centre of the squared region to avoid unintentional damage imposed by scratching. Put a few droplets of diluted KOH solution (0.7%) at the scratched region.

3. KOH will start to penetrate below the PMMA while etching away SiO_2, making PMMA detached from SiO_2. Wait until it fully etches away the inner region of the scratched line. Image #3 in **Figure 5-5** shows the dark-field image of the square area of PMMA membrane floating on the KOH solution. At this stage, $PtSe_2$ is in contact with one side, the KOH solution.

4. Once the membrane is fully detached from the SiO_2, use a glass nano-capillary to pick up the membrane, and transfer it to the DI droplet. Image #4 in **Figure 5-5** shows the dark-field image of the membrane floating on the DI droplet. At this stage, $PtSe_2$ is attached to PMMA, with the other side in contact with DI water.

5. Using the glass nano-capillary again, transfer the membrane onto the target, e.g. TEM grids, and do the necessary alignment.

6. Clean PMMA polymer with Acetone and IPA, and check the transferred sample under a microscope.

5.2.3 Ultrathin $PtSe_2$/graphene electronic device

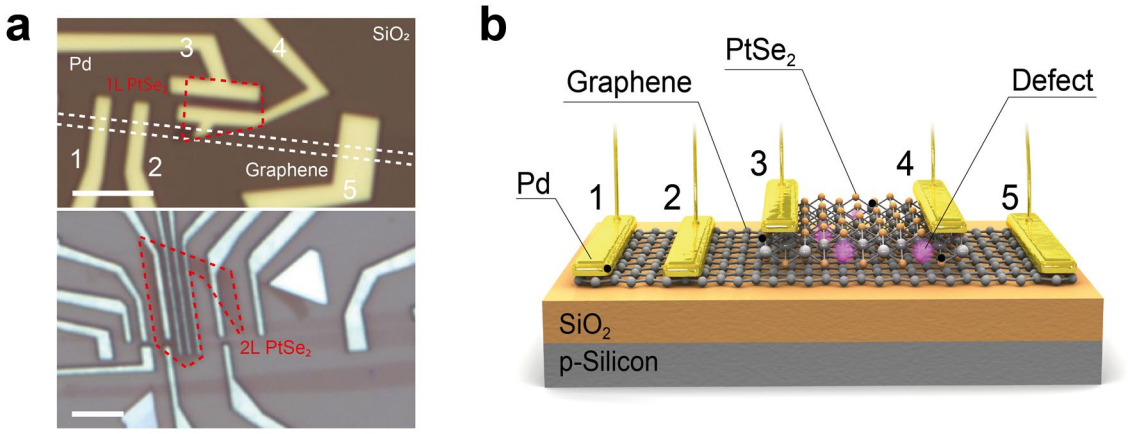

Figure 5-6. **Ultrathin $PtSe_2$ electronic device**.a) Optical image of electronic devices made with monolayer(top) and bi-layer(bottom) $PtSe_2$, with graphene and Pd electrodes. The red and white dotted line denotes the region of $PtSe_2$ and graphene, respectively. For clarity, the area of graphene is not displayed for the bilayer $PtSe_2$ device. b) Device schematics. Pd contacts are labelled with numbers as shown in a). Panel a-b) are adapted with permission from ref[156], Springer Nature Ltd.

It is found from the previous study on thickness-dependent electronic transport of $PtSe_2$[84,157] that the 2D conductivity of a few-layer $PtSe_2$ considerably lowered as thickness is reduced. This low conductance resulted in large background current noise when performing magneto-transport measurements. To circumvent this problem, we have considered Pd/$PtSe_2$/graphene heterostructure on SiO_2/Si where the magnetic property of $PtSe_2$ can be probed with magnetoresistance using out-of-plane current through ultrathin $PtSe_2$ under the magnetic field. Additionally, having graphene as one electrode, its gate transparency also allows us to modulate carrier concentration using the global Si back gate to study the semiconducting charge transport of monolayer $PtSe_2$.

To build such heterostructures, ribbon-shaped graphene was exfoliated on separate SiO_2/Si substrates, and $PtSe_2$ were transferred on top of the ribbons. **Figure 5-6(a)** shows a device made of monolayer(upper) and bilayer(lower) $PtSe_2$. Employing e-beam lithography and evaporation, 80nm Pd electrodes were fabricated to contact graphene as well as $PtSe_2$.

Figure 5-6(b) shows the device schematics. The basic field-effect transport on $PtSe_2$ was done by using #3(Pd) and #4(Pd) as drain and source contacts, respectively, while applying a voltage to the global Si backgate. Contact #4 is only with $PtSe_2$, whereas contact #3 is placed on top of $PtSe_2$/graphene heterostructure, as displayed in the top image of Figure 5-6a.

The geometry of contacts allows us to probe the magnetism of $PtSe_2$ using vertical tunneling transport, as explained earlier, by passing charge current from contact #2(graphene) to contact #3(Pd). Utilizing non-magnetic Pd contacts and graphene rules out the possible influence of electrodes on the magnetic response of the device. Furthermore, we measured the magnetic field dependence of lateral current in graphene/$PtSe_2$ heterostructure by driving charge current through contact pairs #2 & #5, which is compared with the result obtained from isolated graphene using the contact pairs #1 & #2.

5.3 Charge transport in monolayer $PtSe_2$

We first characterize the basic charge transport properties of monolayer $PtSe_2$. **Figure 5-7(a)** shows the back-gate V_{BG} dependence of drain-source current I_{DS} at temperatures selected within the range 1.6-142K. I_{DS} is slightly modulated with the applied gate voltages V_{BG} with relatively low on-state conductance. Below 77K, $PtSe_2$ become insulating in that charge current becomes negligible within the measured range of gate voltage. The semiconducting property of monolayer $PtSe_2$ is reflected in increasing conductivity (σ) with the temperature shown in the inset of Figure 5-7b, measured at different charge density values.

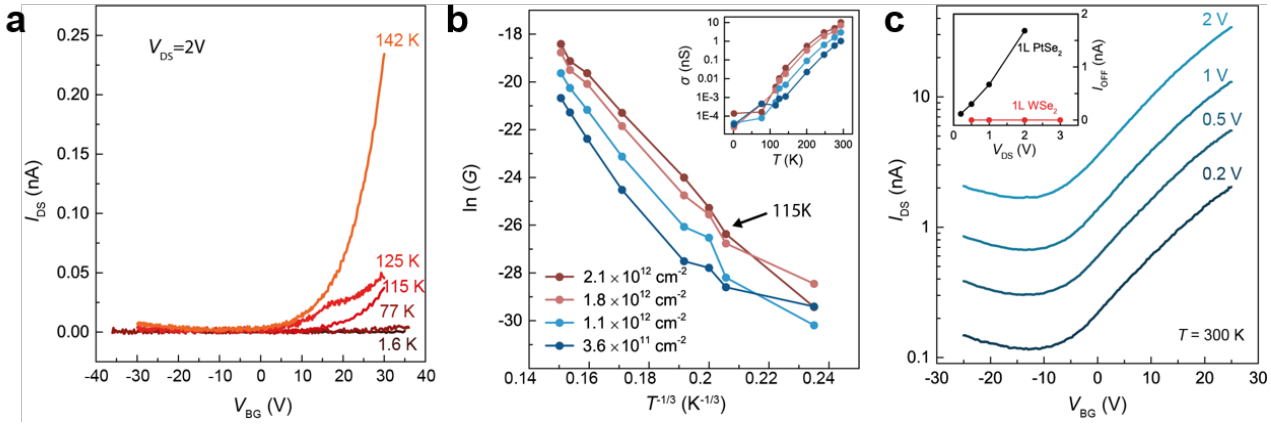

Figure 5-7. **Semiconducting monolayer $PtSe_2$**.a) Back-gate V_{BG} dependence of drain-source current I_{DS} at temperatures ranging from 1.6-142K. The measurement was carried out with fixed bias voltage V_{DS}=2V using contact pairs #3 & #4 shown in Figure 5-6a. b) ln(G) vs $T^{-1/3}$ at the temperature ranging from 77K-300K with different carrier concentrations. Inset shows the charge conductivity measured at the temperature of 1.4-300K. c) V_{BG} dependence of I_{DS} at V_{DS} measured at 300K. Inset shows V_{DS} dependence of off-state I_{DS} from monolayer $PtSe_2$ and monolayer WSe_2. Panel a-c) are adapted with permission from ref[156], Springer Nature Ltd.

In the case of disordered semiconductors, the variable range hopping (VRH) model combined with Mott formalism can explain the low-temperature charge conductivity (G) with characteristic temperature dependence by the following equation:

$$\sigma \sim e^{-(\frac{T_p}{T})^{1/(d+1)}} \tag{11}$$

where σ, T_p and d refers to conductivity, characteristic temperature and sample dimension, respectively. In the case of a 2D channel, d=2.

Figure 5-7(b) shows the linear dependence of ln(G) vs $T^{-1/3}$ found in the temperature range from 115K to 300K at the sub-threshold voltage range (V_{BG}<20V). The linear conductivity of ultrathin $PtSe_2$ can be described by 2D VRH transport (d=2 for the above equation) up to room temperature. This is possibly attributed to the localized density of states near the conduction band edge, induced by structural defects in the probed $PtSe_2$ sample.

The bandgap for monolayer $PtSe_2$ is expected to be as large as 1.2-1.8eV [79,85], where a clear off-state current is expected. However, **Figure 5-7(c)** shows the back-gate V_{BG} dependence of drain-source current I_{DS} at room temperature. The off-state current (around V_{BG}= -10V) is found to be proportional to the applied bias voltages. This character was not observed in other monolayer TMDCs of similar bandgaps, such as WSe_2, under the same condition of using SiO_2/Si substrate[158]. We also measured a monolayer WSe_2 device, which shows clear off-state even with increased voltage bias, as shown in the inset of **Figure 5-7(c)**. This implies that localized mid-gap states are introduced in monolayer $PtSe_2$ by the presence of atomic defects within the crystal.

5.4 Visualizing atomic defects in $PtSe_2$

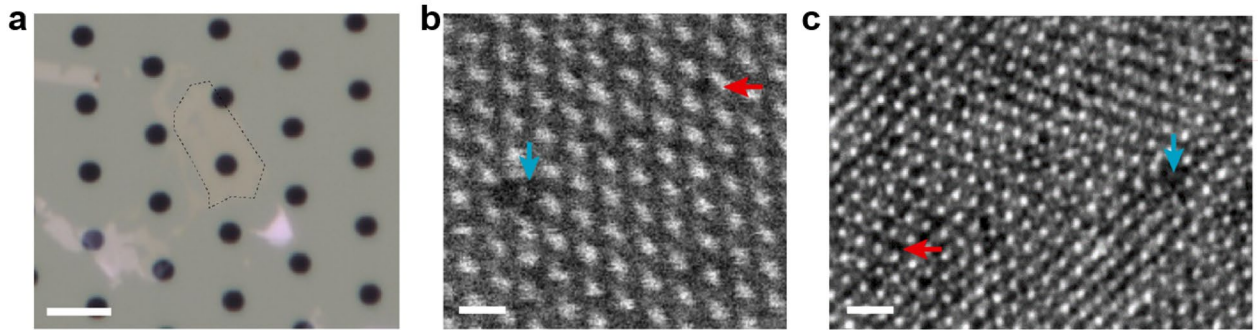

Figure 5-8. **Imaging atomic structure of $PtSe_2$.** (a) Optical image of ultra-thin $PtSe_2$ transferred onto a TEM grid. The dotted line displays the bilayer region of $PtSe_2$. The scale bar is 5μm. (b) Raw HAADF image of a bilayer $PtSe_2$. The scale bar is 1 nm. (c) HAADF image of a monolayer $PtSe_2$. The scale bar is 2nm. Blue and red arrows in panels b-c) show the sites with missing Pt and Se atoms, respectively. Panels b-c) are adapted with permission from ref [85], Springer Nature Ltd.

In order to directly visualize structural defects of $PtSe_2$, we relied on Cs-corrected high-resolution transmission electron microscopy(HRTEM) imaging. **Figure 5-8(a)** shows the optical image of ultrathin $PtSe_2$ transferred on a Si_3N_4 TEM grid. **Figure 5-8(b)** and **Figure 5-8(c)** are TEM images of bilayer and monolayer $PtSe_2$ respectively. Both images are taken with low electron acceleration voltage to avoid unwanted e-beam damage to the structure. In these TEM images, both bilayer and monolayer $PtSe_2$ show 1T phase atomic arrangement where the position of Pt and Se atoms are identifiable by the brighter and slightly darker spots, respectively. Consistent with the earlier TEM and STM investigations on $PtSe_2$[159,160], we also observe native Pt(Se) vacancies where blue(red) arrows in **Figure 5-8(b)** and **Figure 5-8(c)** indicate its position. The other positions of Pt and Se vacancies in these images are not marked for the purpose of image clarity.

As for the density of Pt and Se vacancies, we were able to reliably extract them from the bilayer as it has a larger sampling region on the TEM grid than the monolayer. We have constructed frequency distribution histograms (not shown here) of Pt and Se vacancies by analyzing multiple TEM images of bilayer using ImageJ software, and we found the mean density of Pt vacancies to be $(0.9 \pm 0.06) \times 10^{13} cm^{-2}$ and Se vacancies to be $(3.5 \pm 0.2) \times 10^{13} cm^{-2}$ within the total analyzed area of 1095.81 nm^2.

5.5 Magnetic properties of monolayer and bilayer $PtSe_2$

5.5.1 Magneto-transport in monolayer and bilayer $PtSe_2$

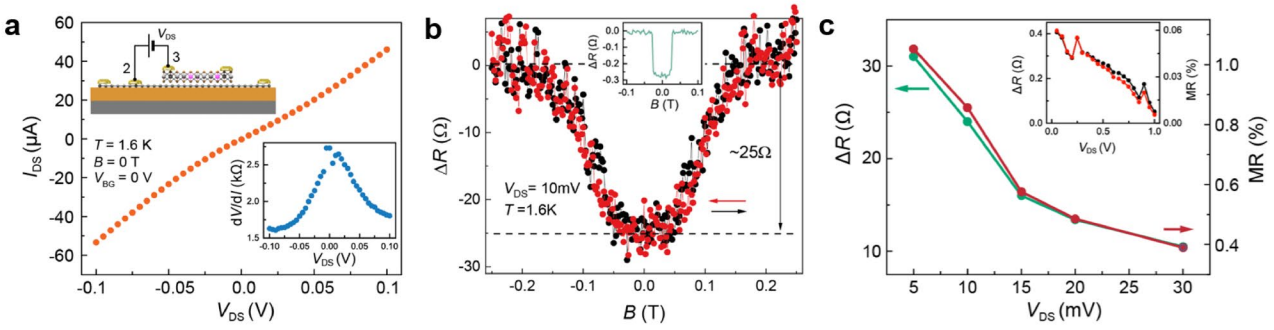

Figure 5-9. **Magneto-transport in monolayer $PtSe_2$.**a) V_{DS} dependence of out-of-plane I_{DS} through $PtSe_2$. The top inset shows the schematic of measurement geometry. The bottom inset shows the numerically derived differential resistance. b) Resistance measured at the fixed V_{DS} = 10mV while sweeping magnetic field. ΔR corresponds to R(B)-R(B=-250mT). Red(black) data points

were obtained by sweeping the magnetic field in the same direction as the red(black) arrow. Inset shows the resistance variation by the applied magnetic field from 7nm thick metallic $PtSe_2$. c) Bias-dependent ΔR and magnetoresistance(MR). Similar bias dependence is observed from 7nm thick metallic $PtSe_2$. Panel a-c) are adapted with permission from ref [85], Springer Nature Ltd.

Next, we moved on to investigating magnetism in ultrathin $PtSe_2$. **Figure 5-9(a)** shows the 2 terminal measurement of I_{DS} while sweeping V_{DS} in the vertical tunneling pathway through monolayer $PtSe_2$ using graphene(drain) and Pd contacts(source). The I-V characteristics show near-linear and symmetric due to the atomically thin tunnel barrier of $PtSe_2$, which is only 0.7nm thick.

Compared to the low in-plane conductance of monolayer $PtSe_2$ as shown in **Figure 5-7(a),** out-of-plane conductance in this vertical current path is improved by several orders of magnitude. In this vertical geometry, the low-noise DC magneto-transport measurement was possible and performed by measuring the 2 terminal resistance with fixed V_{DS} while varying the out-of-plane magnetic field from -250mT to 250mT and vice versa. **Figure 5-9(b)** shows the magnetoresistance at the base temperature 1.6K with V_{DS}=10mV. The data (y-axis) is represented as ΔR, which is R(B)-R(B=-250mT).

The resistance shows a plateau-like constant value in a low magnetic field range between $\pm$50mT, and increases gradually and saturates at higher magnetic fields. The resistance difference (ΔR) between the two plateaus is 25Ω at V_{DS}=10mV. This resistance behavior with the out-of-magnetic fields deviates from the conventional localization signal. However, this two-plateau response is the signature of the antiferromagnetic response demonstrated previously in van der Waals antiferromagnet, CrI_3, with out-of-plane magnetization. The absence of magnetic hysteric behavior from the opposite magnetic field sweep direction supports the argument of antiferromagnetism. Considering that graphene and Pd are the non-magnetic elements in the current path of 2-terminal measurement, this magnetic response should be originated from $PtSe_2$.

The switching of resistance, from one plateau to another, is gradual compared to the abrupt switching observed from the thicker metallic $PtSe_2$ as shown in the inset of **Figure 5-9(b)**. This implies the possible difference in magnetic anisotropy between thin and thick $PtSe_2$, and suggests the presence of in-plane magnetic anisotropy in monolayer $PtSe_2$ making canted magnetic moments energetically favorable at the intermediate field strength.

Figure 5-9(c) shows the summary of ΔR measured at different bias voltages. We observe that ΔR decreases with applied bias, and the calculated magnetoresistance, ΔR/R(B=0T), decreases from 1% to 0.4%. This bias dependence resembles closely that of the zero-bias anomaly of strong tunneling magnetoresistance(TMR) found in magnetic tunnel junction(MTJ) structures[161,162]. In MTJ, TMR is reduced strongly with the applied bias voltage of the order of a few hundredths millivolts.

Although the detailed mechanism of this universal behavior of bias dependence found in both ultrathin(0.7nm) and thick(7nm) $PtSe_2$ remains unclear, we present some possible explanations suggested for the decreasing MR found in MTJ. There are two mechanisms, both of which rely on tunneling electrons with excess energy above Fermi level due to applied bias voltage, known as hot electrons. The first mechanism is related to the collective excitation of spin-wave due to a hot electron injection process[163]. The hot electron generated with a higher bias voltage enhances the spin-wave excitation in the magnetic system. This would lead to a spin flipping process, eventually responsible for reduced MR.

The second mechanism is related to enhanced indirect tunneling of hot electrons through the spin-degenerate density of states. These non-polarized states can be due to structural defects within a material or at the interface of a heterostructure. As bias voltage increases, spin-independent current increases by this indirect tunneling through non-polarized states. Consequently, the spin polarization of total current is reduced and would lead to the reduction of MR[164]. From our previous TEM analysis, we observe point defects, V_{Se} and V_{Pt} in $PtSe_2$, where the V_{Se} defect concentration is higher than that of V_{Pt}, In the next subchapter, we show that from the calculation that V_{Pt} gives a polarized density of state, but V_{Se} produces a non-polarized density of states.

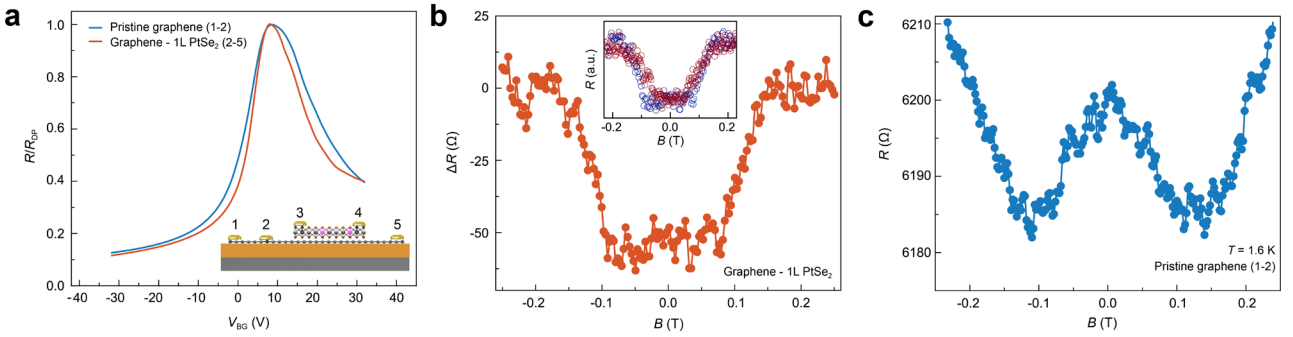

Figure 5-10. **MR of graphene with and without proximitized $PtSe_2$.**a) V_{BG} dependence of resistance for two different graphene channels. The bottom inset shows the schematic of the device with contact assigned with different numbers. b) Magneto-transport on graphene channel with monolayer $PtSe_2$, measured at 1.6K. Inset shows the comparison of two results obtained from lateral (contact #2 & #5) and vertical (contact #2 & #3) geometry. c) Magneto-transport on pristine graphene, measured at 1.6K. Panel a-c) are adapted with permission from ref [85], Springer Nature Ltd.

We next investigate how the magnetic ordering of monolayer $PtSe_2$ can impact the transport properties of graphene. For this aim, we selected two pairs of source and drain contacts: contact #2 & #5 connecting the graphene with monolayer $PtSe_2$, and contact #1 & #2 connecting only the pristine graphene. **Figure 5-10(a)** displays the resistance of these two different channels measured at fixed V_{DS} while varying the back gate V_{BG} without the magnetic field. It shows that two graphene channels have similar characteristics with the same position of their Dirac points. Here, for the purpose of comparison, resistances were normalized to their values at the Dirac point to compensate for the dimensional contributions to the resistance.

However, the magnetic field response of these two channel reveals a clear difference, as shown in **Figure 5-10(b)** and **Figure 5-10(c)**. While **Figure 5-10(c)** shows a conventional weak localization signal from pristine graphene, $PtSe_2$/graphene exhibits the same two-plateau response from the vertical measurement geometry. The inset of **Figure 5-10(b)** displays the in-plane magnetoresistance(red circle) of graphene/$PtSe_2$, compared with the out-of-plane magnetoresistance(blue circle) from vertical geometry which shows the overlapping response. It thus suggests that both magnetoresistances from the two different geometries are from the same mechanism. One possible explanation for this is that carrier tunnels back and forth from graphene to the magnetic defect state of monolayer $PtSe_2$ via quantum tunneling. This type of tunneling is also reported previously in WSe_2/graphene[165].

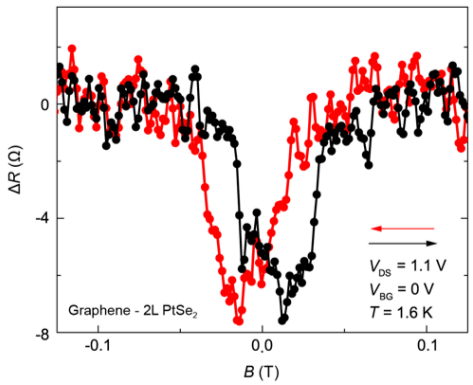

Figure 5-11. **Magneto-transport of graphene channel with bilayer $PtSe_2$.** Resistance of graphene with bilayer $PtSe_2$ from the two opposite magnetic field sweep directions shows magnetic hysteresis. Red and black arrows indicate the sweep direction. Measurement is performed with a fixed V_{DS} of 1.1V and at the base temperature of 1.6K. This measurement is performed with the device shown in Figure 5-6a (bottom). The panel is adapted with permission from ref [85], Springer Nature Ltd.

It has shown in several van der Waals magnets including metallic multilayer $PtSe_2$ that layer dependent magnetic exchange interaction is the key factor in determining the magnetic ground state. Therefore, it motivated us to further characterize the magnetism in bilayer $PtSe_2$ to obtain the complete information of magnetic properties in the ultrathin range.

With the similar device geometry and measurement principle, **Figure 5-11** shows the magneto-transport properties of graphene with bilayer $PtSe_2$ from the device, the image of which is shown in **Figure 5-6(a)** (bottom). We observe negative magnetoresistance peaks around $B = \pm 20mT$ where the peak occurs at the plus(minus) sign of the magnetic field when the magnetic field is increases(decreasing). Red and black arrows indicate the sweep directions. This reflects the hysteresis behaviour of magnetization, which is the hallmark of the ferromagnetic ground state. As a summary, our magneto-transport measurement suggests that monolayer (bilayer) $PtSe_2$ holds the antiferromagnetic (ferromagnetic) ground state.

5.5.2 The first principle calculation – defect-induced magnetic moments

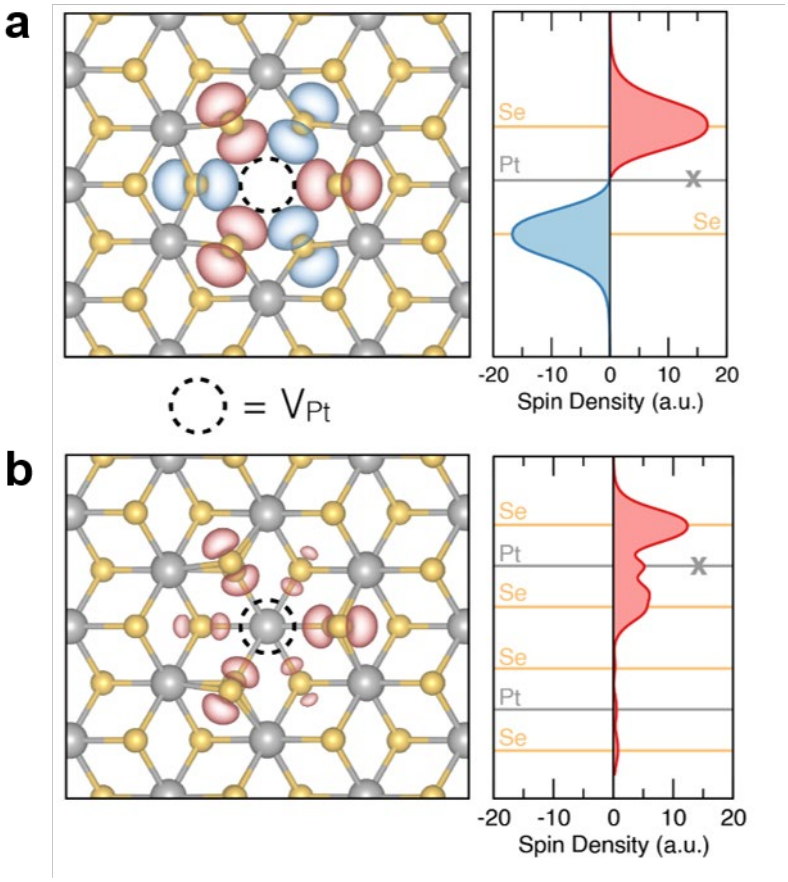

Figure 5-12. **Localized magnetic moments induced by Pt vacancy in $PtSe_2$**.a) Spin density distribution around Pt vacancy for monolayer $PtSe_2$ by the first-principle DFT calculation. Blue and red lope indicate the density distribution for opposite spin orientations. The grey(yellow) sphere displays Pt(Se) atom, and the dotted circle represents the position of the missing Pt atom. The right panel in a) shows in-plane integrated spin density plotted along the out-of-plane direction of the 2D plane, showing the anti-parallel ordering of magnetic ground state in monolayer $PtSe_2$. The position of Pt vacancy is marked with Pt Grey X mark. b) Spin density distribution around Pt vacancy for bilayer $PtSe_2$ when the vacancy is present at the top layer. The right panel in b) shows the ferromagnetic ground state. Panel a-b) are adapted with permission from ref [85], Springer Nature Ltd.

To understand the physical origin of magnetism in monolayer and bilayer $PtSe_2$, atomic defect-induced electronic and magnetic property in ultrathin $PtSe_2$ was examined employing the first-principles DFT calculation, which was hinted by the prior observation of magnetism in multilayer $PtSe_2$[22].

The calculation found that Pt vacancy introduces magnetic moments localized around six neighbouring Se atoms within the top and bottom Se planes. The left panels of **Figure 5-12(a)** and **Figure 5-12(b)** show the spin density distribution created by Pt vacancy for monolayer and bilayer, respectively. Importantly, in the monolayer case, the top and bottom magnetic moments energetically favor the parallel ordering, thereby giving an antiferromagnetic ground state (The right panel of **Figure 5-12(a)**). However, the ferromagnetic ground state is the only solution in the case of the bilayer (The right panel of **Figure**

5-12(b)). These finding matches experimental observation. Additionally, due to the interlayer coupling from the additional layer for the case of the bilayer, the fully polarized configuration of the magnetic moment becomes $1.33\mu_B$, which is lower than that of the monolayer, $4\mu_B$.

5.6 Summary and future perspectives

5.6.1 Achieved results

In short, we have studied the magnetic properties of the ultra-thin layer of vdW $PtSe_2$ by means of magneto-transport measurements. We fabricated electronic devices made of monolayer and bilayer $PtSe_2$ with graphene electrodes, and we observed, indirectly by magnetoresistance, the ground state of ferromagnetic and antiferromagnetic ordering in monolayer and bilayer, respectively. Supported by the presence of atomic vacancies found in the TEM images of ultra-thin $PtSe_2$, the first principle DFT calculation explained the possible origin of magnetism that Pt vacancy induces local magnetic moments in both mono- and bilayer $PtSe_2$. Sharing the same origin of magnetism found in multilayer $PtSe_2$[22], this work unveils defect-induced magnetism down to the monolayer thickness of $PtSe_2$.

5.6.2 Further development

Although the DFT calculation captures the same ground-state ordering as observed in the transport experiments, further questions remain to elucidate the defect-induced magnetism of $PtSe_2$. It was proposed in the previous report that RKKY interaction is the governing mechanism for magnetism found in multilayer $PtSe_2$[22]. The interaction enables the long-range magnetic ordering of magnetic moments, which are locally present at the two surfaces (top and bottom) of the multilayer $PtSe_2$. As RKKY interaction is a function of a distance between the localized moments, magnetism in thin limit may appear with stronger anisotropy, which could give interesting spin-textures in thin $PtSe_2$. On the other hand, when the material is thinned down, $PtSe_2$ become a semiconductor from a metal. The RKKY mechanism, which is valid for metallic/semi-metallic systems, may not play a significant role in the thin limit. So a natural question occurs: how do the magnetic moments interact with each other in the long-range for the thin samples? What is the origin of magnetic anisotropy?

Conventional magneto-transport measurement is a convenient way to characterize the magnetic properties of a material. However, it can only probe the total magnetic properties of the volume through which the charge current flows. It is thus a limited method to provide spatial information on how defect-induced magnetic moments interact in the short range of a few nm. For this matter, scanning tunneling microscopy and scanning tunneling spectroscopy can be more favourable tools to use, providing local information from their sub-nm spatial resolution and energy-resolved spectra. Scanning nitrogen-vacancy center magnetometry can be adopted as well to probe local stray fields[166,167], which can potentially tell us the spin orientations around the defect, which will be informative for studying its magnetic anisotropy.

Additionally, the nature of defect-induced magnetic properties in $PtSe_2$ can be further investigated by studying how the defect concentration plays a role in its magnetic properties. This can be addressed by controlling the atomic defect density of Pt vacancy. Various methods can be applied to achieve this purpose, such as dose-controlled e-beam irradiation[168] or Ar plasma or ion bombardment[169], which have demonstrated their usage in creating point defects in other TMDCs. The information could help tailor the magnetic properties, thereby giving us an additional knob to control its magnetic property with the defect concentration. If successful, this so-called defect engineering, combined with synergic strategies of etching layer by layer of $PtSe_2$, can enable the production of a metal and a semiconductor with various different magnetic properties, all from a single material, $PtSe_2$.

5.6.3 Future perspective

Interfacial-driven phenomena[170] in heterostructure of conventional magnetic thin films, such as interfacial perpendicular magnetic anisotropy(PMA)[139], interfacial generated spin current[171], spin Seebeck effect[172,173], exchange bias[174], spin-orbit torque(SOT)[175,176] has greatly advanced the development of modern spintronics. On the practical side,

magnetic materials with PMA have been the most essential element in the memory application due to their advantage compared to in-plane magnetization materials in terms of low current for magnetization reversal, better thermal stability and miniaturization capability[177]. PMA is more desirable in the lateral spin valve applications where the perpendicular spin current injection is preferred, for example, in the sensing of spin current from spin Hall effect[178].

In this regard, atomically sharp interface from vdW 2D magnets and their natural out-of-plane magnetization can offer new possibilities to discover interesting physics and provide new functionalities in electronics, optics and spintronics devices[179,180]. As for multilayer metallic $PtSe_2$, it has the potential to replace conventional ferromagnet contacts in already investigated spin devices. Ultra-thin $PtSe_2$, where the magnetic properties are examined in this study, can be a good candidate for an active magnetic element to realize low-power, compact spin-torque devices, thanks to its low total magnetization (magnetic moments/volume) originated by the nature of defect-induced magnetism.

Chapter 6 Disorder-induced photovoltaic effect in centrosymmetric semiconducting $PtSe_2$

This chapter presents a work on the defect-induced photovoltaic effect in semiconducting $PtSe_2$. This finding was achieved by close collaborations with Dr. Zhe Sun, Dr. Juan Francisco Gonzalez Marin, who helped me with the laser optics experiments, and with Dr. Mukesh K. Tripathi, who provided the atomic images of ultra-thin $PtSe_2$ through TEM.

6.1 Introduction

When light is illuminated on a crystal without inversion symmetry, it can generate a photo-induced DC current at zero-bias conditions based on bulk photovoltaic effect (BPVE)[181]. The amplitude and direction of generated current are dictated by the symmetry of the host non-centrosymmetric crystal and can be controlled by the properties of the incident light, such as incident angle and polarization. Unlike the photocurrent generated by the photovoltaics effect from the built-in electric field, BPVE can occur in a single material. Thus, BPVE is considered as an alternative light-energy harvest mechanism not restricted by Shockley–Queisser limit of power conversion efficiency in the conventional pn-junction solar cell[182].

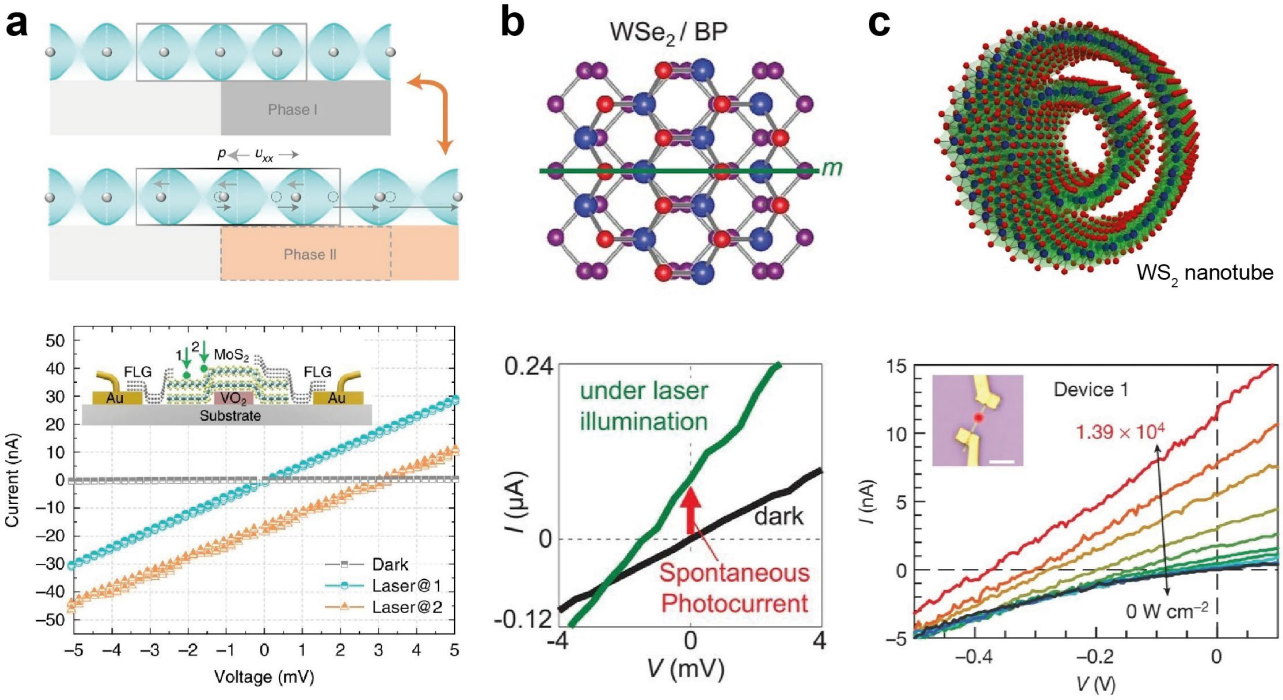

Figure 6-1. **Symmetry engineering for enhanced BPVE.** a) Flexo-photovoltaic effect in MoS_2. b) van der Waal interface hosting spontaneous photocurrent generation. c) Enhanced BPVE in WS_2 1D nanotube. Panels are adapted with permission. Panel a) is from ref [25], Springer Nature Ltd. Panel b) is from ref [183], AAAS. Panel c) is from ref [184], American Chemical Society.

Nevertheless, such advantages of BPVE are strictly applied to a non-centrosymmetric system, where centrosymmetric materials have persistently shown to be absent from BPVE. The broken inversion structural symmetry is thus the pre-requisite condition for a material to host BPVE and this fundamental requirement limits the class of material to be explored and used for photovoltaic application. However, recent advances in symmetry engineering using high crystal quality vdW material have demonstrated novel methods to create and manipulate the effect of BPVE in otherwise symmetry-forbidden materials[185]. **Figure 6-1(a)** shows a method based on applying mechanical strain to a crystal where inversion symmetry is lifted from the strain gradient, generating BPVE. This phenomenon is termed a flexo-photovoltaic effect[25]. Also, a well-designed interface can host the bulk photovoltaic effect[183]. As shown in **Figure 6-1(b)**, the spontaneous photocurrent can be present at the interface of stacked vdW crystals (WSe_2 and black phosphorus). The current direction can be controlled by the interfacial symmetry of the hetero-interface, which can be engineered by the relative rotation angle of two crystals. Last but not least, **Figure 6-1(c)** shows an effective method to create BPVE by reducing the dimensionality and lifting the 3-fold rotational symmetry of 2D WS_2 by scrolling it into a form of 1D nanotube[184]. This method could produce orders of magnitude higher BPVE compared to typical bulk materials.

These aforementioned approaches of symmetry engineering of BPVE are particularly based on external methods to break the centro-symmetry. Yet, the light-matter nonlinearity can also be induced by an intrinsic source, defects in a crystal[186,187]. Optical nonlinearity is strongly related to crystal symmetry, and the symmetries vanish in the presence of defects. For example, vacancy defect can break the inversion symmetry and allows even-order harmonic generation in centrosymmetric media, where defect-enhanced second-order harmonic generation (SHG) has been demonstrated[188]. The bulk photovoltaic effect, which is the DC counterpart of SHG, is also expected to be enhanced in centrosymmetric media by defects. However, this still lacks clear experimental proof.

In this regard, a few-layer $PtSe_2$, a centrosymmetric vdW semiconductor, can provide the ideal testbed for exploring the role of the defect in non-linear DC response from the electromagnetic field of light. For both even and odd number of layers, pristine $PtSe_2$ has inversion centers (even layer at a vdW gap and odd layer within Pt atoms of central $PtSe_2$ layer). The crystal belongs to the centrosymmetric space group of P-3m1 globally, and Se and Pt atomic sites belong to polar point groups C_{3v} and D_{3d}, respectively. The presence of defects in $PtSe_2$ can locally breaks the inversion symmetry. Among various types of defects in this material, 0D point defect, particularly the Se vacancy(V_{Se}), is considered the most stable[76]. The vacancy formation energy and sputtering energy of chalcogen atom in $PtSe_2$ are calculated to be lower than those of other well-known TMDCs, such as MoS_2 and WSe_2[189]. Therefore, $PtSe_2$ is more prone to be defective than other TMDCs. Earlier studies have already visualized the presence of various types of defects in $PtSe_2$, including V_{Se}, through high-resolution atomic imaging[159,160].

In this chapter, we present the work related to the discovery of the defect-induced bulk photovoltaic effect in semiconducting $PtSe_2$, where defective $PtSe_2$ is produced by the Au-assisted exfoliation technique[190]. This finding is achieved by directly comparing the photo-response of pristine and defective $PtSe_2$, and the broken local inversion symmetry in defective $PtSe_2$ is manifested by both strongly enhanced photovoltage and photocurrent response under homogenous sample illumination. We suggest the inversion asymmetry is induced by point defects and cluster-like defects, which are directly visualized by TEM and indirectly confirmed by defect-induced Raman peak shift and broadening. We observe linear- and circular photocurrent, as well as polarization-independent photocurrent. We claim that linear-polarized photocurrent originated from point defects, such as V_{Se}. In contrast, circular polarization and polarization-independent components possibly originated from the structural disorder of lowest reduced symmetry, cluster-like defects, considering the experimental condition of normal incidence of illumination. Our work demonstrates the potential of defective semiconducting $PtSe_2$ to be used for harvesting light and detecting light polarizations.

6.2 Sample fabrication

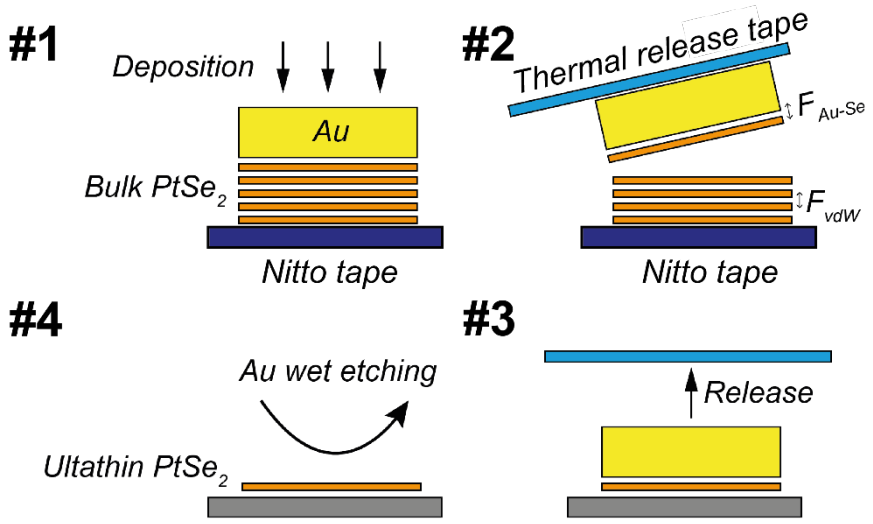

Figure 6-2. **Schematics describing the process of Au-assisted $PtSe_2$ exfoliation.**

We have obtained defective $PtSe_2$ ultrathin flakes through the Au-assisted exfoliation technique following the reported procedure[190]. Here, we summarize the experimental steps of the technique, illustrated in **Figure 6-2**.

1. $PtSe_2$ (CVT-grown PtSe2 source from HQ graphene) was mechanically exfoliated on a Nitto tape. Then, 100nm Au was deposited directly using e-beam evaporation.
2. We used a thermal release tape to detach the Au film. During the process, the ultrathin layer of $PtSe_2$ is picked up by Au film due to the larger bond strength between the adjacent Se layer in $PtSe_2$ with Au film (F_{Au-Se}) than the vdW interaction within $PtSe_2$ layers (F_{vdW}).
3. We transferred the stack of '100nm Au film/few-layer $PtSe_2$' onto a silicon oxide substrate and released the stack by applying the thermal tape releasing temperature of 130°C for 30 seconds.
4. We cleaned the tape residue using O_2 plasma treatment. Then, Au etchant (KI:I_2:DI=1:4:40) is used to remove the 100nm Au film. To make sure to completely remove Au on $PtSe_2$, we left the sample in etchant at a mild temperature condition (40°C) for 30 minutes. From the analysis of energy dispersive x-ray spectroscopy (data not shown here) on $PtSe_2$ exfoliated from this technique, we do not observe characteristic X-ray peaks from Au atoms (Au atomic concentration below the EDX detection limits). We also checked from TEM imaging (see **Figure 6-18**) and we also could not find visually any remaining Au atoms.

Figure 6-3 shows the optical images of ultrathin $PtSe_2$ on the silicon oxide substrate by Au-assisted exfoliation(**Figure 6-3(a)**) and standard tape exfoliation (**Figure 6-3(b)**). We used AFM to confirm the number of layers of $PtSe_2$ based on the multiples of the unit monolayer thickness. **Figure 6-3(c)** and **Figure 6-3(d)** show the thickness of 1L, 2L and 3L $PtSe_2$ obtained by standard tape and the Au-assisted exfoliation methods, respectively. Monolayers produced from two different exfoliation methods show similar thicknesses.

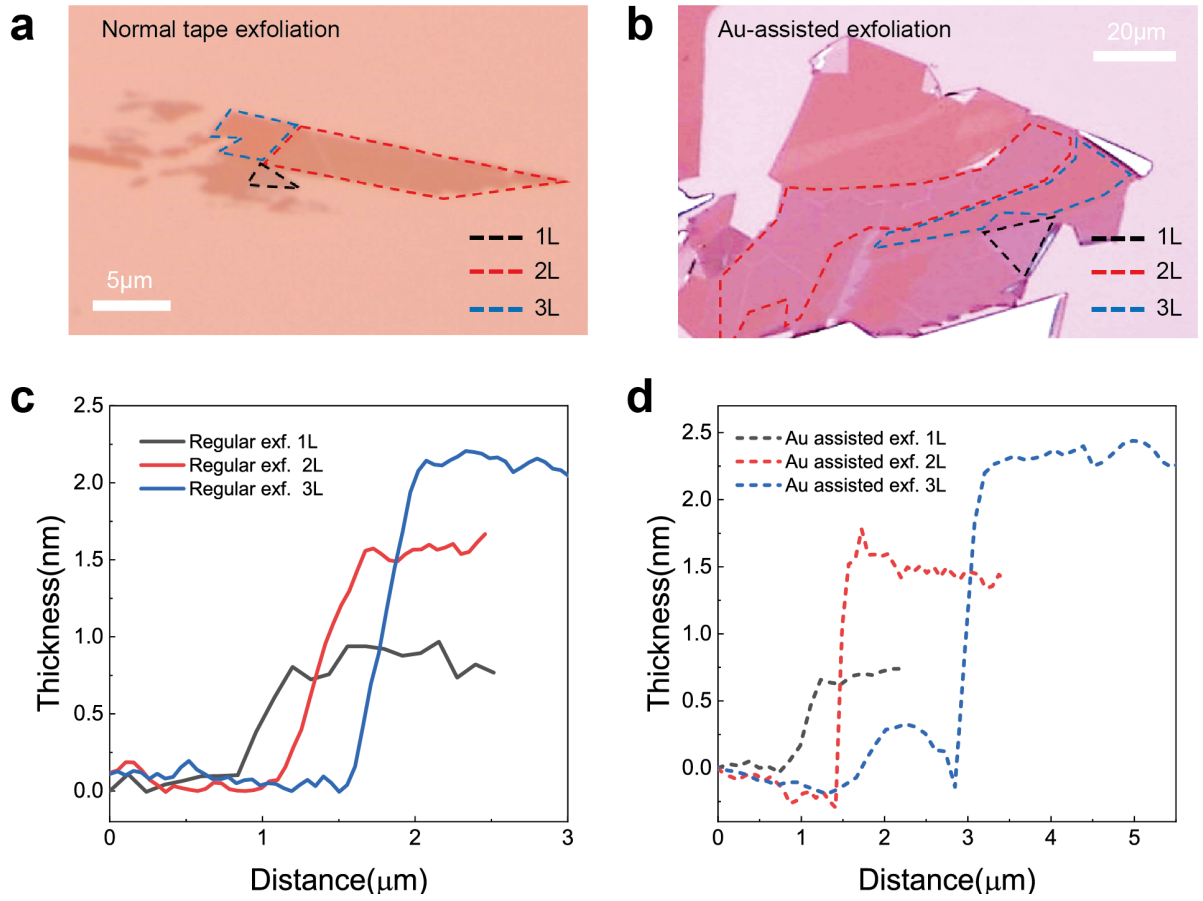

Figure 6-3. **Ultrathin $PtSe_2$ fabricated by regular and Au-assisted tape exfoliation.**a-b) Optical image of $PtSe_2$ obtained by normal regular tape exfoliation a) and Au-assisted tape exfoliation b). The area of mono-, bi- and trilayer $PtSe_2$ is shown as black, red and blue dashed contour lines, respectively. c-d) Thickness of mono-, bi- and trilayer $PtSe_2$ from regular tape exfoliation c) and Au-assisted tape exfoliation d) measured by AFM. Monolayer thickness from the regular(Au-assist) exfoliation is measured to be around 0.75nm (0.7nm).

6.3 Sample characterization

6.3.1 Signature of structural defects by Raman spectroscopy

The structural disorder of Au-assisted exfoliation samples was first identified in the clear differences in Raman spectra compared to the standard exfoliation. Raman spectra were taken by 532nm wavelength excitation using a focused laser and the grating of 3000 lines/mm and we probed the same samples used for AFM measurement. **Figure 6-4(c)** and **Figure 6-4(d)** show their Raman spectra of mono-(black line), bi-(red line) and trilayer(blue line) $PtSe_2$ from regular and Au-assisted exfoliation, respectively, where the colored spots in **Figure 6-4(a)** and **Figure 6-4(b)** correspond to the excitation spots. All the spectra are normalized with respect to the prominent peak intensity around 179cm^{-1}, that is the E_g peak. Si substrate Raman peaks were simultaneously measured as a reference signal (data not shown here), which was used to calibrate Raman peak positions of $PtSe_2$ if needed. However, the Si substrate peaks from all the different samples were found to be within 520.26±0.03cm^{-1}.

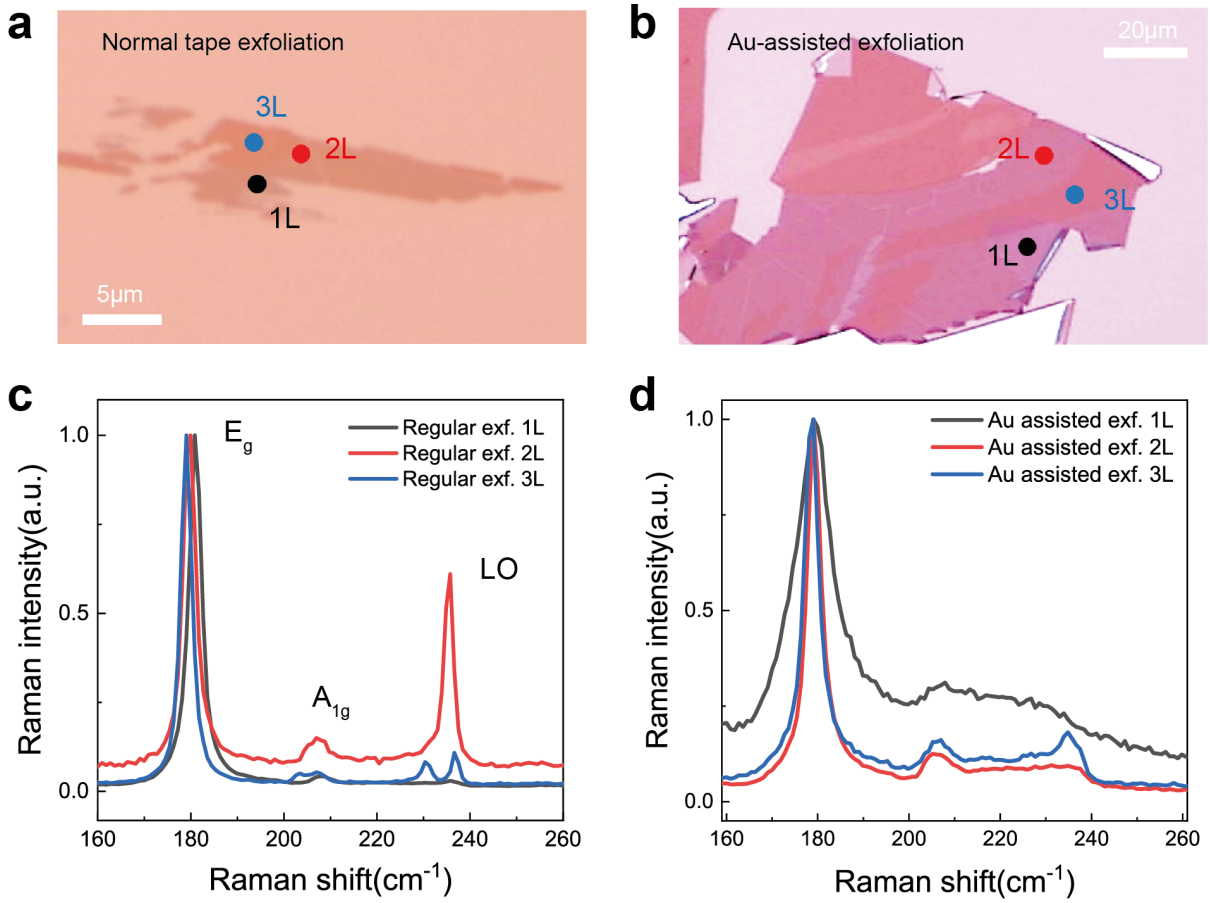

Figure 6-4. **Raman spectra of $PtSe_2$ produced by two different exfoliation techniques.**a-b) Same $PtSe_2$ samples are shown in **Figure 6-3(a-b)**. Black, red, and blue dots are the area of laser excitation spot where the Raman spectra of mono-, bi- and trilayer $PtSe_2$ were measured, respectively. c-d) Raman spectra of ultrathin layers of $PtSe_2$ from regular tape exfoliation c) and Au-assisted tape exfoliation d).

In **Figure 6-4(c)**, we observe three prominent Raman peaks of 1T-phase $PtSe_2$: E_g, A_{1g} and longitudinal optical(LO) phonon modes[80]. In the case of the bilayer (displayed in red curve), we found the E_g, A_{1g} and LO peak to be around 179.7cm^{-1}, 207.4cm^{-1}, and 235.3cm^{-1}, consistent with the previous Raman analysis with the same excitation wavelength[191], and allows regular-tape exfoliation sample to be considered as pristine $PtSe_2$. As thickness increases from monolayer to trilayer, E_g peak redshifts from 180.9cm^{-1} to 179.05cm^{-1}, and A_{1g} peak also redshifts from 208.43cm^{-1} to 207.61cm^{-1}. This red shift may be attributed to long-range Coulomb interaction, which has also been observed in MBE grown $PtSe_2$[80], and other TMDCs as well[192]. In bulk $PtSe_2$, E_g and A_{1g} peaks further redshift to 177.81cm^{-1} and 207.02cm^{-1}, respectively.

Additionally, we found that the LO mode consisting of two vibrational modes, infrared active(A_{2u}) and Raman and infrared active (E_u), shows the strongest peak intensity with respect to E_g mode at bilayer thickness and splits into two vibrational modes at trilayer thickness. This abnormal trend goes against the previous Raman analysis of few-layer $PtSe_2$ grown by MBE [80] and it may require further study on Raman properties of exfoliated $PtSe_2$ from a CVT-grown source to understand the difference.

As for Au-assisted exfoliation samples shown in **Figure 6-4(d)**, we still observe the three prominent Raman peaks owing to the same structural 1T phase of $PtSe_2$. However, compared to Raman spectra from pristine $PtSe_2$, there is no clear redshift of E_g and the FWHM linewidth of E_g peak broadens significantly for monolayer $PtSe_2$. The LO peak splitting from pristine trilayer $PtSe_2$ is also not observed. The large FWMH can be attributed to the structural disorder and we consider the Au-assisted exfoliation sample to be defective.

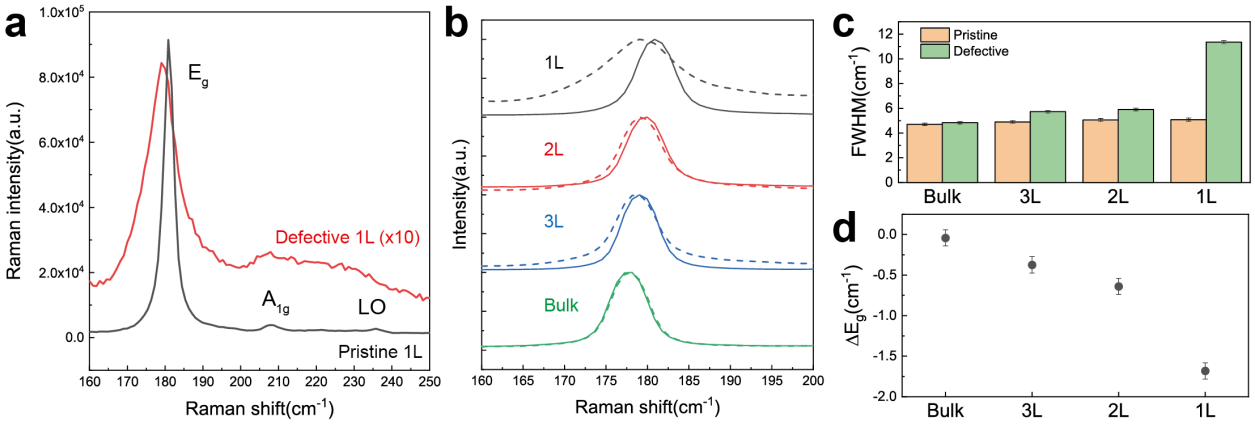

Figure 6-5. **Raman signatures of defective $PtSe_2$**.a) Raman spectra of pristine and defective monolayer $PtSe_2$. Raman intensity from the defective sample is multiplied by 10 for comparison. b) Normalized Raman spectra compared between pristine (solid line) and defective (dashed lines) $PtSe_2$. Raman spectra obtained from the same layer thickness are compared with the intensity being normalized by the intensity of E_g mode. Line colors are assigned to different layers: monolayer(black), bilayer(red), tri-layer(blue) and bulk(green). c) Frequency difference of Eg mode (ΔEg) between pristine and defective $PtSe_2$. E_g peak positions are obtained by Lorenztian fitting, and the shift is calculated by $\Delta E_g = E_g(\text{defective}) - E_g(\text{pristine})$. The amplitude of redshift of E_g mode increases as thickness reduces. d) FWHM of E_g mode compared between pristine and defective $PtSe_2$. The FWMH of Eg mode increases as thickness reduces.

We now directly compare the properties of E_g peak of mono-, bi-, and tri-layer between pristine and defective samples. **Figure 6-5(a)** compares the raw Raman spectra of pristine and defective monolayer $PtSe_2$. We observe that E_g peak redshifts and its intensity drops more than 10-fold with a strong background signal appearing compared to the pristine sample. **Figure 6-5(b)** shows E_g peak spectra between pristine (lines) and defective (dash lines), with offsets for clarify. We extracted E_g peak positions and FWHM values by Lorenztian fitting, summarized in **Figure 6-5(c)**, and **Figure 6-5(d)**, respectively. Unlike bulk samples showing almost the identical overlapping spectra, we found additional E_g peak redshift(ΔE_g) in defective samples, which increases as thickness is reduced, reaching the value of $\Delta E_g = 1.68 cm^{-1}$ for monolayer. This is accompanied by a 3-fold increase in the FWHM of the peak.

We speculate that the structural damage is possibly created during the deposition process of Au atoms (#1 in **Figure 6-2**), which can sputter away the top Pt or Se atoms[49]. We would like to also note again that the sputtering energy of a chalcogen atom for $PtSe_2$ is lower than reported TMDCs (see introduction). **Figure 6-6** shows Raman spectra of pristine $PtSe_2$ after a mild Ar-plasma bombardment and we observe that they are reproducing the Raman spectra of this defective $PtSe_2$ shown in **Figure 6-4(d)**. This result supports the idea that structural defects in Au-assisted exfoliation samples are created from physical damage.

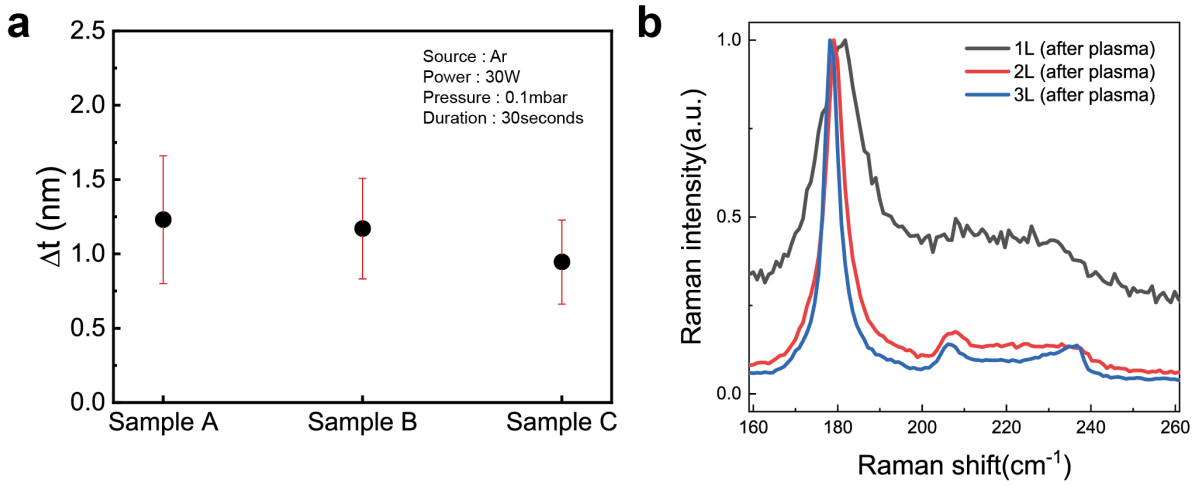

Figure 6-6. **Raman spectra of pristine $PtSe_2$ after mild Ar plasma treatment.**a) Etching $PtSe_2$ by Ar plasma treatment. Using AFM, the thickness variation (Δt) of three different $PtSe_2$ samples (A,B, and C) were checked before and after plasma treatment. Ar plasma effectively etches away $PtSe_2$ at the average rate of 0.36Å/s. b) Raman spectra of regular tape exfoliated $PtSe_2$ after Ar plasma treatment (duration time=7s). $PtSe_2$ is expected to be etched away with the nominal value of 3Å.

Additionally, we show an indication that defects are homogeneously distributed within the entire exposed area. We measured the Raman spectra from different excitation spots as shown in **Figure 6-7(a)**. **Figure 6-7(b-d)** show the Raman spectra taken from mono-, bi- and trilayer thickness, respectively, where the spectra number (e.g. #1) corresponds to the same spot numbered in **Figure 6-7(a)**. We observe well overlapping Raman spectra from the same thickness.

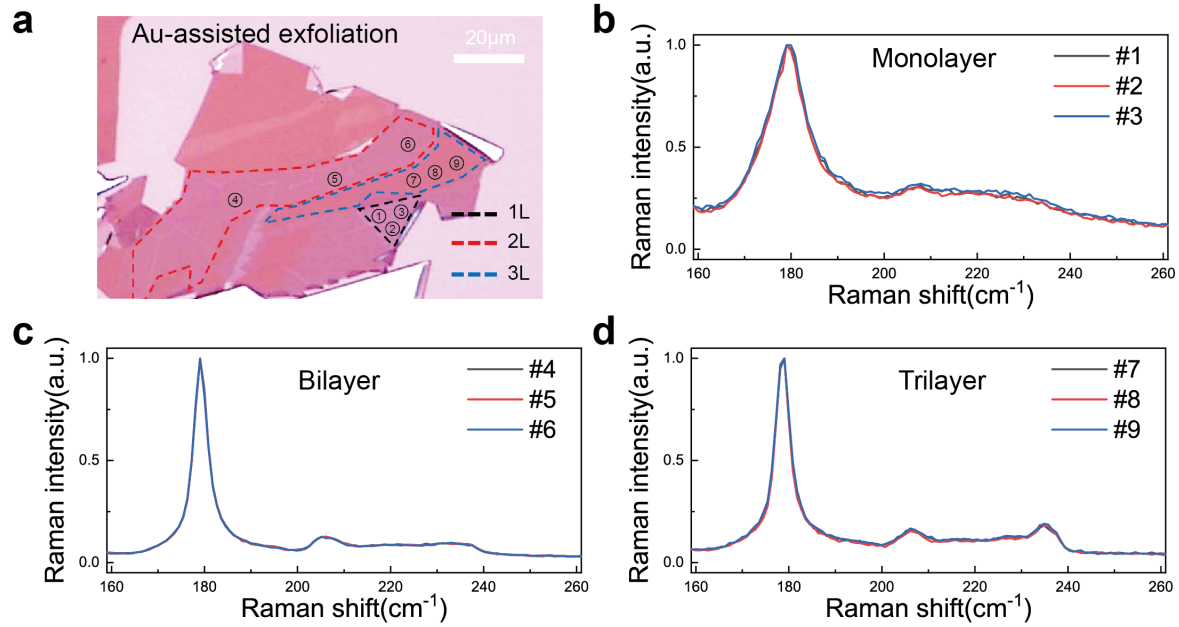

Figure 6-7. **Raman spectra across the area of mono-, bi- and trilayer $PtSe_2$.**a) Optical image of $PtSe_2$ produced by Au-assisted exfoliation. Raman spectra were taken at different laser excitation spots. Laser excitation spots are numbered from 1 to 9. Multiple spots are assigned within the same thickness area: monolayer (#1-#3), bilayer (#4-#6) and trilayer (#7-#9). b-d) Corresponding Raman spectra of $PtSe_2$ obtained from the region of monolayer a), bilayer c), and trilayer d) showing the homogenous Raman signal.

6.4 Optoelectronic measurement result 1

6.4.1 Spatial photovoltage reponse in pristine and defective $PtSe_2$

We now investigate the photoresponse from defective and pristine $PtSe_2$. **Figure 6-8(a)** shows the scanning photovoltage microscopy measurement schematic. A focused 647nm laser under normal incidence was used as the optical excitation, with a focused beam spot size of 1μm achieved by an objective. Light polarization, either linearity or helicity, was controlled by using a quarter-wave plate (QWP) and half-wave plate (HWP), respectively. A piezo-electric nano-positioner was used to scan the laser beam across the entire sample surface by controlling the position of the objective. The resultant photoelectric response, either photocurrent or photovoltage, was measured simultaneously. The electrical connection described in **Figure 6-8(a)** is for describing the open-circuit photovoltage measurement, where we have used lock-in detection to increase the signal-to-noise ratio by using mechanical chopper. All the measurements shown later were taken at room temperature, with the sample being kept under high vacuum condition (P~10^{-6}mbar).

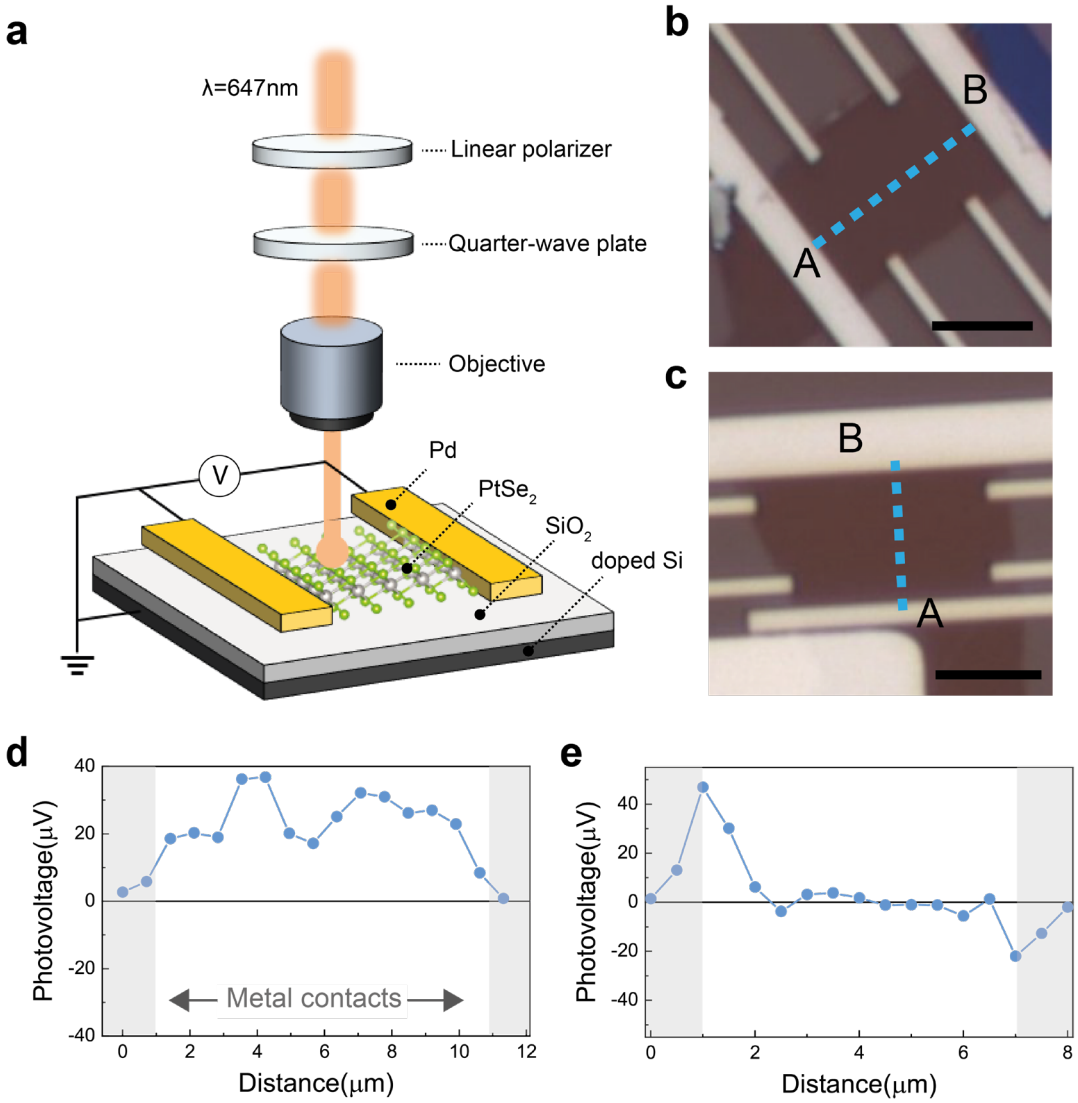

Figure 6-8. **Scanning photovoltage microscopy of defective and pristine 2L $PtSe_2$.**a) Schematic of photovoltage measurement. 647nm wavelength light is used as the optical source. The light polarization is controlled using a linear polarizer and a waveplate (either a quarter-wave plate or a half-wave plate). The laser is focused to 1μm spot size using objective, and the spot is scanned across the device by scanning the objective position using the nano-positioning actuator stage. Simultaneously, generated photovoltage is measured in an open-circuit condition between two Pd electrodes. Laser power of P=200μW with chopper frequency 733Hz is used. b-c) Optical microscopy image of multi-terminal devices made of defective $PtSe_2$ b) and pristine $PtSe_2$ on a SiO_2/doped-Si substrate. c). Scale bar is 5μm. d-e) Photovoltage d) and e) measured by laser line scan along the

dotted blue line in b) and c), respectively. The shaded grey region represents the position of metal electrodes. Here, linear polarization of light is used for the scanning.

Figure 6-8(b) and **Figure 6-8(c)** show the multi-terminal devices on SiO_2/Si substrate from defective and pristine 2L $PtSe_2$, respectively. **Figure 6-8(d)** and **Figure 6-8(e)** show the line profile of open-circuit voltage measured using electrodes A and B for defective, and pristine $PtSe_2$, respectively, while laser scans across the edge of A electrode to the edge of B electrode. From the comparison of the two line profiles, it is evident that there is a significantly different optoelectronic response between pristine and defective samples. For defective $PtSe_2$, photovoltage maximizes around the center position in between the two electrodes and progressively decreases as the laser spot gets close to either edge of the two electrodes. However, for pristine $PtSe_2$, we only observe photovoltage at the edge of the two electrodes with different signs. The latter has been commonly observed at the metal-TMDCs interface and explained by the combination of two main effects: first, electron-hole separation from the built-in electric fields present in the Schottky contact[193] and second, a photo-thermoelectric effect at the interface of two materials with different Seebeck coefficients[194].

6.4.2 Linear- and circular photocurrent in defective $PtSe_2$

To investigate further the abnormal photovoltage response in the defective $PtSe_2$ sample, we measure polarization-dependent photoresponse using the quarter-wave plate while the laser is being positioned at the center of two electrodes. Here, we align the fast axis of the linear polarizer to the principle axis of quarter-wave plate, so that we apply right(left) circular polarization at 45° (135°), and so forth.

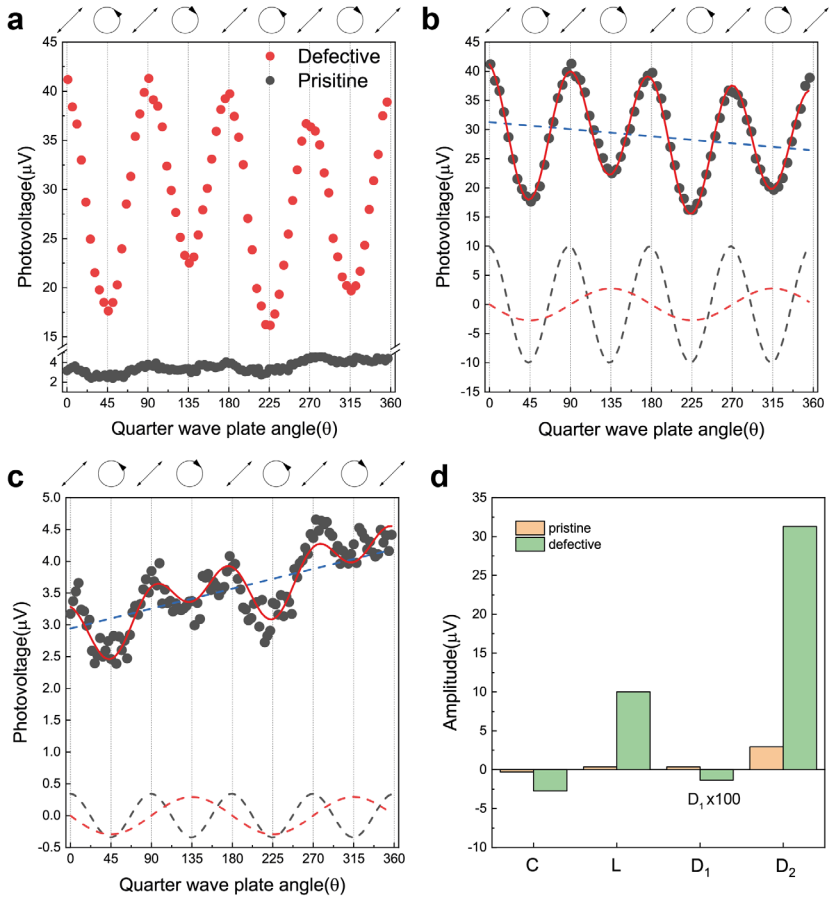

Figure 6-9. **Polarization-resolved photovoltage from defective and pristine 2L $PtSe_2$.** a) Polarization-dependent photovoltage from defective (red dots) and pristine (black dots) bilayer $PtSe_2$. The open-circuit voltage is measured between electrodes A and B (shown in **Figure 6-8(b)** and **Figure 6-8(c)**) while the laser is being focused at the center of two electrodes with the same laser power of 200μW. The laser polarization is simultaneously controlled by quarter wave plate rotation during

the measurement. For both samples, the AC lock-in measurements were performed with the chopper frequency of 723Hz. The background noise level is around 0.7μV. b-c) Photovoltage (black dots) as a function of the quarter wave plate rotation angle for defective b) and pristine c) bilayer $PtSe_2$. Fitting from Eq. (12) is shown as a solid red curve. Dashed color lines represent three major components in the modulation indicated in Eq. (12); $D_1\theta + D_2$ (blue, dashed line), $Csin2\theta$ (red, dashed curve) and $Lsin(4\theta + \theta_0)$ (black, dashed curve). (d) Amplitudes of C, L, D_1 and D_2 in Eq. (12), extracted from defective and pristine samples. D_1 values for both samples are multiplied 100-fold for visibility along with the other amplitudes.

Figure 6-9(a) shows polarization-dependent open-circuit photovoltage measured using A and B electrodes from the defective and pristine sample. Photovoltage from the defective sample shows larger modulation with a quarter wave plate angle and a larger offset value than those obtained from the pristine sample. In order to extract components sensitive to linear and circular polarization, we fit the raw data using a phenomenological expression considering the experimental conditions of quarter-wave plate rotation, which is

$$V_{ph} = Csin2\theta + Lsin(4\theta + \theta_0) + D_1\theta + D_2. \quad (12)$$

Here, θ refers to the angle of the quarter-wave plate defined as the relative angle between the quarter-wave plate fast axis and the axis of the linear-polarizer. C and L indicate the amplitude of circular and linear photocurrent term, and D_2 refers to the amplitude of polarization-independent photocurrent, seen as an offset. Lastly, D_1 accounts for any experimental drift of the sample with respect to the laser spot position during the data acquisition. θ_0 account for a phase shift.

Figure 6-9(b) and **Figure 6-9(c)** represent photovoltage modulation from defective and pristine samples, respectively fitted with Eq. (12). The raw data (black dot) is well fitted with Eq. (12) (red curve), and dotted black, red and blue curves shows the linear-polarization dependent, helicity-dependent, polarization-independent photocurrent components, respectively. **Figure 6-9(d)** summarises the amplitudes of the components between pristine and defective samples. We observe a clear enhancement of all the components (C, L and D_2) in defective $PtSe_2$. We note that the background noise level of voltage when laser is on SiO_2 is around 0.7uV.

The photovoltage generated from a single material away from the contact electrodes narrows down two possible mechanisms, BPVE or photon-drag effect (PDE)[195]. It is generally understood that both effects can produce similar photocurrent response to linear and circular polarization. The light polarization and photocurrent generated from BPVE is in relation under a 3rd-rank tensor, which is written as

$$j_\alpha^{BPVE} = \sigma_{\alpha\beta\gamma}(\omega)E_\beta(\omega)E_\gamma^*(\omega), \quad (13)$$

and the relation for PDE photocurrent is under a 4th-rank tensor, which is

$$j_\alpha^{PDE} = \Phi_{\alpha\beta\gamma\mu}(\omega)q_\mu E_\beta(\omega)E_\gamma^*(\omega). \quad (14)$$

Here, j_α^{BPVE} (j_α^{PDE}) is photocurrent generated from BPVE (PDE). α, β, γ and μ indicate the Cartesian coordinates (x,y and z) and E and q refers to applied electric field and incident photon momentum, respectively. $\sigma_{\alpha\beta\gamma}$ is 3rd rank photogalvanic tensor and $\Phi_{\alpha\beta\gamma\mu}$ is 4th-rank photon-drag tensor. It is worth noting that as the order of tensor rank in Eq. (13) and Eq. (14) dictacts, the bulk photovoltaic effect should appear only in non-centrosymmetric material while PDE can also be present in centrosymmetric material. PDE being sensitive to incident photon momentum, it can only produce non-zero in-plane photocurrent at the experimental condition of oblique incidence ($q_{x,y} \neq 0$).

The condition of normal incidence ($q_{x,y} = 0$) in our experiment is achieved by placing the laser spot at the central position of the lens, which should give net in-plane momenta of focused light to be zero. We have checked such conditions by confirming whether we have a circular and symmetric optical interference fringe pattern in the image of the CCD camera when the laser is being defocused away from the sample plane. Therefore, the photocurrent generated under homogenous illumination from our experimental condition should not be related to PDE mechanism. Importantly, the larger photovoltage signal from the defective sample than the pristine sample cannot be explained by solely PDE considering that the experimental condition of light incidence for both sample measurements is strictly the same. This leads to a conclustion that the enhanced photovoltage signal in defective $PtSe_2$ is attributed to BPVE, which require broken symmetry for $PtSe_2$, and the structural disorder can be a potential source of inducing symmetry breaking.

It is worth exploring another possible source of symmetry breaking reported prior to support our claim that structural defects are the actual main source of BPVE we observe in $PtSe_2$. It has been demonstrated that a built-in electric field from a

Schottky barrier at a metal-semiconductor junction can break the symmetry of the semiconducting material and induce BPVE[196]. We exclude this as a possible source because photovoltage appears when the laser is illuminated away from the electrodes. In addition, symmetry breaking by crystal edge and its concurrent photocurrent under edge illumination are reported[197] but this is not relevant to our experimental condition as the data of **Figure 6-9(a)** is obtained when the laser exciation is focused within the sample and away from the edges. However, there are still some other possible external sources which cannot be neglected at the current stage. One is related to the asymmetric dielectric environment (SiO_2 and vacuum)[91]. The other is the possible formation of local strain during the exfoliation or device fabrication process that is often reported for 2D materials[198]. This motivated us further to fabricate a new device to respond to these other possibilities and to check the validity of our initial claim that structural defects are the actual cause of BPVE for $PtSe_2$.

6.5 h-BN encapsulated sample fabrication

We have fabricated a new h-BN encapsulated $PtSe_2$ device with a top and bottom gate to address the following two questions experimentally.

1. Is the symmetry breaking intrinsic one related to structural defects, or extrinsic one related to either strain or asymmetric dielectric environment?
2. What is the potential explanation for linear and circular photocurrents?

Figure 6-10(a) shows the schematic of materials involved in the device, and **Figure 6-10(b-f)** explain the device fabrication procedure. We first fabricated a local metal gate using Cr 1nm/ Pt 5nm and transferred a bottom h-BN. Then, we pre-patterned contact electrodes (Cr 1nm/Pt 9nm) and transferred $PtSe_2$ by the h-BN pickup transfer method. The h-BN for picking up $PtSe_2$ is used as a top gate dielectric layer. We finalized the device structure by fabricating the top gate electrode made of Pt 5nm.

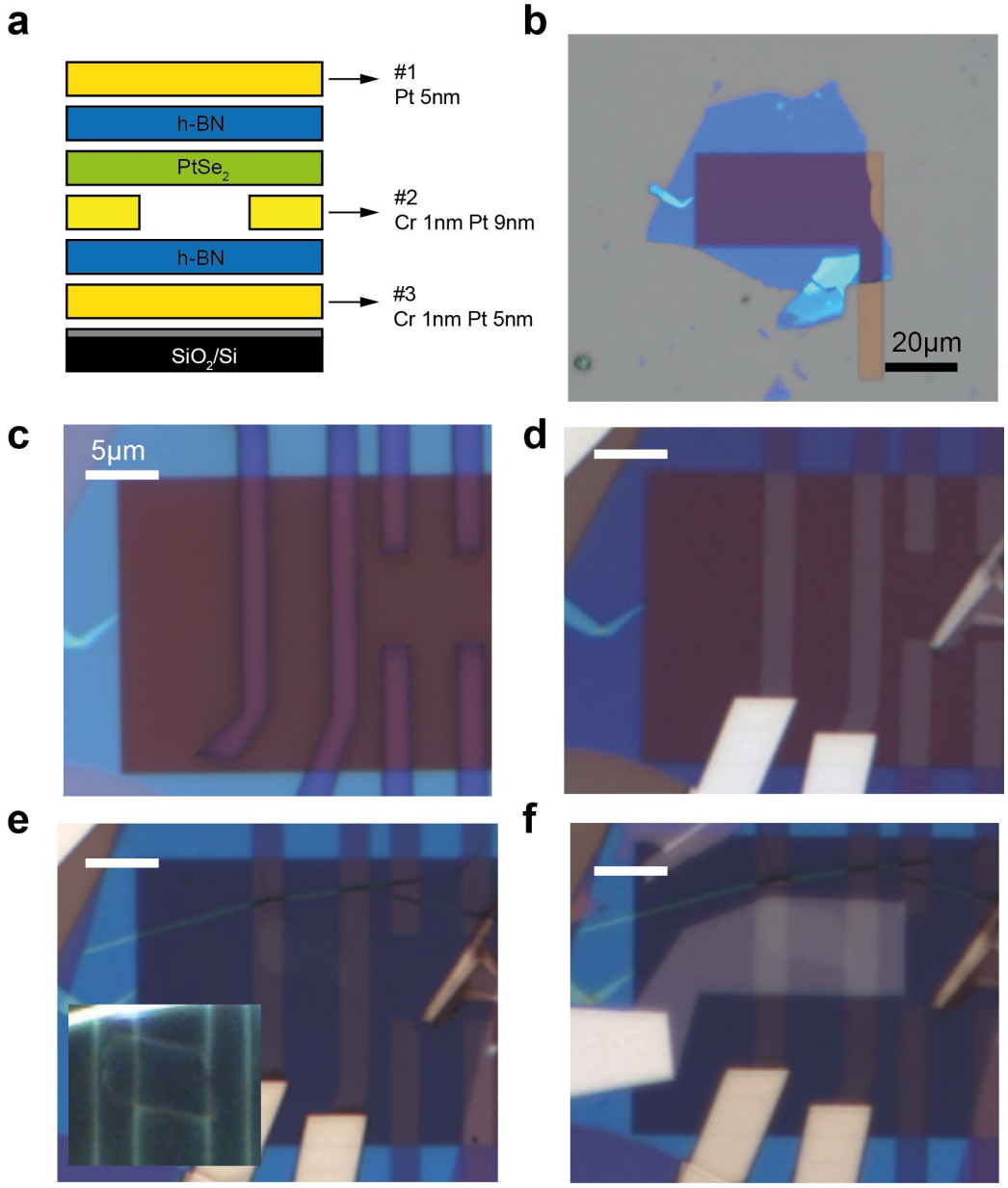

Figure 6-10. **Fabrication of dual-gate h-BN encapsulated $PtSe_2$ device.**a) Schematic showing the material elements used for fabricating the heterostructure. #1, #2, and #3 metal layers colored in yellow serve as a top local gate, pre-contact for $PtSe_2$ and a local bottom gate, respectively. b-f) Optical images showing the fabrication steps. b) Bottom h-BN being transferred on a

local metal gate made of 5nm Pt. c) E-beam pattern of pre-contact electrodes on h-BN layer. d) Deposition of Cr 1nm/Pt 9nm for pre-contact electrodes and Pd 80nm as post-contact electrodes. The post-contact electrode is thick enough to overcome the thickness of the bottom h-BN. e) Bilayer $PtSe_2$ transferred onto the two pre-contact electrodes with top h-BN layer by van der Waals pick up method. Inset shows the dark-field image showing the flake more clearly. f) Fabrication of top metal gate.

Figure 6-11(a) shows the optical microscopy image of a device made of the defective sample, and **Figure 6-11(b)** shows the image of a pristine device where the materials involved are illustrated with color-shaded areas. In these devices, the degree of inversion symmetry breaking can be further tuned by varying the magnitude of the vertical displacement field using the top and the bottom gate electrode. As for the defective device, we fabricated six contact electrodes in circular alignments, which are 60 degrees apart, to examine the tensorial properties of BPVE.

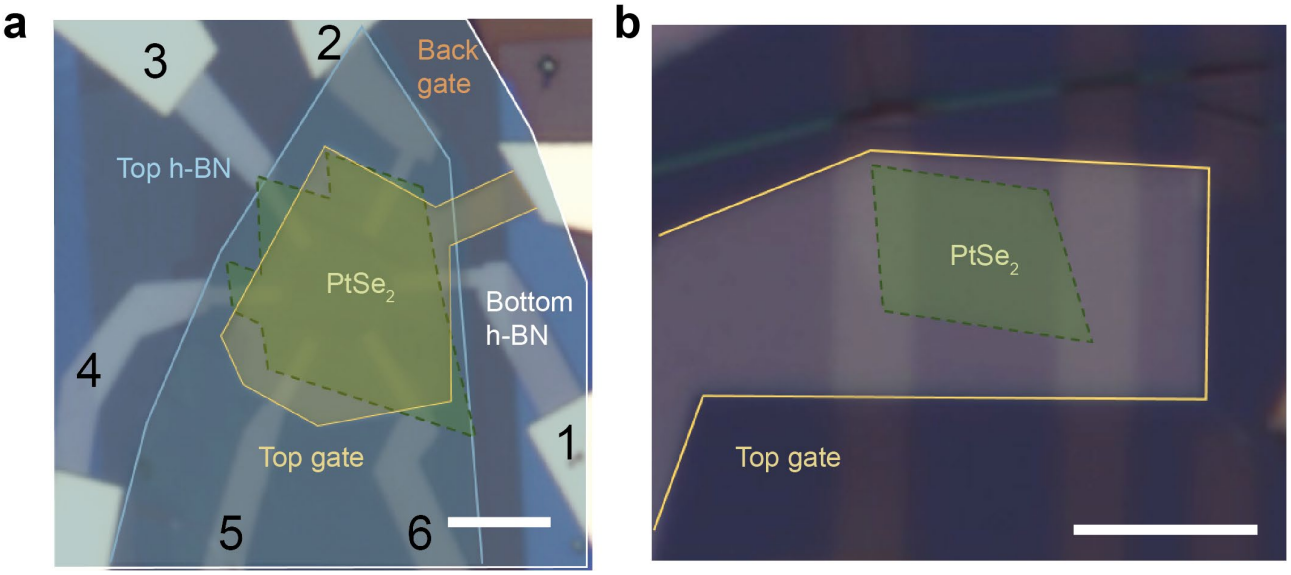

Figure 6-11. **Dual-gate h-BN encapsulated 2L $PtSe_2$ device.**a) Optical image of defective $PtSe_2$ device. b) Optical image of pristine $PtSe_2$ device. The green shaded area represents the area of 2L $PtSe_2$, and the area of the top and bottom metal gates and, h-BN layers are highlighted in different colors. In a), six contact electrodes are numbered. For b), only $PtSe_2$ and top metal gate are displayed for image clarity. Both scale bars are $5\mu m$.

6.6 Optoelectronic measurement result 2

6.6.1 Optoelectronic response reproducing earlier result 1

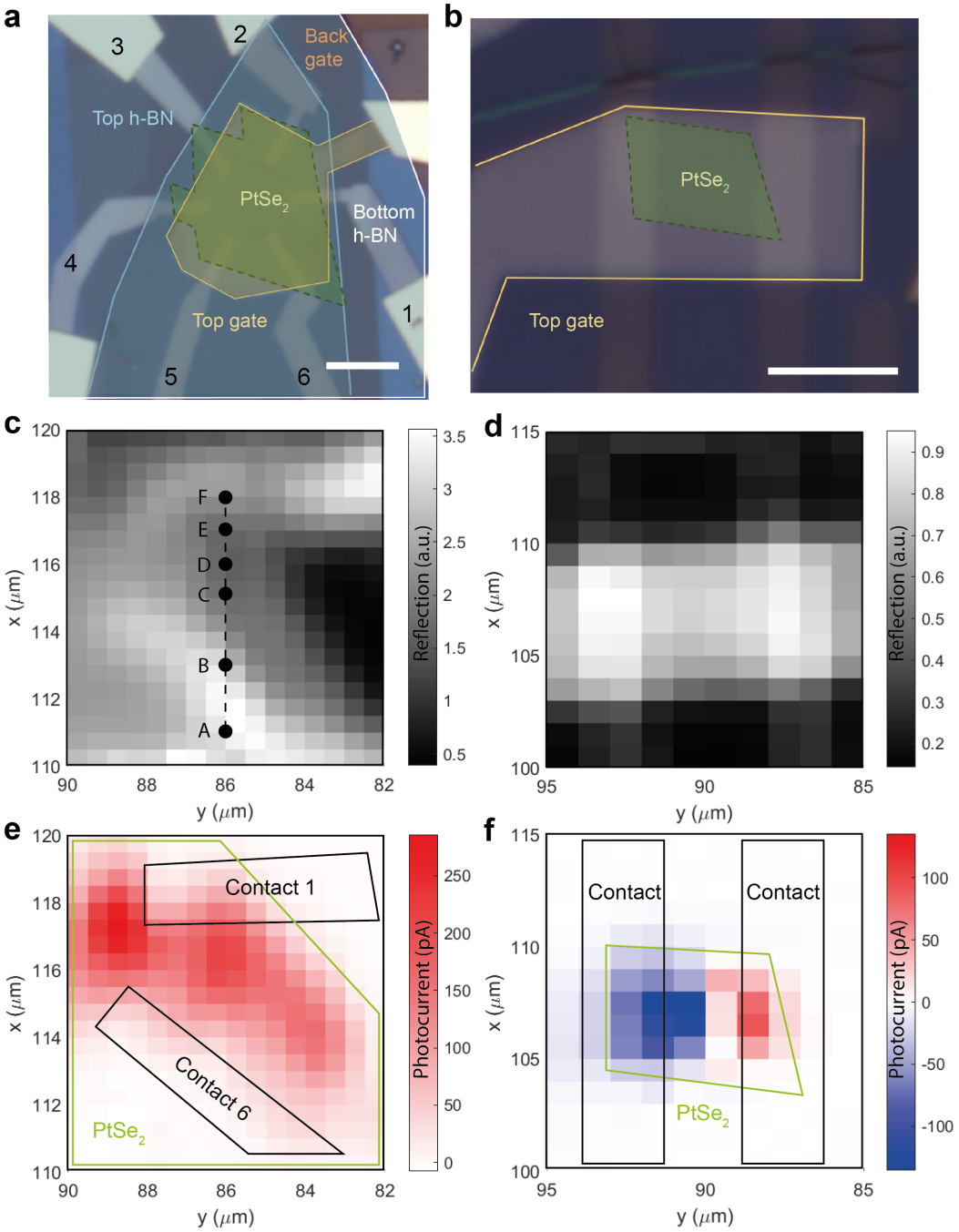

Figure 6-12. **Scanning photocurrent microscopy of h-BN encapsulated 2L $PtSe_2$.**a-b) Optical microscopy image of h-BN encapsulated defective a) and pristine 2L $PtSe_2$ b). c-d) 2D laser reflection mapping of defective c) and pristine sample d). For the defective sample, the mapped area is between contact electrodes #1 and #6. e-f) Zero-biased photocurrent mapping of e) defective and f) pristine sample, simultaneously measured with laser reflection. For defective $PtSe_2$, photocurrent is dominantly generated within the material away from the electrodes, while photocurrent changes its sign at the edges of two opposite electrodes for pristine $PtSe_2$. Here, photocurrent from the defective sample is measured with DC sourcemeter without the chopper at P=160μW. Photocurrent from the pristine sample is measured with lock-in amplifier with chopper frequency of 733Hz at P=200μW. The position of $PtSe_2$ and contact electrodes are highlighted with green and black contour line, respectively.

We first investigate the reproducibility of our previous result of scanning photovoltage microscopies obtained from devices on SiO_2/Si. **Figure 6-12(a)** and **Figure 6-12(b)** show the optical microscopy image of h-BN encapsulated defective and pristine 2L $PtSe_2$, respectively. **Figure 6-12(c)** shows 2D mapping of laser reflection covering the area between the contact electrode #1 and electrode #6 from defective bilayer $PtSe_2$. **Figure 6-12(d)** shows the 2D mapping of laser reflection around the pristine bilayer $PtSe_2$ flake area. Here, linear polarization of light is used for the mapping, and DC photocurrent is measured simultaneously using the two contact electrodes. For the defective device, the rest of non-measured contact electrodes were floated. All the gate electrodes are grounded.

Figure 6-12(e) and **Figure 6-12(f)** compare the obtained result from h-BN encapsulated defective and pristine bilayer $PtSe_2$ under zero-bias condition, respectively. From the reflection map, it is possible to deduce the position of contact electrodes for each device. It is then straightforward to conclude that the photoresponse observed in previous devices on SiO_2/Si are reproducing in h-BN encapsulated devices as well, implying that substrate-induced effect is not the origin of symmetry breaking.

For pristine $PtSe_2$, the sign change of photocurrent is visible at the different edges of the contact electrodes, and for defective $PtSe_2$, photocurrent is generated dominantly within the two contact electrodes and vanishes on the electrodes without changing its sign. The negligible photocurrent generation at the interface between defective $PtSe_2$/contact electrodes is possibly due to the reduced Schottky barrier from the defect-induced mid-gap states in $PtSe_2$.

6.6.2 Consistency between photocurrent and photovoltage

As shown in **Figure 6-13(a)**, both detected modulation of photovoltage and photocurrent against the waveplate rotation angle matches well to each other. This is generally seen in other 2D materials as well[195,199]. Here, the photovoltage is the root-mean-square amplitude of AC photovoltage measured by the lock-in amplifier. This consistent photoresponse is also well-captured also by DC IV-curve measurements at different light polarization, as shown in **Figure 6-13(b)**. Y-intercept value in IV curves corresponds to the spontaneous generation of photocurrent at V_{SD}=0V and shows polarization dependence. X-intercept value corresponds to the open-circuit DC photovoltage (I_{SD}=0A).

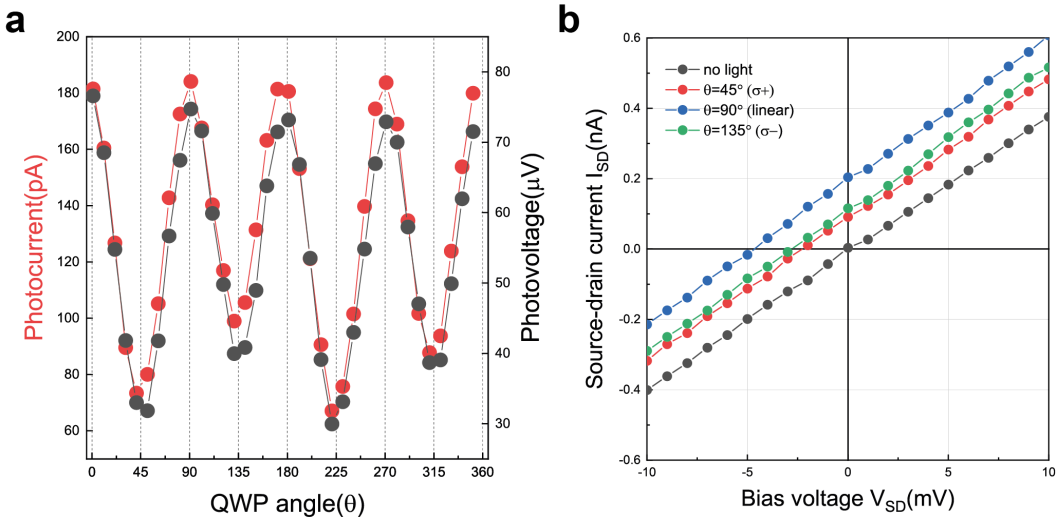

Figure 6-13. **Consistency between photocurrent and photovoltage.**a) Photocurrent and photovoltage measured while rotating quarter wave plate angle. Both short-circuit zero-biased current and open-circuit voltage measurements show the same photoresponse from QWP angle modulation. Here, photocurrent is measured with DC sourcemeter without the chopper at P=160μW, and photovoltage is measured with lock-in amplifier with chopper frequency of 133Hz at P=100μW. b) DC IV-characteristic of defective 2L $PtSe_2$ with linearly and two circularly polarized (σ+ and σ-) light incidence at P=160μW, compared with no light.

6.6.3 Spatial dependence of BPVE

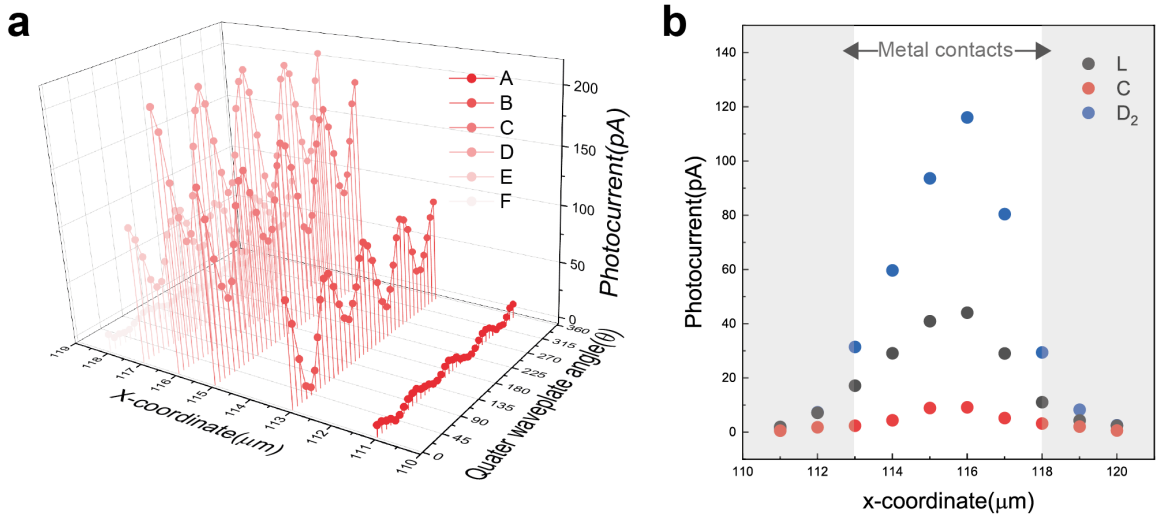

Figure 6-14. **Position-dependent zero-biased photocurrents.**a) Photocurrents measured while rotating QWP angle at different laser spot positions (A,B,…F) marked in Figure d) at P=160μW. b) L, C and D_2 components of photocurrent at different x-coordinates averaged from two vertical lines of y=85μm, and 86μm. The amplitude of all the components increases maximally near the center of two measuring electrodes.

Figure 6-14(a) shows the set of photocurrents by quarter-wave plate rotation measured from different laser spots, labelled by letters, along the line depicted in **Figure 6-12(c)**. The extracted amplitudes of linear and circular components and offsets are displayed in **Figure 6-14(b)** with respect to the x coordinates of the laser spots. We can distinguish linear and circular components and offsets get maximized near the center position between two electrodes.

Notably, the offset we measure is distinctly different from the photothermoelectric effect, induced by an asymmetric thermal gradient where the signal maximizes near the contact electrodes[200]. This polarization-independent offset instead shares the similar origin of other amplitudes components, which will be discussed later.

6.6.4 Power dependence of BPVE

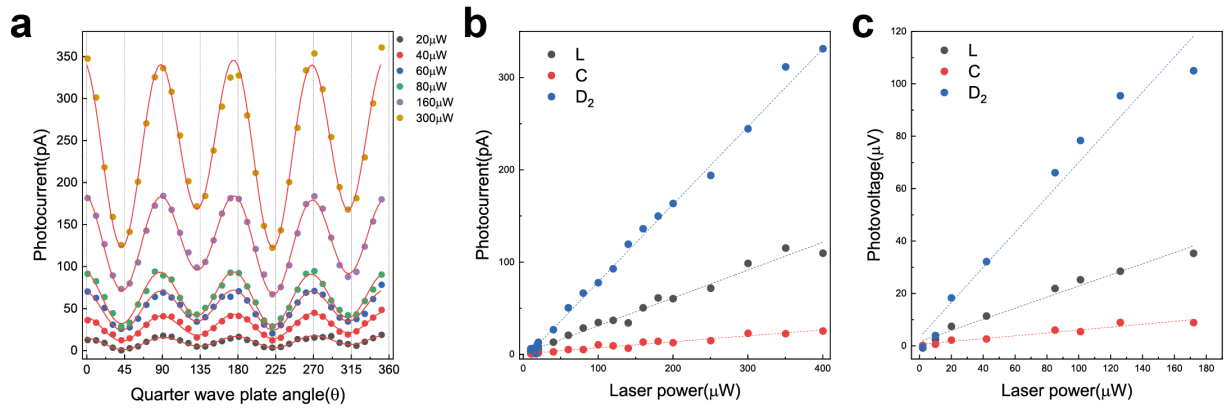

Figure 6-15. **Laser power dependence.**a) Quarter-wave plate angle-dependent zero-biased photocurrent measured at different laser power. The red curve is the fitting from the phenomenological equation. b) Extracted *L*, *C* and D_2 parameters of photocurrent with respect to the laser power where each photocurrent amplitude show linear power dependence fitted by dashed lines.

We have measured photocurrent at different laser illumination power while rotating quarter-wave plate angles, as shown in **Figure 6-15(a)**. The amplitude of *L*, *C* and D_2 components can be extracted by fitting (red curve), and their amplitude with respect to laser power are summarized in **Figure 6-15(b)**. The three photocurrent components (*L*, *C* and D_2) increase linearly with illumination power, confirming that they originated in the second-order response to the light electric field.

6.7 Discussion

6.7.1 Possible origin of LPGE, CPGE and offset

At the excitation with homogeneous radiation at normal incidence, the presence of circular photocurrent gives evidence that the symmetry of defective $PtSe_2$ has reduced to, at most, a single mirror-plane symmetry[195]. From the previously reported literature, non-zero circular photocurrent component under normal incidence has been demonstrated in twisted(θ=0.6°) bilayer graphene[201] and disordered domains of $MoTe_2$[202], where symmetry is expected to be reduced to C_1 symmetry. It is also found that optical field gradients[203] or built-in electric fields[204] can also lower the symmetry externally up to the level where circular photocurrent can appear with normal incidence. Furthermore, the presence of polarization-independent photocurrent in defective $PtSe_2$, which is not due to the thermal gradient, can be possibly explained by the same low symmetry arguments. This is because BPVE can persist without polarization dependence if threefold rotational and mirror symmetries of the 2D sheets are removed[184].

The CPGE and polarization-independent BPVE can be present if our $PtSe_2$ is strained, reducing the crystal symmetry to C_1. In order to examine the possibility of the sample being strained, we have measured linear photogalvanic voltage with diagonal pairs of contacts with the laser excitation at the center of six electrodes. The linear polarization angle(α) is controlled by a half-wave plate. **Figure 6-16(a)** shows the raw data obtained by measuring the voltage of an electrode in reference to the voltage of the opposite side electrode. For example, referencing to the electrode numbering indicated in **Figure 6-12(a)**, $V_{1\text{-}4}$ related to the voltage of electrode #1 in reference to the voltage of electrode #4. The offset and the amplitude of linear photogalvanic voltage measured with different diagonal pairs are not the same, and we attribute this to the inhomogeneities of the transport channel between the diagonal electrodes. **Figure 6-16(b)** shows the polar plot of normalized photovoltage after removing the offset, where, most importantly, we observe a constant phase shift of LPGE signals. This suggests that the rotational symmetry is preserved in probed samples and allows us to exclude strain as the source of breaking crystal symmetry of $PtSe_2$.

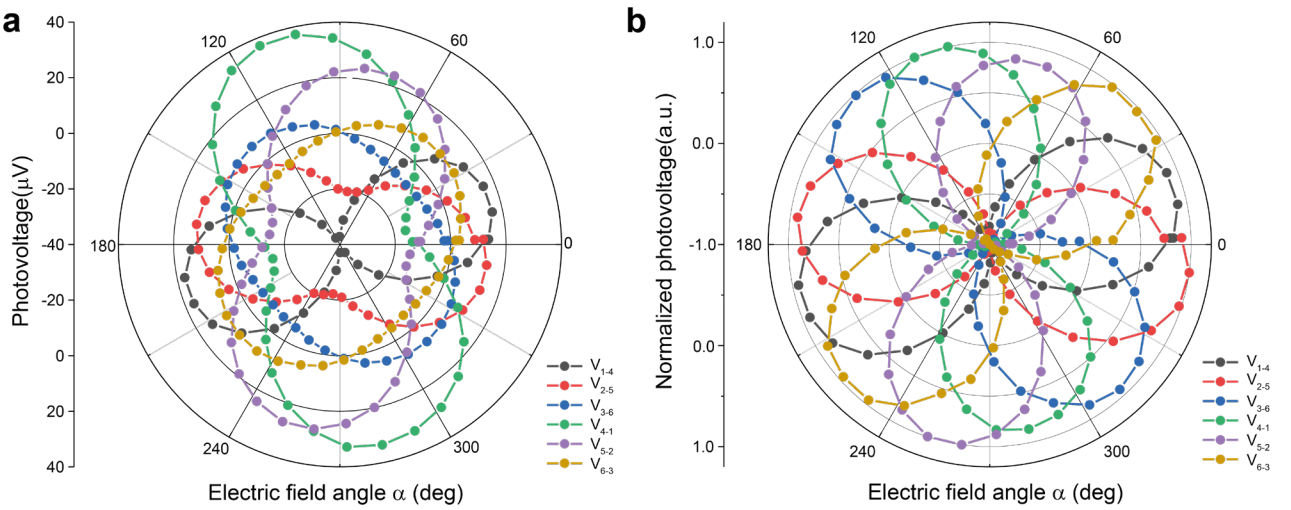

Figure 6-16. **Photovoltage from six diagonal pairs.**a) Polarplot of photovoltage data from six diagonal pairs. The focused laser spot (P=150μW) is positioned at the center of six diagonal pairs and the linear polarization angle(α) is controlled by half-wave plate rotation. Simultaneously, photovoltage (e.g. $V_{1\text{-}4}$) is measured between an electrode (e.g. #1) and the opposite electrode (e.g. #4) via lock-in detection with a reference frequency set to 267Hz. b) Polarplot of photovoltage normalized with its maximum after subtracting its individual offset.

Additionally, we have investigated how externally applied vertical electric field affects the LPGE and CPGE. Upon electrical gating to the top and bottom gate, the average of two electrical displacement fields from the top (D_t) and bottom gate (D_b), which is $\bar{D} = (D_t + D_b)/2$, can further break the symmetry of the material. Displacement fields of the top (D_t) and bottom gate (D_b) by applied gate voltages (V) can be defined under the relation, $D_t = -\varepsilon_r \frac{V_t}{d_t}$ and $D_b = \varepsilon_r \frac{V_b}{d_b}$, where ε_r and d are perimtivity and the thickness of a dielectric layer, respectively. The top and bottom h-BN layers thickness are 18.5nm and 26nm, respectively, measured by AFM.

We have measured photocurrent using electrodes #1 and #6 while positioning laser excitation at the center of those two electrodes. **Figure 6-17(a)** shows the vertical displacement field ($\bar{D}$) dependence of linear and circular photogalvanic photocurrent and **Figure 6-17(b)** shows the dependence of photovoltage. In both our photocurrent and photovoltage experiments, the source contact is grounded while the rest of the contacts are floated, and displacement fields are controlled independently by applied gate voltages to the top and bottom gates.

Both circular photocurrent and photovoltage amplitudes are rather insensitive to the external electrical field. In other words, the external electric field can no longer reduce the symmetry-related to CPGE. This observation can indeed support the lowest symmetry argument, as mentioned earlier for CPGE. However, the amplitudes of linear photocurrent and photovoltage show quadratic improvement with the increment of the vertical displacement field in both directions (see red guideline is the fitted curve from 2nd order polynomial). This can be explained if we assume that LPGE is coming from the source of higher-order symmetry, and the lowering of such symmetry leads to a larger amplitude of LPGE. The linear photogalvanic signal is enhanced 75% at $\bar{D}$=0.2V/nm.

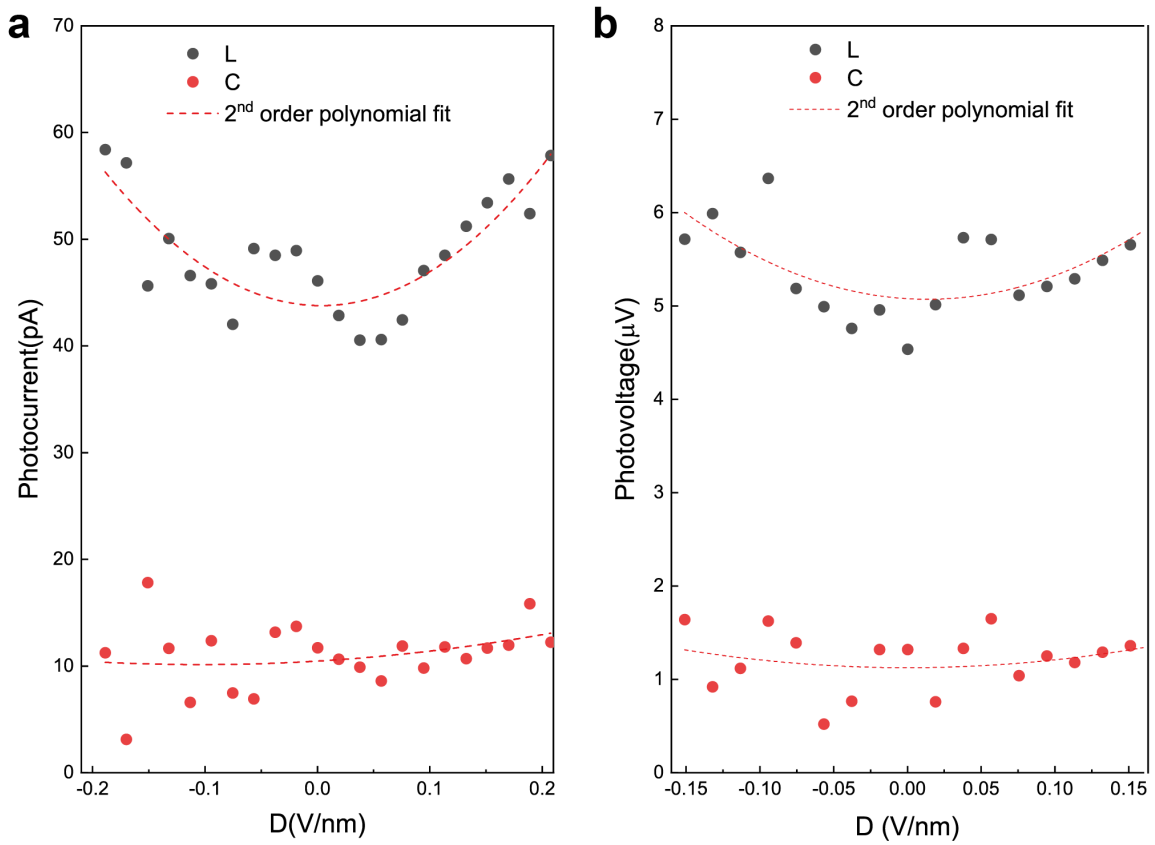

Figure 6-17. **Displacement field dependence of LPGE and CPGE.**a) Amplitude of linear- and circular-polarized current with varying the amplitude and direction of the vertical displacement field. The photocurrent is measured with the laser power of P=160μW. c) Amplitude of linear- and circular-polarized photovoltage with varying the amplitude and direction of the vertical displacement field. The photovoltage is measured with the laser power of P=60μW using lock-in detection at the chopper frequency 733Hz.

6.7.2 TEM analysis on defective $PtSe_2$

With no strain present in our device, we argue that the BPVE stems from broken crystal symmetry induced by structural atomic defects. In order to directly visualize and confirm the presence of structural disorder, we've obtained a high-resolution image of atomic structure by TEM. **Figure 6-18** shows the TEM image of bilayer $PtSe_2$ from Au-assisted exfoliation, where we can see 0D point defects (e.g. V_{se}, V_{pt}) as well as large cluster-like defects. **Figure 6-18(a-b)** shows the large and small field of view of the atomic structure of $PtSe_2$, respectively.

We attribute different types of local atomic defects to the possible origin of LPGE and CPGE. We claim that cluster-like defects are related to the generation of CPGE as well as polarization-independent BPVE, as it reduces the symmetry to the lowest from C_3 to C_1. The point-defects, such as Se-vacancies, hold 3-fold rotation symmetry and can be considered as the candidate for linear-photogalvanic signals.

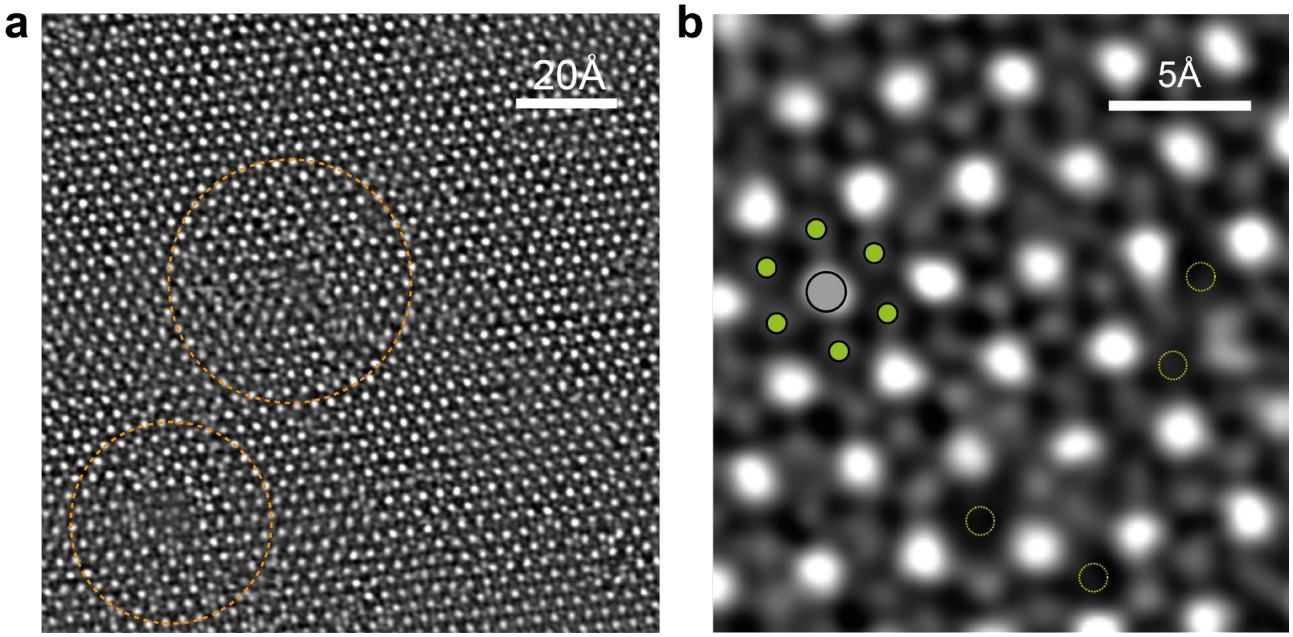

Figure 6-18. **Imaging of atomic defects in 2L $PtSe_2$ through high-resolution TEM.**a) Atomic structure of bilayer $PtSe_2$ (obtained by Au-assisted exfoliation technique) in a large field of view(12nm×12nm). Cluster-like defects (dashed orange circles) are visible. b) Atomic structure with a smaller field of view(2nm×2nm). Pt and Se atoms are marked with grey and green color filled circles, respectively, representing the 1T phase crystal structure of $PtSe_2$. Se point vacancies (dotted yellow circle) are visible. We note that we cannot see Au atoms on the lattice of $PtSe_2$ in the TEM images.

6.7.3 Charge transport in pristine and defective $PtSe_2$

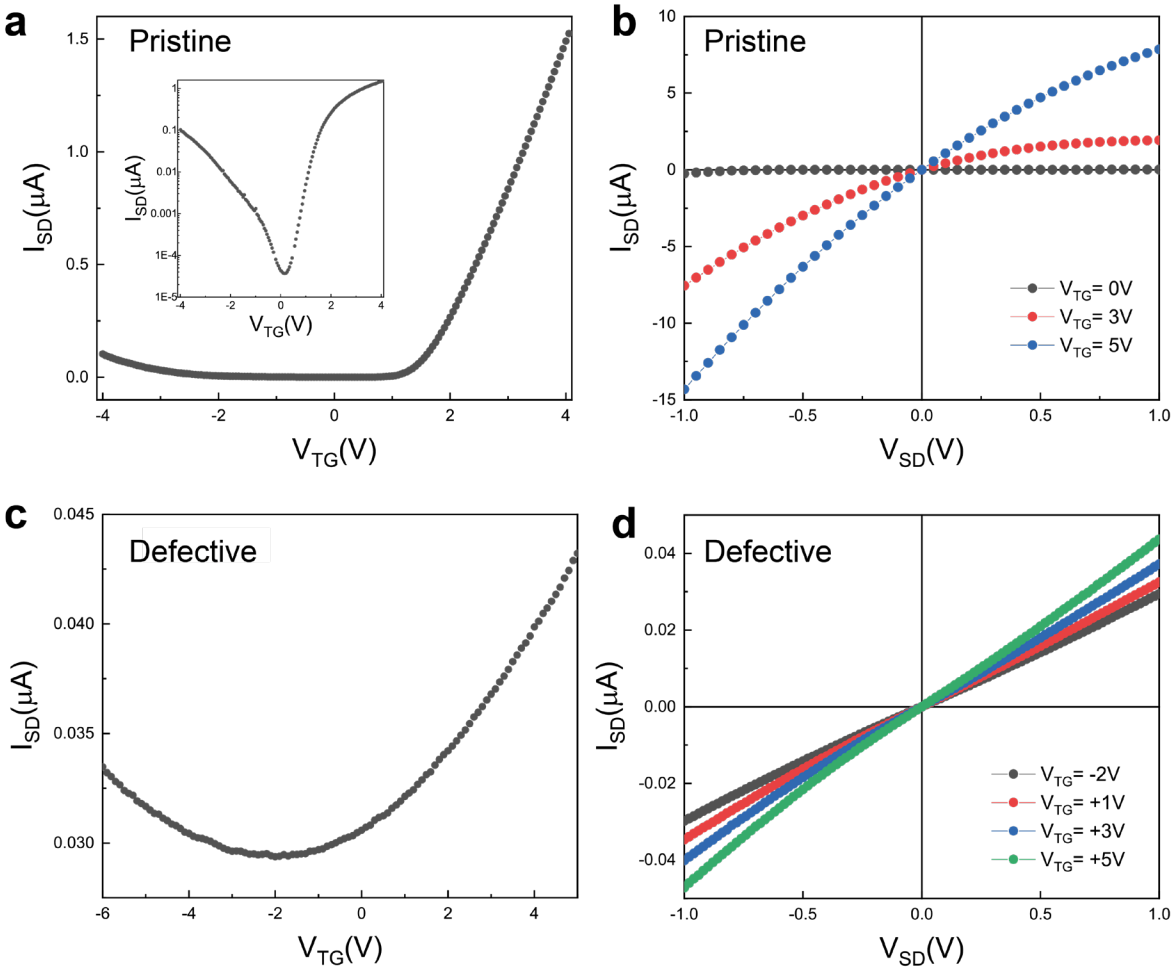

Figure 6-19. **Charge transport showing possible defect-induced midgap states in $PtSe_2$.**a-b) top gate(V_{TG}) dependent source-drain current (I_{SD}) measured from h-BN encapsulated pristine 2L $PtSe_2$ a) with bias voltage of V_{SD}=50mV, and defective 2L $PtSe_2$ b) with V_{SD}=200mV using contact electrode #1(source) and #6(drain). c-d) *IV*-characteristic measured from pristine c) and defective 2L $PtSe_2$ d) at selected top gate values.

Such structural disorder observed from atomic imaging should impact the charge transport in $PtSe_2$. We have measured two-terminal charge transport without light between two electrodes of pristine and defective $PtSe_2$(using electrodes #1 and #6). **Figure 6-19(a)** shows the top gate (V_{TG}) dependence of 2-terminal I_{SD} of pristine bilayer $PtSe_2$, measured at V_{SD}=200mV, showing clear ambipolar conductance (on-off ratio of 10^4). **Figure 6-19(c)** shows the *IV* curves at selected top gate voltages of 0, +3 and +5V, which exhibit strong asymmetric behavior possibly induced by asymmetric Schottky barriers at the Pt/$PtSe_2$ interface.

As shown in **Figure 6-19(b)**, the on-off ratio of the top gate (V_{TG}) dependence of 2-terminal I_{SD} (V_{SD}=200mV) from defective $PtSe_2$, however, is significantly reduced to around 1.4 with a large off-state current within the bandgap, compared to pristine $PtSe_2$. The large reduction of conductance signifies the strong scattering during the charge transport. The *IV* curves presented in **Figure 6-19(d)** show a close to linear relationship for all the selected gate voltages when the Fermi levels of $PtSe_2$ are placed in the valence band, within the bandgap, and conduction band. Both low on-off ratio of conduction modulation with gate voltage and near-linear *IV* characteristic imply a metal-like character that a large amount of mid-gap states exist in $PtSe_2$ due to defects[74].

6.7.4 Macroscopic mechanism of LPGE

The macroscopic origin of LPGE can be due to asymmetric excitation in k-space from the optical selection rule, or the asymmetric elastic scattering of the photo-excited carriers. Here, to obtain an intuitive picture, we describe our observed linear photogalvanic effect with diagonal pairs following the well-known wedge model that accounted for asymmetric elastic scattering[205]. The model explains the generation of DC current from alternating AC *E*-field from light, a process provided by elastic scattering of a particle from a potential lacking inversion symmetry, a wedge-shaped potential. This model has been adopted for describing linear photogalvanic effect in various 2D systems, including 2D GaN/AlGaN[206] and $PdTe_2$[207].

Before moving on, we first explain the conceptual picture of how the scattering of the particles takes place to produce the linear photogalvanic effect. At the illumination of an external alternating *E*-field on a matter, the distribution of charged particle momenta maintains anisotropic (**Figure 6-20(a)**); there is a larger number of particles moving in parallel to the direction of the applied electric field and a smaller number in the perpendicular direction. However, the corresponding stationary momentum distribution, displayed as a grey ellipse, does not produce measurable DC current but upon scattering by trigonal symmetric potentials, resulting in uncompensated charged particle flow (**Figure 6-20(b)**).

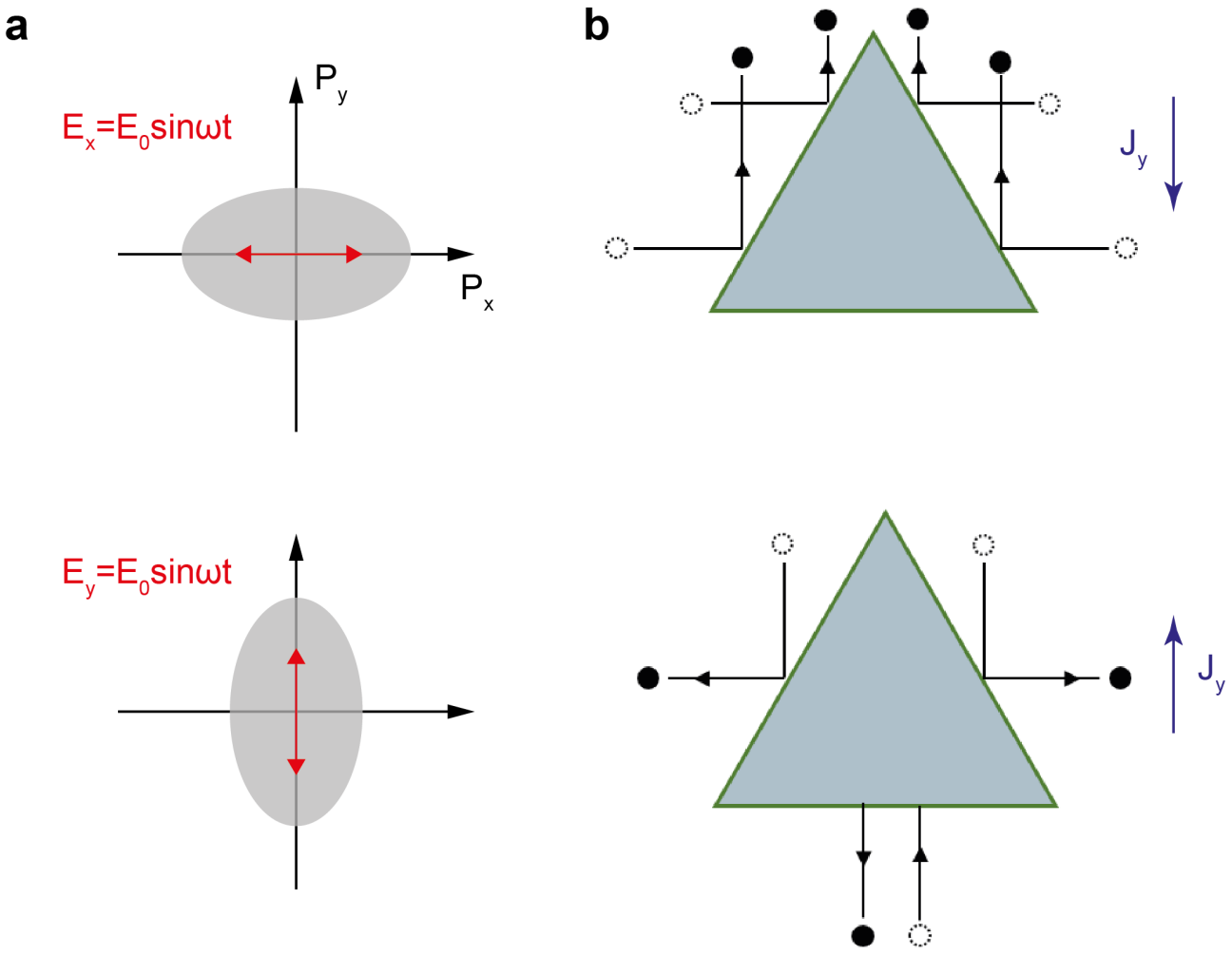

Figure 6-20. **Asymmetric scattering mechanism of LPGE**.a) Anisotropic distribution of in-plane momenta of charged particles with respect to the incident ac electric field from light. b) Schematic of scattering process producing electrical dc current by a wedge-shaped asymmetric potential. This potential has a 3-fold rotation symmetry and lacks inversion symmetry. With ac electric being polarized in the x or y-axis, charge particle momenta in the x-direction are compensated after scattering, producing a net zero dc current (blue arrow) only in the y-direction. Here, the direction of dc current assumes the charged particles to be electrons.

Considering the particles as electrons(n-doped), when the E-field oscillates along the x-axis (y-axis), the momentum-aligned electron gets scattered and produces a net electrical current in the –y (+y) direction, whereas the scattered electron momentum is compensated in the x-direction as a whole. The relative alignment between linear polarization and the wedge plane determines the net electric current direction produced and therefore enables the generation of linear polarization-dependent photocurrent.

6.7.5 Determination of crystallographic axis based on point-defect induced LPGE

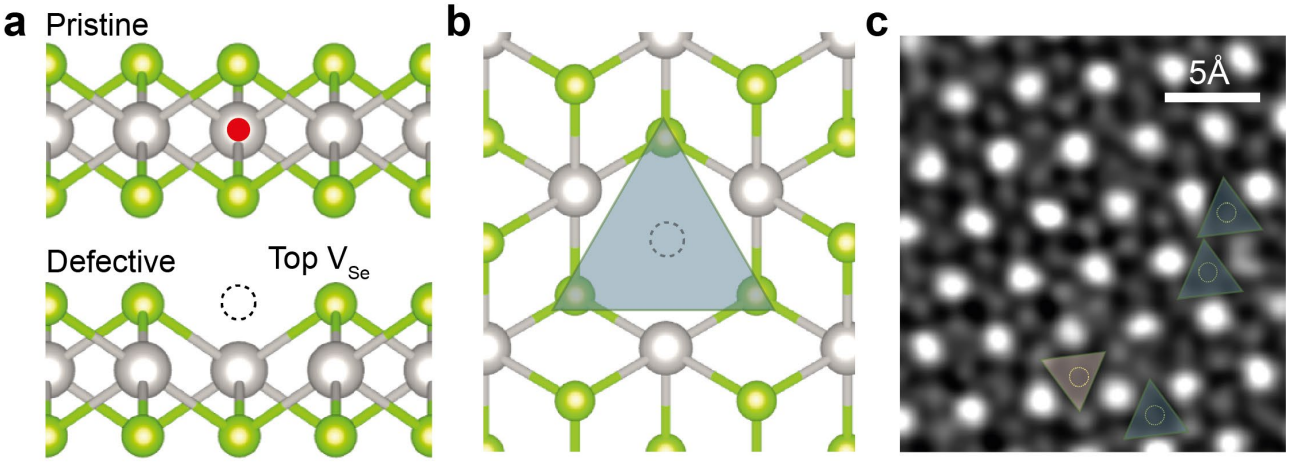

Figure 6-21. **Single Se vacancy in $PtSe_2$, a source of asymmetric scattering potential.**a) Schematic of atomic structure of pristine(top) and defective(below) monolayer $PtSe_2$. The position of the central Pt atom holds the inversion center of pristine $PtSe_2$ while creating one Se vacancy (dotted circle) can locally break the inversion symmetry. The effect of local symmetry breaking from top Se vacancy is expected to increase with decreasing the number of layers, maximizing its effect at the monolayer thickness. b) Wedge-shaped scattering potential overlaid at the center of top Se vacancy (dotted circle). c) Wedge potentials overlaid at the location of top Se vacancies in the TEM image of bilayer $PtSe_2$ shown in **Figure 6-18(b)**. Single Se vacancy from top and bottom Se layer gives two different wedge potentials that are inverted one another, as defined by green and orange colored wedges. The corners of the wedges are placed at the position of bottom(top) Se atoms for the top(bottom) Se vacancy.

Commonly, the wedge model assumes the particles are scattered by randomly located but identically orientated ideal trigonal symmetry edges, which lack an inversion center[205]. As for such scatter, Coulomb impurities or phonons have been considered in the case of 2D GaN/AlGaN[206], grown Sb_2Te_3 and Bi_2Te_3[208], and for in twisted bilayer graphene[201], triangular domain walls connecting AB and BA regions. In the case of $PtSe_2$, we picture Se point-defect as the most suitable scatter, as it breaks inversion symmetry (**Figure 6-21(a)**) and holds local trigonal symmetry (**Figure 6-21(b)**). Chalcogen vacancies are also known to be the most common defects among 0D and 1D type defects in TMDCs[189], and it is also one of the most abundant defects, in $PtSe_2$[160,209].

From the atomic image of **Figure 6-18(b)**, we observe Se vacancies at either top or bottom Se layer. Top and bottom Se vacancy provide wedges that are inverted to one another, illustrated as green and orange colored wedges, respectively, in **Figure 6-21(c)**. As the scattering process is revered between these two inverted wedges, the equal amount of top and bottom Se vacancies would effectively result in the absence of LPGE. Therefore, we assume that Se vacancies in one of two locations outnumber our sample. This assumption is supported by a recent report where they found that top layer Se vacancies in $PtSe_2$ dominate with a ratio of 20:1 due to their difference in the formation energy[159].

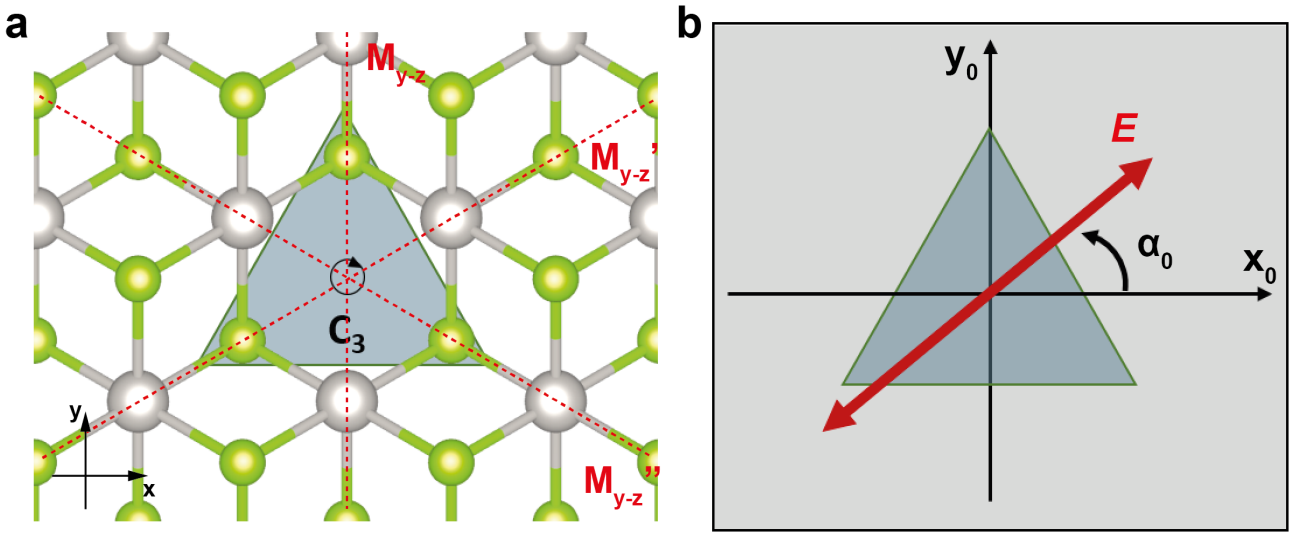

Figure 6-22. **Modeling Se point defect (V_{se})-induced LPGE.**a) Symmetry of Se point defect in $PtSe_2$. Top Se vacancy breaks inversion symmetry. Its point group belongs to C_{3v}. A schematic of the monolayer $PtSe_2$ atomic structure crystal is displayed for clarity in visualising the defect. The local symmetry of V_{se} is the same for monolayer and bilayer $PtSe_2$. b) Schematic representation of a wedge potential. x_0-axis is the axis perpendicular to the mirror plane of the wedge, parallel to y_0. In $PtSe_2$, x_0-axis belongs to one of the zigzag edges, and y_0-axis is along with one of the armchair edges. A double red arrow indicates the ac electric field from the incident light. The azimuth angle α_0 is counted from the x_0 axis.

In order to verify our argument that point-defect can be the source of LPGE, we attempt to experimentally determine the crystallographic axis of $PtSe_2$ from measured linear photogalvanic voltage from **Figure 6-16(b)**. We start with taking into consideration of Neumann's principle of symmetry which states that the symmetry of any physical property of a crystal must include the symmetry elements of the point group of the crystal. The relevent physical property to BPVE is the second-order susceptibility tensor and, without considering the microscopic origin, the linear photogalvanic photovoltage (V^{LPGE}) can be written as,

$$V_{\alpha}^{LPGE} = t\chi_{\alpha\beta\gamma}\left(E_{\beta}(\omega)E_{\gamma}^{*}(\omega) + E_{\beta}(\omega)E_{\gamma}^{*}(\omega)\right). \tag{15}$$

Here, E is the electric field and χ is the third-rank photogalvanic tensor. α, β and γ runs over all the Cartesians coordinates (x, y and z). t is the coefficient referring to the ratio between photogalvanic voltage and current.

When the inversion operation is applied to Eq (15), V_{α}^{LPGE} changes its sign, yet $E_{\beta}(\omega)E_{\gamma}^{*}(\omega)$ does not and if we consider the inversion symmetry of pristine $PtSe_2$, χ maintains the sign under the inversion operation. To satisfy the sign of the equation, all the elements in χ has to be zero, which, in order words, BPVE is not allowed for pristine $PtSe_2$. We consider instead the term, crystal, noted in Neumann's principle to be a structural defect in $PtSe_2$. Following the principle, the local symmetry of Se-vacancy restricts the form of the second-order susceptibility tensor. As shown in **Figure 6-22(a)**, for Se-vacancy in $PtSe_2$, three mirror planes perpendicular to the 2D plane are parallel to the 3-fold rotation axis along with the position of the missing Se atom, constructing C_{3v} point group symmetry. For this point group, there are four linearly independent components in the χ[210]:

$$\chi_1 = \chi_{xxz} = \chi_{yyz}, \tag{16}$$
$$\chi_2 = \chi_{xxy} = \chi_{yxx} = -\chi_{yyy}, \tag{17}$$
$$\chi_3 = \chi_{zxx} = \chi_{zyy}, \tag{18}$$
$$\chi_4 = \chi_{zzz}, \tag{19}$$

where the x-axis is defined perpendicularly to the M_{y-z} mirror plane shown in **Figure 6-22(a)**. Inserting Eq. (16-19) into Eq. (15) gives,

$$\begin{bmatrix} V_x \\ V_y \\ V_z \end{bmatrix} = t \begin{bmatrix} 0 & 0 & 0 & 0 & \chi_1 & -\chi_2 \\ -\chi_2 & \chi_2 & 0 & \chi_1 & 0 & 0 \\ \chi_3 & \chi_3 & \chi_4 & 0 & 0 & 0 \end{bmatrix} \begin{bmatrix} E_x^2 \\ E_y^2 \\ E_z^2 \\ 2E_yE_z \\ 2E_xE_z \\ 2E_xE_y \end{bmatrix}. \tag{20}$$

As we are interested in photovoltage generated in the 2D plane, we only consider V_x and V_y. V_x can be written as

$$V_{x0}^{LPGE} = t\chi_1(E_{x0}E_{z0}^* + E_{z0}E_{x0}^*) + t\chi_2(E_{x0}E_{y0}^* + E_{y0}E_{x0}^*), \tag{21}$$

and V_y can be written as

$$V_{y0}^{LPGE} = t\chi_1(E_{y0}E_{z0}^* + E_{z0}E_{y0}^*) + t\chi_2\left(|E_{x0}|^2 - |E_{y0}|^2\right). \tag{22}$$

Here, we use the notation of x_0, y_0 and z_0 for x, y and z Cartesians coordinate for the sake of convenience for the later explanation. Considering normal incidence ($E_{z0} = 0$), Eq. (21) becomes

$$V_{x0}^{LPGE} = t\chi_2(E_{x0}E_{y0}^* + E_{y0}E_{x0}^*), \tag{23}$$

and Eq. (22) becomes,

$$V_{y0}^{LPGE} = t\chi_2\left(|E_{x0}|^2 - |E_{y0}|^2\right). \tag{24}$$

Consider the angle α_0 of electric field from x_0, Eq. (23) and Eq. (24) can be re-written as

$$V_{x0}^{LPGE} = t\chi_2(E_{x0}E_{y0}^* + E_{y0}E_{x0}^*) = t\chi_2|E_0|^2 sin2\alpha_0, \tag{25}$$

and

$$V_{y0}^{LPGE} = t\chi_2\left(|E_{x0}|^2 - |E_{y0}|^2\right) = t\chi_2|E_0|^2 cos2\alpha_0. \tag{26}$$

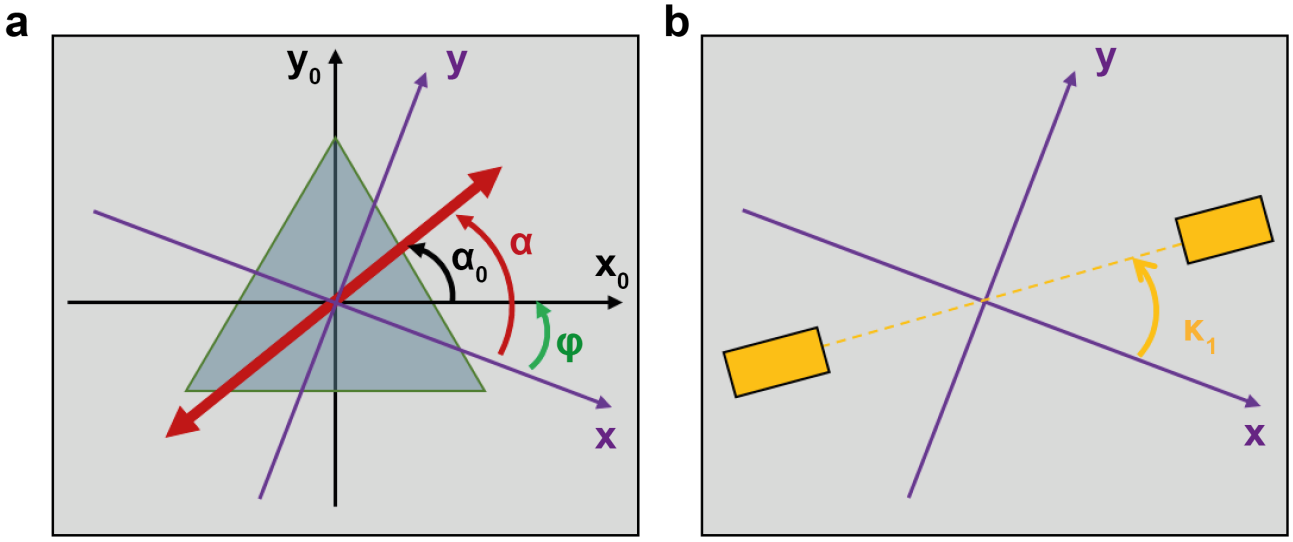

Figure 6-23. **LPGE with experimentally accessible coordinates**.a) Schematic representation of new x- and y-axes tilted by an angle φ with respect to the x_0 and y_0 axes. The azimuth angle is redefined as α counted from the x-axis. Here, the x-axis belongs to the initial linear polarization of light at the 0-degree rotation of HWP. b) Schematic representation of a contact pair positioned in an angle of κ_1 counted from the x-axis.

From the experimental point of view, setting a coordinate axis parallel to the initial *E* field direction is more useful for analysis. We rotate the coordinate with arbitrary – φ wrt to x_0-axis and make new x and y coordinates, the schematic of which is illustrated in **Figure 6-23(a)**.

Defining $\alpha_0 = \alpha - \varphi$, Eq. (25) becomes

$$V_{x0}^{LPGE} = t\chi_2|E_0|^2 2sin2\alpha_0 = t\chi_2|E_0|^2 2sin2(\alpha - \varphi), \tag{27}$$

and Eq. (26) becomes

$$V_{y0}^{LPGE} = t\chi_2|E_0|^2 2cos2\alpha_0 = t\chi_2|E_0|^2 2cos2(\alpha - \varphi). \tag{28}$$

Then, we re-write them in the rotated coordinates. The photogalvanic voltage generated in the x direction is

$$V_x^{LPGE} = V_{x0}^{LPGE}\cos\varphi - V_{y0}^{LPGE} sin\,\varphi. \tag{29}$$

Inserting Eq. (27) and Eq. (28), it becomes

$$V_x^{LPGE} = t\chi_2|E_0|^2 2sin2(\alpha - \varphi)\cos\varphi - t\chi_2|E_0|^2 2cos2(\alpha - \varphi)\sin\varphi = t\chi_2|E_0|^2 sin(2\alpha - 3\varphi). \tag{30}$$

Similarly, the photogalvanic voltage generated in the y direction is

$$V_y^{LPGE} = V_{x0}^{LPGE}\ \sin\varphi + V_{y0}^{LPGE}\cos\varphi, \tag{31}$$

which is

$$V_y^{LPGE} = t\chi_2|E_0|^2 2sin2(\alpha - \varphi)\sin\varphi + t\chi_2|E_0|^2 2cos2(\alpha - \varphi)\cos\varphi = t\chi_2|E_0|^2 cos(2\alpha - 3\varphi). \tag{32}$$

Now we consider the contact geometry of our device. The measured signal is achieved by orthogonal projection of V_x^{LPGE} and V_y^{LPGE} along the direction of diagonal pairs. If we consider the position of the first pair of electrodes is rotated κ_1 with respect to the x-axis as shown in **Figure 6-23(b)**, then the measured photovoltage from this pair of electrodes is

$$V^1 = V_x^{LPGE}\cos\kappa_1 + V_y^{LPGE}\mathrm{si\,n}\,\kappa_1. \tag{33}$$

Inserting Eq. (30) and Eq. (32) into Eq. (33), V^1 can be expressed as

$$V^1 = t\chi_2|E_0|^2 * (\sin(2\alpha - 3\varphi)\cos(\kappa_1) + \cos(2\alpha - 3\varphi)\sin(\kappa_1)), \tag{34}$$

and more simply,

$$V^1 = t\chi_2|E_0|^2\sin(2\alpha - 3\varphi + \kappa_1). \tag{35}$$

We can write Eq. (35) in a general form describing the measured voltage from the n^{th} contact pair, which is

$$V^n = t\chi_2|E_0|^2\sin(2\alpha - 3\varphi + \kappa_n). \tag{36}$$

We have used this equation to fit the measured photovoltage signal from different diagonal pairs (**Figure 6-16(b)**). From the fitting, we can extract the phase of each data as $3\varphi - \kappa_n$, which consists of φ, the relative angle between a line perpendicular to the mirror plane of Se vacancy and the initial direction of the applied electric field, and of κ_n, the relative angle between n^{th} contact and the initial direction of the applied electric field.

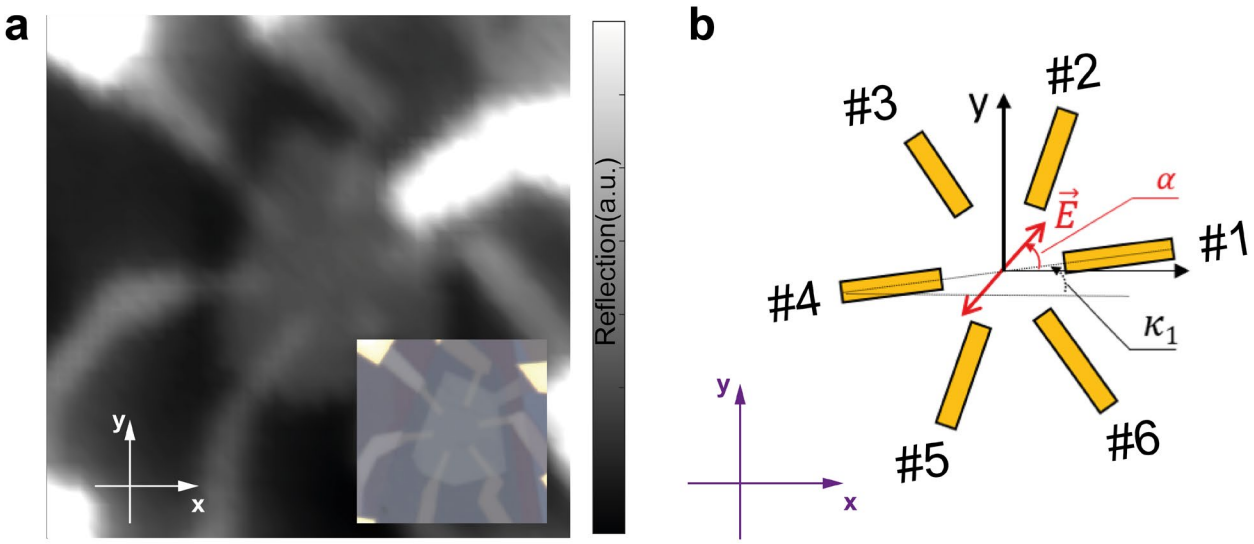

Figure 6-24. **Contact electrode angles in x, and y coordinate axes.**a) 2D reflection map of the h-BN encapsulated $PtSe_2$ device. Inset shows the optical device image. At 0 degree of HWP rotation, the initial linear polarisation of light is aligned parallel to the x-axis of the reflection map. b) Schematic of contact electrode alignments. Numbers assigned to each electrode increase anti-clockwise. n^{th} contact electrodes (n=1,2…6) are positioned at anti-clockwise angle k_n with respect to the x-axis. α is defined as the angle of linear light polarization with respect to the x-axis.

We have aligned our initial electric field along the x-direction of the CCD image, and we have measured the reflection map of the h-BN encapsulated device to define our κ_n values. **Figure 6-24(a)** shows the reflection map, and **Figure 6-24(b)** depicts the schematic of our contact electrodes. Contact electrodes are rotated in x-y coordinates, and the angle of rotation is deduced from the reflection map, which is around 9degree. The is also the angle (k_1) between the first contact pairs (#1 and #4) with respect to the direction of the initial electric field.

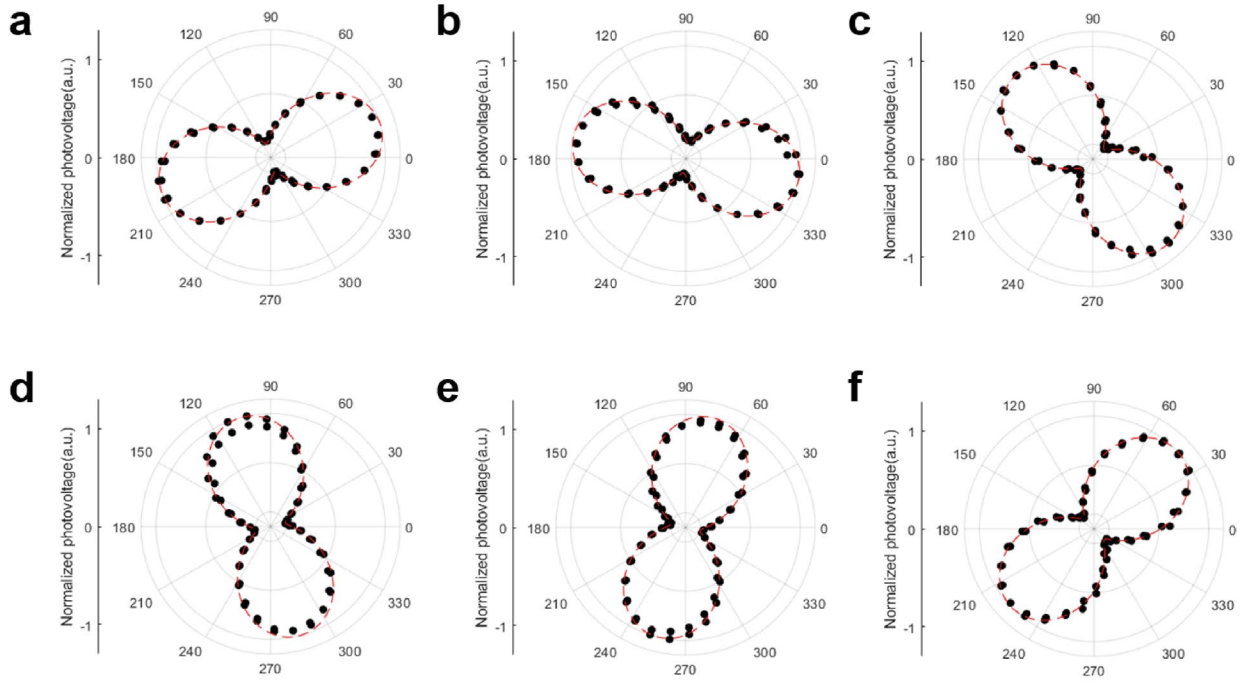

Figure 6-25. **Fitting the measured photovoltage with a model equation.**a-f) Normalized photovoltage polar plots from diagonal pairs 1 to 6 are presented in alphabetical order with the sinusoidal fit (red dash line) by the normalized model equation,

$V_{Norm}^{n} = \sin(2\alpha - 3\varphi + \kappa_n)$ derived previously. Presented data (black dots) are from measurement by one full rotation of the HWP angle.

We first check the validity of this model by inserting an arbitrary φ value. The fitting is presented in **Figure 6-25**, and **Figure 6-26(a)** shows the extracted contact angles (black dots), which are compared with the contact angles (red dots) that are spaced by 60degree, with the first contact angle rotated with 9degree. The extracted value shows some offset due to arbitrary input value of φ. However, they are equally spaced on average 61degree as shown in the inset of **Figure 6-26(a)**. This suggests that the model equation works reasonably well.

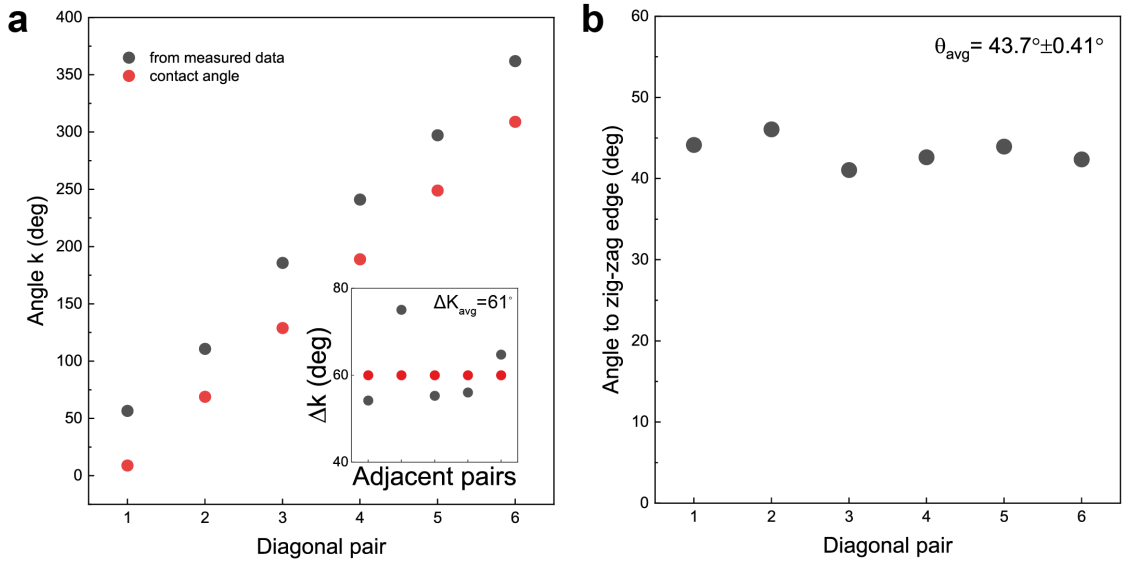

Figure 6-26. **Extracting electrode angles and the angle of one zig-zag edge of PSe_2.**a) Contact angles extracted with an arbitrary input parameter of φ (φ=0), compared to the contact angles from the reference reflection map in **Figure 6-24(a)**. Angles are measured with respect to the x-axis, the initial polarization direction. Inset shows the angle increments computed from the difference between two extracted angles from adjacent diagonal pairs. The average increment value is 61°. b) Extracted angles of zig-zag edge by input parameter of k_n. The average value is 43.7°.

Then, we attempt to find φ from the probed sample. As shown in **Figure 6-23(a)**, we have defined φ as the angle of the x_0 axis rotated from the new x-axis, which is the initial linear polarization direction where the x_0 axis is perpendicular to the mirror plane of wedges. If wedges are due to S-point vacancy, then x_0 axis particularly belongs to the zig-zag edge of $PtSe_2$. For this case, φ should provide us with the angular location of one zig-zag edge of $PtSe_2$, as the Se point defect does not distort the 3-fold symmetric lattice of $PtSe_2$ as seen from our TEM images.

Figure 6-26(b) shows the extracted φ using the parameters of κ_n=9+60× (n − 1), which is found to be around 43.7degree. This corresponds to the angle to the 1st zig-zag plane. In **Figure 6-27(a)**, we overlaid this edge (white dashed line) onto the previous reflection map along with the other two zig-zag edges (blue and red dashed line), which are determined by the 3-fold rotation of the extracted zig-zag edge. The black line connecting #1 and #4 electrodes is drawn as a reference.

It is well-known that the crystal of vdW materials shows sharp edges that are 60 degrees rotated apart. Those edges are commonly assigned to either zig-zag or arm-chair edges. Here in our sample, we could also clearly see from AFM mapping (**Figure 6-27(b)**) and optical microscopy image (inset of **Figure 6-27(b)**) that there are two edges in between contact electrode #4 and #5 that are 60 degrees rotated apart. We found the close approximation of calculated zig-zag edges to the sample edges, with a difference of 5 degrees.

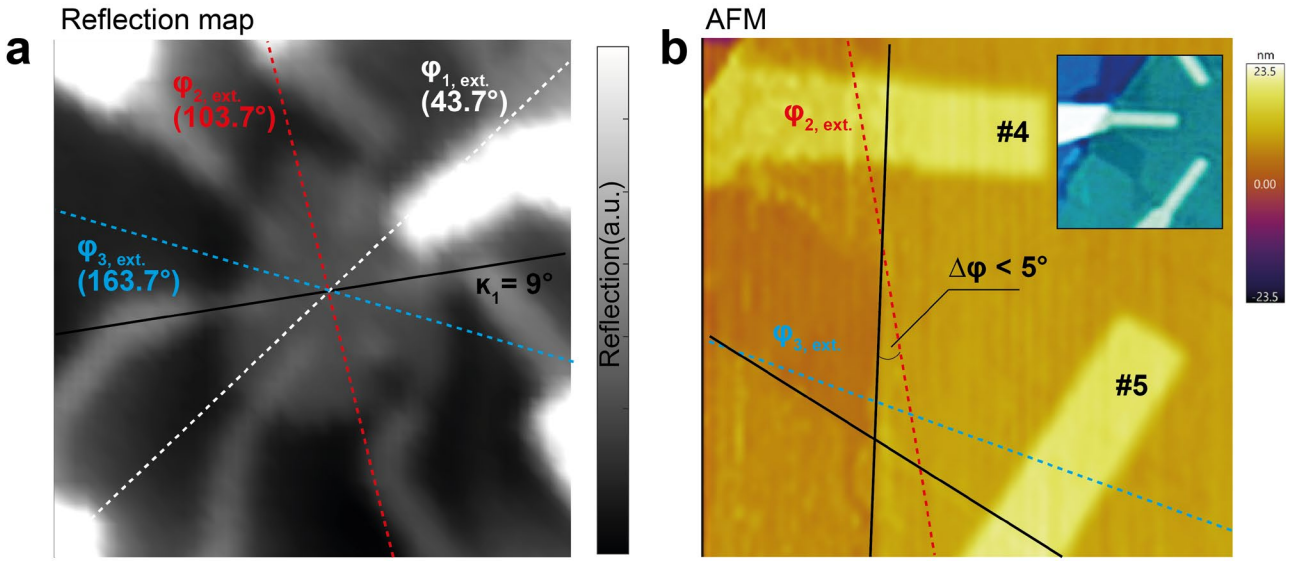

Figure 6-27. **Determining crystallographic axis of $PtSe_2$**.a) The 1st, 2nd and 3rd zig-zag planes (white, red and blue dash lines respectively) overlaid on the 2D reflection map of the probed sample. The position of zia-zag planes are based on the their calculated angles ($\varphi_{1,ext}$, $\varphi_{2,ext}$, and $\varphi_{3,ext}$) with respect to the intial linear polarization direction. The black line is in parallel with electrode #1 and electrode #4, and it is rotated at 9 degrees away from the initial linear polarization direction (0-degree rotation of HWP). b) 2D AFM image around electrodes #4 and #5, with zig-zag planes (blue and red dash lines) overlaid referencing to the direction of electrode #4. Inset is the optical microscopy image around electrodes #4 and #5 showing the cleaved edges of $PtSe_2$. Extracted zig-zag planes align within 5degree with the cleaved edges of $PtSe_2$.

6.8 Summary

6.8.1 Acheived results

We found that bulk photogalvanic effect can appear in centrosymmetric $PtSe_2$ from structural defects. We directly compared the optoelectronic response of pristine and defective $PtSe_2$ under focused laser illumination. A FET device made of the pristine sample showed photovoltaic effect at the metal-$PtSe_2$ interface, which has been commonly observed in other metal-TMDCs interfaces. In sharp contrast, the dominant photoresponse from the device made of the defective sample was by homogenous illumination only on $PtSe_2$. This photocurrent maximally increased at the center of material away from the metal-$PtSe_2$ interface.

We observed linear and circular polarization-dependent photocurrent at zero-bias conditions, both increasing linearly with the laser power, indicating their origin to be 2nd order DC response of light electric fields. This observation can be understood based on linear and circular photogalvanic effect, which primarily requires the material to have broken inversion symmetry. The broken inversion symmetry can be induced by structural defects in $PtSe_2$, where point vacancy defects and large cluster-like defects are confirmed directly from TEM images.

As a macroscopic origin of linear-photogalvanic response, most-abundant Se vacancy preserving 3-fold rotation symmetry is considered. This is supported by determining the crystallographic axis of $PtSe_2$ under 5-degree precision from the measured linear photogalvanic response using a wedge scattering model. On the other hand, the appearance of circular photocurrent under normal incidence requires the low symmetry of material (at most, a single mirror plane)[195]. The cluster-like defects in $PtSe_2$ having the lowest crystal symmetry can act as the local source of circular photogalvanic effect. This lowest crystal defect can also be considered as the origin of the polarization-independent photocurrent that we observed as an offset. This is because photocurrent dependence on linear polarization vanishes at the lowest crystal symmetry of C_1[184].

6.8.2 Future perspective

Our work has extended the potential function of defects in centrosymmetric $PtSe_2$ as a valuable source for harvesting light energy and detecting light polarization. We expect our findings to broaden the material selection for photovoltaic applications. Further studies on defect engineering in $PtSe_2$ will be needed to optimize the photogalvanic efficiency and explore the in-depth role of defect-induced symmetry breaking in centrosymmetric media.

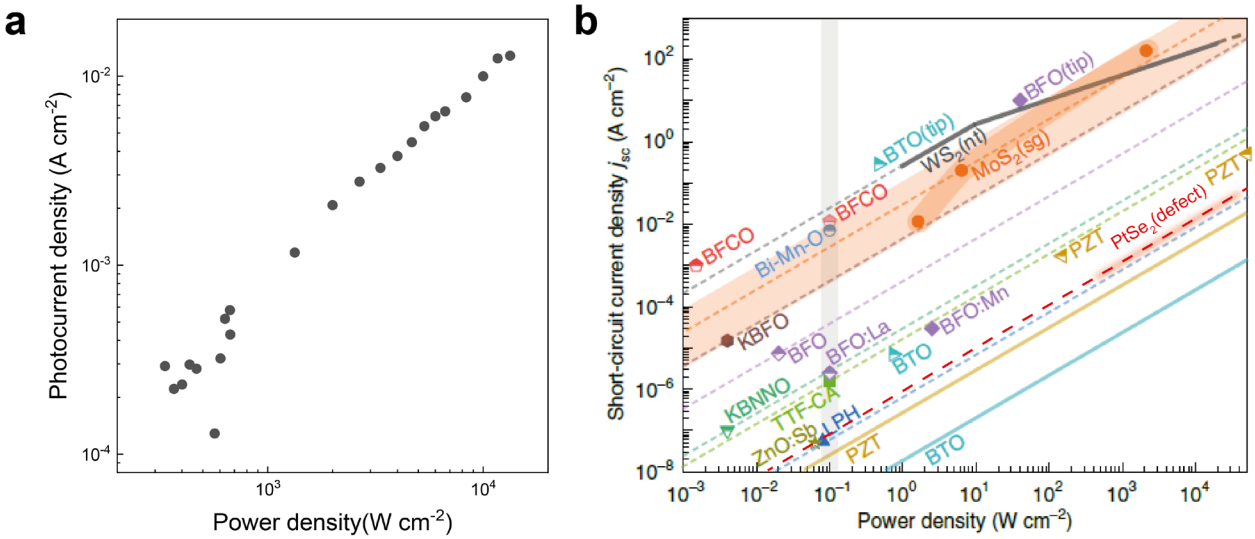

Figure 6-28. **BPVE efficiency of defective $PtSe_2$.**Photocurrent current density as zero-bias condition versus incident light power density from defective 2L $PtSe_2$. Short-circuit current density is calculated by considering the cross-section area($3.43\mu m^2$) between $PtSe_2$ and one of the two Pt contact electrodes. The area is chosen as the largest cross-section area of

the two. Therefore, the current density is at the lower bound. As for calculating power density, incident power is normalized with a Gaussian beam spot size of $0.8\mu m^2$. b) BPVE efficiencies from non-centrosymmetric materials. The original figure is reprinted and adapted with permission from the reference[25]. $PtSe_2$ data is overlaid as a red shaded line for comparison

Chapter 7 Conclusion and outlook

7.1 Epitaxial growth of 2D superconducting NbS_2

To date, 2D van der Waals materials still continue to gain popularity as a versatile platform to engineer heterostructures and to achieve novel material properties by stacking materials of different properties – metal, semiconductor, insulator and more – picked from the same family held under van der Waals force. Material entirely being a surface, however, it is easily affected by external factors such as strain, oxidation, and surface absorbate, reducing overall the targeted device performance. Particularly, TMDCs has been suffered from a large amount of intrinsic defect concentration owing to the lower deformation energy during the synthesis compared to that of graphene, and directly limited the electronic properties of TMDCs monolayers. Structural defects, in general, negatively affect the flow of charge current, degrading the performance of an electronic device and hampering the discovery of new transport phenomena that requires long scattering time. Therefore, to practically realize applications based on TMDCs, continued effort is essential for improving the existing synthesis procedures and producing finer crystalline crystals. In this regard, we investigated the work of 2D NbS_2 crystal synthesis and improved the current CVD growth recipe.

Achieved result 1. Growth and electronic characterization of superconducting NbS_2

In chapter 4, we presented the work of high-quality epitaxial growth of 2D NbS_2 by atmospheric-pressure chemical vapor deposition using Nb precursor pre-coated on a sapphire substrate while applying gaseous precursor H_2S. We have successfully synthesized two polymorphs of NbS_2, that is 2H- and 3R-NbS_2, with the largest lateral size to date, and we found that there is a structural phase-transition from 3R to 2H as thickness increases. This phase transition was confirmed from the analysis based on scanning transmission electron microscopy and Raman spectroscopy. Also, the superconducting and metallic properties of the two polymorphs were examined under low-temperature charge transport measurement. At the intermediate thickness where phase transition occurs, we found that the two electronic properties coexist due to the presence of 2H- and 3R-domains. From temperature-dependent resistance measurement, the lowest RRR value was measured at this thickness due to increased disorder from defects in domain boundaries.

Outlook

Semiconducting TMDCs commonly suffer from large contact resistance when using conventional 3D metal contacts, owing to Fermi-level pinning regardless of their metal work functions[211]. Held by van der Waals force, metallic TMDCs can be favorably integrated with semiconducting TMDCs to lower the contact resistance by weakening the Fermi-level pinning[211,212]. Thus, metallic TMDCs are considered ideal metal electrodes. Our practical synthesis method for phase-controllable growth of 2D metallic NbS_2 can benefit future studies in mesoscopic devices for better device performance. Furthermore, wafer-scale single-crystalline growth could be possible if we further optimize the current recipe, which can further contribute to the large-area application of 2D superconductors. As TMDCs share a similar growth mechanism[125], our recipe can be possibly implanted for the growth of other kinds of vdW materials.

7.2 Disorder-induced novel properties in semiconducting $PtSe_2$

Structural defects in TMDCs can offer a novel route to control the optical, electrical, and optoelectrical properties of TMDCs. Sometimes, completely new functionalities can be introduced by defects.

We studied how structural defects affect the material properties of monolayer and bilayer $PtSe_2$, which are known to be a semiconductor. When we probed the charge transport of this ultrathin $PtSe_2$ that is defective, we observe low conductance with a low on-off current ratio modulated by a gate voltage. Moreover, we found that electron transport in $PtSe_2$ can be described by a variable range hopping mechanism – a dominant type of carrier transport in a disordered semiconductor - similarly observed in other defective TMDCs. In short, the electrical properties of $PtSe_2$ are degraded by structural defects.

However, intriguingly, we discovered that local structural disorder at these thicknesses of $PtSe_2$ could be the source of new properties, magnetism and 2nd-order nonlinear photocurrent, which are absent in the pristine form of $PtSe_2$.

Achieved result 2. Defect-induced magnetism in $PtSe_2$

In chapter 5, we presented the discovery of defect-induced magnetism in semiconducting $PtSe_2$. Under magneto-transport measurements with the perpendicular fields, we compared the properties of magnetoresistance(MR) obtained from monolayer and bilayer $PtSe_2$ using the proximitized graphene probe. While the MR of the monolayer shows a two-plateau response, the MR of the bilayer shows a ferromagnetic response with clear hysteresis. The appearance of different magnetic states is theoretically explained by the first-principle DFT calculation, which suggests that magnetic moment, induced by intrinsic Pt vacancy, plays a significant role.

Achieved result 3. Disorder-induced spontaneous photovoltaic effect in $PtSe_2$

In chapter 6, we showed a disorder-induced spontaneous photovoltaic effect in semiconducting $PtSe_2$. In the pristine structure of $PtSe_2$, we found bulk photovoltaic effect(BPVE) is negligible. This is expected because BPVE is a 2nd-order nonlinear DC response and it is strictly absent for centrosymmetric materials. However, in defective $PtSe_2$ produced by the Au-assisted exfoliation technique, the broken local inversion symmetry from local structural disorder was manifested by BPVE under homogenous illumination. We observed linear and circular polarization-dependent photocurrent at zero-bias conditions, both of which increased linearly with the laser power, indicating the 2nd-order effect of the electric fields. Supported by TEM imaging, we were able to identify the dominant type of structural defects in $PtSe_2$, which are cluster-like defects and chalcogen point defects. We argued that cluster-like defects, which have the lowest level of symmetry, can act as the local source of generating circular and polarization-independent photogalvanic effects. We adopted the macroscopic wedge model to describe the linear-photogalvanic response, where most-abundant Se vacancy preserving 3-fold rotation symmetry can be considered a possible scattering center.

Outlook

Compared to the prototypical MoS_2 and other semiconducting TMDCs, metallic $PtSe_2$ has attracted less attention in material research. Yet, there have been interesting discoveries on the electronic properties of few-layer $PtSe_2$, which include the observation of layer-dependent bandgap opening below 3-4 layers[84], as a consequence of strong interlayer interaction and quantum confinement effect[89]. This metal-to-semiconductor transition allowed one to consider a few-layers semiconducting $PtSe_2$ for optoelectronic applications[72]. The extended functionalities introduced by structural defects, demonstrated in this dissertation, allow us to harness the full potential of semiconducting $PtSe_2$. We foresee the potential of defective $PtSe_2$ in realizing compact magnetic devices for low-power spintronics applications. Furthermore, it can be used for photovoltaic applications for harvesting light energy as well as detecting light polarization.

Future challenge

From another point of view, the various properties introduced from the structural defects in $PtSe_2$ could lead to complexity in its material design as some properties might be not wanted. Therefore, it is essential in future material development to meet the following two requirements; be able to produce the cleanest crystal, and at the same time, if needed, with the desired number of particular defects.

To meet the first requirement of producing high-quality $PtSe_2$, both Pt metal selenization and chemical vapor transport methods have been successful. Yet, the relations between the specific defect types and their concentration to a particular synthesis method have not been well established so far, compared to the relevant work done substantially for MoS_2[47,48]. The structural information would allow us to further optimize the current synthesis recipes and reduce the amount of intrinsic defect concentration. Also, as an alternative approach to reducing the concentration, it would be good to apply post-healing methods for chalcogen vacancies, such as treatments based on thiol chemistry, which has not yet demonstrated its effectiveness for $PtSe_2$. For this approach, material property that is sensitive to the change of defect concentration is used as an indicator for checking the effectiveness of defect curing. Photoluminesce has been the key material indicator for semiconducting TMDCs such as MoS_2 and WSe_2 because the non-radiative recombination process is proportional to the level of defect concentration. However, the same indicator cannot be applied for few-layer $PtSe_2$ as it has an in-direct bandgap with inherently low photoluminesce efficiency. Instead, one may alternatively monitor the change in charge carrier mobility or bulk photovoltaic currents before and after the curing treatment for $PtSe_2$.

With regard to the second requirement stressed above, the 'desired' defect concentration will become clear once the nature of defect-induced properties in $PtSe_2$ is clarified by investigating how the defect concentration plays a role. This can be addressed by controlling the density of defects by so-called defect engineering. Various methods are well-established to create and control the density of point defects in other TMDCs, including e-beam irradiation[168] and ion bombardment[169]. Recently selective plasma treatment was found to be effective in creating Se vacancies of $PtSe_2$, up to 7nm beneath the surface[213]. This controllability of defect concentration would help tailor the defect-induced magnetic and optoelectronic properties of $PtSe_2$, thereby giving us an additional knob to control their properties.

List of abbreviations and symbols

0D	zero-dimensional
1D	one-dimensional
1L	monolayer
1T	1 layers per T(trigonal) unit cell
2D	two-dimensional
2H	2 layers per H(hexagonal) unit cell
2L	bilayer
3D	three-dimensional
3R	3 layers per R(rhombohedral) unit cell
Å	Angstrom
ac, AC	alternating current
ADF STEM	annular dark-field scanning tunneling electron microscope
Al	aluminum
AlGaN	aluminum gallium nitride
Ar	argon
ARPES	angle-resolved photoemission spectroscopy
B	magnetic field
Bi	bismuth
Bi_2Te_3	bismuth telluride
BKT	Berezinskii–Kosterlitz–Thouless
BP	black phosphorus
BPVE	bulk photovoltaic effect
C	amplitude of helicity-dependent photocurrent
C_{3v}	point group C_{3v}
CCD	charged-coupled device
CDW	charge density wave
CPGE	circular photogalvanic effect
Cr	chromium
CrI_3	chromium(III) iodide
Cs	spherical aberration
CVD	chemical vapor deposition
CVT	chemical vapor transport
CW	continuous wave
$\bar{D}$	vertical displacement field
D_1	amplitude of photocurrent from experimental drift
D_2	amplitude of polarization-independent photocurrent
D_{3d}	point group D_{3d}
DC	direct current
DFT	density functional theory
DI	deionized
dI/dV	differential conductance
E	electric-field
E-beam	electron beam
EDX	energy dispersive x-Ray analysis
Eg	band gap
EL	ethyl lactate
Eq.	equation
eV	electron-volt
exf.	exfoliation
FET	field effect transistor
FWHM	full width at half maximum
GaN	gallium nitride
GMR	giant magnetoresistance
H_2S	hydrogen sulfide
HAADF	high-angle annular dark field
h-BN	hexagonal boron nitride
HeNe	helium-neon
hfO_2	hafnium oxide

HMDS	hexamethyldisilazane
HRTEM	high-resolution transmission electron microscopy
HWP	half wave plate
I_2	iodine
I_{ds}	drain-source current
I_{off}	off-state current
I_{on}	on-state current
IPA	isopropanol
IR	infrared
KI	potassium iodide
KOH	potassium hydroxide
L	length
L	amplitude of linear polarization-dependent photocurrent
LHe	liquid helium
LO	longitudinal-optical
LPGE	linear photogalvanic effect
MBE	molecular beam epitaxy
MMA	methyl methacrylate
MoS_2	molybdenum disulfide
$MoSe_2$	molybdenum diselenide
$MoTe_2$	molybdenum ditelluride
MR	magnetoresistance
mSR	Muon spin rotation/relaxation
MTJ	magnetic tunnel junction
MWH	Mermin–Wagner–Hohenberg
Nb_2O_5	niobium pentoxide
$NbCl_5$	niobium(V) chloride
NbS_2	niobium disulfide
$NbSe_2$	niobium diselenide
ND	neutral density
P	Pressure
PC	polycarbonate
PDMS	polydimethylsiloxane
$PdTe_2$	palladium ditelluride
PL	photoluminescence
PMA	perpendicular magnetic anisotropy
PMMA	poly(methyl methacrylate)
$PtSe_2$	platinum diselenide
PVD	physical vapor deposition
QWP	quarter wave plate
ReS_2	rhenium disulfide
RKKY	Ruderman–Kittel–Kasuya–Yosida
R_{xx}	longitudinal resistance
S	sulfur
S	sub-threshold swing
SHE	spin hall effect
SNR	spin Nernst effect
$SnSe_2$	tin diselenide
SOT	spin orbit torque
STEM	scanning tunneling electron microscope
STM	scanning tunneling microscope
TaS_2	tantalum sulfide
TEM	transmission electron microscopy
TFSI	bis(trifluoromethane) sulfonimide
TMR	tunnel magnetoresistance
V_{BG}	back gate voltage
V_{ds}	drain-source voltage
vdW	van der Waals
V_{Pt}	platinum vacancy
VRH	variable range hopping
V_{Se}	selenium vacancy
VSe_2	vanadium diselenide
V_{TG}	top gate voltage
W	width
WS_2	tungsten disulfide
WSe_2	tungsten diselenide

XPS	X-ray photoelectron spectroscopy
℃	degree Celsius
α	azimuthal angle
Δ	delta(difference)
ε	relative permittivity
θ	quarter-wave plate angle
κ	angle of electrode
λ	wavelength
μs	microsecond
μ_B	Bohr magneton
μ_{FE}	field effect mobility
μ_{FE}	field-effect mobility
σ	conductivity
φ	angle of zig-zag edge
χ	susceptibility
ω	angular frequency
Γ	center point in reciprocal space
K	k-point in reciprocal space

Bibliography

1. S. Prawer and A. D. Greentree, Science **320**, 1601 (2008).
2. A. K. Geim and I. V. Grigorieva, Nature **499**, 419 (2013).
3. D. Rhodes, S. H. Chae, R. Ribeiro-Palau, and J. Hone, Nat. Mater. **18**, 541 (2019).
4. J. Martin, N. Akerman, G. Ulbricht, T. Lohmann, J. H. Smet, K. von Klitzing, and A. Yacoby, Nature Phys **4**, 144 (2008).
5. S. Adam, E. H. Hwang, V. M. Galitski, and S. Das Sarma, Proceedings of the National Academy of Sciences **104**, 18392 (2007).
6. J.-H. Chen, C. Jang, S. Adam, M. S. Fuhrer, E. D. Williams, and M. Ishigami, Nature Phys **4**, 377 (2008).
7. Y. Zhang, V. W. Brar, C. Girit, A. Zettl, and M. F. Crommie, Nature Phys **5**, 722 (2009).
8. C. R. Dean, A. F. Young, I. Meric, C. Lee, L. Wang, S. Sorgenfrei, K. Watanabe, T. Taniguchi, P. Kim, K. L. Shepard, and J. Hone, Nature Nanotech **5**, 722 (2010).
9. X. Du, I. Skachko, A. Barker, and E. Y. Andrei, Nature Nanotech **3**, 491 (2008).
10. L. Wang, I. Meric, P. Y. Huang, Q. Gao, Y. Gao, H. Tran, T. Taniguchi, K. Watanabe, L. M. Campos, D. A. Muller, J. Guo, P. Kim, J. Hone, K. L. Shepard, and C. R. Dean, Science **342**, 614 (2013).
11. J. Yang, G. Chen, T. Han, Q. Zhang, Y.-H. Zhang, L. Jiang, B. Lyu, H. Li, K. Watanabe, T. Taniguchi, Z. Shi, T. Senthil, Y. Zhang, F. Wang, and L. Ju, Science **375**, 1295 (2022).
12. A. I. Berdyugin, N. Xin, H. Gao, S. Slizovskiy, Z. Dong, S. Bhattacharjee, P. Kumaravadivel, S. Xu, L. A. Ponomarenko, M. Holwill, D. A. Bandurin, M. Kim, Y. Cao, M. T. Greenaway, K. S. Novoselov, I. V. Grigorieva, K. Watanabe, T. Taniguchi, V. I. Fal'ko, L. S. Levitov, R. K. Kumar, and A. K. Geim, Science **375**, 430 (2022).
13. S. Haldar, H. Vovusha, M. K. Yadav, O. Eriksson, and B. Sanyal, Phys. Rev. B **92**, 235408 (2015).
14. M. Ali, X. Pi, Y. Liu, and D. Yang, AIP Advances **7**, 045308 (2017).
15. D. Edelberg, D. Rhodes, A. Kerelsky, B. Kim, J. Wang, A. Zangiabadi, C. Kim, A. Abhinandan, J. Ardelean, M. Scully, D. Scullion, L. Embon, R. Zu, E. J. G. Santos, L. Balicas, C. Marianetti, K. Barmak, X. Zhu, J. Hone, and A. N. Pasupathy, Nano Lett. **19**, 4371 (2019).
16. S. Roy, A. S. Sharbirin, Y. Lee, W. B. Kim, T. S. Kim, K. Cho, K. Kang, H. S. Jung, and J. Kim, Nanomaterials **10**, 1032 (2020).
17. M. Amani, D.-H. Lien, D. Kiriya, J. Xiao, A. Azcatl, J. Noh, S. R. Madhvapathy, R. Addou, S. Kc, M. Dubey, K. Cho, R. M. Wallace, S.-C. Lee, J.-H. He, J. W. Ager, X. Zhang, E. Yablonovitch, and A. Javey, Science **350**, 1065 (2015).
18. O. A. Ajayi, J. V. Ardelean, G. D. Shepard, J. Wang, A. Antony, T. Taniguchi, K. Watanabe, T. F. Heinz, S. Strauf, X.-Y. Zhu, and J. C. Hone, 2D Mater. **4**, 031011 (2017).
19. J. Wierzbowski, J. Klein, F. Sigger, C. Straubinger, M. Kremser, T. Taniguchi, K. Watanabe, U. Wurstbauer, A. W. Holleitner, M. Kaniber, K. Müller, and J. J. Finley, Sci Rep **7**, 12383 (2017).
20. Z. Wang, D. A. Rhodes, K. Watanabe, T. Taniguchi, J. C. Hone, J. Shan, and K. F. Mak, Nature **574**, 76 (2019).
21. D. Unuchek, A. Ciarrocchi, A. Avsar, K. Watanabe, T. Taniguchi, and A. Kis, Nature **560**, 340 (2018).
22. A. Avsar, A. Ciarrocchi, M. Pizzochero, D. Unuchek, O. V. Yazyev, and A. Kis, Nat. Nanotechnol. **14**, 674 (2019).
23. Z. Guguchia, A. Kerelsky, D. Edelberg, S. Banerjee, F. von Rohr, D. Scullion, M. Augustin, M. Scully, D. A. Rhodes, Z. Shermadini, H. Luetkens, A. Shengelaya, C. Baines, E. Morenzoni, A. Amato, J. C. Hone, R. Khasanov, S. J. L. Billinge, E. Santos, A. N. Pasupathy, and Y. J. Uemura, Science Advances **4**, eaat3672 (2018).
24. Moh. A. U. Absor, I. Santoso, Harsojo, K. Abraha, F. Ishii, and M. Saito, Phys. Rev. B **96**, 115128 (2017).
25. J. Jiang, Z. Chen, Y. Hu, Y. Xiang, L. Zhang, Y. Wang, G.-C. Wang, and J. Shi, Nat. Nanotechnol. **16**, 894 (2021).
26. G. Grosso, H. Moon, B. Lienhard, S. Ali, D. K. Efetov, M. M. Furchi, P. Jarillo-Herrero, M. J. Ford, I. Aharonovich, and D. Englund, Nat Commun **8**, 705 (2017).
27. H. L. Stern, Q. Gu, J. Jarman, S. Eizagirre Barker, N. Mendelson, D. Chugh, S. Schott, H. H. Tan, H. Sirringhaus, I. Aharonovich, and M. Atatüre, Nat Commun **13**, 618 (2022).
28. K. S. Novoselov, A. K. Geim, S. V. Morozov, D. Jiang, Y. Zhang, S. V. Dubonos, I. V. Grigorieva, and A. A. Firsov, Science **306**, 666 (2004).
29. A. A. Balandin, S. Ghosh, W. Bao, I. Calizo, D. Teweldebrhan, F. Miao, and C. N. Lau, Nano Lett. **8**, 902 (2008).
30. C.-W. Huang, J.-Y. Chen, C.-H. Chiu, C.-L. Hsin, T.-Y. Tseng, and W.-W. Wu, Nano Res. **9**, 3663 (2016).
31. P. R. Wallace, Phys. Rev. **71**, 622 (1947).
32. Y. Zhang, T.-T. Tang, C. Girit, Z. Hao, M. C. Martin, A. Zettl, M. F. Crommie, Y. R. Shen, and F. Wang, Nature **459**, 820 (2009).
33. F. Xia, D. B. Farmer, Y. Lin, and P. Avouris, Nano Lett. **10**, 715 (2010).
34. B. Radisavljevic, A. Radenovic, J. Brivio, V. Giacometti, and A. Kis, Nature Nanotech **6**, 147 (2011).
35. K. F. Mak, C. Lee, J. Hone, J. Shan, and T. F. Heinz, Physical Review Letters **105**, (2010).
36. A. Kuc and T. Heine, Chemical Society Reviews **44**, 2603 (2015).
37. A. Splendiani, L. Sun, Y. Zhang, T. Li, J. Kim, C.-Y. Chim, G. Galli, and F. Wang, Nano Lett. **10**, 1271 (2010).
38. A. Pulkin and O. V. Yazyev, Phys. Rev. B **93**, 041419 (2016).
39. S. Manzeli, D. Ovchinnikov, D. Pasquier, O. V. Yazyev, and A. Kis, Nat Rev Mater **2**, 17033 (2017).
40. D. Xiao, G.-B. Liu, W. Feng, X. Xu, and W. Yao, Phys. Rev. Lett. **108**, 196802 (2012).
41. H. Zeng, J. Dai, W. Yao, D. Xiao, and X. Cui, Nature Nanotech **7**, 490 (2012).
42. K. F. Mak, K. He, J. Shan, and T. F. Heinz, Nature Nanotech **7**, 494 (2012).
43. A. M. Jones, H. Yu, N. J. Ghimire, S. Wu, G. Aivazian, J. S. Ross, B. Zhao, J. Yan, D. G. Mandrus, D. Xiao, W. Yao, and X. Xu, Nature Nanotech **8**, 634 (2013).
44. K. F. Mak, K. L. McGill, J. Park, and P. L. McEuen, Science **344**, 1489 (2014).

45. H. Yuan, X. Wang, B. Lian, H. Zhang, X. Fang, B. Shen, G. Xu, Y. Xu, S.-C. Zhang, H. Y. Hwang, and Y. Cui, Nature Nanotech **9**, 851 (2014).
46. S. Cha, M. Noh, J. Kim, J. Son, H. Bae, D. Lee, H. Kim, J. Lee, H.-S. Shin, S. Sim, S. Yang, S. Lee, W. Shim, C.-H. Lee, M.-H. Jo, J. S. Kim, D. Kim, and H. Choi, Nature Nanotech **13**, 910 (2018).
47. W. Zhou, X. Zou, S. Najmaei, Z. Liu, Y. Shi, J. Kong, J. Lou, P. M. Ajayan, B. I. Yakobson, and J.-C. Idrobo, Nano Lett. **13**, 2615 (2013).
48. J. Hong, Z. Hu, M. Probert, K. Li, D. Lv, X. Yang, L. Gu, N. Mao, Q. Feng, L. Xie, J. Zhang, D. Wu, Z. Zhang, C. Jin, W. Ji, X. Zhang, J. Yuan, and Z. Zhang, Nat Commun **6**, 6293 (2015).
49. Y. Liu, J. Guo, E. Zhu, L. Liao, S.-J. Lee, M. Ding, I. Shakir, V. Gambin, Y. Huang, and X. Duan, Nature **557**, 696 (2018).
50. J.-H. Zhong, J. Zhang, X. Jin, J.-Y. Liu, Q. Li, M.-H. Li, W. Cai, D.-Y. Wu, D. Zhan, and B. Ren, J. Am. Chem. Soc. **136**, 16609 (2014).
51. L. Yuan and L. Huang, Nanoscale **7**, 7402 (2015).
52. H. Wang, C. Zhang, and F. Rana, Nano Lett. **15**, 339 (2015).
53. Y. Zhang, J. Ye, Y. Matsuhashi, and Y. Iwasa, Nano Lett. **12**, 1136 (2012).
54. Z. Yu, Y. Pan, Y. Shen, Z. Wang, Z.-Y. Ong, T. Xu, R. Xin, L. Pan, B. Wang, L. Sun, J. Wang, G. Zhang, Y. W. Zhang, Y. Shi, and X. Wang, Nat Commun **5**, 5290 (2014).
55. M. Amani, M. L. Chin, A. G. Birdwell, T. P. O'Regan, S. Najmaei, Z. Liu, P. M. Ajayan, J. Lou, and M. Dubey, Appl. Phys. Lett. **102**, 193107 (2013).
56. W. Wu, D. De, S.-C. Chang, Y. Wang, H. Peng, J. Bao, and S.-S. Pei, Appl. Phys. Lett. **102**, 142106 (2013).
57. H. Liu, M. Si, S. Najmaei, A. T. Neal, Y. Du, P. M. Ajayan, J. Lou, and P. D. Ye, Nano Lett. **13**, 2640 (2013).
58. Q. Feng, Y. Zhu, J. Hong, M. Zhang, W. Duan, N. Mao, J. Wu, H. Xu, F. Dong, F. Lin, C. Jin, C. Wang, J. Zhang, and L. Xie, Advanced Materials **26**, 2648 (2014).
59. N. Ma and D. Jena, Phys. Rev. X **4**, 011043 (2014).
60. K. Kaasbjerg, T. Low, and A.-P. Jauho, Phys. Rev. B **100**, 115409 (2019).
61. S. Ghatak, A. N. Pal, and A. Ghosh, ACS Nano **5**, 7707 (2011).
62. W. Zhu, T. Low, Y.-H. Lee, H. Wang, D. B. Farmer, J. Kong, F. Xia, and P. Avouris, Nat Commun **5**, 3087 (2014).
63. H. Qiu, T. Xu, Z. Wang, W. Ren, H. Nan, Z. Ni, Q. Chen, S. Yuan, F. Miao, F. Song, G. Long, Y. Shi, L. Sun, J. Wang, and X. Wang, Nat Commun **4**, 2642 (2013).
64. Y. Wang, J. C. Kim, R. J. Wu, J. Martinez, X. Song, J. Yang, F. Zhao, A. Mkhoyan, H. Y. Jeong, and M. Chhowalla, Nature **568**, 70 (2019).
65. M. A. Reshchikov, A. Usikov, H. Helava, Y. Makarov, V. Prozheeva, I. Makkonen, F. Tuomisto, J. H. Leach, and K. Udwary, Sci Rep **7**, 9297 (2017).
66. J. Pető, T. Ollár, P. Vancsó, Z. I. Popov, G. Z. Magda, G. Dobrik, C. Hwang, P. B. Sorokin, and L. Tapasztó, Nature Chem **10**, 1246 (2018).
67. R. Chua, J. Yang, X. He, X. Yu, W. Yu, F. Bussolotti, P. K. J. Wong, K. P. Loh, M. B. H. Breese, K. E. J. Goh, Y. L. Huang, and A. T. S. Wee, Advanced Materials **32**, 2000693 (2020).
68. G. Moody, K. Tran, X. Lu, T. Autry, J. M. Fraser, R. P. Mirin, L. Yang, X. Li, and K. L. Silverman, Phys. Rev. Lett. **121**, 057403 (2018).
69. M. M. Furchi, D. K. Polyushkin, A. Pospischil, and T. Mueller, Nano Lett. **14**, 6165 (2014).
70. S. Zhang, C.-G. Wang, M.-Y. Li, D. Huang, L.-J. Li, W. Ji, and S. Wu, Phys. Rev. Lett. **119**, 046101 (2017).
71. Q. Liang, Q. Zhang, J. Gou, T. Song, Arramel, H. Chen, M. Yang, S. X. Lim, Q. Wang, R. Zhu, N. Yakovlev, S. C. Tan, W. Zhang, K. S. Novoselov, and A. T. S. Wee, ACS Nano (2020).
72. X. Yu, P. Yu, D. Wu, B. Singh, Q. Zeng, H. Lin, W. Zhou, J. Lin, K. Suenaga, Z. Liu, and Q. J. Wang, Nature Communications **9**, (2018).
73. M. Okada, N. Nagamura, T. Matsumura, Y. Ando, A. K. A. Lu, N. Okada, W.-H. Chang, T. Nakanishi, T. Shimizu, T. Kubo, T. Irisawa, and T. Yamada, APL Materials **9**, 121115 (2021).
74. M. S. Shawkat, J. Gil, S. S. Han, T.-J. Ko, M. Wang, D. Dev, J. Kwon, G.-H. Lee, K. H. Oh, H.-S. Chung, T. Roy, Y. Jung, and Y. Jung, ACS Appl. Mater. Interfaces **12**, 14341 (2020).
75. J. Peng, Z. Yu, J. Wu, Y. Zhou, Y. Guo, Z. Li, J. Zhao, C. Wu, and Y. Xie, ACS Nano **12**, 9461 (2018).
76. J. Gao, Y. Cheng, T. Tian, X. Hu, K. Zeng, G. Zhang, and Y.-W. Zhang, ACS Omega **2**, 8640 (2017).
77. S. Horzum, D. Çakır, J. Suh, S. Tongay, Y.-S. Huang, C.-H. Ho, J. Wu, H. Sahin, and F. M. Peeters, Phys. Rev. B **89**, 155433 (2014).
78. W. Yao, E. Wang, H. Huang, K. Deng, M. Yan, K. Zhang, K. Miyamoto, T. Okuda, L. Li, Y. Wang, H. Gao, C. Liu, W. Duan, and S. Zhou, Nat Commun **8**, 14216 (2017).
79. Y. Wang, L. Li, W. Yao, S. Song, J. T. Sun, J. Pan, X. Ren, C. Li, E. Okunishi, Y.-Q. Wang, E. Wang, Y. Shao, Y. Y. Zhang, H. Yang, E. F. Schwier, H. Iwasawa, K. Shimada, M. Taniguchi, Z. Cheng, S. Zhou, S. Du, S. J. Pennycook, S. T. Pantelides, and H.-J. Gao, Nano Lett. **15**, 4013 (2015).
80. M. Yan, E. Wang, X. Zhou, G. Zhang, H. Zhang, K. Zhang, W. Yao, N. Lu, Shuzhen Yang, S. Wu, T. Yoshikawa, K. Miyamoto, T. Okuda, Y. Wu, P. Yu, W. Duan, and S. Zhou, 2D Mater. **4**, 045015 (2017).
81. K. Zhang, M. Yan, H. Zhang, H. Huang, M. Arita, Z. Sun, W. Duan, Y. Wu, and S. Zhou, Phys. Rev. B **96**, 125102 (2017).
82. J. Sun, R. S. Deacon, W. Luo, Y. Yuan, X. Liu, H. Xie, Y. Gao, and K. Ishibashi, Commun Phys **3**, 93 (2020).
83. J. Chen, T. Zhang, J. Wang, N. Zhang, W. Ji, S. Zhou, and Y. Chai, Advanced Functional Materials **31**, 2104192 (2021).
84. A. Ciarrocchi, A. Avsar, D. Ovchinnikov, and A. Kis, Nature Communications **9**, (2018).
85. J. Li, S. Kolekar, M. Ghorbani-Asl, T. Lehnert, J. Biskupek, U. Kaiser, A. V. Krasheninnikov, and M. Batzill, ACS Nano **15**, 13249 (2021).
86. M. Yan, H. Huang, K. Zhang, E. Wang, W. Yao, K. Deng, G. Wan, H. Zhang, M. Arita, H. Yang, Z. Sun, H. Yao, Y. Wu, S. Fan, W. Duan, and S. Zhou, Nat Commun **8**, 257 (2017).

87. Z. Li, J. Zhang, Y. Zeng, L. Meng, M. Zhou, and W. Wu, J. Phys.: Condens. Matter **29**, 23LT01 (2017).
88. H. L. Zhuang and R. G. Hennig, J. Phys. Chem. C **117**, 20440 (2013).
89. R. A. B. Villaos, C. P. Crisostomo, Z.-Q. Huang, S.-M. Huang, A. A. B. Padama, M. A. Albao, H. Lin, and F.-C. Chuang, Npj 2D Materials and Applications **3**, 1 (2019).
90. A. Castellanos-Gomez, 9 (2014).
91. J. Lee, K. F. Mak, and J. Shan, Nature Nanotech **11**, 421 (2016).
92. A. F. Hebard and A. T. Fiory, Phys. Rev. Lett. **44**, 291 (1980).
93. D. B. Haviland, Y. Liu, and A. M. Goldman, Phys. Rev. Lett. **62**, 2180 (1989).
94. J. M. Graybeal, Physica B+C **135**, 113 (1985).
95. Y. Saito, T. Nojima, and Y. Iwasa, Nat Rev Mater **2**, 1 (2016).
96. A. Devarakonda, H. Inoue, S. Fang, C. Ozsoy-Keskinbora, T. Suzuki, M. Kriener, L. Fu, E. Kaxiras, D. C. Bell, and J. G. Checkelsky, Science **370**, 231 (2020).
97. R. Yan, G. Khalsa, B. T. Schaefer, A. Jarjour, S. Rouvimov, K. C. Nowack, H. G. Xing, and D. Jena, Appl. Phys. Express **12**, 023008 (2019).
98. R. F. Frindt, Phys. Rev. Lett. **28**, 299 (1972).
99. E. Navarro-Moratalla, J. O. Island, S. Mañas-Valero, E. Pinilla-Cienfuegos, A. Castellanos-Gomez, J. Quereda, G. Rubio-Bollinger, L. Chirolli, J. A. Silva-Guillén, N. Agraït, G. A. Steele, F. Guinea, H. S. J. van der Zant, and E. Coronado, Nat Commun **7**, 11043 (2016).
100. X. Xi, L. Zhao, Z. Wang, H. Berger, L. Forró, J. Shan, and K. F. Mak, Nature Nanotech **10**, 765 (2015).
101. Y. Saito, Y. Nakamura, M. S. Bahramy, Y. Kohama, J. Ye, Y. Kasahara, Y. Nakagawa, M. Onga, M. Tokunaga, T. Nojima, Y. Yanase, and Y. Iwasa, Nature Phys **12**, 144 (2016).
102. J. M. Lu, O. Zheliuk, I. Leermakers, N. F. Q. Yuan, U. Zeitler, K. T. Law, and J. T. Ye, Science **350**, 1353 (2015).
103. X. Xi, Z. Wang, W. Zhao, J.-H. Park, K. T. Law, H. Berger, L. Forró, J. Shan, and K. F. Mak, Nature Phys **12**, 139 (2016).
104. J. Zeng, E. Liu, Y. Fu, Z. Chen, C. Pan, C. Wang, M. Wang, Y. Wang, K. Xu, S. Cai, X. Yan, Y. Wang, X. Liu, P. Wang, S.-J. Liang, Y. Cui, H. Y. Hwang, H. Yuan, and F. Miao, Nano Lett. **18**, 1410 (2018).
105. D. Costanzo, S. Jo, H. Berger, and A. F. Morpurgo, Nature Nanotech **11**, 339 (2016).
106. S. Jo, D. Costanzo, H. Berger, and A. F. Morpurgo, Nano Lett. **15**, 1197 (2015).
107. P. Liu, B. Lei, X. Chen, L. Wang, and X. Wang, Nat Rev Phys 1 (2022).
108. I. Guillamón, H. Suderow, S. Vieira, L. Cario, P. Diener, and P. Rodière, Phys. Rev. Lett. **101**, 166407 (2008).
109. R. Bianco, I. Errea, L. Monacelli, M. Calandra, and F. Mauri, Nano Lett. **19**, 3098 (2019).
110. E. G. C. P. van Loon, M. Rösner, G. Schönhoff, M. I. Katsnelson, and T. O. Wehling, Npj Quant Mater **3**, 32 (2018).
111. F. Güller, V. L. Vildosola, and A. M. Llois, Phys. Rev. B **93**, 094434 (2016).
112. K. Izawa, S. Ida, U. Unal, T. Yamaguchi, J.-H. Kang, J.-H. Choy, and Y. Matsumoto, Journal of Solid State Chemistry **181**, 319 (2008).
113. T. Hotta, T. Tokuda, S. Zhao, K. Watanabe, T. Taniguchi, H. Shinohara, and R. Kitaura, Appl. Phys. Lett. **109**, 133101 (2016).
114. M. M. Ugeda, A. J. Bradley, Y. Zhang, S. Onishi, Y. Chen, W. Ruan, C. Ojeda-Aristizabal, H. Ryu, M. T. Edmonds, H.-Z. Tsai, A. Riss, S.-K. Mo, D. Lee, A. Zettl, Z. Hussain, Z.-X. Shen, and M. F. Crommie, Nature Phys **12**, 92 (2016).
115. A. Kozhakhmetov, T. H. Choudhury, Z. Y. Al Balushi, M. Chubarov, and J. M. Redwing, Journal of Crystal Growth **486**, 137 (2018).
116. Q. Lv, X. Qin, and R. Lv, Frontiers in Materials **6**, (2019).
117. Z. Wang, C.-Y. Cheon, M. Tripathi, G. M. Marega, Y. Zhao, H. G. Ji, M. Macha, A. Radenovic, and A. Kis, ACS Nano **15**, 18403 (2021).
118. X. Wang, J. Lin, Y. Zhu, C. Luo, K. Suenaga, C. Cai, and L. Xie, Nanoscale **9**, 16607 (2017).
119. S. Zhao, T. Hotta, T. Koretsune, K. Watanabe, T. Taniguchi, K. Sugawara, T. Takahashi, H. Shinohara, and R. Kitaura, 2D Mater. **3**, 025027 (2016).
120. A. Niazi and A. K. Rastogi, J. Phys.: Condens. Matter **13**, 6787 (2001).
121. T. Yanase, S. Watanabe, M. Weng, M. Wakeshima, Y. Hinatsu, T. Nagahama, and T. Shimada, Crystal Growth & Design **16**, 4467 (2016).
122. H. Wang, X. Huang, J. Lin, J. Cui, Y. Chen, C. Zhu, F. Liu, Q. Zeng, J. Zhou, P. Yu, X. Wang, H. He, S. H. Tsang, W. Gao, K. Suenaga, F. Ma, C. Yang, L. Lu, T. Yu, E. H. T. Teo, G. Liu, and Z. Liu, Nature Communications **8**, (2017).
123. J. D. Splett, D. F. Vecchia, and L. F. Goodrich, J Res Natl Inst Stand Technol **116**, 489 (2011).
124. W. G. Fisher and M. J. Sienko, Inorg. Chem. **19**, 39 (1980).
125. J. Zhou, J. Lin, X. Huang, Y. Zhou, Y. Chen, J. Xia, H. Wang, Y. Xie, H. Yu, J. Lei, D. Wu, F. Liu, Q. Fu, Q. Zeng, C.-H. Hsu, C. Yang, L. Lu, T. Yu, Z. Shen, H. Lin, B. I. Yakobson, Q. Liu, K. Suenaga, G. Liu, and Z. Liu, Nature **556**, 355 (2018).
126. M. N. Baibich, J. M. Broto, A. Fert, F. N. Van Dau, F. Petroff, P. Etienne, G. Creuzet, A. Friederich, and J. Chazelas, Phys. Rev. Lett. **61**, 2472 (1988).
127. G. Binasch, P. Grünberg, F. Saurenbach, and W. Zinn, Phys. Rev. B **39**, 4828 (1989).
128. W. Gil, D. Görlitz, M. Horisberger, and J. Kötzler, Phys. Rev. B **72**, 134401 (2005).
129. B. Dieny, V. S. Speriosu, S. Metin, S. S. P. Parkin, B. A. Gurney, P. Baumgart, and D. R. Wilhoit, Journal of Applied Physics **69**, 4774 (1991).
130. C. Tannous and R. L. Comstock, in *Springer Handbook of Electronic and Photonic Materials*, edited by S. Kasap and P. Capper (Springer International Publishing, Cham, 2017), pp. 1–1.
131. L. S. Uspenskaya, O. A. Tikhomirov, S. I. Bozhko, S. V. Egorov, and A. A. Chugunov, Journal of Applied Physics **113**, 163907 (2013).
132. R. Peierls, Mathematical Proceedings of the Cambridge Philosophical Society **32**, 477 (1936).

133. N. D. Mermin and H. Wagner, Physical Review Letters **17**, 1133 (1966).
134. P. C. Hohenberg, Phys. Rev. **158**, 383 (1967).
135. L. Onsager, Phys. Rev. **65**, 117 (1944).
136. O. A. Tretiakov, M. Morini, S. Vasylkevych, and V. Slastikov, Phys. Rev. Lett. **119**, 077203 (2017).
137. D. Sander, Rep. Prog. Phys. **62**, 809 (1999).
138. P. Orgiani, A. Yu. Petrov, C. Adamo, C. Aruta, C. Barone, G. M. De Luca, A. Galdi, M. Polichetti, D. Zola, and L. Maritato, Phys. Rev. B **74**, 134419 (2006).
139. P. F. Carcia, Journal of Applied Physics **63**, 5066 (1988).
140. D. P. Pappas, K.-P. Kämper, and H. Hopster, Phys. Rev. Lett. **64**, 3179 (1990).
141. B. Huang, G. Clark, E. Navarro-Moratalla, D. R. Klein, R. Cheng, K. L. Seyler, D. Zhong, E. Schmidgall, M. A. McGuire, D. H. Cobden, W. Yao, D. Xiao, P. Jarillo-Herrero, and X. Xu, Nature **546**, 270 (2017).
142. C. Gong, L. Li, Z. Li, H. Ji, A. Stern, Y. Xia, T. Cao, W. Bao, C. Wang, Y. Wang, Z. Q. Qiu, R. J. Cava, S. G. Louie, J. Xia, and X. Zhang, Nature **546**, 265 (2017).
143. B. Huang, M. A. McGuire, A. F. May, D. Xiao, P. Jarillo-Herrero, and X. Xu, Nature Materials 1 (2020).
144. B. Huang, G. Clark, D. R. Klein, D. MacNeill, E. Navarro-Moratalla, K. L. Seyler, N. Wilson, M. A. McGuire, D. H. Cobden, D. Xiao, W. Yao, P. Jarillo-Herrero, and X. Xu, Nature Nanotechnology **13**, 544 (2018).
145. Y. Deng, Y. Yu, Y. Song, J. Zhang, N. Z. Wang, Z. Sun, Y. Yi, Y. Z. Wu, S. Wu, J. Zhu, J. Wang, X. H. Chen, and Y. Zhang, Nature **563**, 94 (2018).
146. K. L. Seyler, D. Zhong, B. Huang, X. Linpeng, N. P. Wilson, T. Taniguchi, K. Watanabe, W. Yao, D. Xiao, M. A. McGuire, K.-M. C. Fu, and X. Xu, Nano Lett. **18**, 3823 (2018).
147. M. Gibertini, M. Koperski, A. F. Morpurgo, and K. S. Novoselov, Nat. Nanotechnol. **14**, 408 (2019).
148. K. S. Burch, D. Mandrus, and J.-G. Park, Nature **563**, 47 (2018).
149. S. Jiang, L. Li, Z. Wang, K. F. Mak, and J. Shan, Nature Nanotechnology **13**, 549 (2018).
150. H. González-Herrero, J. M. Gómez-Rodríguez, P. Mallet, M. Moaied, J. J. Palacios, C. Salgado, M. M. Ugeda, J.-Y. Veuillen, F. Yndurain, and I. Brihuega, Science **352**, 437 (2016).
151. O. V. Yazyev and L. Helm, Phys. Rev. B **75**, 125408 (2007).
152. M. Weser, Y. Rehder, K. Horn, M. Sicot, M. Fonin, A. B. Preobrajenski, E. N. Voloshina, E. Goering, and Yu. S. Dedkov, Appl. Phys. Lett. **96**, 012504 (2010).
153. Y. Zhang, S.-Y. Li, H. Huang, W.-T. Li, J.-B. Qiao, W.-X. Wang, L.-J. Yin, K.-K. Bai, W. Duan, and L. He, Phys. Rev. Lett. **117**, 166801 (2016).
154. J. J. Palacios, J. Fernández-Rossier, and L. Brey, Phys. Rev. B **77**, 195428 (2008).
155. Z. Zhang, X. Zou, V. H. Crespi, and B. I. Yakobson, ACS Nano **7**, 10475 (2013).
156. A. Avsar, C.-Y. Cheon, M. Pizzochero, M. Tripathi, A. Ciarrocchi, O. V. Yazyev, and A. Kis, Nat Commun **11**, 4806 (2020).
157. Y. Zhao, J. Qiao, Z. Yu, P. Yu, K. Xu, S. P. Lau, W. Zhou, Z. Liu, X. Wang, W. Ji, and Y. Chai, Advanced Materials **29**, 1604230 (2017).
158. N. R. Pradhan, D. Rhodes, S. Memaran, J. M. Poumirol, D. Smirnov, S. Talapatra, S. Feng, N. Perea-Lopez, A. L. Elias, M. Terrones, P. M. Ajayan, and L. Balicas, Sci Rep **5**, 8979 (2015).
159. J. Chen, J. Zhou, W. Xu, Y. Wen, Y. Liu, and J. H. Warner, Nano Lett. **22**, 3289 (2022).
160. H. Zheng, Y. Choi, F. Baniasadi, D. Hu, L. Jiao, K. Park, and C. Tao, 2D Mater. **6**, 041005 (2019).
161. J. S. Moodera, L. R. Kinder, T. M. Wong, and R. Meservey, Phys. Rev. Lett. **74**, 3273 (1995).
162. M. Julliere, Physics Letters A **54**, 225 (1975).
163. S. Zhang, P. M. Levy, A. C. Marley, and S. S. P. Parkin, Phys. Rev. Lett. **79**, 3744 (1997).
164. J. Zhang and R. M. White, Journal of Applied Physics **83**, 6512 (1998).
165. A. Avsar, J. Y. Tan, T. Taychatanapat, J. Balakrishnan, G. K. W. Koon, Y. Yeo, J. Lahiri, A. Carvalho, A. S. Rodin, E. C. T. O'Farrell, G. Eda, A. H. Castro Neto, and B. Özyilmaz, Nat Commun **5**, 4875 (2014).
166. P. Maletinsky, S. Hong, M. S. Grinolds, B. Hausmann, M. D. Lukin, R. L. Walsworth, M. Loncar, and A. Yacoby, Nature Nanotech **7**, 320 (2012).
167. L. Thiel, Z. Wang, M. A. Tschudin, D. Rohner, I. Gutiérrez-Lezama, N. Ubrig, M. Gibertini, E. Giannini, A. F. Morpurgo, and P. Maletinsky, Science **364**, 973 (2019).
168. W. M. Parkin, A. Balan, L. Liang, P. M. Das, M. Lamparski, C. H. Naylor, J. A. Rodríguez-Manzo, A. T. C. Johnson, V. Meunier, and M. Drndić, ACS Nano **10**, 4134 (2016).
169. S. Mignuzzi, A. J. Pollard, N. Bonini, B. Brennan, I. S. Gilmore, M. A. Pimenta, D. Richards, and D. Roy, Phys. Rev. B **91**, 195411 (2015).
170. F. Hellman, A. Hoffmann, Y. Tserkovnyak, G. S. D. Beach, E. E. Fullerton, C. Leighton, A. H. MacDonald, D. C. Ralph, D. A. Arena, H. A. Dürr, P. Fischer, J. Grollier, J. P. Heremans, T. Jungwirth, A. V. Kimel, B. Koopmans, I. N. Krivorotov, S. J. May, A. K. Petford-Long, J. M. Rondinelli, N. Samarth, I. K. Schuller, A. N. Slavin, M. D. Stiles, O. Tchernyshyov, A. Thiaville, and B. L. Zink, Rev. Mod. Phys. **89**, 025006 (2017).
171. V. P. Amin, J. Zemen, and M. D. Stiles, Phys. Rev. Lett. **121**, 136805 (2018).
172. K. Uchida, S. Takahashi, K. Harii, J. Ieda, W. Koshibae, K. Ando, S. Maekawa, and E. Saitoh, Nature **455**, 778 (2008).
173. J. Xiao, G. E. W. Bauer, K. Uchida, E. Saitoh, and S. Maekawa, Physical Review B **81**, (2010).
174. Z. Wei, A. Sharma, A. S. Nunez, P. M. Haney, R. A. Duine, J. Bass, A. H. MacDonald, and M. Tsoi, Physical Review Letters **98**, (2007).
175. L. Liu, O. J. Lee, T. J. Gudmundsen, D. C. Ralph, and R. A. Buhrman, Phys. Rev. Lett. **109**, 096602 (2012).
176. I. M. Miron, K. Garello, G. Gaudin, P.-J. Zermatten, M. V. Costache, S. Auffret, S. Bandiera, B. Rodmacq, A. Schuhl, and P. Gambardella, Nature **476**, 189 (2011).

177. B. Dieny and M. Chshiev, Reviews of Modern Physics **89**, (2017).
178. T. Seki, Y. Hasegawa, S. Mitani, S. Takahashi, H. Imamura, S. Maekawa, J. Nitta, and K. Takanashi, Nature Materials **7**, 125 (2008).
179. E. C. Ahn, Npj 2D Materials and Applications **4**, 1 (2020).
180. X. Lin, W. Yang, K. L. Wang, and W. Zhao, Nature Electronics **2**, 274 (2019).
181. B. I. Sturman and V. M. Fridkin, *The Photovoltaic and Photorefractive Effects in Noncentrosymmetric Materials* (Routledge, London, 2021).
182. J. E. Spanier, V. M. Fridkin, A. M. Rappe, A. R. Akbashev, A. Polemi, Y. Qi, Z. Gu, S. M. Young, C. J. Hawley, D. Imbrenda, G. Xiao, A. L. Bennett-Jackson, and C. L. Johnson, Nature Photon **10**, 611 (2016).
183. T. Akamatsu, T. Ideue, L. Zhou, Y. Dong, S. Kitamura, M. Yoshii, D. Yang, M. Onga, Y. Nakagawa, K. Watanabe, T. Taniguchi, J. Laurienzo, J. Huang, Z. Ye, T. Morimoto, H. Yuan, and Y. Iwasa, Science **372**, 68 (2021).
184. Y. J. Zhang, T. Ideue, M. Onga, F. Qin, R. Suzuki, A. Zak, R. Tenne, J. H. Smet, and Y. Iwasa, Nature **570**, 349 (2019).
185. L. Du, T. Hasan, A. Castellanos-Gomez, G.-B. Liu, Y. Yao, C. N. Lau, and Z. Sun, Nat Rev Phys **3**, 193 (2021).
186. J. Xu and E. Plum, Opt. Express, OE **30**, 7162 (2022).
187. R. Cunha, A. Cadore, S. L. L. M. Ramos, K. Watanabe, T. Taniguchi, S. Kim, A. S. Solntsev, I. Aharonovich, and L. M. Malard, J. Phys.: Condens. Matter **32**, 19LT01 (2020).
188. L. Zhou, H. Fu, T. Lv, C. Wang, H. Gao, D. Li, L. Deng, and W. Xiong, Nanomaterials **10**, 2263 (2020).
189. H.-P. Komsa, J. Kotakoski, S. Kurasch, O. Lehtinen, U. Kaiser, and A. V. Krasheninnikov, Physical Review Letters **109**, (2012).
190. S. B. Desai, S. R. Madhvapathy, M. Amani, D. Kiriya, M. Hettick, M. Tosun, Y. Zhou, M. Dubey, J. W. Ager, D. Chrzan, and A. Javey, Advanced Materials **28**, 4053 (2016).
191. D. P. Gulo, H. Yeh, W.-H. Chang, and H.-L. Liu, Sci Rep **10**, 19003 (2020).
192. C. Lee, H. Yan, L. E. Brus, T. F. Heinz, J. Hone, and S. Ryu, ACS Nano **4**, 2695 (2010).
193. M. Buscema, J. O. Island, D. J. Groenendijk, S. I. Blanter, G. A. Steele, H. S. J. van der Zant, and A. Castellanos-Gomez, Chem. Soc. Rev. **44**, 3691 (2015).
194. M. Buscema, M. Barkelid, V. Zwiller, H. S. J. van der Zant, G. A. Steele, and A. Castellanos-Gomez, Nano Lett. **13**, 358 (2013).
195. J. Quereda, T. S. Ghiasi, J.-S. You, J. van den Brink, B. J. van Wees, and C. H. van der Wal, Nat Commun **9**, 3346 (2018).
196. S. Dhara, E. J. Mele, and R. Agarwal, Science **349**, 726 (2015).
197. Q. Wang, J. Zheng, Y. He, J. Cao, X. Liu, M. Wang, J. Ma, J. Lai, H. Lu, S. Jia, D. Yan, Y. Shi, J. Duan, J. Han, W. Xiao, J.-H. Chen, K. Sun, Y. Yao, and D. Sun, Nat Commun **10**, 5736 (2019).
198. L. Mennel, M. Paur, and T. Mueller, APL Photonics **4**, 034404 (2019).
199. S. Wang, H. Zhang, J. Zhang, S. Li, D. Luo, J. Wang, K. Jin, and J. Sun, Phys. Rev. Lett. **128**, 187401 (2022).
200. Y. Zhao, L. Du, J. Liang, M. Bahramy, M. Yang, Y. Guang, Z. Wei, M. Liao, J. Tang, J. Zhao, C. Shen, X. Li, Q. Wang, R. Yang, D. Shi, K. Liu, Z. Sun, and G. Zhang, *Spin-Layer Locking Induced Second-Order Nonlinear Effect in Centrosymmetric Crystals* (In Review, 2020).
201. M. Otteneder, S. Hubmann, X. Lu, D. A. Kozlov, L. E. Golub, K. Watanabe, T. Taniguchi, D. K. Efetov, and S. D. Ganichev, Nano Lett. **20**, 7152 (2020).
202. M. P. Singh, J. Kiemle, I. Ozdemir, P. Zimmermann, T. Taniguchi, K. Watanabe, M. Burghard, O. Üzengi Aktürk, C. Kastl, and A. W. Holleitner, 2D Mater. **9**, 011002 (2022).
203. Z. Ji, G. Liu, Z. Addison, W. Liu, P. Yu, H. Gao, Z. Liu, A. M. Rappe, C. L. Kane, E. J. Mele, and R. Agarwal, Nat. Mater. **18**, 955 (2019).
204. J. Quereda, J. Hidding, T. S. Ghiasi, B. J. van Wees, C. H. van der Wal, and M. H. D. Guimarães, Npj 2D Materials and Applications **5**, 1 (2021).
205. V. I. Belinicher and B. I. Sturman, Sov. Phys. Usp. **23**, 199 (1980).
206. W. Weber, L. E. Golub, S. N. Danilov, J. Karch, C. Reitmaier, B. Wittmann, V. V. Bel'kov, E. L. Ivchenko, Z. D. Kvon, N. Q. Vinh, A. F. G. van der Meer, B. Murdin, and S. D. Ganichev, Phys. Rev. B **77**, 245304 (2008).
207. C. Guo, Y. Hu, G. Chen, D. Wei, L. Zhang, Z. Chen, W. Guo, H. Xu, C.-N. Kuo, C. S. Lue, X. Bo, X. Wan, L. Wang, A. Politano, X. Chen, and W. Lu, Sci. Adv. **6**, eabb6500 (2020).
208. P. Olbrich, L. E. Golub, T. Herrmann, S. N. Danilov, H. Plank, V. V. Bel'kov, G. Mussler, Ch. Weyrich, C. M. Schneider, J. Kampmeier, D. Grützmacher, L. Plucinski, M. Eschbach, and S. D. Ganichev, Phys. Rev. Lett. **113**, 096601 (2014).
209. J. Li, T. Joseph, M. Ghorbani-Asl, S. Kolekar, A. V. Krasheninnikov, and M. Batzill, Advanced Functional Materials **32**, 2110428 (2022).
210. R. W. Boyd, in *Nonlinear Optics (Fourth Edition)*, edited by R. W. Boyd (Academic Press, 2020), pp. 1–64.
211. A. Allain, J. Kang, K. Banerjee, and A. Kis, Nature Materials **14**, 1195 (2015).
212. Y. Liu, P. Stradins, and S.-H. Wei, Science Advances **2**, e1600069 (2016).
213. J. Jo, J. H. Kim, C. H. Kim, J. Lee, D. Choe, I. Oh, S. Lee, Z. Lee, H. Jin, and J.-W. Yoo, Nat Commun **13**, 2759 (2022).

Cheol-yeon Cheon Last update: 2022.03.17

Contact

Address: EPFL, BM 2141, Station 17, 1015 Lausanne, Switzerland
Phone : +41 789741992
E-mail : chulyeon25@gmail.com (primary), cheol-yeon.cheon@epfl.ch (secondary)

Research Interest

Emerging novel electronic and magnetic properties in 2D van der Waal materials

Education

École Polytechnique Fédérale de Lausanne(EPFL)

Ph.D., in Material Science and Engineering, August, 2022

Dissertation title : *Disorder-induced electronic, magnetic, and optoelectronic properties in two-dimensional materials.*
Thesis advisor : Andras Kis

Korea Advanced Institute of Science and Technology(KAIST)

M.S., in Material Science and Engineering, August, 2017

Dissertation title : *Enhancement on spin thermoelectric voltage of CoFeB/Pt bilayer from Au and Ag localized surface plasmon resonance.*
Thesis adviosr : Byong-Guk Park

Yonsei University

B.S., in Material Science and Engineering, August 2015

Publications

1. **Cheon, CY.** et al. Disorder-induced photovoltaic effect in centrosymmetric layered $PtSe_2$, in preparation (2022).
2. Zhao, Y., Tripathi, M., Cernevics, K., Avsar, A., Ji, H., Marin, JG., **Cheon, CY.** et al Electrical spectroscopy of defect states and their hybridization in monolayer MoS2, submitted (2022).
3. Marin, JG., Unuchek, D., Sun Z., **Cheon, CY.**, Tagarelli, F., Watanabe K., Taniguchi, T., Kis, A. Room-temperature electrical control of polarization and emission angle in a cavity-integrated 2D pulsed LED, submitted (2022).
4. Glushkov, E., Macha, M., Rath, E., Navikas, V., Ronceray, N., **Cheon, CY.** et al. Engineering Optically Active Defects in hexagonal Boron Nitride using Focused Ion Beam and Water. *ACS Nano* 16, 3, 3695-3703 (2022).
5. Wang, Z.*, **Cheon, CY.*** et al. Superconducting 2D NbS_2 grown epitaxially by chemical vapor deposition. *ACS Nano* 15, 18403–18410 (2021).
6. Kim, J.-M., Kim, D.-J., **Cheon, C.-Y.** et al. Observation of thermal spin–orbit torque in W/-CoFeB/MgO structures. *Nano Letters* 20, 7803–7810 (2020).
7. Avsar, A.*, **Cheon, CY.*** et al. Probing magnetism in atomically thin semiconducting $PtSe_2$. *Nature Communications* 11, (2020).
8. Kim, J.-M., **Jeon, C.-Y.** et al. Amplification of spin thermoelectric signals in multilayer spin thermopiles. *ACS Applied Electronic Materials* 2, 2906–2912 (2020).
9. **Jeon, C.-Y.** et al. Plasmon-enhanced photodetection in ferromagnet/nonmagnet spin thermoelectric structures. *Advanced Functional Materials* 28, 1802936 (2018).
10. Kim, DJ., **Jeon, CY.** et al. Observation of transverse spin Nernst magnetoresistance induced by thermal spin current in ferromagnet/non-magnet bilayers. *Nature Communications* 8, 1400 (2017).

Patents

1. Park, B. G., Kim, D. J. **Jeon, C. Y.** Semiconductor device, semiconductor device control method and optical switch. US Patent 10 , 276 , 780 (2019).

Awards

1. **Best Poster Award**
   61th Magnetism and Magnetic Materials conference, New Orleans, USA
   (Nov. 2016)
2. ***Cum Laude***, Yonsei University (Aug. 2015)
3. **S. Korea National Science and Technology Scholarship**
   (Mar. 2013 - Aug. 2015)

Extracurricular Activities

1. **Main organizer (EPFL-ETHZ 2021 Summer School)**
   "Spintronics and Magnetism on 2D materials", August 23-27, 2021
   Webpage : `https://2dspintronics2021.epfl.ch/`

Teaching Assistant

1. **Optical detector (2021)** Lecturer: Dr. Besse Pierre-André, EPFL
2. **Nanoscale heat transfer (2021)**, Lecturer: Prof. Giulia Tagliabue, EPFL
3. **Introduction to magnetic materials in modern technologies (2019)**
   Lecturer: Prof. Dirk Grundler, EPFL
4. **Advanced metalluragy (2019)** Lecturer: Dr. Ludger Weber, EPFL
5. **Measurement Systems Laboratory (2019)** Lecturer: Prof. Andras Kis, EPFL
6. **Measuring systems (2018)** Lecturer: Prof. Andras Kis, EPFL

Hand-On Experience

- **Cryogenics**
  - Wet bath cryostat, flow cryostat, and closed-cycle cryostat systems.
- **Optical Measurements**
  - CW laser spectroscopies, optoelectronics.
- **Electronic Measurements**
  - Low noise, low current measurements, lock-in and current amplifiers.
- **2D van der Waals Heterostructure**
  - Handling 2D materials (e.g. h-BN, CrI_3, WSe_2) and its transfer techniques.
- **Clean Room**
  - Photo/e-beam lithography, thin film deposition(evaporation/sputtering), etching(gas, ion-beam), wire-bonding, and wafer-dicing.
- **Metrology**
  - SEM, AFM, Raman, photoluminescence, EDX, VSM, UV-Vis spectrometer, XRD.
- **Computer Software**
  - LABVIEW, COMSOL, Matlab, Python, Origin, OOMMF, 3D Max, DesignCAD

Language

English(Fluent), Korean(Native), French(Basic), Chinese(Basic)